

AD-A135 903

RANDOM CHOICE SOLUTIONS FOR WEAK SPHERICAL SHOCK-WAVE
TRANSITIONS OF N-WAVE (U) TORONTO UNIV DOWNSVIEW
(ONTARIO) INST FOR AEROSPACE STUDIES H HONMA ET AL.

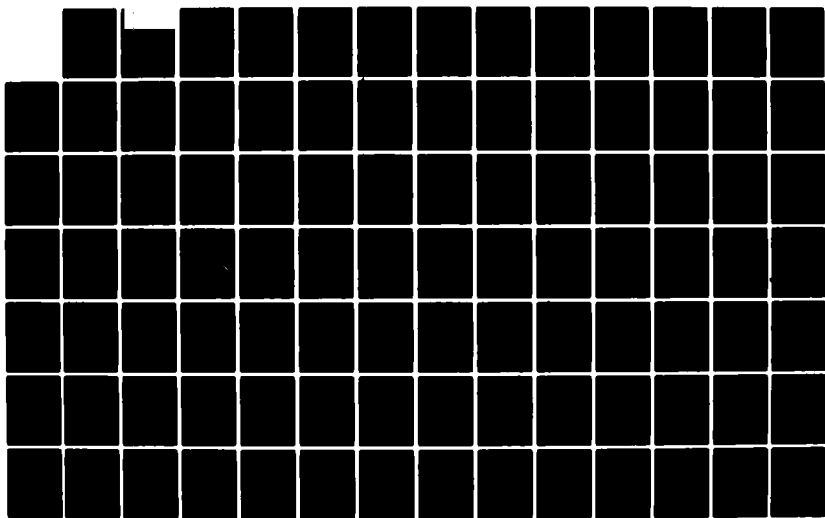
1/2

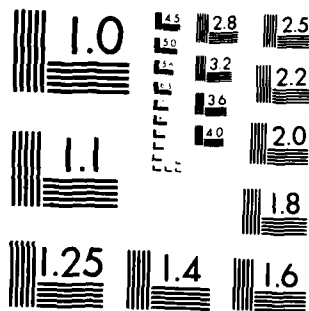
UNCLASSIFIED

JUL 83 UTIAS-253 AFOSR-TR-83-1041

F/G 20/1

NL





MICROCOPY RESOLUTION TEST CHART
NATIONAL BUREAU OF STANDARDS-1963-A



INSTITUTE
FOR
AEROSPACE STUDIES

UNIVERSITY OF TORONTO

AFOSR-TR. 83-1041

12

RANDOM CHOICE SOLUTIONS
FOR WEAK SPHERICAL SHOCK-WAVE TRANSITIONS OF N-WAVES IN AIR
WITH VIBRATIONAL EXCITATION

BY

H. HONMA AND I. I. GLASS

DMC FILE COPY

JULY, 1983

UTIAS REPORT NO. 253
CN ISSN 0082-5255

83 12 13 279

Approved for public release.
Distribution unlimited.

UNCLASSIFIED

SECURITY CLASSIFICATION OF THIS PAGE (When Data Entered)

REPORT DOCUMENTATION PAGE		READ INSTRUCTIONS BEFORE COMPLETING FORM
1. REPORT NUMBER AFOSR-TR- 83-1041	2. GOVT ACCESSION NO.	3. RECIPIENT'S CATALOG NUMBER
4. TITLE (and Subtitle) RANDOM CHOICE SOLUTIONS FOR WEAK SPHERICAL SHOCK-WAVE TRANSITIONS OF N-WAVES IN AIR WITH VIBRATIONAL EXCITATION		5. TYPE OF REPORT & PERIOD COVERED Interim
7. AUTHOR(s) H. HONMA and I. I. GLASS		6. PERFORMING ORG. REPORT NUMBER UTIAS Report No. 253
9. PERFORMING ORGANIZATION NAME AND ADDRESS Institute for Aerospace Studies, University of Toronto, 4925 Dufferin St., Downsview, Ontario, Canada, M3H 5T6		8. CONTRACT OR GRANT NUMBER(s) AFOSR 82-0097
11. CONTROLLING OFFICE NAME AND ADDRESS Air Force Office of Scientific Research (N A) Bolling AFB, DC 20332		10. PROGRAM ELEMENT, PROJECT, TASK AREA & WORK UNIT NUMBERS 61102F 2307/A1
14. MONITORING AGENCY NAME & ADDRESS (if different from Controlling Office)		12. REPORT DATE July, 1983
		13. NUMBER OF PAGES ///
		15. SECURITY CLASS. (of this report) UNCLASSIFIED
		15a. DECLASSIFICATION/DOWNGRADING SCHEDULE
16. DISTRIBUTION STATEMENT (of this Report) Approved for public release; distribution unlimited.		
17. DISTRIBUTION STATEMENT (of the abstract entered in Block 20, if different from Report)		
18. SUPPLEMENTARY NOTES		
19. KEY WORDS (Continue on reverse side if necessary and identify by block number) 1. Shock-wave transitions 2. Effects of viscosity, heat-conduction and vibrational excitation. 3. Spherical shock waves 4. Exploding wires 5. Numerical methods		
20. ABSTRACT (Continue on reverse side if necessary and identify by block number) In order to clarify the effects of vibrational excitation on shock-wave transitions of weak, spherical N-waves, which were generated by using sparks and exploding wires as sources, the compressible Navier-Stokes equations were solved numerically, including a one-mode vibrational-relaxation equation. A small pressurized air-sphere explosion was used to simulate the N-waves generated from the actual sources. By employing the random-choice method (RCM) with an operator-splitting technique, the effects		

DD FORM 1 JAN 73 1473

EDITION OF 1 NOV 65 IS OBSOLETE

UNCLASSIFIED

SECURITY CLASSIFICATION OF THIS PAGE (When Data Entered)

83 12 13 279

UNCLASSIFIED

SECURITY CLASSIFICATION OF THIS PAGE(When Data Entered)

of artificial viscosity appearing in finite-difference schemes were eliminated and accurate profiles of the shock transitions were obtained. However, a slight randomness in the variation of the shock thickness remains. It is shown that a computer simulation is possible by using a proper choice of initial parameters to obtain the variations of the N-wave overpressure and half-duration with distance from the source. The calculated rise times are also shown to simulate both spark and exploding-wire data. It was found that, in addition to the vibrational-relaxation time of oxygen, both the duration and the attenuation rate of a spherical N-wave are important factors controlling its rise time.

The effects of the duration and the attenuation rate of a spherical N-wave on its rise time, which are designated as *the N-wave effect* and *the nonstationary effect*, respectively, are discussed in more detail pertaining to Lighthill's analytical solutions and the RCM solutions for nonstationary plane waves and spherical N-waves. It is also shown that the duration and the attenuation rate of a spherical N-wave are affected by viscosity and vibrational nonequilibrium, so that they can deviate from the results of classical, linear acoustic theory for very weak spherical waves.

UNCLASSIFIED

SECURITY CLASSIFICATION OF THIS PAGE(When Data Entered)

AIR FORCE OFFICE OF SCIENTIFIC RESEARCH (AFSC)
NOTICE OF INITIAL TO DTIC
This technical report has been reviewed and is
approved for release under AFR 190-12.
DISTRIBUTION STATEMENT
MATTHEW J. K. [unclear]
Chief, Technical Information Division

RANDOM-CHOICE SOLUTIONS
FOR WEAK SPHERICAL SHOCK-WAVE TRANSITIONS OF N-WAVES IN AIR
WITH VIBRATIONAL EXCITATION

by

H. Honma and I. I. Glass

Submitted July, 1982

July, 1983

UTIAS Report No. 253
CN ISSN 0082-5255



AI

Acknowledgements

We would like to thank Dr. J. P. Sislian and Dr. T. Saito for their valuable suggestions and discussions. The assistance received from Mr. O. Holst-Jensen in conducting the experiments and from Mr. Y. Tsumita in performing the numerical calculations is very much appreciated.

The financial assistance received from the U.S. Air Force of Scientific Research under Grant AFOSR-82-0097, the Natural Sciences and Engineering Research Council of Canada, the Japan Society for the Promotion of Science, and the Scientific Research Aid of the Ministry of Education of Japan are acknowledged with thanks.

Summary

In order to clarify the effects of vibrational excitation on shock-wave transitions of weak, spherical N-waves, which were generated by using sparks and exploding wires as sources, the compressible Navier-Stokes equations were solved numerically, including a one-mode vibrational-relaxation equation. A small pressurized air-sphere explosion was used to simulate the N-waves generated from the actual sources. By employing the random-choice method (RCM) with an operator-splitting technique, the effects of artificial viscosity appearing in finite-difference schemes were eliminated and accurate profiles of the shock transitions were obtained. However, a slight randomness in the variation of the shock thickness remains. It is shown that a computer simulation is possible by using a proper choice of initial parameters to obtain the variations of the N-wave overpressure and half-duration with distance from the source. The calculated rise times are also shown to simulate both spark and exploding-wire data. It was found that, in addition to the vibrational-relaxation time of oxygen, both the duration and the attenuation rate of a spherical N-wave are important factors controlling its rise time.

The effects of the duration and the attenuation rate of a spherical N-wave on its rise time, which are designated as *the N-wave effect* and *the nonstationary effect*, respectively, are discussed in more detail pertaining to Lighthill's analytical solutions and the RCM solutions for nonstationary plane waves and spherical N-waves. It is also shown that the duration and the attenuation rate of a spherical N-wave are affected by viscosity and vibrational nonequilibrium, so that they can deviate from the results of classical, linear acoustic theory for very weak spherical waves.

Contents

	<u>Page</u>
Acknowledgements	ii
Summary	iii
List of Symbols	v
1. INTRODUCTION	1
2. SPARK AND EXPLODING-WIRE DATA	2
3. SOME ANALYSES FOR WEAK SHOCK TRANSITIONS	3
3.1 Classical Taylor Plane Shock-Wave Transitions	3
3.2 Viscous Plane N-Waves	4
3.3 Nonstationary Viscous Plane Waves	6
3.4 Shock Transitions with Vibrational Excitation	6
4. RANDOM-CHOICE ANALYSES FOR WEAK-SHOCK TRANSITIONS	10
4.1 Basic Equations	10
4.2 Numerical Method	11
4.3 Solutions for Plane Waves	12
4.3.1 Perfect-Inviscid Solution	12
4.3.2 Perfect-Viscous Solution	12
4.3.3 Real-Inviscid Solution	13
4.4 Solutions for Spherical Waves	14
4.4.1 Near-Field Solutions for Perfect-Inviscid Flows	14
4.4.2 Comparison Between Perfect-Inviscid, Perfect-Viscous, Real-Inviscid and Real-Viscous Far-Field Solutions	15
4.4.3 Simulations for Spark and Exploding-Wire Generated N-Waves	15
4.4.4 Effects of Vibrational-Relaxation Time	17
4.4.5 Effects of N-Wave Duration	17
4.4.6 Effects of Nitrogen Vibrational Relaxation	18
5. CONCLUSIONS	19
REFERENCES	19
TABLES	21
FIGURES	
APPENDIX A: EVALUATION OF \bar{P}_{max} , ΔZ AND Z_d IN THE Lighthill N-WAVE SOLUTION	
APPENDIX B: DERIVATION OF ANALYTICAL RELATIONS IN SECTION 3.4	
APPENDIX C: PROGRAM LISTING FOR RANDOM-CHOICE METHOD	
APPENDIX D: PROGRAM OF MacCORMACK'S FINITE-DIFFERENCE METHOD	
APPENDIX E: COMPARISON BETWEEN NEAR-FIELD SOLUTIONS OF THE EXPLOSION OF A PRESSURIZED AIR SPHERE USING LAX, MacCORMACK AND RANDOM-CHOICE METHODS FOR A PERFECT-INVISCID FLOW	
APPENDIX F: BULK VISCOSITY ANALYSIS FOR VIBRATIONAL RELAXATION FOR OXYGEN	

List of Symbols

a	speed of sound
a_1	undisturbed speed of sound
a_e	equilibrium speed of sound
a_f	frozen speed of sound
c_j	normalized vibrational specific heat for j-molecule ($= c_j'/R$)
C	viscous term in Eq. (4.1)
e	internal energy
E	total energy
h	absolute humidity
H_I	spherical correction of convection term in Eq. (4.1)
H_R	vibrational relaxation term in Eq. (4.1)
H_V	spherical correction of viscous term in Eq. (4.1)
j	$j = 0$, plane wave; $j = 2$, spherical wave [Eq. (4.1)]
k	coefficient in Eq. (3.24)
m	$(a_f^2 - a_e^2)/a_e^2$
M_e	equilibrium Mach number
M_f	frozen Mach number
M_s	shock Mach number
n	decay index of $(\Delta p)_{\max}$ for spherical wave
p	pressure
p_0	normal pressure, 101.3 KPa
p_1	undisturbed pressure
p_{sat}	partial pressure of water vapour at saturation
p_{41}	initial diaphragm pressure ratio
Pr	Prandtl number
\bar{p}	similarity variable for plane N-waves, defined by Eq. (3.12)
\bar{p}_{\max}	maximum value of \bar{p}
(Δp)	overpressure ($= p - p_1$)
$(\Delta p)_2$	equilibrium overpressure behind steady plane shock wave
$(\Delta p)_{\max}$	maximum overpressure of N-wave
$(\Delta p)_f$	overpressure immediately behind frozen shock wave
$(\Delta p)_{\text{cr},j}$	critical overpressure for j-molecule
r	radial distance
r_0	radius of pressurized sphere
r^*	normalized radial distance ($= r/r_0$)

List of Symbols - Continued

R	gas constant
Re	Reynolds number defined by Eq. (3.10)
RH	relative humidity
Δr	increment of r
Δr^*	increment of r^*
S	discharge voltage for spark and exploding-wire sources
t	time
t_d	half duration of N-wave
t_r	rise time
$t_{r,0}^*$	Taylor rise time for 10-90% maximum overpressure
t_s	characteristic shock-thickening time
t^*	normalized time ($= a_1 t / r_0$ or $a_1 t / x_0$)
t_d^*	normalized half duration of N-wave ($= a_1 t_d / r_0$)
\bar{t}	normalized time ($= t / t_d$)
T	temperature
T_0	normal temperature
T_1	undisturbed temperature
T_{41}	initial diaphragm temperature ratio
$(T_v)_j$	vibrational temperature for j-molecule
Δt	increment of t
(\overline{T})	over-temperature ($= T - T_1$)
$(\overline{T})_2$	equilibrium over-temperature behind steady plane shock wave
$(\overline{T})_{\max}$	maximum over-temperature of N-wave
$(\overline{T}_v)_j$	vibrational over-temperature for j molecule
u	excess wavelet velocity ($= u + v - a_1$)
u_2	u at $X \rightarrow \infty$
u	flow velocity for steady shock wave
u_1	flow velocity ahead of steady shock wave
u_2	flow velocity behind steady shock wave
U	nonstationary term in Eq. (4.1)
U_s	shock speed
v	flow velocity
v_2	flow velocity behind moving plane shock wave
v	flow velocity in a moving coordinate system, Eq. (3.24)
v_0	absolute value of v at upstream and downstream infinity

List of Symbols - Continued

x	distance
x_0	length of high-pressure chamber of shock tube
x_d	half distance of N-wave corresponding to t_d
x_s	characteristic shock-thickening distance
x^*	normalized distance ($= x/x_0$)
X	coordinate defined as $X = x - a_1 t$
λ_d	half distance of N-wave, defined for X
λ_n	node of N-wave ($u = 0$), defined for X
Δx	increment of x
Δx^*	increment of x^*
$(\Delta x)_0^*$	Taylor thickness for 10-90% equilibrium overpressure
ΔX	shock thickness of N-wave, defined for X [Eq. (3.14)]
y	time in Eq. (3.24)
z	distance parameter defined by Eqs. (3.5), (3.16), (3.21), (3.35), (3.36), (3.39)
z_d	duration parameter defined by Eq. (3.15)
Δz	thickness parameter defined for z
$(\Delta z)_0$	Taylor-thickness parameter defined by maximum slope of velocity
$(\Delta z)_0^*$	Taylor-thickness parameter defined by 10-90% equilibrium overpressure
$(\Delta z)_0^{**}$	Taylor-thickness parameter defined by 5-95% equilibrium overpressure
γ	ratio of specific heats
κ	diffusivity defined by Eq. (3.2)
$(\kappa_v)_j$	diffusivity based on vibrational bulk viscosity for j -molecule
n_j	molar concentration for j -molecule
θ_j	characteristic vibrational temperature for j -molecule
k	thermal conductivity
μ	viscosity
μ_R	bulk viscosity for rotational relaxation
$(\mu_v)_j$	bulk viscosity for vibrational relaxation of j -molecule
ν	kinematic viscosity
ρ	density
ϵ_j	vibrational energy for j -molecule
$(\epsilon_j)_e$	equilibrium vibrational energy for j -molecule

List of Symbols - Concluded

τ	time parameter defined by Eq. (3.21)
τ_s	characteristic-time parameter for shock thickening
τ_j	relaxation time for j-molecule
ξ	similarity parameter for plane N-wave, defined by Eq. (3.12)
ξ_d	ξ corresponding to half duration of N-wave
ξ_m	ξ for \bar{p}_{\max}
$\Delta\xi$	shock thickness defined for ξ

Subscripts

N	nitrogen
O	oxygen

1. INTRODUCTION

The pressure waves generated by supersonic transport aircraft (SSI) and from explosions in air are often observed as weak N-waves far from the source. Such pressure waves are heard as sonic booms. The loudness of these waves depends on their maximum overpressures and rise times (Ref. 1). The N-waves with short (microseconds) rise times are perceived as louder and more startling than the ones with long (milliseconds) rise times. As a consequence, N-wave rise times were investigated extensively for SSI sonic booms and for explosions in air (Refs. 2-4). However, the observed SSI rise times were often found to be larger than those which were estimated from classical theory for viscous shock structures of steady, plane waves, derived by Taylor (Ref. 5). A recent review of this matter may be found in Ref. 6.

This discrepancy was attributed mainly to the effects of atmospheric turbulence (Refs. 7-10), and real-gas effects arising from the vibrational excitation of the oxygen and nitrogen air molecules (Refs. 11, 12). However, the decisive factor for this increased rise time was still in question. There were difficulties in providing correlations between the observed and analytically estimated rise times, owing to a lack of information regarding the ambient temperature, humidity and air turbulence. Such quantities are not always readily available. It was therefore necessary to carry out some simulation experiments under controlled conditions where known atmospheric conditions could be obtained.

Holst-Jensen (Ref. 6) was able to generate well-formed weak spherical N-waves by using sparks or exploding wires as a source in a still-air dome, usually used for air-cushion experiments (Ref. 13). In this manner he wanted to clarify the vibrational effects on the rise time of SSI N-waves. He found that the observed rise times were much shorter than the rise times estimated from the analysis of plane, fully-dispersed waves (Ref. 12). The results could not be explained by any existing analysis. The object of this report is to provide a theoretical basis for explaining Holst-Jensen's data, which will be outlined in Section 2.

The processes involved in the generation of N-waves by exploding sparks and wires are very complex and are not readily predicted. Consequently, it is necessary to assume a reasonable source model in order to simulate the explosions. In this paper it is assumed that the expanding plasma can be simulated by a pressurized sphere of small radius at room temperature. The computer simulation requires adjusting the radius of the pressurized sphere and the imaginary diaphragm pressure ratio to fit the experiments for maximum overpressure and half-duration of the N-wave with distance from the source. It is then possible to determine the initial energy of the source. The latter is of academic interest as it is not possible to determine the actual energy release from the voltage and capacitance of the discharge without a great deal of additional time-dependent measurements.

The nonstationary, spherical-symmetric Navier-Stokes equations were solved numerically, including the equation of one-mode vibrational relaxation for explosions of pressurized spheres in atmospheric

air. An operator splitting technique was used in which, at the first stage of calculation, the solutions for inviscid, frozen flow were obtained by applying the Random-Choice Method (RCM) and then the effects of viscosity and vibrational nonequilibrium were evaluated by using an explicit finite-difference method.

The RCM is a numerical method which was developed by Glimm (Ref. 14), Chorin (Ref. 15) and Sod (Ref. 16) for flow problems including shock waves. In this method, a Riemann problem is solved for each spatial mesh at each time step and then one of its solutions is chosen at random as a solution for the next time step by using a random sampling technique. It is the great merit of this method that shock waves and contact surfaces can be expressed as discontinuous surfaces without smearing arising from artificial viscosities inherent in all finite-difference methods. This is the main reason for adopting the RCM for the present analysis. The algorithm is based on a program developed by Saito and Glass (Ref. 17). The application of the operator-splitting technique for analyzing the Navier-Stokes equations was first introduced by McCormack (Ref. 18). In his analysis, the inviscid solutions were obtained using a characteristic method. Recently, Satofuka and Shimizu (Ref. 19) have tried to solve the Navier-Stokes equations for a shock-tube problem by applying the RCM with an operator-splitting technique. In the present analysis, the RCM with an operator-splitting technique was extended to include vibrational relaxation effects for spherically-symmetric waves.

It will be shown subsequently that the rise times of weak, spherical N-waves generated by sparks and exploding wires are seriously affected by two factors which never appear in steady plane waves. These are designated as an *N-wave effect* and a *nonstationary effect*, respectively. The N-wave effect means that the rise times of weak N-waves are affected by the expansion of the flow immediately behind the shock front. The nonstationary effect means that the rise times of weak shock waves respond to changes in shock strength so slowly that their transient behaviours must be considered. The fundamental analytical ideas about these effects were provided by Lighthill (Ref. 20) for both viscous N-waves and impulsively-generated viscous plane waves. In Section 3, his results are re-examined for use in the present study.

In order to consider the effects of vibrational excitation of oxygen and nitrogen air molecules, the papers of Polyakova et al (Ref. 21) and Johannsen and Hodgson (Ref. 12) for plane, dispersed waves are also re-examined in Section 3, and an approximate relation is derived for the rise time of a fully or partly-dispersed wave. Furthermore, the modified Taylor and Lighthill solutions for fully-dispersed waves are discussed.

In Sections 4.1 and 4.2, the basic equations and the numerical method of solution are described. In Section 4.3, to validate the method of solution for nonstationary shock transitions, RCM solutions for nonstationary viscous and dispersed plane waves are compared with analytical solutions described in Section 3. As for solutions for spherical waves (Section 4.4), some numerical results for weak spherical N-waves in air are presented for the following five cases: (i) formation of N-waves in

the near-field of a pressurized sphere, (ii) comparison between perfect-inviscid, perfect-viscous, real-inviscid and real-viscous solutions, (iii) effects of vibrational relaxation time or ambient temperature and humidity, (iv) effects of N-wave duration or radius of pressurized sphere, and (v) effects of nitrogen vibrational relaxation. The observed rise times of spark and exploding-wire generated N-waves are also compared with those obtained from the analytical simulations.

In this report, the usual definition of rise time is followed, and is taken as the time-interval for the overpressure to vary from 10% to 90% of its peak value. This definition is quite arbitrary and is especially useful for actual SST signatures, as discussed in Ref. 6. Figure 1.1 illustrates the definition of an N-wave rise time t_r and its half-duration t_d . Figure 1.2 also illustrates the definition of a plane-wave rise time t_r . The corresponding shock thickness Δx and half-duration length x_d may approximately be given by

$$\Delta x = a_1 t_r, \quad x_d = a_1 t_d$$

where a_1 is the undisturbed speed of sound, since we consider only very weak waves.

2. SPARK AND EXPLODING-WIRE DATA

In this section, the spark and exploding-wire experiments which were carried out by Holst-Jensen (Ref. 6) and the resulting data are summarized. The purpose of these experiments was to generate weak, fully-developed N-waves with overpressure below 100 Pa in air, which would have interference-free shock fronts. This was accomplished by using sparks and exploding wires. The dome containing the UTIAS air cushion vehicle (ACV) circular track facility (Ref. 13) was used as a still-air reservoir for part of the experiments. Its major internal diameter is about 42.1 m. This provided waves free from interference with walls and other objects.

For detecting weak shocks in the overpressure range 5-100 Pa, a condenser microphone was used [Bruel & Kjaer 4135 free field 6.3 mm (1/4 in) dia]. Amplification of the microphone signal was provided by a preamplifier B&K 2619. The response of the microphone system was tested in the UTIAS Travelling-Wave Sonic-Boom Simulator (Ref. 22). When measuring without its protective grid at zero angle of incidence, the microphone has an approximate minimum rise time $t_r = 2.9$ μ sec. The oscilloscopes used were Tektronix types 555 and 535 with a type D plug-in that has a bandwidth better than 300 KHz. The microphone was calibrated with a B&K pistophone type 4220, which gives a sound pressure level at 250 Hz of 124 dB.

In the first series of experiments, sparks were used as a source of N-waves. The sparks were generated by the energy released from a charged 7.5 μ F capacitor. The maximum charging voltage was 8 kV and the discharge device was a thyatron. A microphone was placed ahead of the measuring microphone in parallel to get the trigger signal for the oscilloscope. The source and microphone were set up at 1.8 m above the floor to avoid interference from reflected signals.

Fairly extensive measurements were done by using sparks at temperatures of 273-277 K and relative humidities of 50-73%. Five source-receiver distances (4.1 m, 4.9 m, 9.8 m, 15.6 m and 21.6 m) were employed with four different charging voltages of 4.4 kV, 5.0 kV, 5.4 kV and 6.0 kV. This series of measurements is termed Series-I. Another series of measurements (Series-II) was also done at a temperature of 289 K and relative humidity of 50% for the distance range of 11.8-19.0 m and a charging voltage of 4.4 kV.

Exploding wires were used to produce N-waves by replacing the resistor in the spark circuit by a thin nickel wire 0.125 mm dia and optimum length of 5 cm. The sudden discharge of energy vaporized the wire. The expansion of the metal vapour generated an N-wave in the far field. The measurements were done at two conditions for Series-III ($T_1 = 277$ K, RH = 75%, $r = 6.7$ m, 12.8 m, 24.3 m, $S = 4.6$ kV, 6.0 kV), and Series-IV ($T_1 = 280$ K, RH = 87.5%, $r = 24.3$ m, 29.3 m, $S = 4.6$ kV, 6.0 kV), where T_1 is the room temperature, RH the relative humidity, r the distance from the source and S the charging voltage.

The vibrational relaxation times for oxygen and nitrogen were evaluated by using the empirical relation obtained from the absorption of sound waves by Bass and Shields (Ref. 23), as tabulated in Table 2.1. The vibrational relaxation time at room temperature strongly depends on the absolute humidity of the atmosphere, as water molecules significantly reduce its value.

Representative oscillograms from sparks and exploding wires are shown in Fig. 2.1. It can be seen that both a spark and an exploding-wire source make it possible to produce well-established N-waves far from the source. In the exploding-wire experiments, the N-waves were much cleaner than those generated by a spark, especially with regard to the rear shock. It was found that the wire length L plays a significant role in shaping the rear shock pressure profile. After testing several wire lengths, a wire length $L = 5.0$ cm proved to generate the most symmetrical N-waves, and was used in all subsequent runs. The microphones were set up normal to the wire to minimize any line-source effect.

In Figs. 2.2 - 2.4, the maximum (peak) overpressure $(\Delta p)_{\max}$, the half-duration t_d and the rise time t_r are plotted against the distance from the source r . Figure 2.5 shows plots of t_r vs $(\Delta p)_{\max}$. The data for different series are represented by different symbols, which are common through Figs. 2.2 - 2.5. For the Series-I experiment, the data are plotted only for $S = 4.4$ kV and 6.0 kV to avoid confusion.

In Fig. 2.2, the lines indicate the curves of $(\Delta p)_{\max} \propto r^{-n}$, which are drawn from the arbitrary points to fit the experimental data, where n is termed the decay index of maximum overpressure. The solid and broken lines correspond to the curves for $n = 1$ and 1.4, respectively. For 100 > $(\Delta p)_{\max}$ 20 Pa both spark and exploding-wire data show that maximum overpressures decay nearly inversely proportional with distance from the source, as estimated from linear-acoustic theory. On the other hand, the spark data show that the decay index increases below 20 Pa. This deviation from linear-acoustic theory can be attributed to real-gas effects arising from

vibrational excitation of oxygen (see Section 4.4). It is noted that the same input energy does not result in the same decay of $(\Delta p)_{\max}$ for different energy sources. The exploding-wire source makes for a stronger explosion in air than the spark source for the same discharge voltage. It should also be noted that the overpressure decays are different for the different series of spark experiments despite the same discharge voltage.

In Figs. 2.5 - 2.5, the broken lines indicate the tendency of the experimental data. The half-duration t_d increases with r . The durations for the exploding-wire experiment (85-135 μ sec) are longer than those for the spark experiments (50-75 μ sec). The rise times t_r also increase with r , while the maximum overpressure decreases with r . It should be noted from Fig. 2.5 that the rise times t_r are different for the different series of experiments and supply voltages at the same maximum overpressure.

5. SOME ANALYSES FOR WEAK SHOCK TRANSITIONS

In this section, some analytical solutions for weak shock transitions are reviewed and discussed in connection with the spark and exploding-wire data, which were shown in Section 2. In Sections 5.1 - 5.5, some analytical solutions for viscous-shock transitions are shown in cases of steady planar waves, quasi-stationary N-waves and nonstationary planar waves, respectively. The analytical solution for steady planar waves was derived by Taylor (Ref. 5), and will be designated as the Taylor solution or the Taylor shock transition. The analytical solutions for quasi-stationary N-waves and nonstationary planar waves were defined by Lighthill (Ref. 20), and will be designated as the Lighthill solutions, or the Lighthill N-wave and the Lighthill shock transition, respectively. In Section 5.4, solutions for dispersed waves with vibrational excitation are shown for a steady plane wave, and an approximate expression is derived for the rise time of a fully or partly-dispersed wave. The Taylor and Lighthill solutions are extended to dispersed waves with vibrational relaxation by using a bulk-viscosity concept, and the extended solutions will be designated as the modified Taylor solution and the modified Lighthill solution, respectively. Some insight is also given into the structures and rise times of weak spherical N-waves.

5.1 Classical Taylor Plane Shock-Wave Transitions

In the following three sections, Sections 5.1 - 5.3, the γ - μ or γ - μ - ν -shock transitions are considered, where the vibrational mode of molecular internal energy is assumed to be γ - μ - ν . Viscous, steady shock waves are formed as a result of a balance between the wave-form-steepening tendency due to the finite-amplitude compression (convection) effects and the wave-form-easing tendency due to the viscous-diffusion effects. This balancing determines the thickness of a steady shock wave and depends on the shock strength.

The classical Taylor solution (Ref. 5) for weak, plane shock-wave transitions is expressed by Lighthill (Ref. 20) as

$$\frac{v}{v_2} = \left[1 + \exp \left(\frac{(\gamma+1)v_2(x-U_s t)}{2\tau} \right) \right]^{-1} \quad (5.1)$$

for a shock wave travelling with steady profile at a constant speed U_s , where v = flow velocity relative to the ground; v_2 = flow velocity at $x = 0$; γ = ratio of specific heats; x = distance; t = time; τ = diffusivity of sound, defined by

$$\tau = \frac{4}{3} \frac{\nu}{a^2} + \frac{\nu_r}{Pr} \quad (5.2)$$

where ν = kinematic viscosity, ν_r = viscosity, ν_r = bulk viscosity due to rotational relaxation, Pr = Prandtl number. All the thermodynamic and transport coefficients, γ , ν , ν_r , and Pr , may be assumed to be constant throughout the flow, since the shock waves are weak. The original Taylor solution did not include the bulk viscosity due to rotational relaxation as it appears in Eq. (5.2). However, in the present paper, the term *Taylor solution* is used when it includes only the effects of rotational relaxation in order to distinguish from the *modified Taylor solution* which includes both the effects of rotational and vibrational relaxation.

From the weak-wave assumption, we have

$$v/a_1 \approx (\Delta p)/(\gamma p_1) \quad (5.3)$$

where Δp is the overpressure ($\Delta p = p - p_1$); a_1 , the undisturbed speed of sound; p_1 , the undisturbed pressure. Then Eq. (5.1) can be rewritten as

$$\frac{(\Delta p)}{(\Delta p)_2} = \left[1 + \exp \left(\frac{(\gamma+1)}{2} \frac{a_1(x-U_s t)}{P_1} \frac{(\Delta p)_2}{P_1} \right) \right]^{-1} \quad (5.4)$$

where $(\Delta p)_2$ is the overpressure at $x = 0$. Define a dimensionless variable,

$$z = \frac{a_1(x-U_s t)}{P_1} \frac{(\Delta p)_2}{P_1} \quad (5.5)$$

Then

$$\frac{(\Delta p)}{(\Delta p)_2} = \left[1 + \exp \left(\frac{(\gamma+1)}{2} z \right) \right]^{-1} \quad (5.6)$$

or

$$\frac{(\gamma+1)}{2} z = \ln \left[1 - \frac{(\Delta p)}{(\Delta p)_2} \right] = \ln \left[\frac{(\Delta p)}{(\Delta p)_2} \right] \quad (5.7)$$

Figure 3.1 exhibits the Taylor velocity or pressure profile in a plot of v/v_2 or $(\Delta p)/(\Delta p)_2$ against z . The variable z is a similarity variable, since the velocity or pressure profile can be obtained as a unique curve against z for shock waves with different strength $(\Delta p)_2/P_1$, and it will be termed the distance parameter.

Three different definitions of shock thickness for z are also shown in Fig. 3.1. The thickness $(z)_0$ is defined by

$$(\Delta Z)_0 = \frac{v_2}{dv/dZ}|_{Z=0} = \frac{(\Delta p)_2}{d(\Delta p)/dZ}|_{Z=0}$$

This thickness corresponds to the velocity or density-based thickness, and it has been used in some literature for shocks of moderate strength. The thicknesses $(\Delta Z)_0'$ and $(\Delta Z)_0''$ are defined by the distances for the overpressure to vary from 10% to 90% and from 5% to 95%, respectively, of its equilibrium value behind the shock. The last definition was used by Lighthill (Ref. 20) for the shock thickness derived from the velocity profile. From Eq. (3.6) or (3.7), we can evaluate the values of $(\Delta Z)_0$, $(\Delta Z)_0'$ and $(\Delta Z)_0''$ as

$$(\Delta Z)_0 = 4.667, \quad (\Delta Z)_0' = 5.127, \quad (\Delta Z)_0'' = 6.870$$

These will be termed the thickness parameters. The second definition of the shock thickness (10-90% overpressure) is used throughout this report because it can give a reasonable criterion for evaluating the thickness of a shock wave with an antisymmetric structure, which is found in N-waves and in partly or fully dispersed plane waves.

The actual Taylor thickness $(\Delta x)_0'$ and the Taylor rise time t_{r0}' (10-90% overpressure) can be related to the Taylor thickness parameter $(\Delta Z)_0'$ as

$$\frac{(\Delta x)_0'}{(\Delta Z)_0'} = \frac{t_{r0}'}{(\Delta Z)_0'} = \frac{2}{\gamma+1} \frac{(\Delta Z)_0'}{(\Delta p)_2/p_1} \quad (3.8)$$

from Eq. (3.5), where t_{r0}' is the Taylor rise time corresponding to the Taylor thickness $(\Delta x)_0'$. We assume $t_{r0} = (\Delta x)_0'/a_1$, since the wave speed is nearly equal to a_1 for very weak waves.

In Fig. 3.2, the Taylor thickness $(\Delta x)_0'$ or the Taylor rise time t_{r0}' are plotted in a nondimensional form against $(\Delta p)_2/p_1$ for a range of $(\Delta p)_2/p_1 = 10^{-5} - 10^{-3}$ or $(\Delta p)_2 = 1 \text{ Pa} - 100 \text{ Pa}$ in the atmosphere. At NTP for air $\gamma = 1.333 \times 10^{-5} \text{ m}^2/\text{s}$, $\mu_r/\rho = 2/3$, $\rho = 1.4$, $Pr = 0.7$ and, from Eq. (3.2), $\nu = 3.43 \times 10^{-5} \text{ m}^2/\text{s}$. Using $a_1 = 331.7 \text{ m/s}$, the characteristic length and time are

$$\lambda/a_1 = 1.03 \times 10^{-7} \text{ m}, \quad \tau/a_1 = 3.1 \times 10^{-10} \text{ sec}$$

Therefore, for $(\Delta p)_2/p_1 = 10^{-4}$ or $(\Delta p)_2 = 10 \text{ Pa}$ at NTP, then $(\Delta x)_0' = 5.3 \text{ mm}$ and $t_{r0}' = 16 \text{ } \mu\text{sec}$, from Fig. 3.2. The Taylor thickness or rise time is inversely proportional to the shock strength $(\Delta p)_2/p_1$. As the shock speed is weakened, the Taylor thickness increases and tends to infinity as $(\Delta p)_2 \rightarrow 0$.

As mentioned at the beginning of this section, the balance between the finite-amplitude (nonlinear) compression effects and the viscous-diffusion effects determines the thickness of a steady shock wave. As the wave is weakened, the nonlinear effects are gradually diminished, while the viscous-diffusion effects remain unchanged regardless of the shock strength. Therefore, for very weak shocks, the diffusion effects exceed overwhelmingly the nonlinear compression effects and broaden the shock thickness to very large values. In the limit of $(\Delta p)_2 \rightarrow 0$, the nonlinear effects disappear and only the diffusion effects remain, so that the thickness tends to infinity. However, in an actual case, the steady structure of such a very weak wave would not

be realized because it requires an infinitely long time for the wave to reach a steady state through viscous diffusive action. In the case when the shock strength increases, the nonlinear effects are strengthened, while the diffusive effects remain unchanged. However, the shock thickness cannot be less than the molecular mean-free-paths, since the shock compression process is after all a result of molecular collisions. In other words, for strong shocks, the shock thickness has a lower limit which is controlled by molecular-collision processes.

Figure 3.3 shows a comparison between the experimental and theoretical (Taylor) rise time t_r vs the maximum overpressure $(\Delta p)_{\max}$. The Taylor curves shown in Fig. 3.2 are reproduced for $T_1 = 273 \text{ K}$ and 290 K . As seen from Fig. 3.3, the rise times for the spark data (Series I and II) are shorter than the Taylor rise times for the same maximum overpressure, while the rise times for the exploding-wire data (Series III and IV) are longer. Both data do not coincide with the Taylor curves. It is clearly seen that the Taylor rise times for steady viscous shocks can give no reasonable explanation for the observed rise times for weak spherical N-waves. Therefore, another analysis is required for this purpose.

3.2 Viscous Plane N-Waves

In this section, consideration is given to the case of a *balanced N-wave*, which is produced by moving a piston forward and then retracting it to its original position in a tube. The generated plane N-wave gradually decays due to viscous effects as it proceeds. Lighthill (Ref. 20) solved this problem and obtained a similar solution for weak plane N-waves, where the velocity profile is given as

$$u = \frac{X/t}{1 + \exp(X^2/2t)/\exp(Re) - 1} \quad (3.9)$$

where X is a coordinate measured in a frame of reference which moves in the same direction as the waves, with an undisturbed speed of sound a_1 and is defined as $X = x - a_1 t$; u is the excess wavelet velocity whose variations are responsible for the *nonlinear* effects and is defined as $u = a + v - a_1$ (a is the local speed of sound, v , the particle velocity); Re is a Reynolds number of each half of the N-waves, which is defined in terms of the mass flow in that half. For example, for the front half

$$Re = \frac{1}{\tau} \int_{X_n}^{\infty} u dX \quad (3.10)$$

where X_n is the node $u = 0$ and τ is the diffusivity defined by Eq. (3.2). Note that Re is not invariant, but varies with time as the mass flow varies with the decay of the wave. The *balanced N-wave* means that its total mass flow always vanishes as

$$\int_{-\infty}^{\infty} u dX = 0$$

From the nonlinear wave relation,

$$u = \frac{\gamma+1}{2} v \quad (3.11)$$

Using Eqs. (3.3) and (3.11) and defining the similarity variables

$$\bar{p} = \frac{\gamma+1}{2} a_1 \sqrt{\frac{t}{\tau}} \frac{(\Delta p)}{p_1}, \quad \tau = \frac{X}{a_1^2} \quad (3.12)$$

then from Eq. (3.9),

$$\bar{p} = \xi \left[1 + \frac{\exp(\xi^2/2)}{\exp(\text{Re}) - 1} \right]^{-1} \quad (3.13)$$

Figure 3.4 shows the pressure profiles for several different Reynolds number Re in a plot of \bar{p} against ξ .

For a given Reynolds number Re , we can obtain \bar{p}_{\max} (the maximum value of \bar{p}), $\Delta\xi$ (the shock thickness defined by 10-90% overpressure) and ξ_d (the half length of the N-wave measured from the origin to the point of 10% overpressure in the wave front). Then the following parameters can be obtained:

$$\Delta Z = \frac{2\gamma}{\gamma+1} (\Delta\xi) \bar{p}_{\max} = \frac{a_1 (\Delta X)}{\tau} \frac{(\Delta p)_{\max}}{p_1} \quad (3.14)$$

$$Z_d = \frac{2\gamma}{\gamma+1} \xi_d \bar{p}_{\max} = \frac{a_1 X_d}{\tau} \frac{(\Delta p)_{\max}}{p_1} = \frac{a_1^2 t_d}{\tau} \frac{(\Delta p)_{\max}}{p_1} \quad (3.15)$$

where ΔX is the shock thickness corresponding to $\Delta\xi$, $\Delta X = \Delta\xi \sqrt{X_d}$; X_d , the half length of the N-wave corresponding to ξ_d , $X_d = \xi_d^2 \sqrt{X_d}$; $(\Delta p)_{\max}$, the maximum value of (Δp) . The parameters ΔZ and Z_d correspond to the shock thickness and the flow duration of the N-wave with reference to the dimensionless variable Z , which is defined similarly to Eq. (3.5) as

$$Z = \frac{a_1 X}{\tau} \frac{(\Delta p)_{\max}}{p_1} \quad (3.16)$$

ΔZ is the thickness parameter defined in the previous section and Z_d will be termed the duration parameter. Details of the derivation of \bar{p}_{\max} , ΔZ and Z_d are given in Appendix A.

Figure 3.5 exhibits the pressure profiles for the same cases as shown in Fig. 3.4 in a plot of $(\Delta p)/(\Delta p)_{\max}$ against $Z - Z_0$, where Z_0 is the Z at $(\Delta p)/(\Delta p)_{\max} = 0.5$. The solid line indicates the Taylor solution for steady plane waves, which is given by Eq. (3.6) or (3.7). The Lighthill N-wave solution approaches the Taylor solution as $Z_d \rightarrow \infty$ or $\text{Re} \rightarrow \infty$. This can also be shown from Eq. (3.13) as follows. Assume that \bar{p} reaches its maximum \bar{p}_{\max} at $\xi = \xi_m$ for large Re . Then, approximately,

$$\bar{p}_{\max} = \xi_m, \quad \text{Re} = \xi_m^2/2$$

Put $\xi = \xi_m + \xi'$ ($\xi' \ll \xi_m$), then

$$\bar{p} = \xi_m [1 + \exp(\xi_m^2 \xi')]^{-1} = \bar{p}_{\max} [1 + \exp(\bar{p}_{\max} \xi')]^{-1} \quad (3.17)$$

in the limit of $\text{Re} \rightarrow \infty$. Equation (3.17) has the

same form as Eq. (3.6), the Taylor solution, since $\bar{p}_{\max} \xi'$ can be replaced by $Z - Z_0$, where Z_0 is the Z at $\xi = \xi_m$. It should be noted that the shock thickness decreases as the Reynolds number Re or the duration parameter Z_d decreases for the same maximum overpressure.

In Fig. 3.6, the ratio of the thickness parameter $(\Delta Z)/(\Delta Z)_0$ is plotted against the duration parameter Z_d , where $(\Delta Z)_0$ is the (ΔZ) for $Z_d \rightarrow \infty$ (Taylor solution) and is given by $(\Delta Z)_0 = 5.127$. This figure clearly shows the dependence of the shock thickness on the duration of the N-wave. As the duration or the maximum overpressure increases, the shock thickness approaches the Taylor value. As the duration or the maximum overpressure increases, the shock thickness approaches the Taylor value. As the duration or the maximum overpressure decreases, the deviation from the Taylor value increases.

In Fig. 3.7, the normalized shock thickness $(\Delta X)/(t/a_1)$ or the normalized rise time $t_r/(t/a_1^2)$ is plotted against the normalized maximum overpressure $(\Delta p)_{\max}/p_1$ for the normalized duration $X_d/(t/a_1)$ or $t_d/(t/a_1^2) = \text{constant}$. It can also be seen from Fig. 3.7 that the shock thickness or rise time decreases for a fixed maximum overpressure $(\Delta p)_{\max}$ as the duration of N-wave decreases. This is the N-wave behavior described in the Introduction.

In Fig. 3.8, the experimental data of Ref. 6 are compared with the Lighthill solutions for N-waves. The rise time t_r is plotted against the maximum overpressure $(\Delta p)_{\max}$. The solid lines exhibit the N-wave solutions for $t_d = 50 \mu\text{sec}$ and $70 \mu\text{sec}$ which correspond to the half-durations in the spark experiments. The Taylor rise time for $T_1 = 273 \text{ K}$ is also plotted against $(\Delta p)_{\max}$. The figure shows that the rise times obtained in the spark experiments are adequately explained by the Lighthill model of viscous (frozen) N-wave shocks though the measured rise times slightly deviate from the theoretical curves in the range of the lower overpressure.

In Fig. 3.9, the experimental data are plotted on a figure showing the ratio of the thickness parameters $(\Delta Z)/(\Delta Z)_0$ vs the duration parameter Z_d , shown in Fig. 3.6. The data cover the range of $Z_d = 10-100$, in which the spark data lie between $Z_d = 10$ and 60 and the exploding-wire data lie between $Z_d = 50$ and 100. Using the duration parameter Z_d , the data may be categorized into three domains. Above $Z_d > 50$, the measured (ΔZ) -values deviate from the Lighthill curve and steeply increase with increasing Z_d . In the range $Z_d = 15-50$, the measured (ΔZ) -values nearly coincide with the Lighthill curve, a scatter of the data exists. Below $Z_d < 15$, the measured (ΔZ) -values again deviate from the curve and steeply decrease with decreasing Z_d . The broken lines are drawn to stress the tendency of the data.

Figure 3.10 shows a comparison between the observed and Lighthill N-wave pressure profiles. Typical profiles in the Series I-IV are plotted by the broken lines in comparison with the corresponding analytical ones, which are evaluated from Eq. (3.13) to have the same maximum overpressure $(\Delta p)_{\max}$ and the same half-duration t_d as the experimental ones, and plotted by the solid lines to fit each other at the nodes of the N-waves. As seen from the figure, the pressure profiles observed in the spark experiments [Series I and II; Figs. 3.10(a) and (b)] nearly coincide with the analytical

ones, while the pressure profiles observed in the exploding-wire experiments [Series III and IV; Fig. 3.10(c) and (d)] deviate from those predicted analytically. The main difference between both experiments is that of the half-duration of the N-wave. Figure 3.10, as well as Figs. 3.8 and 3.9, suggests that the Lighthill viscous N-wave model does not always explain the rise times of N-waves over the entire range of t_d or z_d .

3.3 Nonstationary Viscous Plane Waves

In this section, consideration is given to a nonstationary plane wave, which is generated by the impulsive motion of a piston in a tube. The initially discontinuous wave-front is smoothed out due to viscous diffusion and it tends to form a final steady profile. It will be shown in the succeeding sections that this process of shock thickening (*nonstationary effect*) plays an important role in determining the rise times of weak spherical N-waves.

Lighthill (Ref. 20) has given a solution for the nonstationary plane wave by solving Burger's Equation. He obtained the following result:

$$u(X, t) = \frac{u_2}{1 + \exp \left[\frac{u_2 \left(X - \frac{1}{2} u_2 t \right)}{a_1^2} \right]} \frac{\int_0^X e^{-y^2/2} dy}{\int_0^{X - u_2 t} e^{-y^2/2} dy} \quad (3.18)$$

in which the initial wave form is given by

$$u(X, 0) = u_2 \text{ for } X > 0, \text{ and zero for } X < 0 \quad (3.19)$$

where u_2 is the excess wavelet velocity for $X \rightarrow \infty$.

Using Eqs. (3.3) and (3.11),

$$\frac{(\Delta p)_2}{(\Delta p)_1} = \left[1 + \exp \left\{ \frac{z}{2\tau} - \frac{z+1}{4\tau} \sqrt{\frac{\tau}{2}} \right\} \right]^{-1} \frac{\text{erfc} \left[\frac{z}{\sqrt{2\tau}} - \frac{z+1}{4\tau} \sqrt{\frac{\tau}{2}} \right]}{\text{erfc} \left[\frac{z}{\sqrt{2\tau}} - \frac{z+1}{4\tau} \sqrt{\frac{\tau}{2}} \right]} \quad (3.20)$$

where z and τ are the distance parameter and the time parameter, respectively, defined by

$$z = \frac{a_1 \left(X - \frac{1}{2} u_2 t \right)}{P_1} \frac{(\Delta p)_2}{P_1}, \quad \tau = \frac{a_1^2 t}{P_1} \left[\frac{(\Delta p)_2}{P_1} \right]^2 \quad (3.21)$$

The complementary error function is defined by

$$\text{erfc}(X) = \frac{2}{\sqrt{\pi}} \int_X^\infty e^{-y^2} dy$$

Note that the shock strength $(\Delta p)_2/p_1$ depends on the piston velocity v_2 [$= 2u_2/(\gamma+1)$] and is invariant throughout the process. When $\tau \rightarrow \infty$, Eq. (3.20) becomes

$$\frac{(\Delta p)_2}{(\Delta p)_1} = \left[1 + \exp \left\{ \frac{z+1}{2\tau} \right\} \right]^{-1} \quad (3.22)$$

which is the Taylor solution for steady plane waves, Eq. (3.6).

Figure 3.11 shows the pressure profiles for several different time parameters in a plot of $(\Delta p)/(\Delta p)_2$ against the distance parameter z . The pressure profile approaches the Taylor profile as $\tau \rightarrow \infty$. It can be seen that the shock thickness (Δz) increases as τ increases [whether based on maximum slope or 10-90% of $(\Delta p)/(\Delta p)_2$].

In Fig. 3.12, the ratio of the thickness parameters $(\Delta z)/(\Delta z)_0$ is plotted against τ . If we define a characteristic-time parameter of shock thickening t_s as τ at $(\Delta z)/(\Delta z)_0 = 0.99$, then

$$\sqrt{\tau}_s = 5.5 \quad \text{or} \quad x_s = 30.25$$

from which the corresponding time t_s and distance x_s are obtained from Eq. (3.21) as

$$\frac{t_s}{(a_1^2/P_1)} = \frac{x_s}{(a_1^2/P_1)} = \frac{1}{P_1} \left[\frac{(\Delta p)_2}{P_1} \right]^{-2} \quad (3.23)$$

which are designated as the shock-thickening time and distance, respectively. These are inversely proportional to the square of the shock strength $(\Delta p)_2/p_1$. This means that it takes a progressively longer time and distance to reach a final steady state for weaker shock waves or for lower $(\Delta p)_2/p_1$. Physically, this tendency of longer shock-thickening time or distance for weaker shocks is attributed to the decline of shock steepening due to nonlinear (convective) effects.

In Fig. 3.13, the normalized shock-thickening time $t_s/(a_1^2/P_1)$ or distance $x_s/(a_1^2/P_1)$ is plotted against the shock strength $(\Delta p)_2/p_1$. The time scale on the right hand side indicates the shock thickening time at NTP in air. For $(\Delta p)_2/p_1 = 10^{-4}$ or $(\Delta p)_2 = 10$ Pa, $t_s = 1$ sec or $x_s = 330$ m. These values suggest that the nonstationary effect on the rise time or the shock thickness becomes very important for weak shock waves, for it takes a long time or a large distance to reach a steady state. This result is of value in interpreting Fig. 3.4 or 3.5, which provides solutions for quasi-stationary N-waves at the final values after a very long time without specifying how long it may actually take. The above solution quantifies the time or distance in specific cases. The spark and exploding-wire generated N-waves, described in Section 2, are also expected to be affected by this nonstationary effect, since the maximum overpressures are below 20 Pa only over a distance of 10 m.

3.4 Shock Transitions with Vibrational Excitation

The structure and thickness of shock waves with vibrational excitation in air will be considered now. The analytical results of Polyakova, Solyan and Khokhlov (Ref. 21) and Johannsen and Hodgson (Ref. 12) for plane dispersed waves are re-examined and compared with Holst-Jensen's data (Ref. 6). Furthermore, extensions of Lighthill solutions for N-waves and nonstationary waves to shock transitions with vibrational excitation are

made possible by using a bulk-viscosity concept.

For weak shock waves with vibrational excitation, steady shock waves are formed as a result of a balance between the wave-form-steepening tendency due to finite-amplitude-compression effects and the wave-easing tendency due to both effects of viscous diffusion and vibrational relaxation. For very weak waves, the compression effects diminish and the wave-form-easing effects become predominant. As discussed in Section 3.1 for *viscous* or *frozen* shock transitions, in the limit of $(\Delta p)_2 \rightarrow 0$, the nonlinear compression effects disappear and the wave-form-easing effects remain, so that the wave thickness tends to infinity. For weak shocks whose strengths are slightly above the limit of zero overpressure, the vibrational relaxation is more effective than the viscous diffusion for the wave-easing tendency. In this case, the compression process is so slow that the energy dissipation due to vibrational nonequilibrium becomes predominant compared with that due to translational and rotational nonequilibrium which requires a more rapid change of the flow properties. As the wave strength increases, the shock thickness decreases owing to the increase in nonlinear-compression effects. When the nonlinear-compression effects overcome the wave-easing effects due to vibrational relaxation, the *frozen* shock transition appears in the compression process of the wave.

Figure 3.14 illustrates these two types of shock transition with vibrational excitation through pressure and temperature profiles. The vibrational temperature T_v is also plotted to show the process of vibrational energy excitation. The former wave dominated by the vibrational excitation is called a fully dispersed wave, and the latter wave including the *frozen* (relatively sharp, viscous) shock transition is called a partly dispersed wave. For strong shocks, the nonlinear compression mainly balances with the viscous diffusion, though it is accompanied by the slower process of vibrational excitation. As shown in Fig. 3.14, for stronger shocks, the temperature goes up to the maximum (Rankine-Hugoniot) value through the *frozen* shock compression and then it falls to the final equilibrium state through the *relaxation zone* as vibration attains its share of energy.

Polyakova et al (Ref. 11) have obtained an analytical solution for the structure of steady, plane dispersed waves for nonviscous and nonconductive gases as

$$\frac{y + y_0}{t_j} = \ln \frac{(v_0 + v)^{k-1} v_0^2}{(v_0 - v)^{k+1}} \quad (3.24)$$

where $y = t - z/a_e$; z = Lagrangian coordinate, a_e = equilibrium speed of sound; y_0 = constant of integration; t_j = vibrational relaxation time for j -molecule; v = velocity in a moving coordinate system, v_0 = absolute value of the velocity at the spatial coordinate $z \rightarrow \infty$; $k = ma_e/(2\tilde{v}_0)$; $m = (a_f^2 - a_e^2)/a_e^2$; a_f = frozen speed of sound; $z = (\gamma+1)/2$.

In order to rewrite Eq. (3.24) using the normalized overpressure $(\Delta p)/(\Delta p)_2$ and the distance parameter Z , which were introduced in the previous sections, introduce two quantities: the bulk viscosity and a critical overpressure.

The bulk viscosity $(\mu_v)_j$ for the j -molecule can be expressed as

$$(\mu_v)_j = \tau_j \rho_0 (a_f^2 - a_e^2) = \tau_j \rho_0 m a_e^2 \quad (3.25)$$

for processes sufficiently slow, where ρ_0 is the equilibrium density of the medium. Then the diffusivity $(D_v)_j$ for j -molecule with a bulk viscosity $(\mu_v)_j$ can be expressed as

$$(D_v)_j = (\mu_v)_j / \rho_0 = \tau_j m a_e^2 \quad (3.26)$$

This diffusivity will be used as a reference physical property. It should be noted that the use of this property does not mean that the vibrational relaxation processes can always be replaced by the bulk viscosity, which is valid only for processes sufficiently slow.

The critical overpressure is defined as the equilibrium overpressure behind a plane dispersed wave whose wave velocity is equal to the frozen speed of sound. When the equilibrium overpressure exceeds the critical overpressure, the steady plane wave is a partly dispersed wave with a frozen (viscous) shock front, which is followed by the vibrational relaxation region. When the equilibrium overpressure is below the critical overpressure, the steady plane wave is a fully dispersed wave with a smooth transition, which is controlled by the vibrational excitation of the molecules.

The equilibrium overpressure across a normal shock wave with vibrational excitation can be given as

$$\frac{(\Delta p)_2}{p_1} = \frac{2\gamma(M_f^2 - 1) + 2(\gamma - 1)(M_f^2 - 1)c_j}{(\gamma + 1) + 2(\gamma - 1)c_j} \quad (3.27)$$

where M_f is the frozen Mach number, c_j the vibrational specific heat for j -molecule normalized by the gas constant $c_j = c_j/R$ in which c_j is assumed to be constant across the shock wave. Details of the derivation of Eq. (3.27) are given in Appendix B. If the harmonic oscillator approximation is applied to the vibrational energy level, the vibrational specific heats for O_2 and N_2 in air may be written as

$$c_{O_2} = 0.209 \left[\frac{T_0}{T_1} \right]^2 \exp \left[-\frac{T_0}{T_1} \right] \quad (3.28a)$$

$$c_{N_2} = 0.781 \left[\frac{T_N}{T_1} \right]^2 \exp \left[-\frac{T_N}{T_1} \right] \quad (3.28b)$$

where T_1 is the initial gas temperature (room temperature), T_0 the vibrational characteristic temperature $T_0 = 2239.1$ K, $T_N = 3352$ K. For $M_f = 1$, we have the critical overpressure for the j -molecule as

$$\frac{(\Delta p)_{cr,j}}{p_1} = \frac{2(\gamma - 1)^2 c_j}{(\gamma + 1) + 2(\gamma - 1)c_j} = \frac{2(\gamma - 1)^2}{\gamma + 1} c_j \quad (3.29)$$

for $c_j \ll 1$, which is usually valid for atmospheric air, as very little vibrational excitation can exist at nearly room temperature. The critical overpres-

sure $(\Delta p)_{cr,j}$ depends on the gas temperature T_1 , since the vibrational specific heat c_j depends on T_1 .

In Fig. 3.15, the critical overpressures $(\Delta p)_{cr,0}$ and $(\Delta p)_{cr,0+N}$ are plotted against T_1 . The lines denoted by O_2 and O_2+N_2 are calculated from

$$\frac{(\Delta p)_{cr,0}}{p_1} = \frac{2(\gamma-1)^2}{\gamma+1} c_0 \quad (3.30a)$$

$$\frac{(\Delta p)_{cr,0+N}}{p_1} = \frac{2(\gamma-1)^2}{\gamma+1} (c_0 + c_N) \quad (3.30b)$$

respectively. That is, in the former case, only the vibrational excitation for O-molecules in air is taken into account. For $(\Delta p)_2 \leq (\Delta p)_{cr,j}$, the steady plane wave is fully dispersed, and for $(\Delta p)_2 > (\Delta p)_{cr,j}$ it is partly dispersed.

The diffusivity $(\delta_v)_j$ can be expressed by the critical overpressure as

$$(\delta_v)_j = \frac{\gamma+1}{2\gamma} a_1^2 \tau_j \frac{(\Delta p)_{cr,j}}{p_1} \quad \text{for } c_j \ll 1 \quad (3.31)$$

The parameter k , which appears in Eq. (3.24), can be rewritten as

$$\frac{1}{k} = \frac{(\Delta p)_2}{(\Delta p)_{cr,j}} \quad \text{for } c_j \ll 1 \quad (3.32)$$

That is, the parameter k is the ratio of the critical and equilibrium overpressures. For $k > 1$, the wave is a partly dispersed wave, and for $k \leq 1$ the wave is a fully dispersed wave. The derivations of Eqs. (3.31) and (3.32) are given in Appendix B.

Using the relation

$$1 + \frac{\hat{v}}{v_0} = 2 \frac{(\Delta p)}{(\Delta p)_2} \quad (3.33)$$

then

$$\begin{aligned} \frac{\gamma+1}{2\gamma} (Z-Z_0) &= \left[1 + \frac{(\Delta p)_2}{(\Delta p)_{cr,j}} \right] \ln \left[1 - \frac{(\Delta p)}{(\Delta p)_2} \right] \\ &- \left[1 - \frac{(\Delta p)_2}{(\Delta p)_{cr,j}} \right] \ln \left[\frac{(\Delta p)}{(\Delta p)_2} \right] \end{aligned} \quad (3.34)$$

from Eq. (3.24), where the distance parameter Z is defined as

$$Z = - \frac{a_1^2 \gamma}{(\delta_v)_j} \frac{(\Delta p)_2}{p_1} \quad (3.35)$$

in a similar way to Eqs. (3.16) and (3.21) in the previous sections, it can be rewritten as

$$Z = - \frac{2\gamma}{\gamma+1} \frac{\gamma}{\tau_j} \frac{(\Delta p)_2}{(\Delta p)_{cr,j}} \quad (3.36)$$

Z_0 is an arbitrary constant. Details of the deriva-

tion of Eq. (3.34) are also given in Appendix B.

Johannesen and Hodgson (Ref. 12) have also obtained an exact solution for steady plane dispersed waves for nonviscous and non-conductive gases, as follows:

$$\begin{aligned} \frac{M_f^2 [(\gamma+1) + 2(\gamma-1)c_j]}{2\tilde{u}_1 \tau_j} x &= -(\gamma+1)M_f^2 \frac{\tilde{u}}{u_1} \\ &+ \frac{1 - M_f^2}{1 - \frac{\tilde{u}_2}{\tilde{u}_1}} \ln \left[1 - \frac{\tilde{u}}{\tilde{u}_1} \right] \\ &- \frac{\left[1 + \gamma M_f^2 - (\gamma+1)M_f^2 \frac{\tilde{u}_2}{\tilde{u}_1} \right] \frac{\tilde{u}_2}{\tilde{u}_1}}{1 - \tilde{u}_2/\tilde{u}_1} \ln \left(\frac{\tilde{u}}{\tilde{u}_1} - \frac{\tilde{u}_2}{u_1} \right) \end{aligned} \quad (3.37)$$

where \tilde{u} is the flow velocity, \tilde{u}_1, \tilde{u}_2 are the flow velocities at $x \rightarrow +\infty$. Using the relations

$$1 - \frac{\tilde{u}}{\tilde{u}_1} = \frac{1}{\gamma M_f^2} \frac{(\Delta p)_2}{p_1} \frac{(\Delta p)}{(\Delta p)_2} \quad (3.38a)$$

$$\frac{\tilde{u}}{\tilde{u}_1} - \frac{\tilde{u}_2}{\tilde{u}_1} = \frac{1}{\gamma M_f^2} \frac{(\Delta p)_2}{p_1} \left[1 - \frac{(\Delta p)}{(\Delta p)_2} \right] \quad (3.38b)$$

and neglecting the higher order terms of $O(c_j)$, the same equation as Eq. (3.34) is obtained, which was derived from the Polyakova et al (Ref. 21) formula, by using the distance parameter defined by

$$Z = - \frac{a_1 x}{(\delta_v)_j} \frac{(\Delta p)_2}{p_1} = - \frac{2\gamma}{\gamma+1} \frac{x}{a_1 \tau_j} \frac{(\Delta p)_2}{(\Delta p)_{cr,j}} \quad (3.39)$$

Further details can be found in Appendix B. Equation (3.34) will be used as a solution for steady plane dispersed waves.

In the limit of a weak wave $(\Delta p)_2 \rightarrow 0$, Eq. (3.34) tends to

$$\frac{\gamma+1}{2\gamma} (Z-Z_0) = \ln \left[1 - \frac{(\Delta p)}{(\Delta p)_2} \right] - \ln \left[\frac{(\Delta p)}{(\Delta p)_2} \right] \quad (3.40)$$

This has the same form as the Taylor solution, Eq. (3.7), in which the diffusivity δ is replaced by $(\delta_v)_j$. In the limit of weak shocks, the shock compression process is infinitely slow, so that the bulk viscosity concept may be applied to the vibrational relaxation process. The solution, in which the diffusivity δ is replaced by $(\delta_v)_j$ or $\delta + (\delta_v)_j$, will be called the modified Taylor solution.

Figure 3.16 shows the pressure profiles for several different values of $(\Delta p)_2/(\Delta p)_{cr,j}$ in a plot of $(\Delta p)/(\Delta p)_2$ against $Z-Z_0$. The curve for $(\Delta p)_2/(\Delta p)_{cr,j} \rightarrow 0$ corresponds to the modified Taylor solution. For partly-dispersed waves $[(\Delta p)_2 > (\Delta p)_{cr,j}]$, there appears a discontinuous shock front. The overpressure $(\Delta p)_f$ immediately behind the frozen shock is given by

$$\frac{(\Delta p)_f}{(\Delta p)_2} = 1 - \frac{(\Delta p)_{cr,j}}{(\Delta p)_2} \quad (3.41)$$

In Fig. 3.16, the chain curve indicates the pressure profile for $(\Delta p)_2/(\Delta p)_{cr,j} = 2$, in which the discontinuous shock strength at $z = z_0$ is $(\Delta p)_f = 0.5(\Delta p)_2$.

The thickness parameter (Δz) is defined by the 10-90% equilibrium overpressure, and can be related to the rise time t_r as

$$\Delta z = \frac{2}{\pi} \frac{t_r}{j} \frac{(\Delta p)_2}{(\Delta p)_{cr,j}} \quad (3.42)$$

For fully-dispersed waves where $[(\Delta p)_2 = (\Delta p)_{cr,j}]$, then from Eq. (3.34)

$$\Delta z = \frac{2}{\pi} \ln 9 = 5.127 = (\Delta z)_0' \quad (3.43)$$

regardless of the value of $(\Delta p)_2/(\Delta p)_{cr,j}$. That is, the thickness or rise time of a fully-dispersed wave, which is based on the 10-90% equilibrium overpressure, has the same value of the thickness parameter as the Taylor thickness or rise time, if the diffusivity $(\nu)_j$ is used instead of ν .

In Fig. 3.17, the ratio of the thickness parameter $(\Delta z)/(\Delta z)_0'$ is plotted against the equilibrium overpressure normalized by the critical overpressure for fully and partly-dispersed waves. It can be seen in the figure that the effect of dispersion on (Δz) remains up to $(\Delta p)_2 = 10(\Delta p)_{cr,j}$. This means that the rise times for steady plane waves are affected by the vibrational relaxation up to $(\Delta p)_2 = 500$ -1,000 Pa in air, since $(\Delta p)_{cr,j} = 50$ -100 Pa in the usual range of ground temperatures (see Fig. 3.15).

The Lighthill solutions for N-waves (Section 3.2) and nonstationary waves (Section 3.3) may be applied to fully-dispersed waves for small $(\Delta p)_2/(\Delta p)_{cr,j}$ by replacing the diffusivity ν with the vibrational diffusivity $(\nu)_j$ in order to provide a rough estimate of the N-wave and nonstationary effects on the thickness or rise time of dispersed waves with vibrational excitation.

Assume that,

$$a_1 = 331.7 \text{ m/s}, \quad t_j = 10^{-5} \text{ sec}, \\ (\Delta p)_{cr,j} = 50 \text{ Pa}, \quad p_1 = 101.3 \text{ kPa}$$

then, from Eq. (3.31),

$$(\nu)_j = 47 \times 10^{-5} \text{ m}^2/\text{s}$$

(Compare with ν above for translation and rotation of $3.43 \times 10^{-5} \text{ m}^2/\text{s}$, that is, the dispersed shock structure is entirely controlled by the vibrational relaxation.)

$$(\nu)_j/a_1 = 14 \times 10^{-7} \text{ m}, \quad (\nu)_j/a_1^2 = 43 \times 10^{-10} \text{ sec}$$

(Compare with $\delta/a_1 = 1.03 \times 10^{-7} \text{ m}$ and $\nu/a_1^2 = 3.1 \times 10^{-10} \text{ sec}$ noted above.) These values are about ten times as long as the ones evaluated for viscous shocks in Section 3.1. This means that the thickness or the rise time of a plane dispersed wave is about ten times as long as that of a viscous shock wave for the same shock strength $(\Delta p)_2/p_1$. The shock-thickening time or distance of an impulsive step wave is also tenfold greater for a dispersed wave than for a viscous wave, as seen from Eq.

(3.23). For $(\Delta p)_2/p_1 = 10^{-4}$ or $(\Delta p)_2 = 10 \text{ Pa}$, $t_s = 15 \text{ sec}$ or $x_s = 5 \text{ km}$. This shows that it is very difficult to obtain a plane dispersed wave in a steady state on a laboratory scale.

As for the N-wave effect, the dispersed wave is affected by the expansion behind the shock front more seriously than the viscous wave, since the former has a larger thickness than the latter for the same duration and maximum overpressure. Therefore, both the N-wave and nonstationary effects will seriously modify N-waves with vibrational nonequilibrium.

In Fig. 3.18, the exploding-wire data are compared with several theoretical curves in a plot of the rise time t_r against the maximum overpressure $(\Delta p)_{\max}$. The chain lines indicate the Taylor and the modified Taylor rise times. The broken lines indicate the modified Lighthill rise times for N-waves of $t_d = 100$ and $120 \text{ } \mu\text{sec}$. The vibrational diffusivity $(\nu)_0$ for oxygen is used for the modified Taylor and the modified Lighthill solutions. All calculations are evaluated for the gas temperature $T_1 = 280 \text{ K}$ and the relative humidity $RH = 87.5\%$ (Series IV). The corresponding vibrational-relaxation time and the critical overpressure for oxygen are about $5.75 \text{ } \mu\text{sec}$ and 61 Pa , respectively. The measured rise times are much shorter than the modified Lighthill rise times for fully-dispersed N-waves. This discrepancy can be attributed to the nonstationary effect.

Figure 3.19 shows a comparison between the observed and modified Lighthill N-wave pressure profiles in a similar way to Fig. 3.10 for viscous N-waves. Typical profiles from Series I-IV are plotted using broken lines in comparison with the corresponding analytical ones shown as solid lines, which are evaluated from Eq. (3.15), with ν replaced by $(\nu)_0$. The profiles have the same maximum overpressure $(\Delta p)_{\max}$ and the same half-duration t_d as the experimental ones, and fit at the nodes of the N-waves. By contrast to Fig. 3.10, the discrepancy between the observed and analytical profiles is clear.

To conclude this section, consideration is given to a characteristic feature of weak N-waves with vibrational nonequilibrium. Figure 3.20 illustrates a classification of weak N-waves by their degree of vibrational nonequilibrium. The profiles of gas and vibrational temperatures are plotted under the following assumptions: (i) the maximum (peak) overpressures are below the critical overpressure for steady, plane waves; (ii) the maximum overpressure is the same for all cases in Fig. 3.20; (iii) only one mode of vibrational excitation is considered. As seen, the N-waves can be classified into five categories: (a) quasi-equilibrium wave, (b) moderately-nonequilibrium wave, (c) highly-nonequilibrium wave, (d) nearly-frozen wave, (e) quasi-frozen wave.

The degree of excitation of vibrational energy is denoted by the vibrational temperature T_v , which is plotted by broken lines in Fig. 3.20. The time lag between the gas and vibrational temperatures corresponds to the vibrational relaxation time t_j . In a quasi-equilibrium wave, the vibrational temperature nearly follows the gas temperature. This is the case where the concept of bulk viscosity is valid and the modified Lighthill solution for N-waves may be applied. The structure of the shock front is

controlled by the vibrational relaxation, that is, the wave is a fully-dispersed wave. In a moderately-nonequilibrium wave, an appreciable deviation of the vibrational temperature from the gas temperature can be seen. In this case, the concept of bulk viscosity cannot be applied to the vibrational relaxation, though the front structure is still controlled by the vibrational relaxation. This wave can also be considered as a fully-dispersed wave. In a highly-nonequilibrium wave, the front structure is controlled by both processes of vibrational excitation and viscous dissipation. The wave becomes a partly-dispersed wave in the sense that the front structure is partly controlled by viscous effect. The structure of a nearly-frozen-flow frozen wave is mainly controlled by viscous effect, though vibrational excitation still remains in the rest of the flow field. In a quasi-frozen wave, the vibrational excitation is marginal so that the whole flow field can be considered as frozen.

The discrepancy between the observed and analytical rise times and pressure profiles described in the preceding sections may be explained by considering the above classification for N-waves. The N-waves generated by sparks could be highly-nonequilibrium waves or nearly-frozen waves, since the front structures seem to be mainly controlled by viscous effect. The N-waves generated by exploding wires could be moderately-nonequilibrium waves. The coupling of the N-wave and nonstationary effects would make the situations even more complex.

4. RANDOM-CHOICE ANALYSES FOR WEAK SHOCK TRANSITIONS

4.1 Basic Equations

The analysis is based on the following assumptions:

- The flow is a nonstationary one-dimensional (planar or spherically symmetric) viscous, compressible air flow.
- The viscosity μ and thermal conductivity κ are assumed to be constant, as the shock waves are weak.
- The gas is assumed to be thermally perfect; the equation of state for a thermally-perfect gas is used.
- Both cases of calorically-perfect and imperfect gases are analysed. For calorically-imperfect cases (referred to as real gases), the vibrational relaxation of air molecules are taken into account. However, for most of the analyses, only the vibrational relaxation of oxygen is taken into account, since the vibrational-relaxation time of nitrogen is much longer than the duration of most N-waves analysed in this study. The effects of nitrogen vibrational relaxation are discussed only in the last part of this section. The harmonic-oscillator approximation is applied to the vibrational energy level.
- The rotational relaxation is taken into account through the bulk-viscosity concept. The bulk viscosity due to the rotational relaxation is assumed to be $\mu_r = (2/3)\mu$.

Then the basic flow equations can be written as:

$$\frac{\partial U}{\partial t} + \frac{\partial F}{\partial r} = \left(\frac{v^2}{r^2} + \frac{1}{r} \frac{\partial v}{\partial r} \right) C + j(H_I + H_V) - H_R = 0 \quad (4.1)$$

$$\begin{aligned} U &= E, & F &= (E+p)v, & C &= (1+v^2), \\ &0, & & & & \\ &0, & & & & \\ &0, & & & & \end{aligned}$$

$$\begin{aligned} H_I &= \frac{1}{r} (E+p)v, & H_V &= \frac{1}{r^2} 0, \\ &0, & & \\ &0, & & \end{aligned}$$

$$\begin{aligned} H_R &= 0 \\ &= \frac{1}{r} \left[\frac{\partial U}{\partial t} e^{-\frac{t}{\tau_0}} \right] / \tau_0 \\ &= \frac{1}{r} \left[\frac{\partial U}{\partial t} e^{-\frac{t}{\tau_N}} \right] / \tau_N \end{aligned}$$

$$p = RT, \quad I = e + \frac{1}{2} v^2, \quad e = \frac{5}{2} RT + \epsilon_0 + \epsilon_N \quad (4.2)$$

where $j = 0$ for plane flows and $j = 2$ for spherical flows, ρ - density, v - velocity, p - pressure, T - temperature, I - total energy, e - internal energy, R - gas constant, ϵ_j - vibrational energy for the j -molecule ($j = 0$ for oxygen and $j = N$ for nitrogen), $(\epsilon_j)_e$ - equilibrium vibrational energy for the j -molecule, τ_j - vibrational relaxation time for the j -molecule.

Based on the harmonic oscillator approximation, the equilibrium vibrational energy for the j -molecule $(\epsilon_j)_e$ can be expressed as

$$(\epsilon_j)_e = \frac{R}{\exp(\theta_j/T) - 1} \quad (4.3)$$

where θ_j is the characteristic vibrational temperature for the j molecule: $\theta_0 = 2259$ K, $\theta_N = 5550$ K, ϵ_0 - molar concentration for the j molecule: $\epsilon_0 = 0.209$, $\epsilon_N = 0.781$. The vibrational temperature $(T_V)_j$ for the j molecule can also be defined as

$$(T_V)_j = \frac{R}{\exp(\theta_j/(T_V)_j) - 1} \quad (4.4)$$

The vibrational relaxation times for oxygen τ_0 and nitrogen τ_N are evaluated using the empirical relations obtained from the absorption of sound waves by Bass and Shields (Ref. 23), as follows:

$$\tau_0 = \frac{1}{2} \frac{p_0}{p} \left[24 + 4.4 \times 10^4 h \frac{0.05 + h}{0.391 + h} \right]^{-1} \quad (4.5)$$

$$\tau_N = \frac{1}{2} \frac{p_0}{p} \frac{T}{T_0} \left[9 + 350h \exp \left\{ -6.142 \left(\frac{T_0}{T} - 1 \right) \right\} \right]^{-1} \quad (4.6)$$

where $p_0 = 101.3$ KPa, $T_0 = 293.15$ K, h - absolute humidity of air (%). As seen in Eqs. (4.5) and (4.6), the vibrational relaxation times for oxygen and nitrogen strongly depend on the absolute humidity of air. In Fig. 4.1, τ_0 and τ_N are plotted as functions of the absolute humidity for $p = 101.3$ KPa (Ref. 12). The relaxation time for nitrogen is two or three orders longer than the relaxation time for oxygen. The relative humidity is defined as

$$RH = h(p/p_{\text{sat}}) \quad (4.7)$$

where p_{sat} is the partial pressure of water vapour at saturation, and given by the Goff-Gratch equation (Ref. 24) as

$$\begin{aligned} \log_{10}(p_{\text{sat}}/p_0) &= 10.79586[1 - (T_0/T)] - 5.02808 \log_{10}(T/T_0) \\ &+ 1.50474 \times 10^{-4} [1 - 10^{-8.29692[(1/T_0) - 1]}] \\ &+ 0.42873 \times 10^{-5} [10^{4.76955[1 - T_0/T]} - 1] \\ &- 2.2195983 \end{aligned} \quad (4.8)$$

4.2 Numerical Method

An operator-splitting technique was applied to Eq. (4.1). The calculation is done for each spatial mesh in each time step using the following procedure:

- (1) The hyperbolic equations are solved for an inviscid frozen flow,

$$\frac{\partial U_1}{\partial t} = - \frac{\partial F}{\partial r} \quad (4.9)$$

where the subscript 1 indicates the solution of step (1).

- (2) The spherical corrections are made by using the values of the physical properties evaluated in step (1).

$$\frac{\partial U_2}{\partial t} = -j(H_1)_1 \quad (4.10)$$

- (3) The viscous diffusion equations are solved by using the values of the physical properties evaluated in step (2).

$$\frac{\partial U_3}{\partial t} = \left(\frac{\partial^2}{\partial r^2} + \frac{j}{r} \frac{\partial}{\partial r} \right) C_2 - j(H_V)_2 \quad (4.11)$$

- (4) The vibrational relaxation equations are solved by using the values of the physical properties evaluated in step (3).

$$\frac{\partial U_4}{\partial t} = (H_R)_3 \quad (4.12)$$

The final solutions are obtained in step (4).

The RCM is applied to step (1) and the explicit method of finite difference is applied to steps (2) and (3). In step (4), the integrated relation was used. If one step is passed over among steps (2)-(4), then the following solutions result: plane flow, an inviscid-nonequilibrium flow or a viscous-frozen flow, respectively. These are termed as a plane solution, a real-inviscid solution and a perfect-viscous solution, respectively. The full solution including both effects of vibrational excitation and viscosity is called a real-viscous solution.

An outline of RCM is described below. Figure 4.2 shows an illustrative diagram for grid construction and sequence of the sampling procedure. The notations Δr and Δt are increments of space and time, respectively. For arbitrary integers n and i , the properties U_i^{n+1} at time $(n+1)\Delta t$ are calculated from the properties U_i^n at time $n\Delta t$. The intermediate values $U_{i+1/2}^{n+1/2}$ are evaluated at time $(n+1/2)\Delta t$. In the region of $i\Delta r < r < (i+1)\Delta r$ and $n\Delta t < t < (n+1/2)\Delta t$ (surrounded by the broken lines in Fig. 4.2), the Riemann problem (shock-tube problem) is solved for the discontinuous initial values

$$U = \begin{cases} U_{i+1}^n & r < i + \frac{1}{2} \Delta r \\ U_i^n & r > i + \frac{1}{2} \Delta r \end{cases} \quad (4.13)$$

in this region. Then, for example, the solution consists of a shock wave S , an expansion wave R and a contact surface C , as shown in Fig. 4.2. At time $(n+1/2)\Delta t$, the region $i\Delta r < r < (i+1)\Delta r$ can be divided into four subregions (1)-(4) (or five subregions, if the interior of the expansion fan is taken into account), and the physical properties in each subregion can be determined from the solution of the shock-tube problem for the initial condition (4.13). The values $U_{i+1/2}^{n+1/2}$ are equated to those of $U_p^{n+1/2}$ at point P [$r = r_p$; $i\Delta r < r_p < (i+1)\Delta r$], which is chosen at random. That is, we assume $U_{i+1/2}^{n+1/2} = U_p^{n+1/2}$. The choice of P is made by a random-sampling technique in such a way that the sampled points are uniformly distributed within a finite-sampling frequency. In a similar way, the values of $U_{i-1/2}^{n+1/2}$ are obtained from the initial values of U_i^n and U_{i-1}^n . At the second half-time step, the values of U_i^{n+1} are evaluated from the values of $U_{i-1/2}^{n+1/2}$ and $U_{i+1/2}^{n+1/2}$ as initial ones. Godunov's iterative technique is applied to solve the Riemann problem. As the vibrational energies are assumed to be frozen, they are invariant across the waves, and keep their initial values, whose boundary is the contact surface.

In the second and third steps of the operator-splitting technique, explicit finite-difference schemes are employed. The finite-difference forms of Eqs. (4.10) and (4.11) reduce to

$$(U_2)_{i+1}^{n+1} = (U_1)_{i+1}^{n+1} - j[(H_1)_1]_{i+1}^{n+1} \Delta t \quad (4.14)$$

$$(U_3)_i^{n+1} = (U_2)_i^{n+1} + \frac{\Delta t}{(\Delta r)^2} [(C_2)_{i+1}^{n+1} - 2(C_2)_i^{n+1} + (C_2)_{i-1}^{n+1}] + \frac{j}{2r_i} \Delta t [(C_2)_{i+1}^{n+1} - (C_2)_{i-1}^{n+1}] - j[(H_v)_2]_i^{n+1} \Delta t \quad (4.15)$$

The multiple time step is used to evaluate $(U_3)_i^{n+1}$ to improve accuracy. At the intermediate substep

$$(U_3)_i^{n+(i+1)/k} = (U_3)_i^{n+(i/k)} + \frac{\Delta t/k}{(\Delta r)^2} [(C_3)_{i+1}^{n+(i/k)} - 2(C_3)_i^{n+(i/k)} + (C_3)_{i-1}^{n+(i/k)}] + \frac{j}{2r_i} \frac{\Delta t/k}{\Delta r} [(C_3)_{i+1}^{n+(i/k)} - (C_3)_{i-1}^{n+(i/k)}] - j[(H_v)_3]_i^{n+(i/k)} \frac{\Delta t}{k} \quad (i = 0, 1, \dots, k) \quad (4.16)$$

where the time increment Δt is subdivided by k . Most of the calculations were carried out for $k = 10$.

In the 4th step, the vibrational relaxation equations for air molecules

$$\frac{dC_j}{dt} = \frac{(C_j)_{eq} - C_j}{\tau_j} \quad (j = O, N) \quad (4.17)$$

are solved in each spatial mesh under the assumption of constant temperature and pressure, thereby yielding the analytical relation

$$[(C_j)_i]^{n+1} = [(C_j)_i e^{-\frac{\Delta t}{\tau_j}}]_i^{n+1} \exp \left(-\frac{\Delta t}{\tau_j} \right) \quad (j = O, N) \quad (4.18)$$

The finite-difference schemes with multiple time steps, similar to Eq. (4.16), were also applied to Eq. (4.17), and found to give the same results as Eq. (4.18). In order to reduce the computation time, Eq. (4.18) was used for most of the calculations. As described in Section 4.1, in the present study, only the vibrational relaxation equation for oxygen was solved (except Section 4.4.6). Furthermore, the bulk viscosity concept was applied, instead of Eq. (4.17), to the vibrational relaxation for oxygen in Sections 4.4.5 and 4.4.6, in which the N-waves with long durations were analysed.

The condition of symmetry is imposed on the wall boundary and at the centre of the sphere. That is, at the boundary r_0

$$U_{i_0+1/2}(v) = U_{i_0-1/2}(-v) \quad (4.19)$$

The condition of continuity of gradient is imposed on the free boundary. That is, at the free boundary r_1

$$U_{i_1-1} - U_{i_1} = U_{i_1} - U_{i_1+1} \quad (4.20)$$

The entire programs are given in Appendix C.

4.3 Solutions for Plane Waves

As a check on the method, the one-dimensional shock-tube problem was solved for a perfect-inviscid flow, perfect-viscous flows and real-inviscid flows. The thickness and structure of the shock waves are compared with those obtained analytically in Chapter 3.

4.3.1 Perfect-Inviscid Solution

Figure 4.3 shows a computer plot of a perfect-inviscid solution of overpressure (\bar{p}) against distance x for several time intervals for a diaphragm pressure ratio $P_{d1} = 2$ and initial temperature ratio $T_{d1} = 1$. The overpressure (\bar{p}) is normalized by the initial pressure p_1 , and the distance x is normalized by the length of the high-pressure chamber x_0 ($x^* = x/x_0$). The diaphragm is placed at $x^* = 1$. The time t is normalized by x_0/a_1 ($t^* = a_1 t/x_0$). After starting the calculation or the removal of the diaphragm, a shock wave as a discontinuous front propagates towards the right hand side, and a rarefaction wave propagates towards the left hand side. When $t^* = 1$ the head of the rarefaction wave arrives at the end wall of the high-pressure chamber. The shock Mach number M_s is about 1.16, and the normalized equilibrium overpressure or the shock strength $(\bar{p})_2/p_1$ is about 0.403. It should be noted that, unlike finite-difference schemes, the shock wave as a discontinuous front occupies one mesh jump without smearing, where the normalized one-mesh size $\Delta x^* = 1/40$.

4.3.2 Perfect-Viscous Solutions

Figure 4.4 shows a computer plot of a perfect-viscous solution for the same case as Fig. 4.3. The rarefaction wave reflects at the end wall ($x^* = 0$) and proceeds towards the right hand side. As expected, smooth shock transitions due to actual viscosity are obtained. In order to show these smooth transitions clearly, a hypothetical chamber length $x = 0.001$ cm was assumed at an initial pressure and temperature of $p_1 = 101.5$ kPa and $T_1 = 273.15$ K. Consequently, $t = 0.106$ μ sec for $t^* = 3.506$.

Here, it was not necessary to obtain the whole flow field. The fine structure of the shock front was important. Therefore, in order to save computation time, the calculation was done only in a confined region near the front for the wave far from the diaphragm, neglecting the behaviour of the rarefaction wave. Figure 4.5 illustrates the region of calculation and a plot of the shock-front path in the x^*-t^* plane. In the calculation, 30-80 mesh points around the front were used, and the physical properties at each mesh point were transferred back to two points in the computational space as the wave proceeds over two points in physical space. The condition of continuity, Eq. (4.20), is imposed on the free boundary of the region of calculation. In Fig. 4.5, the white circles indicate the perfect-viscous RCM solutions, in which the position of the shock front is defined as the position of 50% of $(\bar{p})_2$. The solid and broken lines indicate analytical shock and sound-wave paths, respectively. The numerical solution for the shock path is in excellent agreement with

analysis.

Figures 4.6(a)-(c) show perfect-viscous numerical solutions for the shock-tube problem described above by comparison with Taylor's and Lighthill's analytical solutions for the shock thickness, which is defined by 10-90% of $(\Delta p)_2$. The ratio of the thickness parameters $(\Delta Z)/(\Delta Z)_0$, which corresponds to the thickness or rise time normalized by the Taylor thickness or rise time, is plotted against the time parameter τ defined by Eq. (3.21). The figures indicate that the step wave with zero thickness is reduced to a plane wave with a smooth transition owing to viscous action, as the wave proceeds. The broken and solid lines indicate Taylor's and Lighthill's solutions, respectively. The various numerical solutions are indicated by symbols. All calculations were carried out for the same case as Fig. 4.4 [$P_1 = 2$, $T_1 = 1$, $T_2 = 273$ K, $p_1 = 101.3$ kPa, $M_5 = 1.16$, $(\Delta p)_2 = 40.7$ kPa].

Figure 4.6(a) shows the effect of multiple time step for viscous correction. The mesh size is $\Delta x^* = 1/40$ ($\Delta x = 2.5 \times 10^{-5}$ cm). The black and white circles indicate the cases for $k = 1$ and 10 in Eq. (4.16), respectively. The $k = 10$ result for the transient behaviour of the shock thickness is closer to Lighthill's solution. It is seen that the multiple time step for viscous correction improves the result for the transient behaviour of the shock thickness. The random walk due to the random sampling in RCM and the overshoot of the thickness value above Taylor's value can be seen. The multiple time step of $k = 10$ was used for all calculations described below.

Figure 4.6(b) shows the effect of the choice of random numbers. The mesh size is $\Delta x^* = 1/80$ ($\Delta x = 1.25 \times 10^{-5}$ cm). The black and white circles indicate the cases using the random numbers by maximum-length linearly recurring sequence and linear congruential sequence, respectively. It can be seen that the latter method is in better agreement. Therefore, linear congruential sequence was used for all other calculations in the present study, as well as by Saito and Glass (Ref. 17). It is also seen in Fig. 4.6(b) that the result is improved by reducing the mesh size by half, in comparison with the result in Fig. 4.6(a).

Figure 4.6(c) shows the comparison between the RCM and MacCormack's finite-difference method (MFM), which is shown in Appendix D. The MFM solution is in poor agreement with Lighthill's solution. Its thickness or rise time values are much larger than the analytical ones owing to the effect of artificial viscosity. The RCM solution with operator-splitting techniques is superior to the MFM solution for the same mesh size, although random scattering of the thickness or rise time values do occur. Better agreement with Lighthill's solution was attained by using a finer RCM mesh as shown. Computer costs would limit the ultimate mesh size to be used.

In Fig. 4.7, the normalized overpressure $(\Delta p)/(\Delta p)_2$ is plotted against the distance parameter Z at times $\tau = 0.99$, 45.0 and 58.3 for cases of $\Delta x = 1.25 \times 10^{-5}$ cm [white circle in Fig. 4.6(c)]. The origin of Z is taken at the place of $(\Delta p)/(\Delta p)_2 = 0.5$. The solid lines indicate Lighthill's solution for the transient state at $\tau = 0.99$ and Taylor's solution for the final steady state at $\tau \rightarrow \infty$. The

RCM pressure profiles show very good agreement with the analyses. This result suggests that the RCM with the operator-splitting technique may be applied to analyse the transient behaviour of a viscous shock structure, though some random walks and overshoot above the Taylor value were observed for the thickness or rise time data.

4.3.3 Real-Inviscid Solution

The initial conditions ($P_1 = 1.0018$, $T_1 = 1.0$, $p_1 = 101.3$ kPa, $T_1 = 303.15$ K and $RH = 90\%$) were chosen so as to give a fully-dispersed wave in the final steady state for a real-inviscid flow, and to give a fast approach to the steady state in order to reduce the computational cost. Only the vibrational excitation for oxygen molecules was taken into account for atmospheric air. The corresponding relaxation time for oxygen is $\tau_0 = 1.04$ μ sec and the characteristic time using the bulk viscosity $(\gamma_v)_0$ for oxygen is $(\gamma_v)_0/a_1^2 = 8.4 \times 10^{-10}$ sec. The equilibrium shock Mach number $M_5 = 1.0004$ and the equilibrium overpressure is $(\Delta p)_2 = 91.1$ Pa, which is less than the corresponding critical overpressure for oxygen $(\Delta p)_{cr,0} = 95.5$ Pa, so that the wave may become a fully-dispersed wave in the final steady state.

Figure 4.8 shows the transient behaviour of the pressure and temperature profiles of the dispersed wave obtained for the condition described above ($x_0 = 0.5$ cm and $\Delta x = 0.0125$ cm). The solid lines indicate the pressure and temperature profiles, which are the same in normalized plots of $(\Delta p)/(\Delta p)_2$ and $(T)/(T)_2$ as the wave is very weak. The broken lines indicate the normalized vibrational temperature profiles $(T_v)/(T)_2$. Ten profiles are shown for the time parameter $\tau = 0.0003, 0.41, 0.81, 1.6, 3.3, 4.9, 6.5, 8.1, 9.7$ and 11.4 or the normalized distance $x^* = 1.2, 30, 60, 120, 238, 360, 476, 593, 716$ and 830, where τ is defined using the bulk viscosity $(\gamma_v)_0$ for oxygen as $\tau = [a_1^2 t / (\gamma_v)_0] [(\Delta p)_2 / p_1]^2$. The calculation was also carried out only for a confined region near the front for the wave far from the diaphragm, similar to the perfect-viscous flow as shown in Fig. 4.5. The initial step wave is smoothed out owing to the dissipative effect of the vibrational relaxation. It should be noted that this process which smears the wave is largely different from that of the viscous wave. This tendency of smoothing has been shown analytically for linear waves (Ref. 25) and for nonlinear waves (Ref. 26). In a transient state, the wave is a partly-dispersed wave with a frozen shock front, even if the equilibrium shock pressure is below the critical overpressure. This suggests that the nonstationary effect is more important for dispersed waves than for viscous shocks.

Figure 4.9 shows plots of $(\Delta Z)/(\Delta Z)_0$ vs τ for real-inviscid shocks. The solid and broken lines indicate the modified Lighthill solution and the modified Taylor solution, respectively. The symbols indicate the RCM solutions for $\Delta x = 0.025$ cm and 0.0125 cm, respectively. The latter case corresponds to the one in Fig. 4.8. The RCM solutions of shock thickness show random walks and overshoot above the Taylor value, similar to the viscous solutions shown in Fig. 4.6. The thickness tends to approach the modified Taylor value using the bulk viscosity for oxygen vibrational relaxation. It should be noted that the shock-thickening time of the RCM solution is nearly the same as that of the modified Lighthill

solution, although the $(\bar{p})_2/(\bar{p})_0$ vs \bar{x} plot of the RCM solution deviates from Lighthill's solution owing to the difference in the transient-wave profiles between the two solutions shown in Figs. 3.11 and 4.8. That is, the shock-thickening time based on the modified Lighthill solution provides a reasonable estimate.

In Fig. 4.10, the normalized overpressure $(\bar{p})_2/(\bar{p})_0$ is plotted against the distance parameter \bar{x} at $\bar{t} = 25.0$ and 27.6 for the case of $\Delta x = 0.0125$ cm (white circle in Fig. 4.9), where \bar{x} is also defined using the bulk viscosity for oxygen vibrational relaxation. The solid line indicates the analytical solution for $(\bar{p})_2/(\bar{p})_{cr,0} = 0.954$ evaluated from Eq. (3.54) for steady dispersed waves. The RCM pressure profile for $\bar{t} = 27.6$ shows very good agreement with analysis, but the $\bar{t} = 25.0$ solution shows a slight deviation from the analytical one at the upstream side of the front. This deviation would be attributed to the randomness associated with the RCM solution. However, in general, the RCM solution for real-inviscid flow provides very reasonable results.

4.1 Solutions for Spherical Waves

As described in chapter 3, the shock structures of spherical waves may be affected by N-wave and nonstationary effects and would be different from those of plane waves in some situations. The purpose of this section is to show some characteristic features of transient behaviour of shock structures of spherical waves through the RCM analysis associated with the spark and exploding-wire experiments.

Twenty-three cases of numerical results are presented in this section for spherical waves, and termed as cases A1, A2, ..., B1, B2, ..., C1, C2, ..., D1, D2, ..., respectively. The A-series (A1, A2, ...) corresponds to perfect-inviscid solutions; B-series, perfect-viscous solutions; C-series, real-inviscid solutions; and D-series, real-viscous solutions. The parameters, which should be given as initial conditions, are the radius of the pressurized sphere r_0 , the pressure and temperature ratios P_{q1} and T_{q1} across the initial inner pressurized air and the ambient atmosphere, the atmospheric pressure p_1 and temperature T_1 , and the relative humidity RH. These are tabulated for each case in table 4.1. We assumed $p_1 = 101.3$ kPa for all cases. The relaxation time τ_1 and the spatial meshes Δr^* and Δr are also tabulated in table 4.1. The atmospheric conditions (T_1 and RH) are chosen from data in the spark and exploding-wire experiments described in Chapter 2 (Series I - IV).

In the C and D-series analyses (real gases), the vibrational excitation is taken into account only for oxygen except case D8, in which both vibrational excitations for oxygen and nitrogen are included. In cases D5 through D8, the vibrational relaxation for oxygen is evaluated by using the bulk viscosity concept instead of solving the relaxation equation for oxygen.

4.1.1 Near-Field Solutions for Perfect-Inviscid Flows

In this section, perfect-inviscid solutions for spherical waves are shown in the near field of the pressurized sphere. The process of N-wave

formation from an explosion of a pressurized air sphere and the effects of the pressure and temperature ratios are discussed.

Case A1 is a perfect-inviscid solution for $P_{q1} = 2$ in the near-field of a pressurized sphere. Figures 4.11(a)-(c) exhibit computer plots of overpressure distribution at various times after the explosion.

Figure 4.11(a) shows the initial process of explosion of a pressurized air sphere. The front shock, which is formed immediately after bursting the sphere, decays as it propagates outwards, leaving an expanding flow behind it. The rarefaction wave, which propagates inwards into the sphere, reflected at the centre of the sphere and produces a highly rarefied region behind it. A second imploding shock wave of ever increasing strength is formed at the boundary between the inner and outer expansion regions. Some "noise" in the pressure profiles in the expansion region can be attributed to the random walk inherent in the RCM. The comparison between near-field solutions of the explosion of a pressurized air sphere using Lax, MacCormack and Random-Choice methods for a perfect-inviscid flow is given in Appendix E.

The succeeding process of N-wave formation is shown in Fig. 4.11(b). The imploding second shock reflects at the centre of the sphere and produces a highly compressed region around it. The reflected second shock is initially very strong, but rapidly decays as it proceeds outwards. It follows the front shock and forms the rear shock of an N-wave. Figure 4.11(c) exhibits the propagation of an established N-wave, which maintains a similar profile as it propagates outwards. Its maximum (peak) overpressure decays gradually and the duration increases slowly.

Figures 4.12(a)-(d) show a comparison of established N-waves for cases A1-A4. Figure 4.12(a) exhibits a pressure profile for the same case as Fig. 4.11(c), though the mesh size is increased to $\Delta r^* = 1/10$ to be compared with cases A2-A4. In case A2, the temperature ratio T_{q1} is twice that for case A1. In case A3, the pressure ratio P_{q1} is increased from 2 to 9. In case A4, both pressure and temperature ratios are higher. Figure 4.12(b) shows that case A2 results in a more symmetric N-wave than case A1 owing to the hotter sphere, which enables the second shock to form sooner. This suggests that the half-duration of the negative overpressure of an N-wave can be controlled through a choice of T_{q1} . Figures 4.12(c) and 4.12(d) show that for higher P_{q1} and T_{q1} the N-waves generated by a spark or an exploding wire cannot be simulated using a pressurized-sphere explosion model.

As seen in Figs. 4.12(a)-(d), the overpressure profiles of the positive phase show only a slight change in shape regardless of P_{q1} and T_{q1} (although \bar{p} and the durations are different). However, the negative phases strongly depend on these ratios. The length of the positive side is of the order of $r^* = 1$ or $r = r_0$ in each case. That is, the half-duration of an N-wave is determined mainly by a choice of the sphere radius within the range of P_{q1} and T_{q1} considered here. In the following, use is made of $T_{q1} = 1$, in order to simplify the analysis, since attention is focussed on the front-shock structures of the N-waves in this work.

4.4.2 Comparison Between Perfect-Inviscid, Perfect-Viscous, Real-Inviscid and Real-Viscous, Far-Field Solutions

The calculation for cases A5, B1, C1 and D1 were carried out for the same parameters in order to make the comparison clear between perfect-inviscid, perfect-viscous, real-inviscid and real-viscous solutions in the far field. The vibrational excitation for oxygen was taken into account for real cases (C1 and D1). The ambient conditions correspond to the series-I experiment, and the relaxation time $\tau_0 = 15.6 \text{ } \mu\text{sec}$.

The results are shown in Figs. 4.15-4.17. Figure 4.15 shows the path of the shock front by plotting the centre of the front $[0.5(p)_{\max}]$. The normalized radius r^* and the normalized time t^* are defined by $r^* = r/r_0$ and $t^* = at/r_0$, respectively. The solid line indicates the path of a sonic line. It is seen that away from the explosion the front path nearly coincides with the sonic-line path. This result indicates the validity of the method of solution with regard to the propagation of the wave. The calculations were also carried out only in a confined computational region near the front in the far-field as well as the calculations for plane waves shown in Fig. 4.5.

The maximum overpressure $(p)_{\max}$ for spherical waves decay with increasing distance r from the centre. According to classical acoustic theory $(p)_{\max} \propto r^{-1}$ for weak spherical waves. However, as shown in the following, the decay of the maximum overpressure can deviate from classical theory if the effects of viscosity and vibrational nonequilibrium are taken into account. In order to readily evaluate the decay rate of the maximum overpressure, the decay index n is introduced, where n is defined locally as $(p)_{\max} \propto r^{-n}$. In general, the value of n varies with r , while $n = 1$ applies to spherical acoustic waves.

Figure 4.14 shows the decay of the maximum overpressure for four cases as a function of the distance r . In the perfect-inviscid solution (case A5), the maximum overpressure decays at a rate inversely proportional to r ($n = 1$) for $(p)_{\max} < 100 \text{ Pa}$, though $n = 1$ for $(p)_{\max} > 100 \text{ Pa}$. In other cases, B1, C1 and D1, the decay indices n increase for $(p)_{\max} > 100 \text{ Pa}$ due to the dissipative effects of viscosity and vibrational nonequilibrium in comparison with case A5. While almost the same overpressures are obtained for $(p)_{\max} < 100 \text{ Pa}$ for all cases including case A5, at $r = 20\text{m}$, $n = 1.25$ for case B1 and $n = 1.465$ for cases C1 and D1. The deviation from the classical acoustic theory for $(p)_{\max} > 100 \text{ Pa}$ is attributed to the nonlinear effects in a wave of finite amplitude.

Figure 4.15 exhibits the half-duration t_d as a function of distance r . The rapid increase of t_d near the centre is attributed to nonlinear effects. In case A5, t_d is constant for $(p)_{\max} < 100 \text{ Pa}$, while in cases B1, C1 and D1, t_d increases with r due to dissipative effects of viscosity and vibrational nonequilibrium.

Figure 4.16 shows the rise times t_r as a function of distance r , and Fig. 4.17 shows the pressure profiles at several locations for cases A5, B1, C1 and D1. The perfect-inviscid solution results in a discontinuous front so that $t_r = 0$ in this case,

unlike the smoothing causes by artificial viscosity in finite-difference methods. As seen in case C1, the effect of vibrational nonequilibrium contributes to t_r only for weak waves. The rise times for the real-viscous case D1 are almost the same as the rise times of the perfect-viscous case B1, until the effect of vibrational nonequilibrium becomes noticeable. The viscous effect plays a dominant role in determining the rise time in these cases. However, the vibrational nonequilibrium plays an important role in reducing the maximum overpressure.

The profile of the perfect-viscous transition at $r = 21.6\text{m}$ [Fig. 4.17(b)] is not similar to either the profile for a steady plane wave (Section 3.1), the quasi-stationary N-wave for moderate Reynolds number (Section 3.2), or the nonstationary, plane wave (Section 3.2). This shows a characteristic feature of the nonstationary effect for spherical N-waves. Figure 4.17(c) indicates that the wave is a partly-dispersed wave with a discontinuous front, even though the steady plane wave becomes a fully-dispersed wave with a smooth transition for the corresponding overpressure at $r = 21.6\text{m}$ (Section 3.4). Again, this is a nonstationary effect for dispersed waves, which is discussed in Section 4.3.5. The nonstationary dissipative effects due to viscosity and vibrational nonequilibrium are coupled in the real-viscous solution [Fig. 4.17(d)].

The results for cases A5, B1, C1 and D1 show that the decay behaviour of the maximum overpressure, the half-duration, the rise time for the shock thickness and the pressure profile of a weak spherical N-wave can be affected by both viscosity and vibrational nonequilibrium. This shows that both effects must be taken into account when analysing the shock structure of a weak spherical N-wave.

4.4.3 Simulations for Spark and Exploding-Wire-Generated N-Waves

In this section, the numerical simulations are shown for the spherical N-waves, which were generated from spark and exploding-wire sources, described in Chapter 2. A requirement was set for the simulation of weak spherical N-waves that the calculated maximum overpressure $(p)_{\max}$ and the half-duration t_d should coincide with the experimental values at a specified location r . This requirement can be fulfilled by giving appropriate values to the initial pressure ratio P_{11} and the radius r_0 of the pressurized sphere. However, in practice, the adjustment of the values of P_{11} and r_0 is a laborious task in order to match required values of $(p)_{\max}$ and t_d at a specified location. Several trial calculations were needed to get the final result. Cases B2, C2, D1, D2 and D5 are the results of simulations for the spark and exploding-wire data.

In Figs. 4.18-4.21, the results of the numerical calculations are compared with the experimental data by plotting $(p)_{\max}$ vs r , t_d vs r , t_r vs r , and t_r vs $(p)_{\max}$. In these figures, the experimental points are plotted by white symbols and the numerical ones by black symbols. The solid and broken lines denote the interpolated lines for the numerical and experimental data, respectively. In Fig. 4.21, the

broken lines denote the Lighthill rise times for N waves with $t_d = 50$ and 70 μ sec, and the chain line denotes the Taylor rise time for steady, plane waves. The abrupt changes in rise time are attributed to the randomness inherent in the RCM.

Figures 4.18 and 4.19 show that one can simulate the change of $(\bar{p})_{\max}$ and t_d against r by a proper choice of r_0 and T_{11} . Curves B2 and C2 in Figs. 4.20 and 4.21 indicate that the perfect-viscous (B2) and real-inviscid (C2) solutions cannot simulate the nonstationary behaviour of the rise time, even if $(\bar{p})_{\max}$ and t_d can be simulated against r . Curves B1, B2 and B3 indicate that the real viscous solutions simulate the experimental results reasonably well, when one considers the flow complexities at the spark discharge and exploding wire. Curves D1, D2 and D3 almost simulate the data for series I, II and IV, respectively.

The general features of the results can be summarized as follows:

1. The decay index of $(\bar{p})_{\max}$ evaluated from the series I and II spark data is about 1.45, while for the simulated spark case D1, $n = 1.40$ at $r = 21.6$ m and $n = 1.421$ at $r = 19$ m. The deviation of the n value from the linear acoustic theory ($n = 1$) is simulated reasonably well and can be attributed to the dissipative effects of viscosity and vibrational nonequilibrium for oxygen.

2. The half duration t_d increases with r (Fig. 4.19). Its rate of increase is about 1.0 μ sec/m and simulates the experimental data. The increase of t_d may also be attributed to dissipative effects of viscosity and vibrational nonequilibrium for oxygen.

3. The spark data (series I and II) and their simulation for rise time (cases D1 and D2) show that the shorter relaxation time (5.5 μ sec, case D2) gives the longer rise time, and the longer relaxation time (15.6 μ sec, case D1) gives the shorter rise time. This tendency is due to the nonstationary effect. The long relaxation time gives the slow rate of change of the shock thickness, as discussed in Sections 3.4 and 4.3.3, so that the rise time remains short even for weak waves. Further discussion about the effect of relaxation time on t_d will be given in the succeeding section.

4. The exploding wire data (series IV) and their simulation (case D3) show, by comparison with the spark data, that the stronger explosion and longer duration give the longer rise time for the same overpressure (Fig. 4.21). This is again due to the nonstationary effects. The strong explosion gives a slower rate of change of the maximum overpressure for the same overpressure (see Fig. 4.18) so that the rise time has enough time to increase. Furthermore, a longer duration provides a margin for increasing the rise time. This effect will be discussed in more detail in Section 4.4.5.

Figures 4.22(a)-(c) show the pressure, temperature and vibrational-temperature profiles at several locations for real viscous cases, D1, D2 and D3, respectively. The solid lines indicate the pressure and temperature profiles, which are the same for weak waves in normalized forms of $(\bar{p})_{\max}/(\bar{p})_{\max}$ and $(T)/(T)_{\max}$. The broken lines indicate the vibrational temperature in a normalized form of

$$(T_V)/(T_V)_{\max}, \text{ where } (T_V) = T_V - T_1.$$

Figure 4.22(a) shows the simulation for the spark (series I) experiment. The wave profiles are shown at $r = 0.27$ m, 2.44 m, 7.54 m, 9.78 m, 12.64 m, 15.6 m, 18.6 m and 21.6 m, and the maximum overpressures are 1662 Pa, 135 Pa, 36.0 Pa, 25.0 Pa, 17.7 Pa, 13.2 Pa, 10.4 Pa and 8.5 Pa, respectively. As seen, the peak pressure and temperature become gradually blunted due to the energy transfer from the translational and rotational modes to the vibrational mode, while the back (expansion) pressure and temperature profile becomes gradually rounded due to the reverse energy transfer from the vibrational mode to the translational and rotational modes. This arises owing to slow-relaxing behaviour of the vibrational energy and leads to an elongation of the half duration. The shock thickness or the rise time is mainly controlled by the dissipative effect of viscosity, though it is only partly affected by the energy transfer from the translational and rotational modes to the vibrational mode for waves at $r = 18.6$ m and 21.6 m. In a sense that the shock front is mainly controlled by viscous dissipation, these waves may be called partly dispersed waves.

Figure 4.22(b) exhibits the simulation for the spark (series II) experiment. The wave profiles are shown at $r = 0.20$ m, 1.50 m, 4.58 m, 6.27 m, 8.57 m, 10.67 m, 12.9 m, 15.1 m and 19.0 m, and the maximum overpressures are 1662 Pa, 134 Pa, 36.0 Pa, 25.0 Pa, 17.7 Pa, 13.2 Pa, 10.4 Pa, 8.5 Pa and 6.55 Pa, respectively, approximately in accordance with the maximum overpressures in Fig. 4.22(a). The difference in profiles between cases D1 and D2 can readily be seen. In case D2, the process of peak-blunting occurs between $r = 1.5$ m and 4.58 m or $(\bar{p})_{\max} = 35.1$ Pa and 131 Pa, while in case D1 it occurs between $r = 7.54$ m and 21.6 m or $(\bar{p})_{\max} = 5.5$ Pa and 35.1 Pa. This can be attributed to the differences in vibrational relaxation time for oxygen and initial temperature: $\tau_v = 15.6$ μ sec, $T_1 = 273$ K in case D1, and $\tau_v = 5.6$ μ sec, $T_1 = 289$ K in case D2. In case of the shorter relaxation time, the peak blunting occurs in the earlier stage when the shock thickness is still relatively thin. Furthermore, in case of the higher initial temperature, more energy is required to excite the vibrational mode so that the effect of vibrational excitation appears for waves at higher maximum overpressure. In the range $r = 8.57$ m-19.0 m or $(\bar{p})_{\max} = 6.17$ Pa-17.2 Pa, the front structures are mainly controlled by vibrational excitation and the wave profiles nearly follow the vibrational temperature profiles owing to the energy transfer to the vibrational mode. In this sense, the waves may be called fully-dispersed waves in this range. However, it should be noted that the viscous dissipation also plays an important role in increasing the shock thickness or rise time, by contrast with steady, fully dispersed, plane waves, as seen in Figs. 4.20 and 4.21 in which the real-viscous solutions (D2) are compared with the perfect-viscous and real-inviscid solutions (B2, C2).

Figure 4.22(c) shows the simulation for the exploding wire (series IV) experiment. The wave profiles are shown at $r = 0.48$ m, 4.13 m, 6.3 m, 13.6 m, 18.3 m, 24.4 m and 29.3 m, and the maximum overpressures are 1670 Pa, 135 Pa, 82.1 Pa, 35.9 Pa, 25.0 Pa, 17.7 Pa and 14.1 Pa, respectively. The waves below 35 Pa show characteristic features of fully-dispersed waves, though the shock thicknesses are different

from the ones in Fig. 4.22(b). The peak-blunting occurs between $r = 4.15\text{m}$ and 6.3m . Figures 4.22(a)-(c) show that wide variations of wave profiles are possible depending on combinations of relaxation time, initial temperature, half-duration, and strength of explosion.

In Figs. 4.23 and 4.24, the calculated pressure profiles are compared with those observed at several locations for series I and II, respectively. Figure 4.23 shows a comparison between case D1 and series I profiles at $r = 4.85\text{m}$, 15.6m and 21.6m , while Fig. 4.24 shows a comparison between case D2 and series II profiles at $r = 11.7\text{m}$ and 19m . The solid and broken lines indicate the numerical and experimental pressure profiles, respectively. The shock transition and overall profiles are simulated reasonably well, if we consider the difficulty of adjusting P_{41} and r_0 to get the required values for $(p)_{\text{max}}$ and t_d at the desired positions. (Compare with Figs. 3.10 and 3.19 for the Lighthill and modified Lighthill pressure profiles.)

In Figs. 4.25-4.27, the full N-wave profiles of pressure, temperature and vibrational temperature are plotted at the longest distances of observation in series I, II and IV for cases D1A, D2A and D3A. In order to save computation time, the full N-wave solutions were obtained with larger mesh sizes, which were two or three times as large as those for the half N-wave solutions for D1, D2 and D3 shown above. These figures show that the transition profiles and rise times of the rear shocks are different from the front shock due to the difference in vibrational nonequilibrium.

In Fig. 4.28, the calculated full N-wave profile of pressure is compared with the observed one at 29.3m for series IV, in which the full N-wave profiles were obtained (Ref. 6). Although the calculated half-duration t_d is 20% longer than the observed one, both profiles are similar. The precise simulation for full N-waves would require an adjustment of the initial temperature ratio T_{41} in addition to the finer adjustment of P_{41} and r_0 . This may be done in a future study.

4.4.4 Effects of Vibrational Relaxation Time

The purpose of this section is to show the effect of vibrational relaxation time more clearly by comparing cases D2 and D4. The initial pressure ratio P_{41} and the sphere radius r_0 are the same for both cases, but the initial temperature and humidity are different and gives rise to a τ_0 of 5.54 and 15.6 μsec , respectively. (The initial temperature and humidity of case D4 correspond to case D1.)

Figures 4.29-4.31 show $(p)_{\text{max}}$, t_d and t_r as functions of r . The discontinuous change of t_r in Fig. 4.31 is also attributed to the randomness which appears in the RCM solutions. Figure 4.32 shows a comparison of both pressure profiles at the same distance $r = 19\text{m}$.

The attenuation behaviour of $(p)_{\text{max}}$ (Fig. 4.29) is slightly affected by the vibrational relaxation times for these cases. The decay indices at $r = 20\text{m}$ are $n = 1.31$ for D2 and $n = 1.40$ for D4. As easily seen in Figs. 4.29-4.31, $(p)_{\text{max}}$ and t_d are not affected appreciably by the difference in τ_0 , but t_r is very much affected by it. The rise time for case D4 with a longer relaxation time is

shorter at a fixed distance than the rise time for case D2 with a shorter relaxation time. This tendency can be explained by the nonstationary effect.

For steady, dispersed plane waves, as shown in Section 3.4, the longer relaxation time gives a thicker transition or a longer rise time, since t_r is proportional to τ_0 [see Eq. (3.42)]. However, the shock thickening time, which was defined by the time of approach of an impulsive step wave to the final steady state, is also proportional to τ_0 in the modified Lighthill solution for a nonstationary fully dispersed wave. Furthermore, it was shown in Section 4.3.3 that this shock thickening time was in close agreement with the RCM solution. That is, the longer the relaxation time, the slower is the rate of change of shock thickness. For case D4 with the longer relaxation time, the wave still remains a partly-dispersed wave whose shock transition is mainly controlled by viscous action, while for case D2 with a shorter relaxation time the wave becomes a fully-dispersed wave whose transition is mainly controlled by vibrational nonequilibrium. This is the reason why the longer relaxation time gives us the shorter rise time for the weak spherical waves in contrast with steady plane waves.

4.4.5 Effects of N-Wave Duration

In this section, the effects of the duration of the N-wave on the decay rate of $(p)_{\text{max}}$, the rate of increase of t_d and the rise time t_r are investigated by changing the radius r_0 of the pressurized air sphere. In cases D5 and D6, real-viscous solutions are obtained for the same conditions as case D2 except for the sphere radius. The radii for cases D5 and D6 are ten and fifty times, respectively, as large as the radius for D2. Consequently, the half-durations of the generated N-waves for D5 and D6 are about ten and fifty times as long as the half-duration for D2. Furthermore, the distances travelled by the wave fronts in cases D5 and D6 are about ten and fifty times as long as the distance in case D2 to reach nearly the same maximum overpressure.

In cases D5 and D6, the vibrational relaxation time for oxygen is much shorter than the half-durations of the N-waves, and $\tau_0/t_d = 10^{-2}$ for D5 and 2×10^{-5} for D6 ($\tau_0 = 5.6 \mu\text{sec}$), by contrast with D2, where $\tau_0/t_d = 0.8$ at $r = 19\text{m}$. According to the classification described in the last part of Section 3, the former cases correspond to quasi-equilibrium waves, while the latter corresponds to a moderate nonequilibrium wave. In this section, the bulk-viscosity concept is introduced to evaluate the vibrational relaxation for oxygen instead of solving the relaxation equation for oxygen. This assumption is reasonable for these cases due to the fact that the relaxation time or length for oxygen is much shorter than the characteristic-flow time or length, such as the half-duration or N-wave length. In practice, a typical time step Δt for D5 and D6 becomes longer than τ_0 ($\Delta t = 11.2 \mu\text{sec}$ for D5 and $56.2 \mu\text{sec}$ for D6). In the basic equations [Eq. (4.1)], the coefficient of viscosity $\mu + \mu_T$ was replaced by $\mu + \mu_T + (\mu_V/\tau_0)$, and the method of solving the equations for perfect viscous flows was used. That is, only spherical and viscous corrections were carried out in the operator-splitting technique. Details of the bulk viscosity analysis are shown in Appendix F.

Figure 4.33 shows the attenuation of $(p)_{\text{max}}$ vs

the normalized distance r^* for cases A6, D2, D5 and D6. Case A6 is a perfect-inviscid solution for the same P_{41} as cases D2, D5 and D6. In the initial stage of $(p/p)_{\max} = 100$, the decay indices are almost the same for all cases at higher $(p/p)_{\max}$ but vary as the waves weaken. At $r^* = 2,000$, $n = 1$ for case A6, 1.42 for case D2, 1.15 for case D5 and 1.06 for case D6. The decay index n decreases at a fixed distance as the half-duration t_d increases. That is, the effect of vibrational nonequilibrium on the decay rate of $(p/p)_{\max}$ is weakened as the wave approaches equilibrium. Since $n = 1$ for a weak frozen wave (case A6), the maximum value of n would exist for a moderate nonequilibrium wave. Among the cases shown in this section, the maximum value of n was obtained for case D2.

Figure 4.54 shows the normalized half duration t_d^* as a function of r^* , where t_d^* is defined by $t_d^* = a(t_d/r_p)$. The half-durations rapidly increase in the initial stage for all cases due to the nonlinear effect, but are quite different at the later stage of weakened waves depending on the degree of vibrational nonequilibrium. For weak waves below 100 Pa, the rate of increase is zero for a frozen wave (case A6), but positive for nonequilibrium waves (cases D2, D5, D6). The maximum rate of increase of t_d^* vs r^* is obtained for the moderate nonequilibrium wave (case D2) [as well as for the decay rate of $(p/p)_{\max}$ (Fig. 4.55)].

Figure 4.55 shows the rise time t_r as a function of $(p/p)_{\max}$. The broken line indicates the modified Taylor solution for steady, real-viscous, plane waves, in which the coefficient of viscosity $(\mu + \mu_r + \mu_v)/\rho$ is used instead of μ in the Taylor solution. The chain lines indicate the modified Lighthill solutions for real viscous N-waves with $t_d = 70 \mu\text{sec}$, $570 \mu\text{sec}$ and $2,900 \mu\text{sec}$, respectively, which correspond to the half durations at $r^* = 2,000$ in cases D2, D5 and D6. It can be seen in Fig. 4.55 that the rise time increases with increasing t_d at a fixed $(p/p)_{\max}$ and approaches the modified Taylor or Lighthill value. In case D6, the rise time t_r overshoots the modified Taylor value for the higher $(p/p)_{\max}$. This overshoot would correspond to the overshoot of t_r above the Taylor value for an impulsive step wave described in Section 4.3.2, and can be improved by using a finer mesh size. As described for plane waves in Section 4.5, the present method of calculation gives good results for the transient behaviour of t_r , but has the defect that there appear some overshoots of t_r above the Taylor value for quasi-steady waves. Some improvement will be required in the calculations in a future study. The nonstationary effect clearly appears for $(p/p)_{\max} = 40$ Pa in case D5 and for $(p/p)_{\max} = 10$ Pa for case D6, so that the t_r values tend to freeze and have lower values than the modified Taylor and Lighthill values.

Figure 4.56 shows the rise time t_r as a function of $(p/p)_{\max}$ for comparison between cases D6 and D6A. In case D6A, the relaxation equation for oxygen was solved without using the bulk viscosity concept for the same parameters as case D6. The black and white circles correspond to cases D6 and D6A, respectively. The broken line indicates the modified Taylor solution. The rise time values of D6A result in a higher overshoot of the modified Taylor values than those of D6. This is the reason why the bulk viscosity concept was used in the analysis of N waves of long durations.

Figure 4.57 shows the normalized overpressure profiles $(p/p)_{\max}$ plotted against the normalized time $(t - t_d)/t_d$ for the same maximum overpressure for cases D2, D5 and D6. As the wave approaches equilibrium, the peak (rise time) becomes sharp and the back becomes straight.

4.4.6 Effects of Nitrogen Vibrational Relaxation

The effects of vibrational relaxation for nitrogen on the attenuation of $(p/p)_{\max}$, the half duration t_d and the rise time t_r are investigated by introducing the vibrational relaxation equation for nitrogen into the governing equations used in the previous section. The vibrational relaxation for oxygen is taken into account through the bulk viscosity concept. The real viscous calculation was carried out by introducing the real gas correction for nitrogen in the operator splitting technique. The details can be seen in Appendix E.

The lower initial pressure ratio of $P_{41} = 1.08$ was chosen for cases D7 and D8, since it was expected that the effect of vibrational relaxation for nitrogen would appear for the lower maximum overpressure. Case D7 is a real viscous solution for the same conditions as case D6 except for P_{41} . In D6, only the vibrational relaxation for oxygen is taken into account by using the bulk viscosity concept ($\gamma = 5.04$). Case D8 is a real viscous solution for the same conditions as case D7 including the vibrational relaxation for nitrogen ($\gamma = 0.04$ msec). Initially, it was desirable to carry out the calculation for the effect of nitrogen by adding the vibrational excitation for nitrogen to case D6; however, it was found that it took a long computation time for the wave to reach the maximum overpressure, enough to show the effect of nitrogen. Instead, the initial pressure ratio was reduced to attain this aim within a reasonable computational time.

Figures 4.58-4.60 show plots of $(p/p)_{\max}$ vs r^* , t_d^* vs r^* and t_r vs $(p/p)_{\max}$, respectively, for cases D6, D7 and D8. The broken and chain lines in Fig. 4.60 indicate the modified Taylor rise time and the modified Lighthill rise time for $t_d = 20 \mu\text{sec}$ and $1.9 \mu\text{sec}$ for real viscous waves, respectively. The value $t_d = 1.9 \mu\text{sec}$ at $r^* = 2,000$ for cases D7 and D8.

Figure 4.58 shows that the initial decay of $(p/p)_{\max}$ are almost the same for both D7 and D8, but the decay rate increases for $(p/p)_{\max}$ below 20 Pa in D8 due to vibrational nonequilibrium in nitrogen. At $r^* = 2,000$, $n = 1.048$ for D7 and 1.21 for D8. In Fig. 4.59, the increasing rate of t_d^* vs r^* is slightly larger in D8 than in D7 due to the effect of vibrational nonequilibrium for nitrogen. However, as easily seen from Fig. 4.60, the rise time t_r is not affected by it.

Figure 4.41 shows a comparison between the pressure profiles at $r^* = 1,200$ for cases D7 and D8, and Fig. 4.42 shows profiles of temperature and vibrational temperature for nitrogen at the same location for D8. These figures indicate that the wave of D7 at $r^* = 1,950$ corresponds to a highly nonequilibrium wave for vibrational excitation of nitrogen, and thus the shock transition is mainly controlled by the vibrational relaxation of oxygen. The nitrogen nonequilibrium acts only to lower the maximum overpressure. It can be said that the dissipative effect of vibrational nonequilibrium for nitrogen in case D8 plays a role like oxygen in

case D1, while the vibrational relaxation of oxygen acts as a bulk viscosity in case D8. Figure 4.42 shows that the wave is a partly-dispersed wave for nitrogen. Fully-dispersed waves for nitrogen could be obtained for waves with longer duration and lower maximum overpressure.

5. CONCLUSIONS

The foregoing results can be summarized as follows:

(1) It was shown that the transient shock structures of weak plane and spherical waves in air can be analysed by solving the unsteady, compressible Navier-Stokes equations with a vibrational-relaxation equation for oxygen or nitrogen, using the random-choice method (RCM) with an operator-splitting technique.

(2) The perfect-viscous and real-inviscid solutions for impulsive step-waves show that the smearing processes due to dissipative effects of viscosity and vibrational nonequilibrium for shock fronts are in reasonable agreement with analysis. However, there is some randomness in the shock thickness or the rise time value and there are some overshoots above the steady-state value.

(3) The initial N-wave formation process was established for a perfect-inviscid wave for exploding pressurized air spheres. It was found that the attenuation of the maximum (peak) overpressure and the half-duration of an N-wave in the far field can be controlled by a proper choice of sphere radius and initial diaphragm-pressure ratio.

(4) The perfect-inviscid, perfect-viscous, real-inviscid and real-viscous far-field solutions for weak spherical waves in air were compared. It was found that the dissipative effects of viscosity and vibrational nonequilibrium of oxygen on the decay of the maximum overpressure, half-duration and N-wave rise time become distinguishable for values of $(\bar{p})_{\max} < 100$ Pa.

(5) The numerical simulations were carried out for weak spherical N-waves generated in atmospheric air from sparks and exploding wires. The numerical results show good agreement with the experimental data with regard to the decay rate of $(\bar{p})_{\max}$, the increasing rate of t_d , the rise time t_r and the wave profiles. The results indicate that the observed shock structures of weak spherical N-waves are controlled by the coupled dissipative effects of viscosity and vibrational nonequilibrium of oxygen.

(6) The calculated and observed rise times (or shock thicknesses) for weak spherical N-waves are mostly much smaller than those predicted analytically for steady plane waves. It is found that this phenomenon is attributed to the \bar{p} -wave and the \bar{p} -wave coupling, coupled with vibrational relaxation of oxygen. The shorter half-durations give shorter rise times for the same maximum overpressures due to flow expansion behind the front shock of an N-wave (N-wave effect). A more rapid decrease of the maximum overpressure also results in a shorter rise time for the same maximum overpressure, since the shock-thickening time becomes increasingly long as a wave is weakened, so that

the increase of shock thickness cannot follow the change in maximum overpressure (nonstationary effect). Furthermore, a longer relaxation time results in a shorter rise time in contrast to a steady wave, since the shock-thickening time is nearly proportional to the relaxation time for dispersed waves (nonstationary effect).

(7) As the duration increases, the rise time approaches the modified Taylor value for steady plane waves or the modified Lighthill value for quasi-stationary N-waves, which is obtained by introducing the bulk viscosity concept into the viscous-flow analysis. For waves with longer durations, the nonstationary effect on rise time appears only for lower maximum overpressures.

(8) The decay index n , which denotes the local decay rate of $(\bar{p})_{\max}$, defined by $(\bar{p})_{\max} \propto r^{-n}$, is equal to unity for a classical, linear acoustic wave, but increases due to the dissipative effects of viscosity and vibrational nonequilibrium for moderate non-equilibrium, weak spherical N-waves. It approaches unity for quasi-equilibrium waves of long duration.

(9) The effects of N_2 vibrational nonequilibrium on $(\bar{p})_{\max}$, t_d and t_r are found to be similar to those of O_2 , such as an increase in decay index and half-duration, and smearing of the pressure peak. These effects appear only at lower maximum overpressure (below 20 Pa) for waves of long duration.

Finally, as noted in Section 1, the original motivation for the present study was to answer the question whether N-waves generated by sparks or exploding wires can simulate SSI-generated N-waves including real-gas effects on N-wave rise times. The answer is 'no', since unlike SSI-generated N-waves produced by sparks and exploding wires, the rise times are determined by N-wave duration and the non-stationary distance travelled from the source. Nevertheless, the present study is important since it has succeeded in providing appropriate explanations for the rise times of spark and exploding-wire generated N-waves by using the concepts of the \bar{p} -wave and the \bar{p} -wave coupling, with the aid of very good RCM simulations of the actual experiments.

REFERENCES

1. Niedzwiecki, A., Ribner, H. S., "Subjective Loudness of N-Wave Sonic Booms", J. Acoust. Soc. America, Vol. 64(6), Dec. 1978, pp. 1617-1621.
2. Hilton, D. A., Newman, J. W., "Instrumentation Techniques for Measurement of Sonic Boom Signatures", J. Acoust. Soc. America, Vol. 59, No. 5, Part 2, 1966.
3. Maglieri, D. J., Huckel, V., Henderson, H. R., "Sonic Boom Measurements for SR-71 Aircraft Operating at Mach Numbers to 3.0 and Altitudes to 24384 Meters", NASA TN D-6823, 1972.
4. Reed, J. W., "Atmospheric Attenuation of Explosion Waves", J. Acoust. Soc. America, Vol. 61(1), Jan. 1977, pp. 39-47.
5. Taylor, G. I., "The Conditions Necessary for Discontinuous Motion in Gases", Proc. Royal Soc., Vol. 34, 1910, pp. 371-377.

6. Holst-Jensen, O., "An Experimental Investigation of Rise Times of Very Weak Shock Waves", OTHAS Tech. Note No. 229, March 1981.
7. Ribner, H. S., Morris, P. J., Chu, W. H., "Laboratory Simulation of Development of Superbooms by Atmospheric Turbulence", *J. Acoust. Soc. America*, Vol. 55, No. 3, 1975, pp. 926-928.
8. Plotkin, K. J., George, A. R., "Propagation of Weak Shock Waves Through Turbulence", *J. Fluid Mechanics*, Vol. 54, Part 3, 1972, pp. 449-467.
9. Pierce, A. D., Maglieri, D. J., "Effects of Atmospheric Irregularities on Sonic-Boom Propagation", *J. Acoust. Soc. America*, Vol. 51, No. 2, Feb. 1972, pp. 702-712.
10. Howes-Williams, J. F., Howe, M. S., "On the Possibility of Turbulent Thickening of Weak Shock Waves", *J. Fluid Mechanics*, Vol. 58, Part 1, 1973, pp. 461-480.
11. Hodgson, J. P., "Vibrational Relaxation Effects in Weak Shock Waves in Air and the Structure of Sonic Bangs", *J. Fluid Mechanics*, Vol. 58, Part 1, 1973, pp. 187-196.
12. Johannsen, N. H., Hodgson, J. P., "The Physics of Weak Waves in Gases", 'Report on Progress in Physics', Vol. 42, 1979, pp. 629-676.
13. Sullivan, P. A., Hinchey, M., Murra, L., Parravano, G. J., "Research on the Stability of Air Cushion Systems", OTHAS Report No. 238, Nov. 1979.
14. Glimm, J., "Solution in the Large for Nonlinear Hyperbolic Systems of Equations", *Comm. Pure Appl. Math.*, Vol. 18, 1965, p. 697.
15. Chorin, A. J., "Random Choice Solution of Hyperbolic System", *J. Comp. Phys.*, Vol. 22, 1976, pp. 517-535.
16. Sod, G. A., "A Numerical Study of a Converging Cylindrical Shock", *J. Fluid Mech.*, Vol. 85, Part 4, 1977, pp. 785-794.
17. Saito, I., Glass, I. I., "Applications of Random-Choice Method to Problems in Shock and Detonation-Wave Dynamics", OTHAS Report No. 240, 1979.
18. McCormack, R. W., "An Efficient Numerical Method for Solving the Time-Dependent Compressible Navier-Stokes Equations at High Reynolds Number", NASA TM X-75,129, July 1976.
19. Satofuka, N., Shimizu, J., "Applications of Random choice Method to Compressible Navier-Stokes Equations", 11th Conf. Japan Soc. Aero. Space Sci., Apr. 1980, pp. 52-53 (in Japanese).
20. Lighthill, M. J., "Viscosity Effects in Sound Waves of Finite Amplitude", 'Surveys in Mechanics', Eds. Batchelor, G. K. and Davies, R. M., University Press, Cambridge, 1956, pp. 294-351.
21. Polyakova, A. I., Soluyan, S. I., Khokhlov, R. V., "Propagation of Finite Disturbances in a Relaxing Medium", *Soviet Physics-Acoustics*, Vol. 8, 1962, pp. 78-82.
22. Gottlieb, J. J., "Simulation of a Travelling Sonic Boom in a Pyramidal Horn", OTHAS Report No. 196, July 1974; see also *Progress in Aerospace Sciences*, Vol. 17, 1976, pp. 1-66.
23. Bass, H. E., Shields, E. D., "Absorption of Sound in Air: High Frequency Measurements", *J. Acoust. Soc. America*, Vol. 62, No. 5, Sept. 1977, pp. 571-576.
24. Bass, H. E., Shields, E. D., "Atmospheric Absorption of High Frequency Noise and Application to Fractional-Octave Bands", NASA CR 2760, 1977.
25. Chu, R. T., "Wave Propagation and the Method of Characteristics in Reacting Gas Mixtures with Applications to Hypersonic Flow", Wright Air Development Center, DA 57-213, 1957.
26. Ockendon, H., Spence, D. A., "Non-Linear Wave Propagation in a Relaxing Gas", *J. Fluid Mech.*, Vol. 39, Part 2, 1969, pp. 529-545.

Table 2.1

Vibrational Relaxation Times for Oxygen (τ_O) and Nitrogen (τ_N)

Series		T_1 (K)	RH (%)	AH (%)	τ_O (μ sec)	τ_N (msec)
I	Spark	273-277	50-75	0.38-0.45	14-17	1.05-1.22
II	Spark	289	50	0.86	5.8	0.52
III	EW	277	75	0.61	9.1	0.75
IV	EW	280	87.5	0.88	5.7	0.52

T_1 -room temperature, RH-relative humidity,
AH-absolute humidity, EW-exploding wire

Table 4.1

Parameters for Computation of Spherical Waves

(a) Perfect-Inviscid Flows

Case	P_{41}	T_{41}	r^*
A1	2.0	1.0	1/80, 1/40
A1A	2.0	1.0	1/10
A2	2.0	2.0	1/10
A3	9.0	1.0	1/10
A4	9.0	9.0	1/10
A5	2.44	1.0	1/30
A6	1.8	1.0	1/30

(b) Perfect-Viscous Flows

Case	P_{41}	T_{41}	T_1 (K)	r_0 (cm)	r^*	r (cm)
B1	2.44	1.0	273	1.15	1/30	0.0383
B2	1.2	1.0	273	1.8	1/40	0.045

(c) Real-Inviscid Flows

Case	P_{41}	T_{41}	T_1 (K)	RH (%)	τ_O (μ s)	r_0 (cm)	r^*	r (cm)
C1	2.44	1.0	273	67	15.6	1.15	1/30	0.0383
C2	1.2	1.0	273	67	15.6	1.8	1/40	0.045

(d) Real-Viscous Flows

Case	P_{41}	T_{41}	T_1 (K)	RH (%)	τ_O (μ s)	r_0 (cm)	r^*	r (cm)
D1	2.44	1.0	273	67	15.6	1.15	1/30	0.0383
D1A	2.44	1.0	273	67	15.6	1.15	1/10	0.115
D2	1.8	1.0	289	50	5.54	1.15	1/30	0.0383
D2A	1.8	1.0	289	50	5.54	1.15	1/10	0.115
D3	3.3	1.0	280	87.5	5.73	1.8	1/20	0.09
D3A	3.3	1.0	280	87.5	5.73	1.8	1/10	0.115
D4	1.8	1.0	273	67	15.6	1.15	1/30	0.0383
D5	1.8	1.0	289	50	5.54	11.5	1/30	0.383
D6, D6A	1.8	1.0	289	50	5.54	57.5	1/30	1.917
D7	1.08	1.0	289	50	5.54	57.5	1/30	1.917
D8	1.08	1.0	289	50	510 (N ₂)	57.5	1/30	1.917

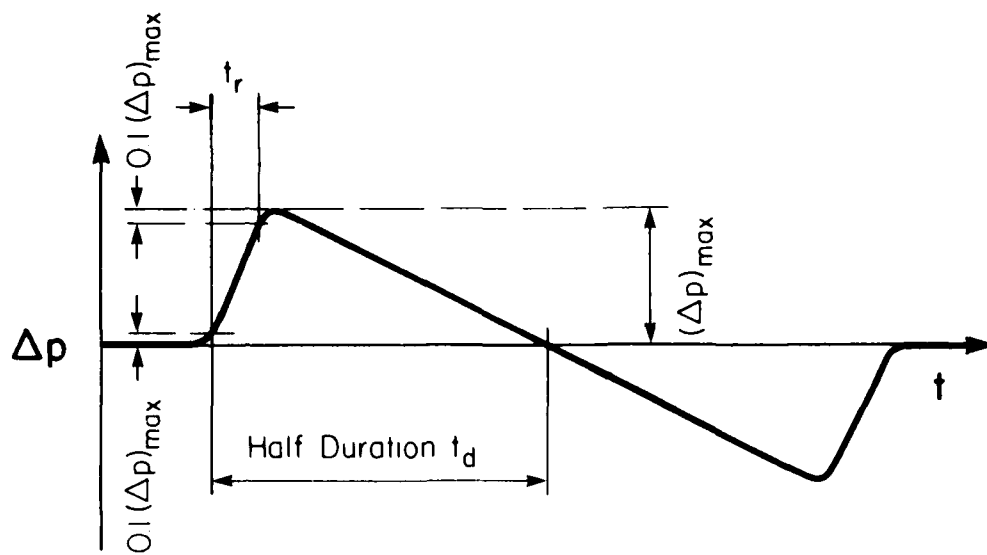


FIG. 1.1 DEFINITION OF RISE TIME t_r AND HALF-DURATION OF AN N-WAVE t_d .

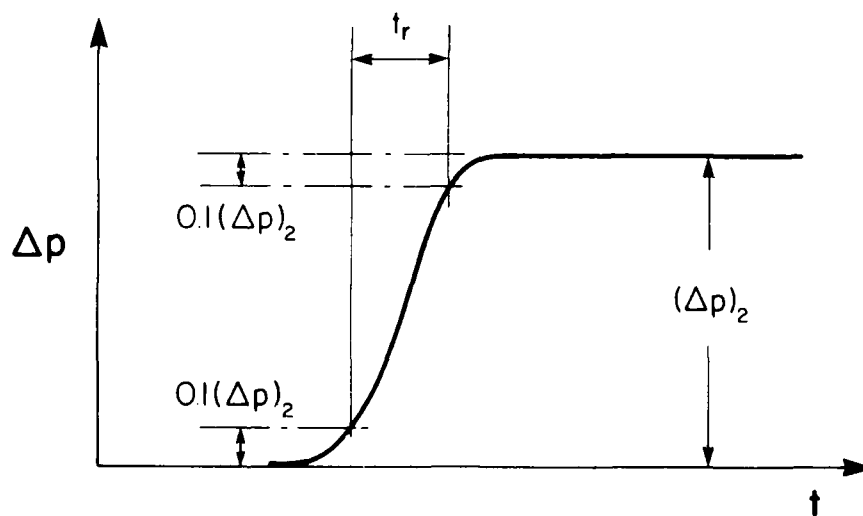


FIG. 1.2 DEFINITION OF RISE TIME t_r OF A PLANE WAVE.

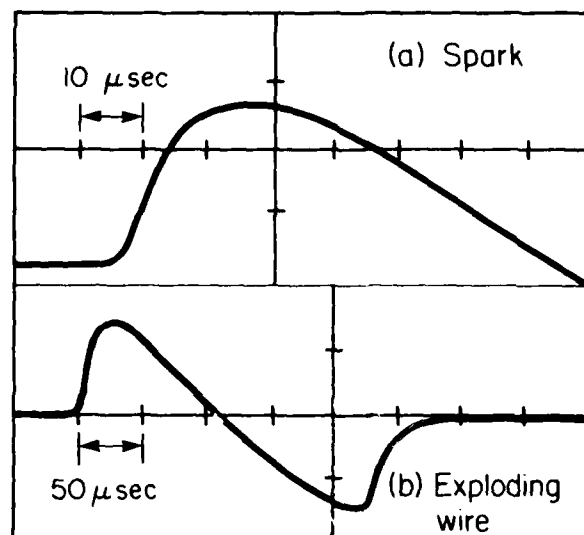


FIG. 2.1 SPARK AND EXPLODING-WIRE-GENERATED N-WAVES.

(a) SERIES I - SPARK

$S = 6.0 \text{ KV}$, $r = 21.6\text{m}$; $(\Delta p)_{\text{max}} = 8.2 \text{ Pa}$,
 $t_d = 72 \text{ } \mu\text{s}$, $t_r = 11.9 \text{ } \mu\text{s}$.

(b) SERIES IV - EXPLODING WIRE

$S = 6.0 \text{ KV}$, $r = 29.3\text{m}$; $(\Delta p)_{\text{max}} = 20.2 \text{ Pa}$,
 $t_d = 122 \text{ } \mu\text{s}$, $t_r = 15.2 \text{ } \mu\text{s}$.

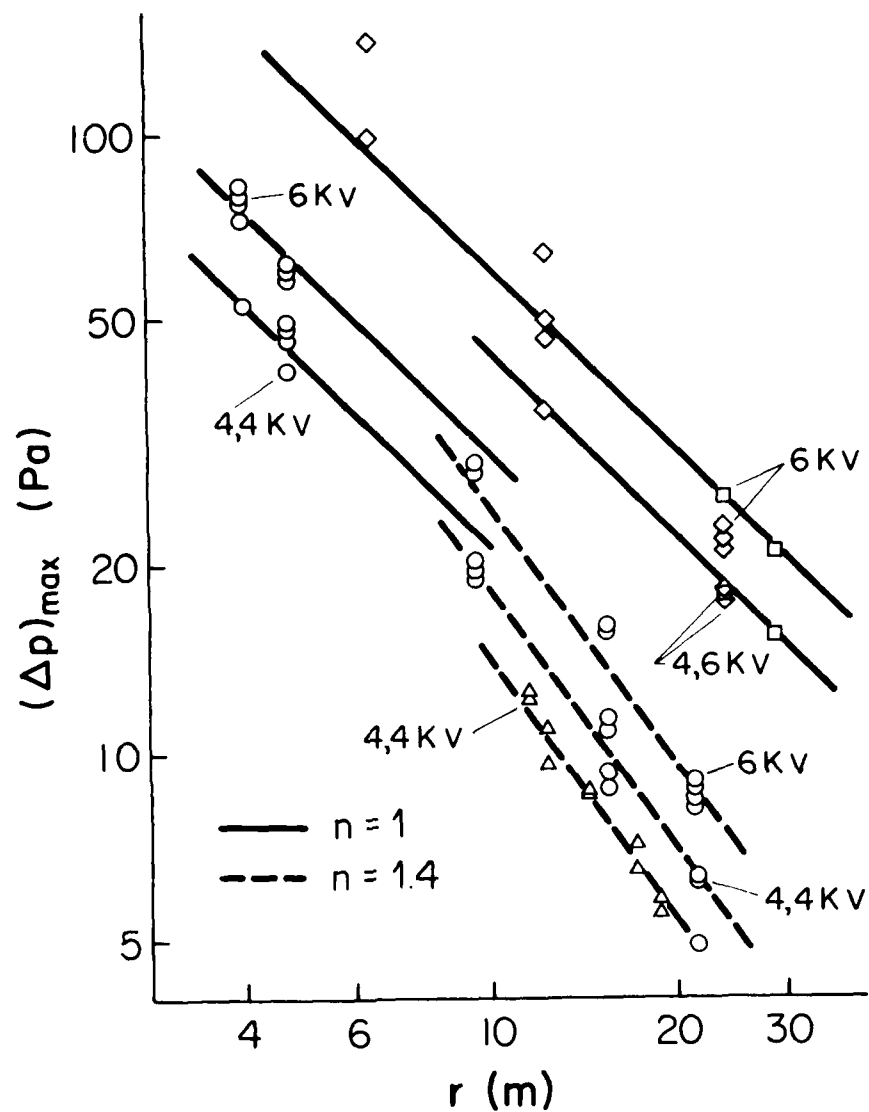


FIG. 2.2 MAXIMUM OVERPRESSURE DATA $(\Delta p)_{\max}$ vs r .
 $n: (\Delta p)_{\max} \propto r^{-n}$.

SPARK: SERIES I - \circ AND II - \triangle ;
 EXPLODING WIRES: SERIES III - \diamond AND IV - \square .

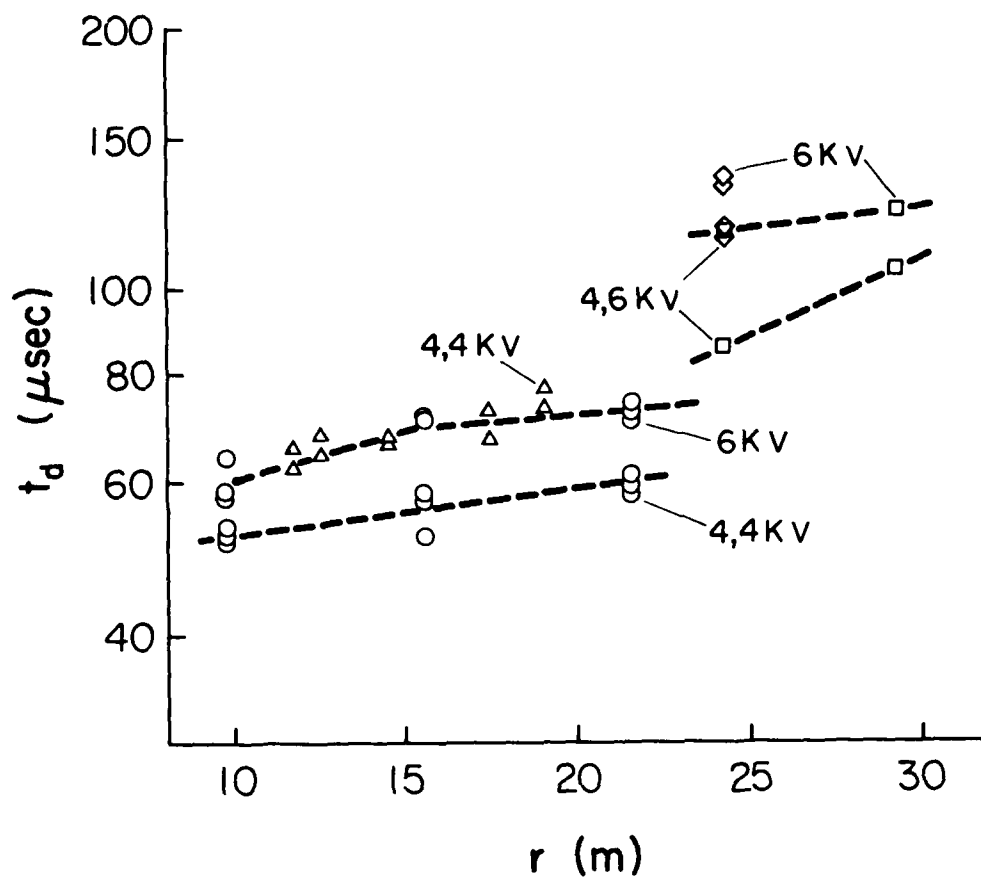


FIG. 2.3 HALF-DURATION DATA t_d vs r .

SPARK: SERIES I - ○ AND II - △ ;
EXPLODING WIRES: SERIES III - ◇ AND IV - □ .

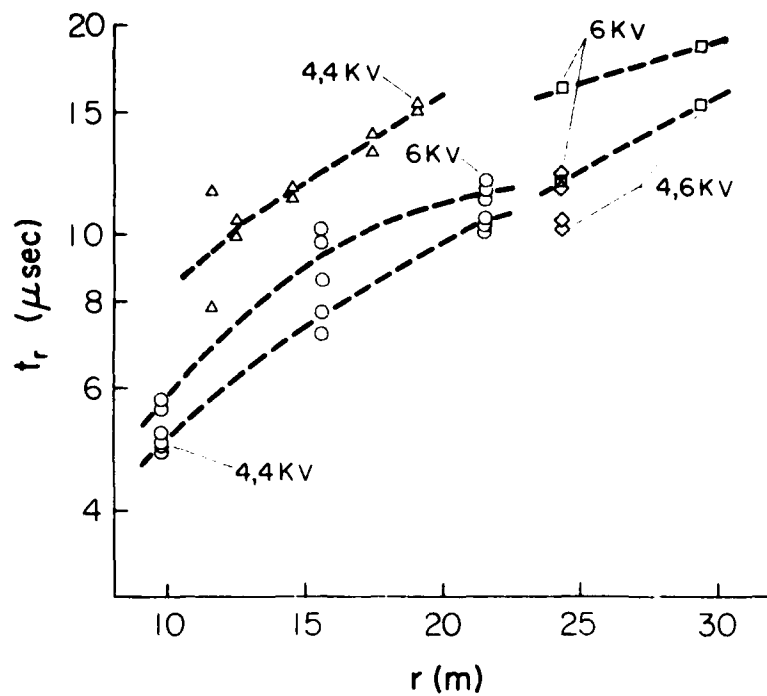


FIG. 2.4 RISE TIME DATA t_r vs r .

SPARK: SERIES I - \circ AND II - Δ ;
EXPLODING WIRES: SERIES III - \diamond AND IV - \square .

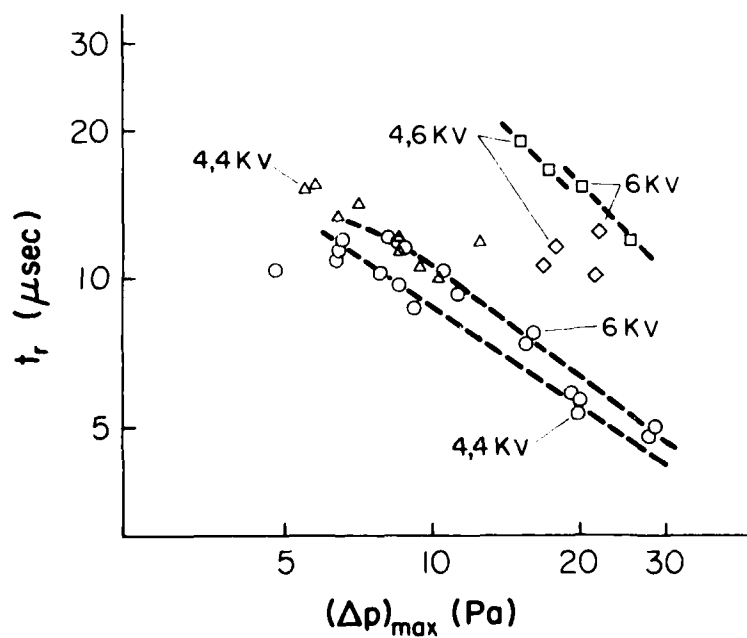


FIG. 2.5 RISE TIME DATA t_r vs $(\Delta p)_{\text{max}}$.

SPARK: SERIES I - \circ AND II - Δ ;
EXPLODING WIRE: SERIES III - \diamond AND IV - \square .

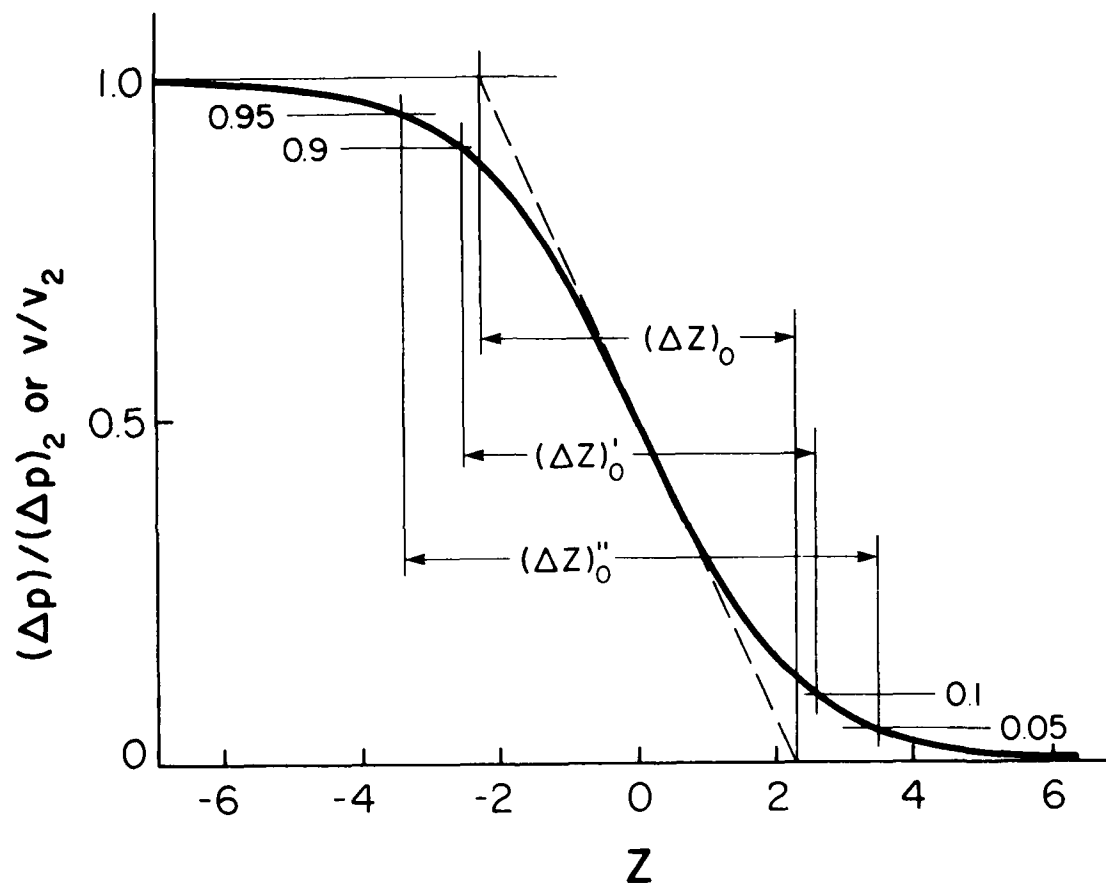


FIG. 3.1 TAYLOR VELOCITY OR PRESSURE PROFILE AND DEFINITIONS OF SHOCK THICKNESS.

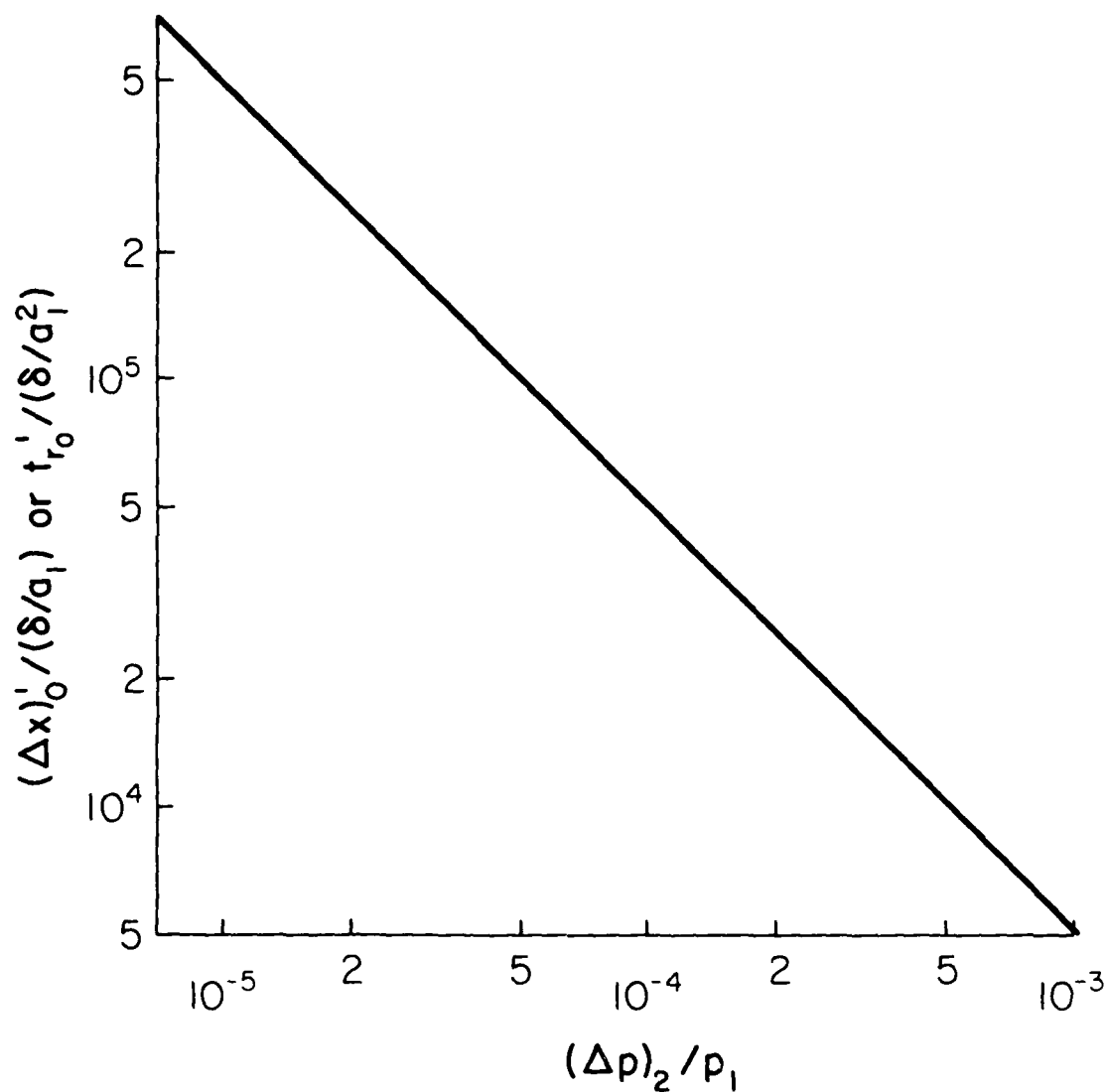


FIG. 3.2 NORMALIZED TAYLOR THICKNESS $(\Delta x)'_0/(\delta/a_1)$ OR NORMALIZED TAYLOR RISE TIME $t'_{r0}/(\delta/a_1^2)$ PLOTTED AGAINST SHOCK STRENGTH $(\Delta p)_2/p_1$.

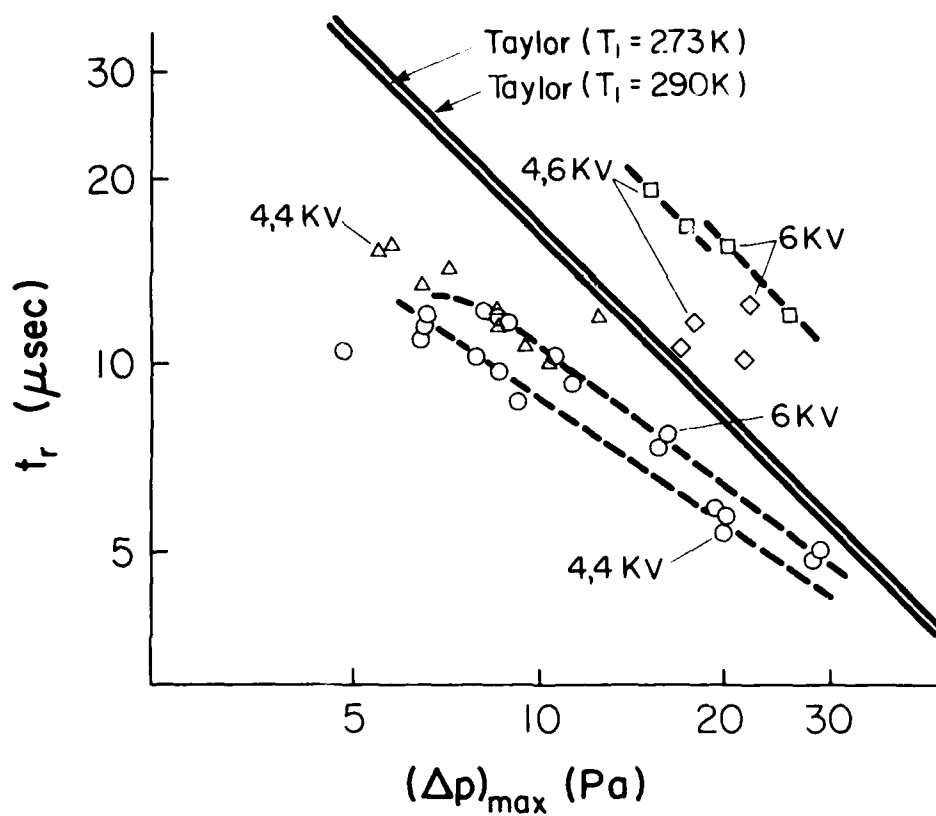


FIG. 3.5 COMPARISON BETWEEN EXPERIMENTAL AND THEORETICAL (TAYLOR) RISE TIMES PLOTTED AGAINST MAXIMUM OVERPRESSURE.

SPARK: SERIES I - \circ AND II - Δ ;
EXPLODING WIRE: SERIES III - \diamond AND IV - \square .

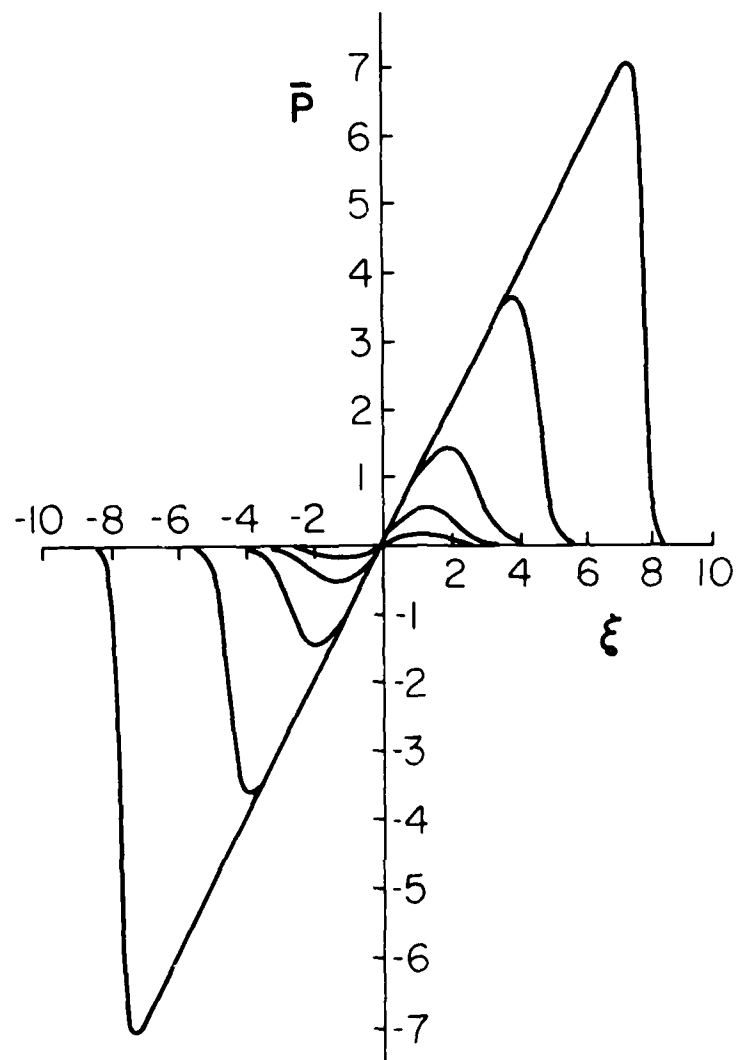


FIG. 3.4 LIGHTHILL N-WAVES (ASYMPTOTIC FORMS OF PULSES WITH ZERO MASS FLOW) FOR REYNOLDS NUMBERS $Re = 30, 10, 5, 1, 0.5$ (REF. 20).

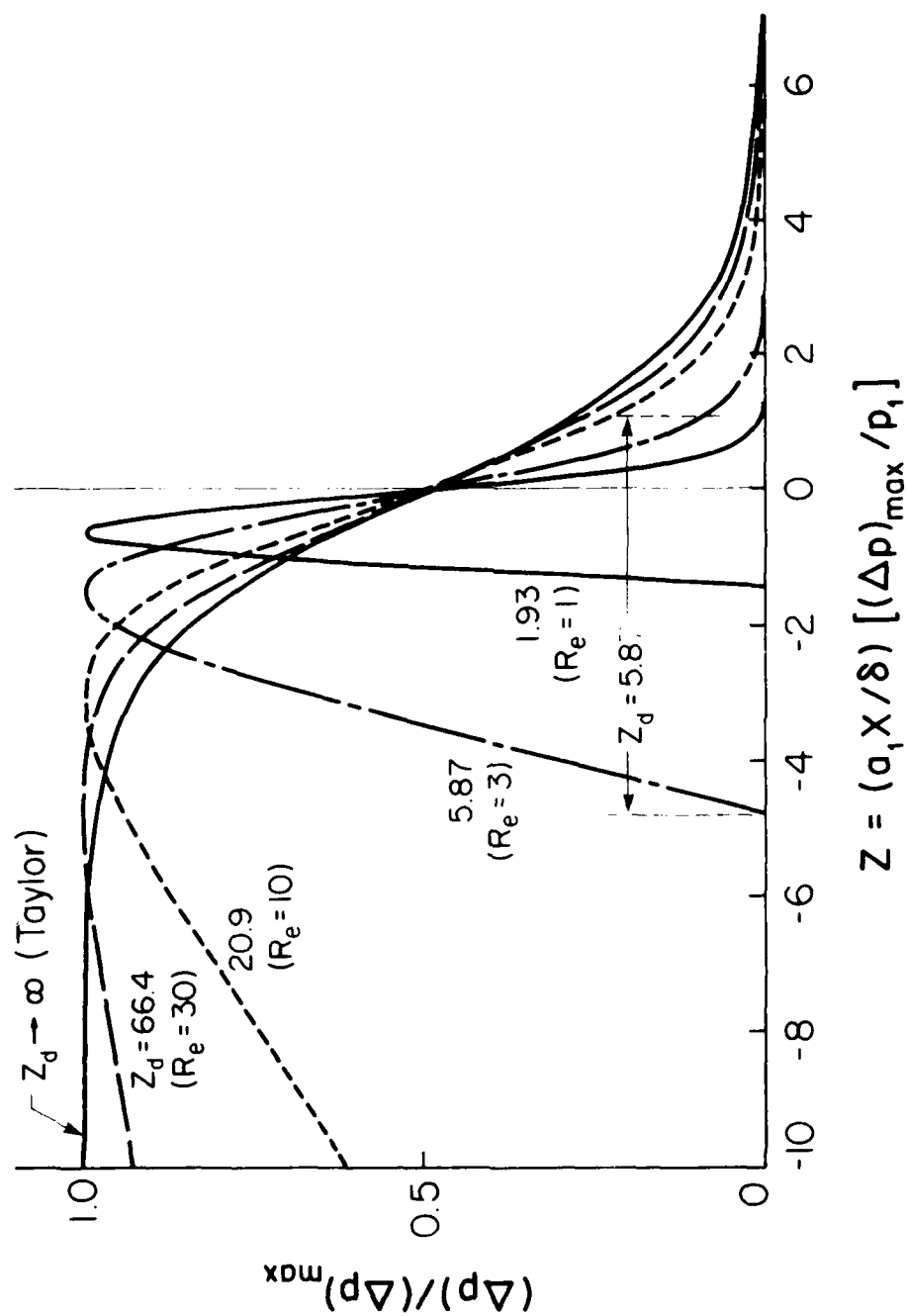


FIG. 3.5 LIGHTHILL N-WAVES IN A PLOT OF THE NORMALIZED OVERPRESSURE $(\Delta p)/(\Delta p)_{\max}$ VS THE DISTANCE PARAMETER Z FOR DURATION PARAMETERS $Z_d = 1, 5.87, 20.9, 66.4, \infty$.

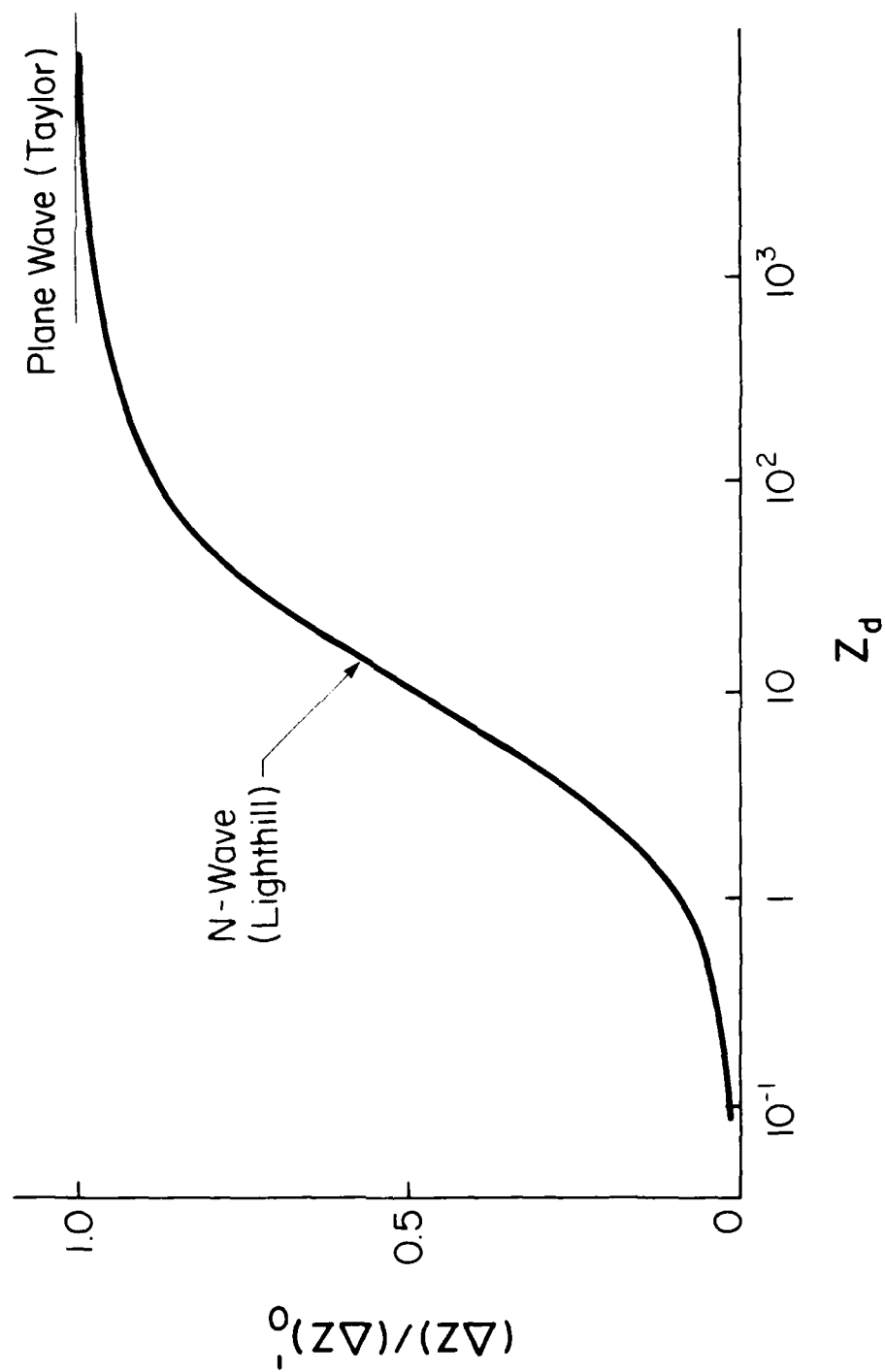


FIG. 5.6 THICKNESS PARAMETER (ΔZ) , NORMALIZED BY TAYLOR THICKNESS PARAMETER $(\Delta Z)_0 = 5.127$, AS A FUNCTION OF DURATION PARAMETER Z_d FOR LIGHT N WAVES.

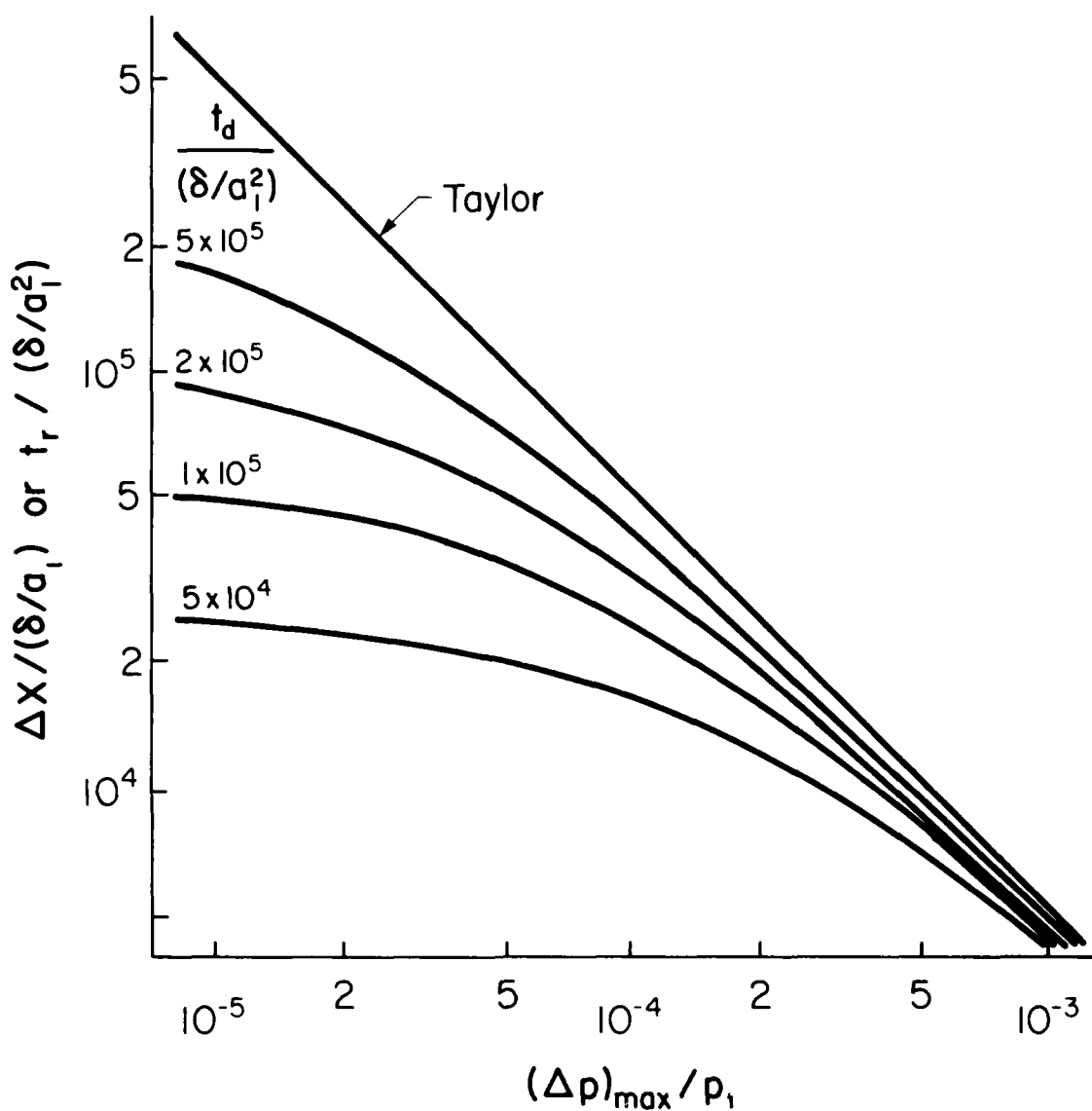


FIG. 3.7 NORMALIZED SHOCK THICKNESS $\Delta X / (\delta / a_1)$ OR NORMALIZED RISE TIME $t_r / (\delta / a_1^2)$ VS NORMALIZED MAXIMUM OVERPRESSURE $(\Delta p)_{\max} / p_1$ FOR NORMALIZED DURATION $t_d / (\delta / a_1^2) = 5 \times 10^5, 2 \times 10^5, 10^5, 5 \times 10^4$ FOR LIGHTHILL N-WAVES.

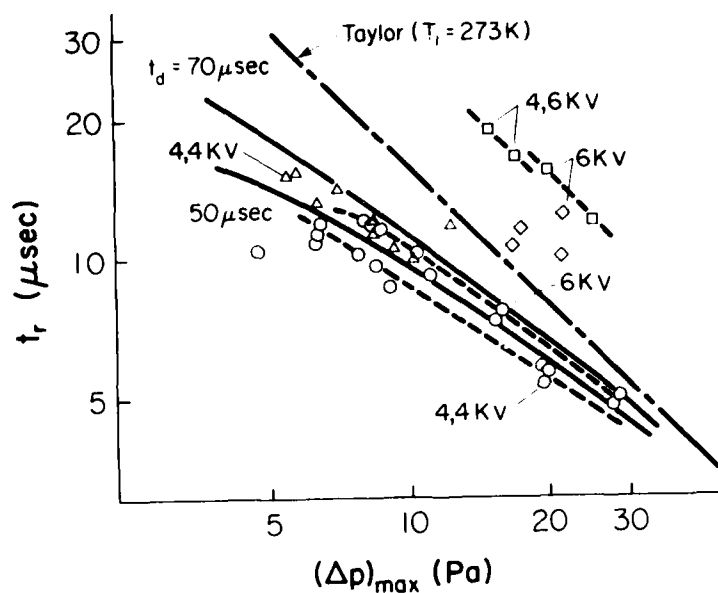


FIG. 5.8. COMPARISON BETWEEN EXPERIMENTAL AND THEORETICAL LIGHTHILL N-WAVE RISE TIMES PLOTTED AGAINST MAXIMUM OVERPRESSURE ($t_d = 70 \mu\text{sec}$, $\mu = 1.8 \text{ sec}$).

SPARK: SERIES I: \circ AND II: Δ .
EXPLODING WIRE: SERIES III: \diamond AND IV: \square .

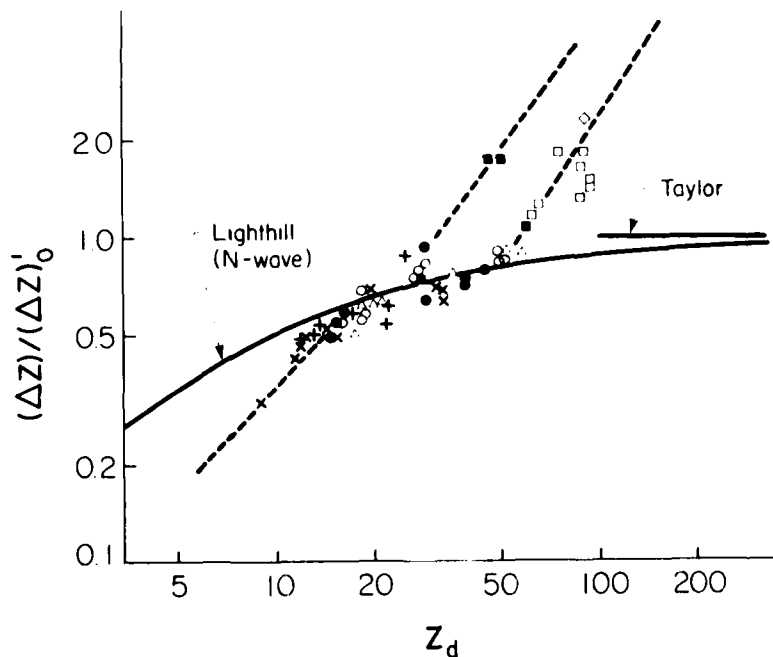
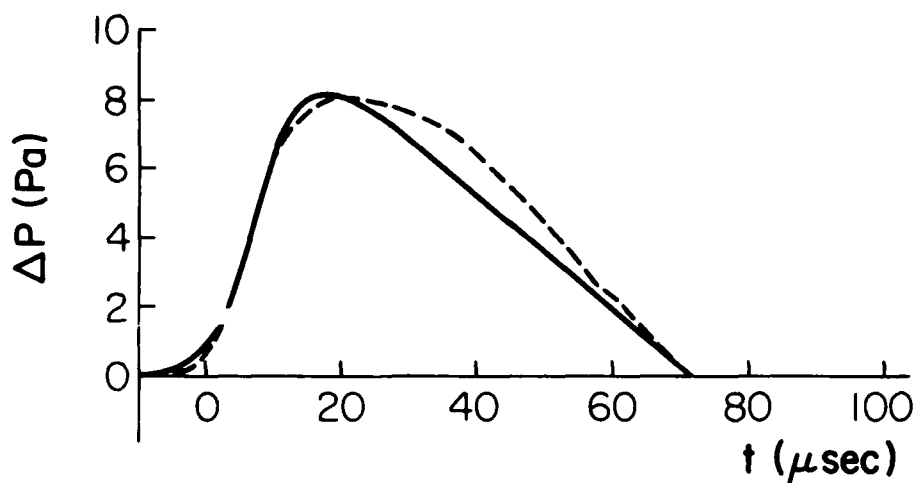
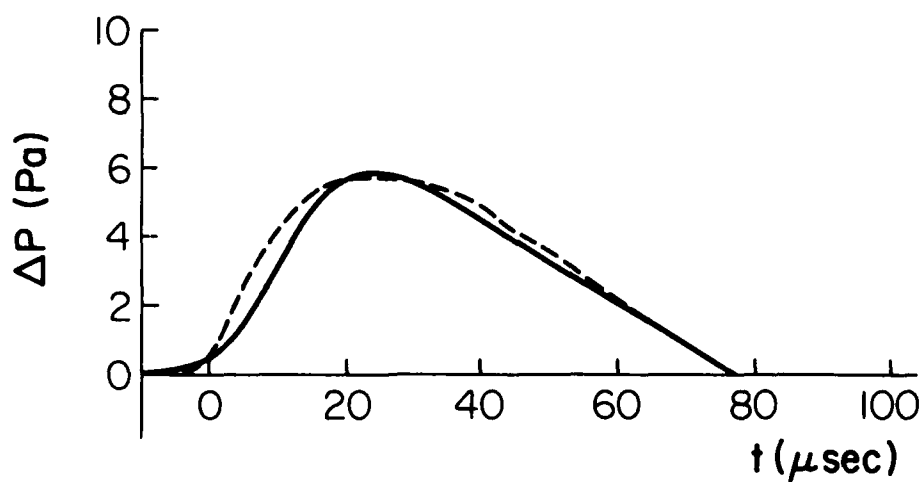


FIG. 5.9. COMPARISON BETWEEN EXPERIMENTAL AND THEORETICAL LIGHTHILL N-WAVE THICKNESS PARAMETERS $(\Delta Z)/(\Delta Z)_0$ NORMALIZED BY TAYLOR THICKNESS PARAMETER $(\Delta Z)_0 = 1.77$, PLOTTED AGAINST DURATION PARAMETER Z_d .

SPARK: \bullet 4.4 kV, \circ 4.6 kV, Δ 6 kV.
EXPLODING WIRE: \blacksquare 4.6 kV, \square 6 kV, \diamond 7 kV.

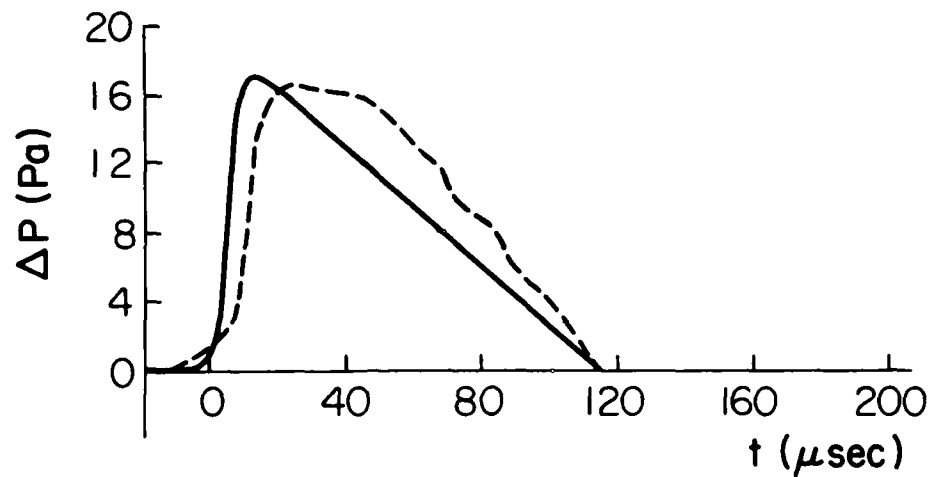


(a) SERIES I - SPARK DATA
 Lighthill: $(\Delta p)_{\text{max}} = 8.52 \text{ Pa}$, $t_r = 12 \mu\text{s}$, $t_d = 72 \mu\text{s}$.
 SERIES I: $r = 21.6\text{m}$, $(\Delta p)_{\text{max}} = 8.52 \text{ Pa}$, $t_r = 11.4 \mu\text{s}$, $t_d = 72 \mu\text{s}$.



(b) SERIES II - SPARK DATA
 Lighthill: $(\Delta p)_{\text{max}} = 5.83 \text{ Pa}$, $t_r = 16.7 \mu\text{s}$, $t_d = 76.8 \mu\text{s}$.
 SERIES II: $r = 19.0\text{m}$, $(\Delta p)_{\text{max}} = 5.83 \text{ Pa}$, $t_r = 15.5 \mu\text{s}$, $t_d = 76.8 \mu\text{s}$.

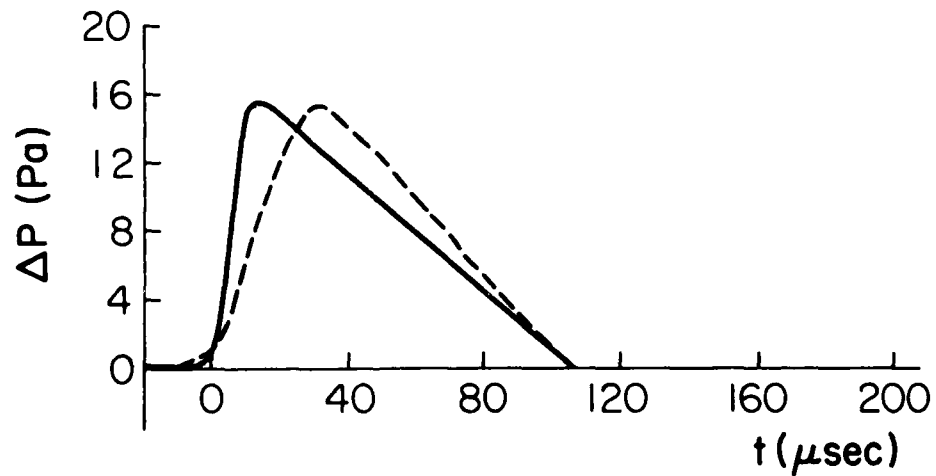
FIG. 3.10 COMPARISON BETWEEN EXPERIMENTAL ---- AND THEORETICAL — (Lighthill) PRESSURE PROFILES OF N-WAVES.



(c) SERIES III - EXPLODING-WIRE DATA

LIGHTHILL: $(\Delta p)_{\max} = 17.0 \text{ Pa}$, $t_r = 7.97 \text{ } \mu\text{s}$, $t_d = 113.6 \text{ } \mu\text{s}$.

SERIES III: $r = 27.6\text{m}$, $(\Delta p)_{\max} = 17.0 \text{ Pa}$, $t_r = 10.5 \text{ } \mu\text{s}$, $t_d = 113.6 \text{ } \mu\text{s}$



(d) SERIES IV - EXPLODING-WIRE DATA

LIGHTHILL: $(\Delta p)_{\max} = 15.3 \text{ Pa}$, $t_r = 8.68 \text{ } \mu\text{s}$, $t_d = 105.3 \text{ } \mu\text{s}$.

SERIES IV: $r = 29.3\text{m}$, $(\Delta p)_{\max} = 15.3 \text{ Pa}$, $t_r = 18.7 \text{ } \mu\text{s}$, $t_d = 105.3 \text{ } \mu\text{s}$.

FIG. 3.10 - CONTINUED

COMPARISON BETWEEN EXPERIMENTAL --- AND THEORETICAL ———
(LIGHTHILL) PRESSURE PROFILES OF N-WAVES.

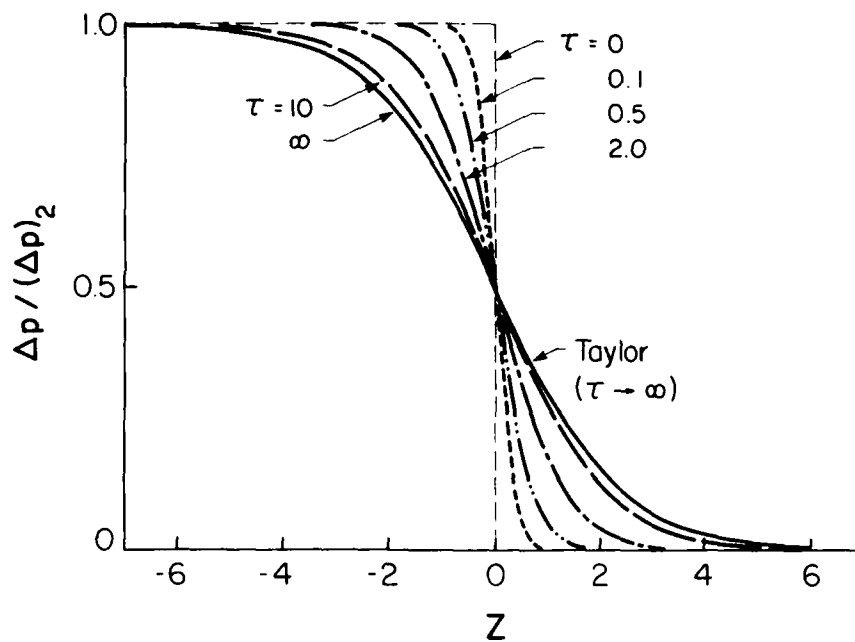


FIG. 3.11 PRESSURE PROFILES $(\Delta p) / (\Delta p)_2$ VS DISTANCE PARAMETER Z FOR VARIOUS TIME PARAMETERS $\tau = 0, 0.1, 0.5, 2.0, 10, \infty$, FOR LIGHTHILL NONSTATIONARY VISCOUS PLANE WAVES.

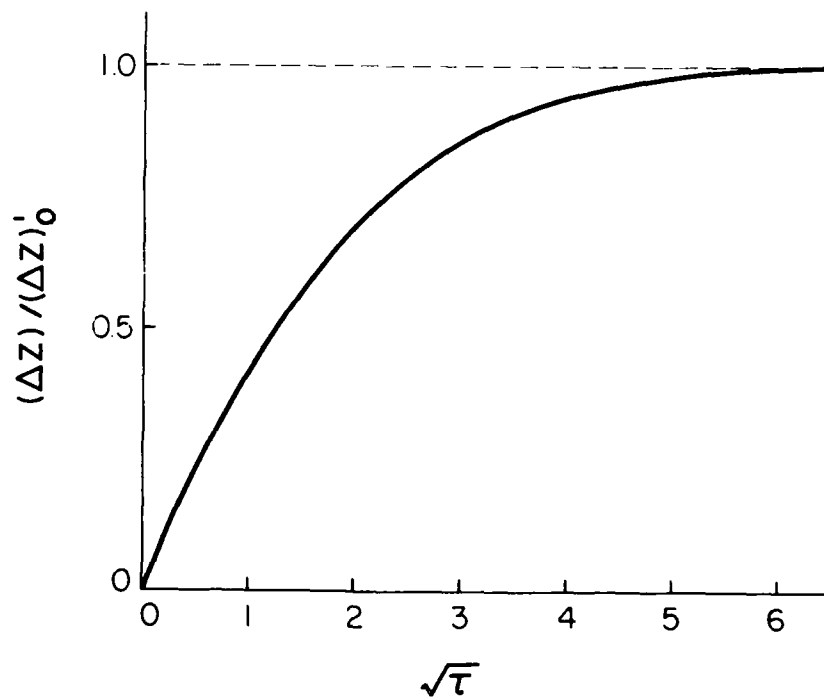


FIG. 3.12 RATIO OF THICKNESS PARAMETER $(\Delta Z) / (\Delta Z)_0^{1/2}$ PLOTTED AGAINST SQUARE ROOT OF TIME PARAMETER $\sqrt{\tau}$ FOR LIGHTHILL NONSTATIONARY VISCOUS PLANE WAVES.

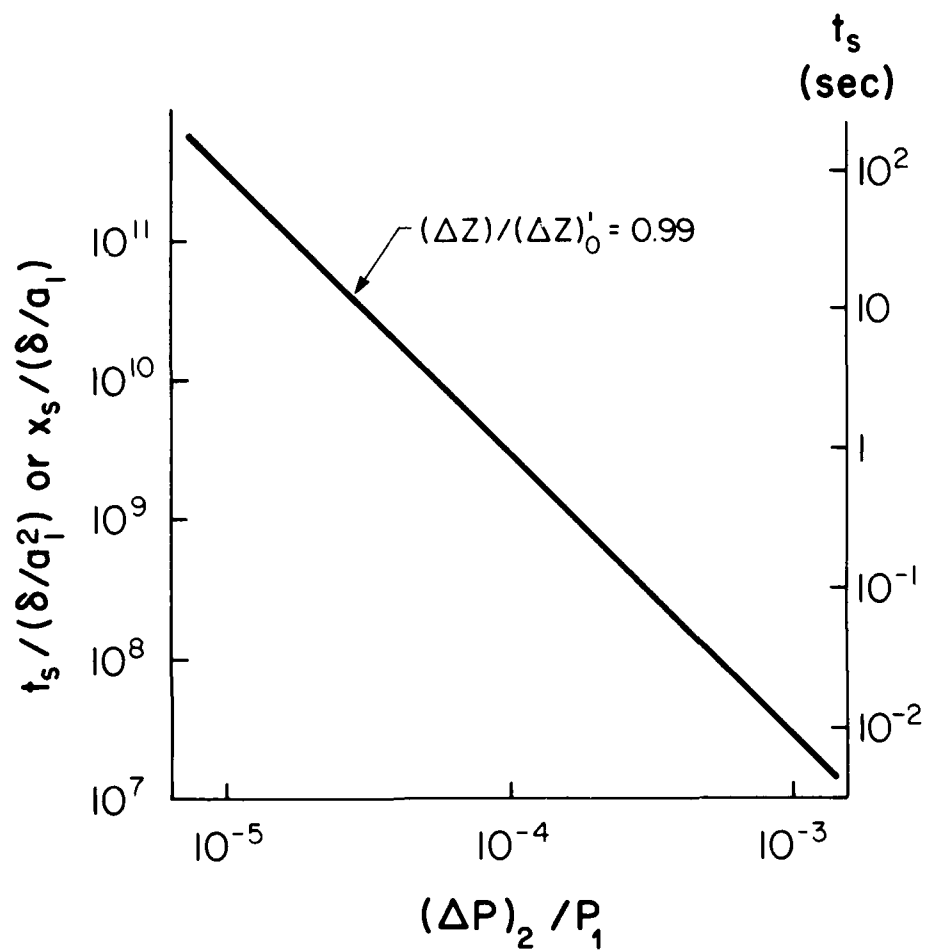
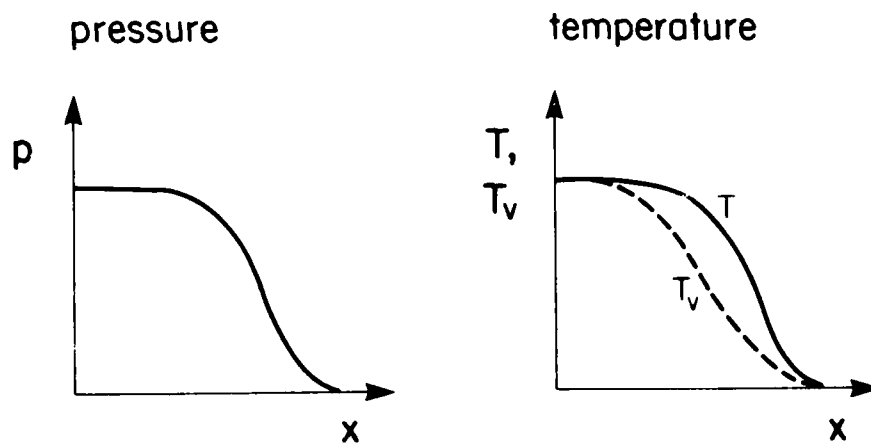
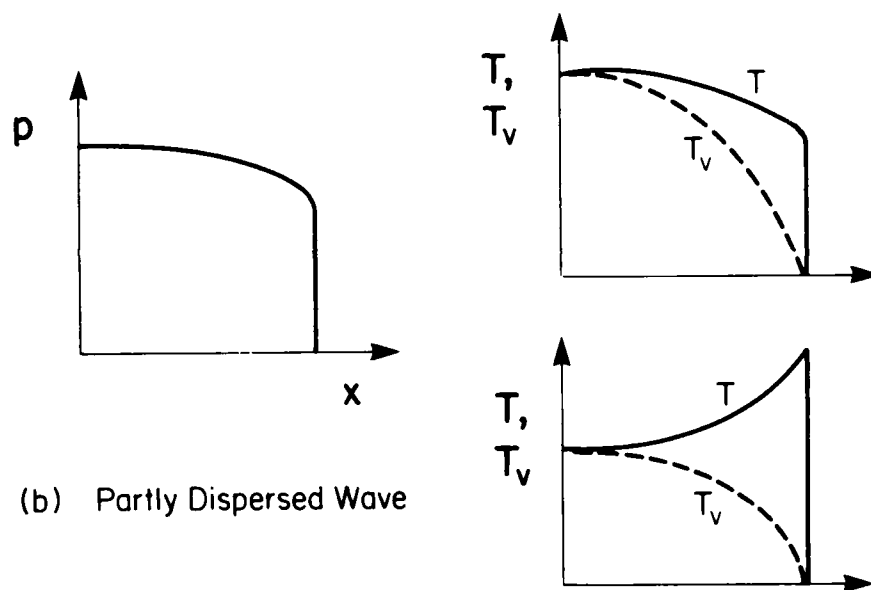


FIG. 3.13 NORMALIZED SHOCK-THICKENING TIME $t_s/(\delta/a_1^2)$ OR DISTANCE $x_s/(\delta/a_1)$ PLOTTED AGAINST SHOCK STRENGTH $(\Delta p)_2/p_1$ FOR NONSTATIONARY VISCOUS PLANE WAVES.



(a) Fully Dispersed Wave



(b) Partly Dispersed Wave

FIG. 5.14 PRESSURE p , AND TEMPERATURE (TRANSLATION + ROTATION T , AND VIBRATION T_v) PROFILES OF SHOCK TRANSITIONS WITH VIBRATIONAL EXCITATION FOR FULLY AND PARTLY DISPERSED WAVES.

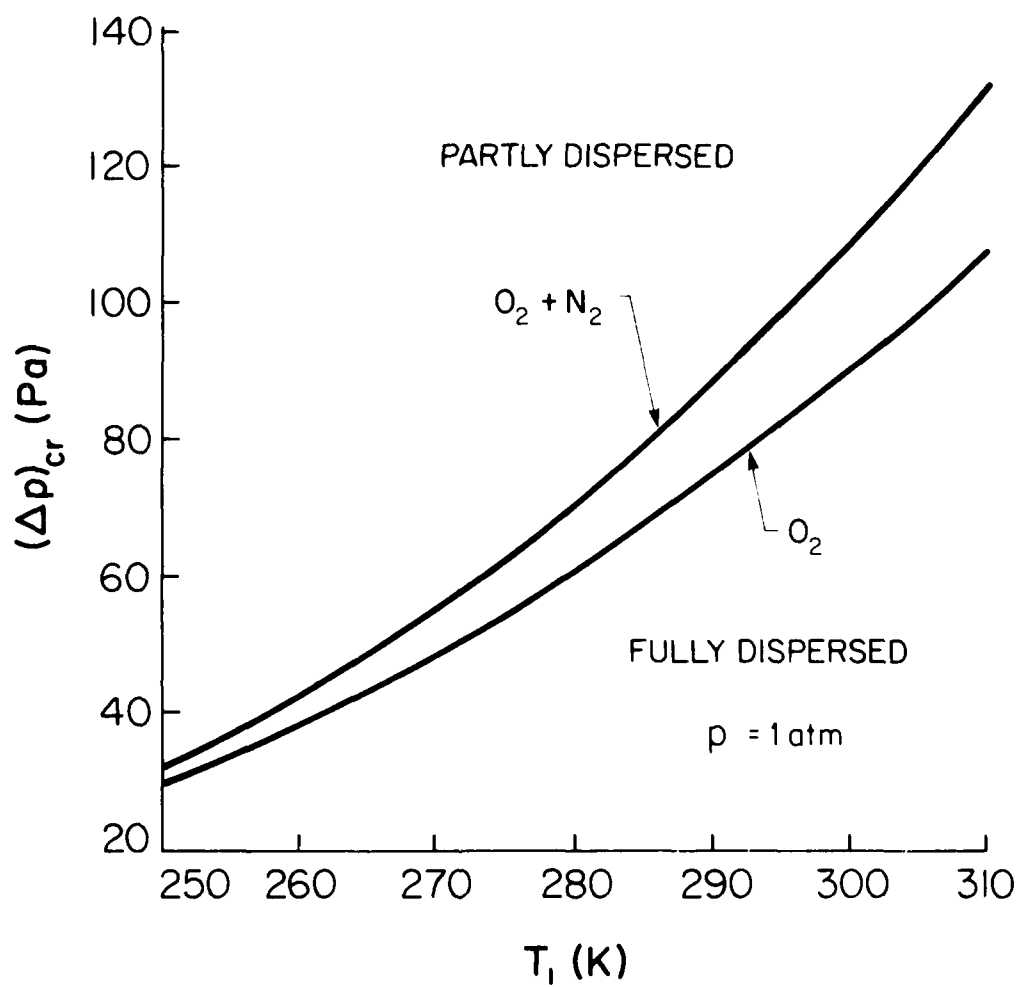


FIG. 5.15 CRITICAL OVERPRESSURE $(p)_{cr,0}$ AND $(p)_{cr,0+N}$ AS FUNCTIONS OF INITIAL TEMPERATURE T_1 FOR AIR.

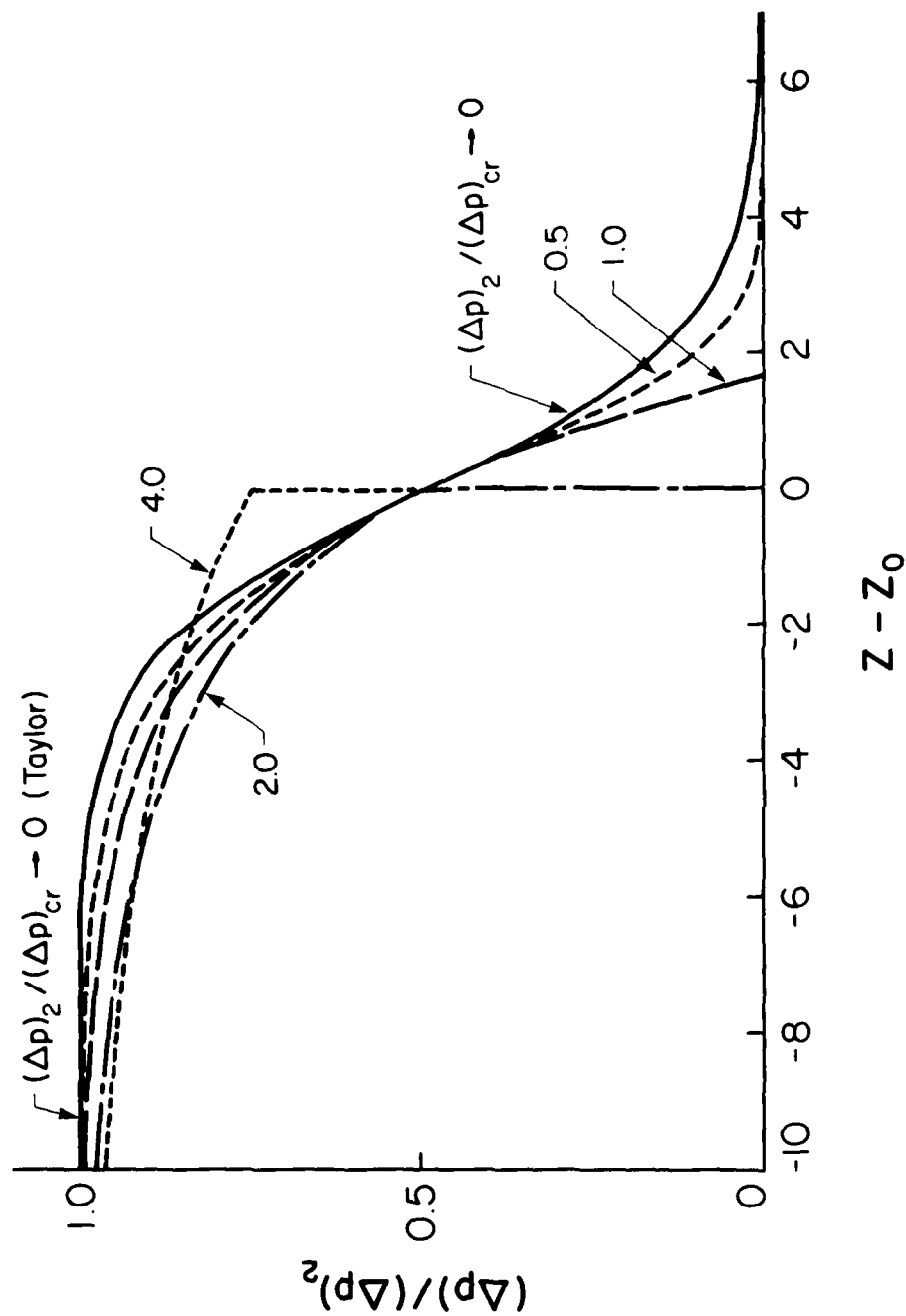


FIG. 3.16 PRESSURE PROFILES OF DISPERSED WAVES USING NORMALIZED OVERPRESSURE $(\Delta p)/(\Delta p)_2$ VS DISTANCE PARAMETER $Z - Z_0$ FOR OVERPRESSURE RATIOS $(\Delta p)/(\Delta p)_{cr,j} = 0, 0.5, 1.0, 2.0, 4.0$.

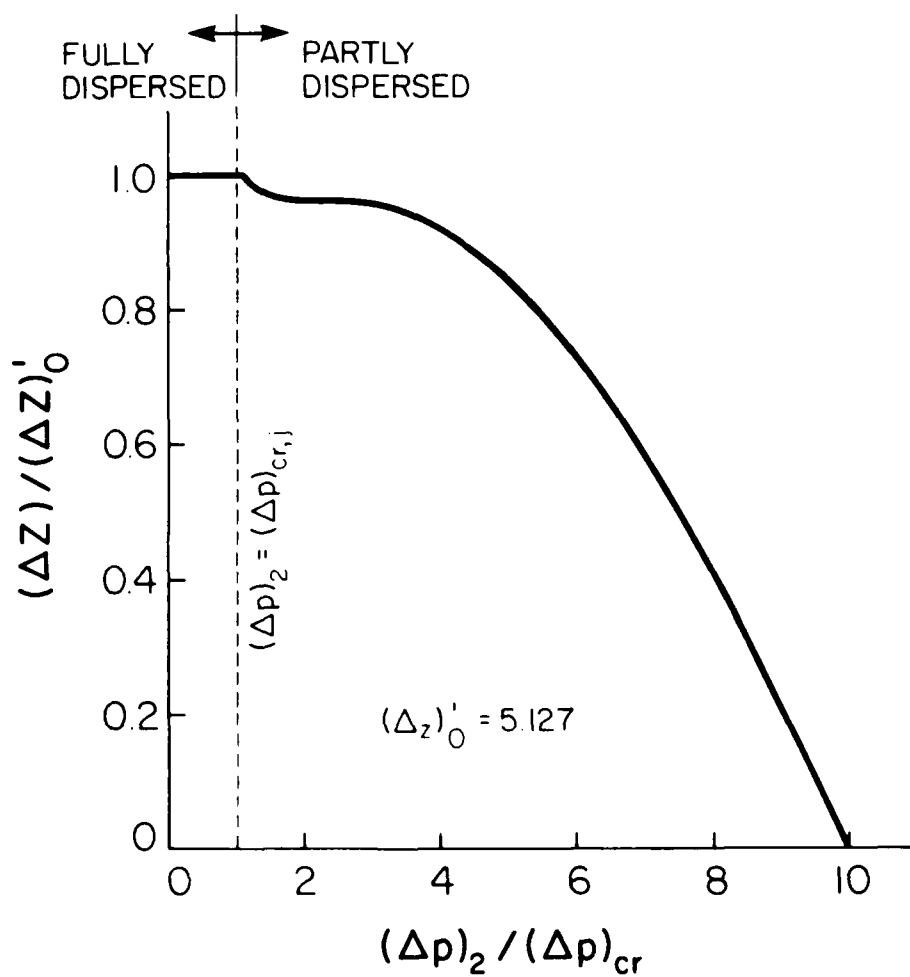


FIG. 5.17 THICKNESS PARAMETER (Δz) , NORMALIZED BY TAYLOR-THICKNESS PARAMETER $(\Delta z)_0' = 5.127$, AS A FUNCTION OF OVERPRESSURE RATIO $(\Delta p)_2 / (\Delta p)_{cr,j}$ FOR FULLY AND PARTLY-DISPERSED WAVES.

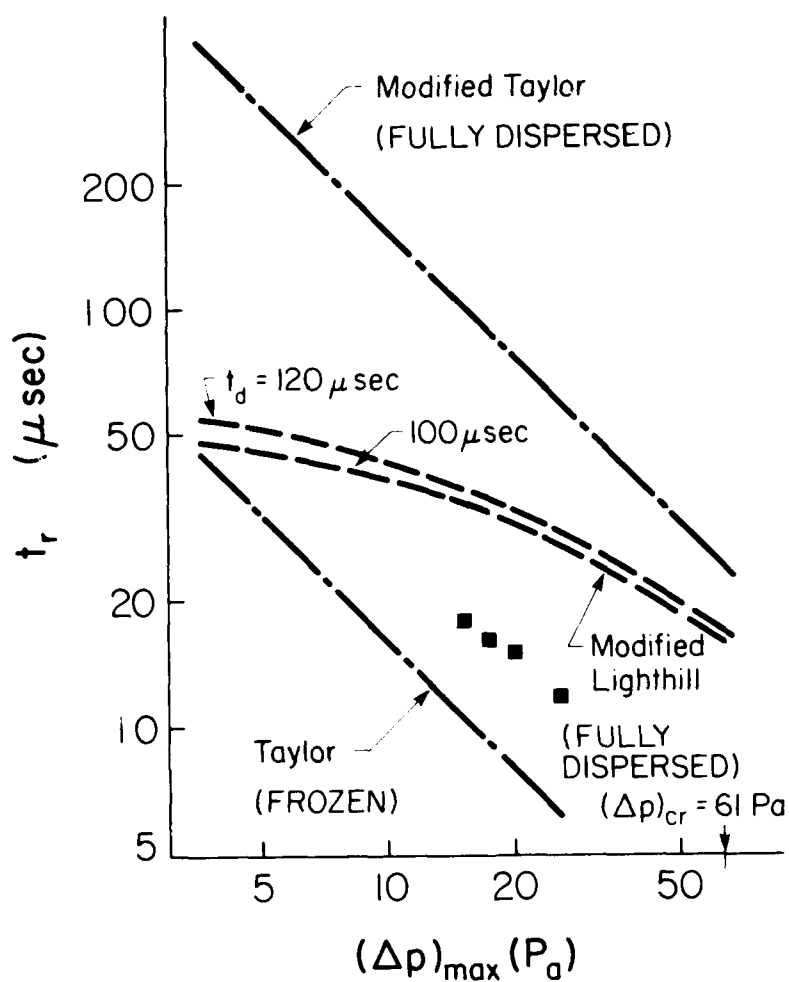
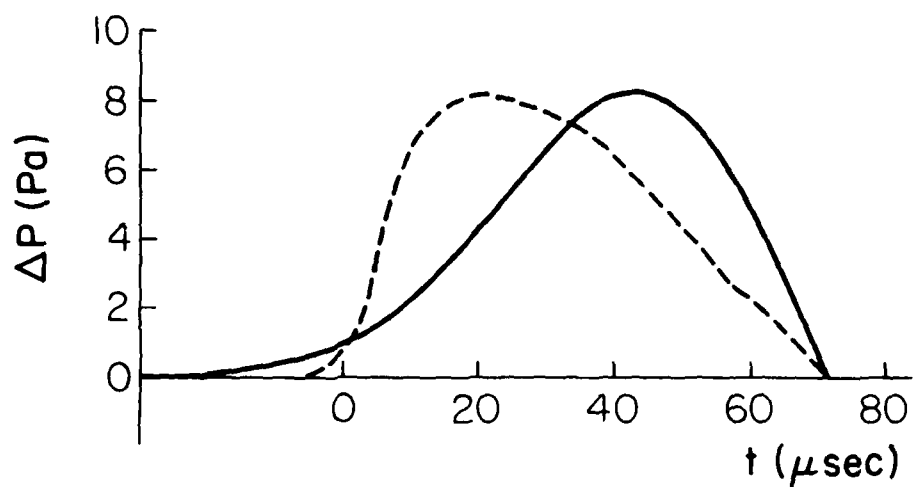


FIG. 3.18 COMPARISON BETWEEN EXPERIMENTAL (SERIES IV), EW ■ AND THEORETICAL (TAYLOR, MODIFIED TAYLOR, MODIFIED LIGHTHILL N-WAVES) RISE TIMES t_r PLOTTED AGAINST MAXIMUM OVERPRESSURE $(\Delta p)_{\text{max}}$. $T_1 \approx 280 \text{ K}$, $\text{RH} = 87.5\%$, $\tau_0 = 5.75 \text{ μsec}$.

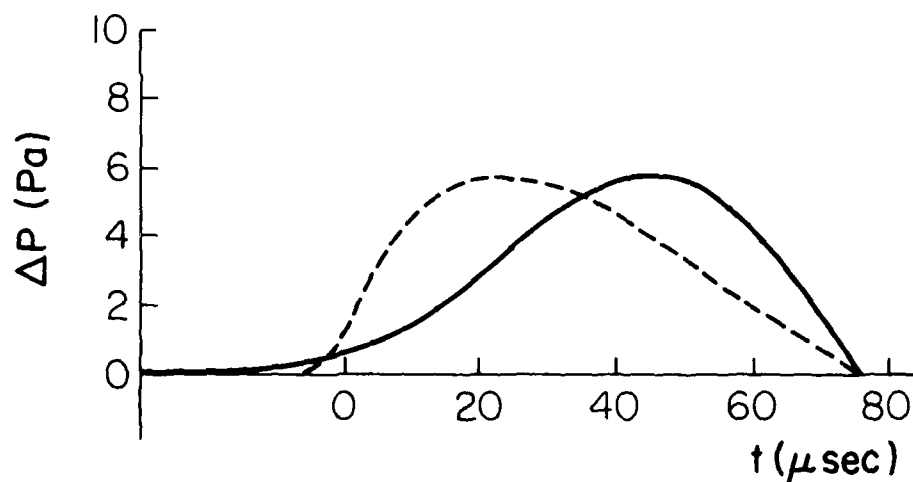


(a) Series-I: Spark data

(a) SERIES I: SPARK DATA

MODIFIED LIGHTHILL: $(\Delta p)_{\max} = 8.52 \text{ Pa}$, $t_r = 34.6 \mu\text{s}$, $t_d = 72 \mu\text{s}$.

SERIES I: $r = 21.6\text{m}$, $(\Delta p)_{\max} = 8.26 \text{ Pa}$, $t_r = 41.4 \mu\text{s}$, $t_d = 72 \mu\text{s}$.



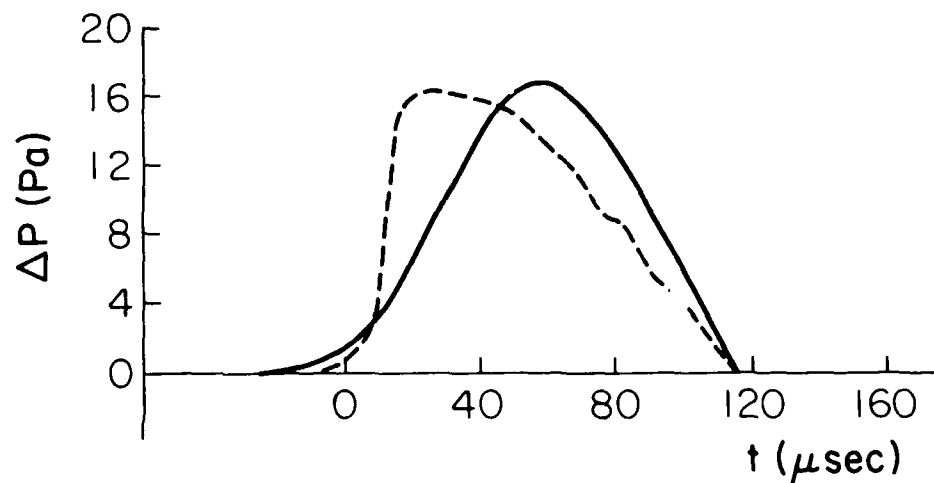
(b) Series-II: Spark data

(b) SERIES II: SPARK DATA

MODIFIED LIGHTHILL: $(\Delta p)_{\max} = 5.85 \text{ Pa}$, $t_r = 36.1 \mu\text{s}$, $t_d = 76.8 \mu\text{s}$.

SERIES II: $r = 19\text{m}$, $(\Delta p)_{\max} = 5.85 \text{ Pa}$, $t_r = 45.5 \mu\text{s}$, $t_d = 76.8 \mu\text{s}$.

FIG. 3.19 COMPARISON BETWEEN EXPERIMENTAL AND THEORETICAL (MODIFIED LIGHTHILL) PRESSURE PROFILES OF N-WAVES.

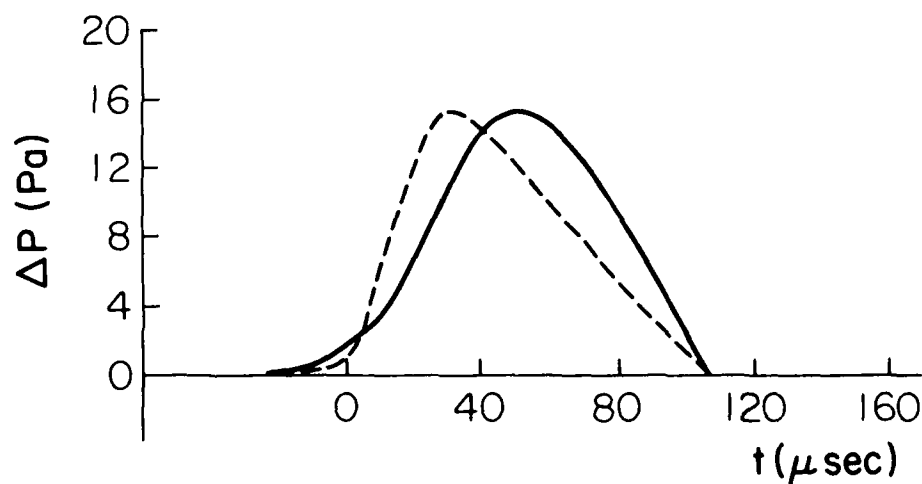


(c) Series - III : Exploding - wire data

(c) SERIES III: EXPLODING-WIRE DATA

MODIFIED LIGHTHILL: $(\Delta p)_{\text{max}} = 17 \text{ Pa}$, $t_r = 42.8 \mu\text{s}$, $t_d = 115.6 \mu\text{s}$.

SERIES III: $r = 27.6\text{m}$, $(\Delta p)_{\text{max}} = 17 \text{ Pa}$, $t_r = 10.5 \mu\text{s}$, $t_d = 115.6 \mu\text{s}$.



(d) Series - IV : Exploding - wire data

(d) SERIES IV: EXPLODING-WIRE DATA

MODIFIED LIGHTHILL: $(\Delta p)_{\text{max}} = 15.3 \text{ Pa}$, $t_r = 37.4 \mu\text{s}$, $t_d = 105.3 \mu\text{s}$.

SERIES IV: $r = 29.3\text{m}$, $(\Delta p)_{\text{max}} = 17 \text{ Pa}$, $t_r = 18.7 \mu\text{s}$, $t_d = 105.3 \mu\text{s}$.

FIG. 3.19 - CONTINUED - COMPARISON BETWEEN EXPERIMENTAL AND THEORETICAL (MODIFIED LIGHTHILL) PRESSURE PROFILES OF N-WAVES.

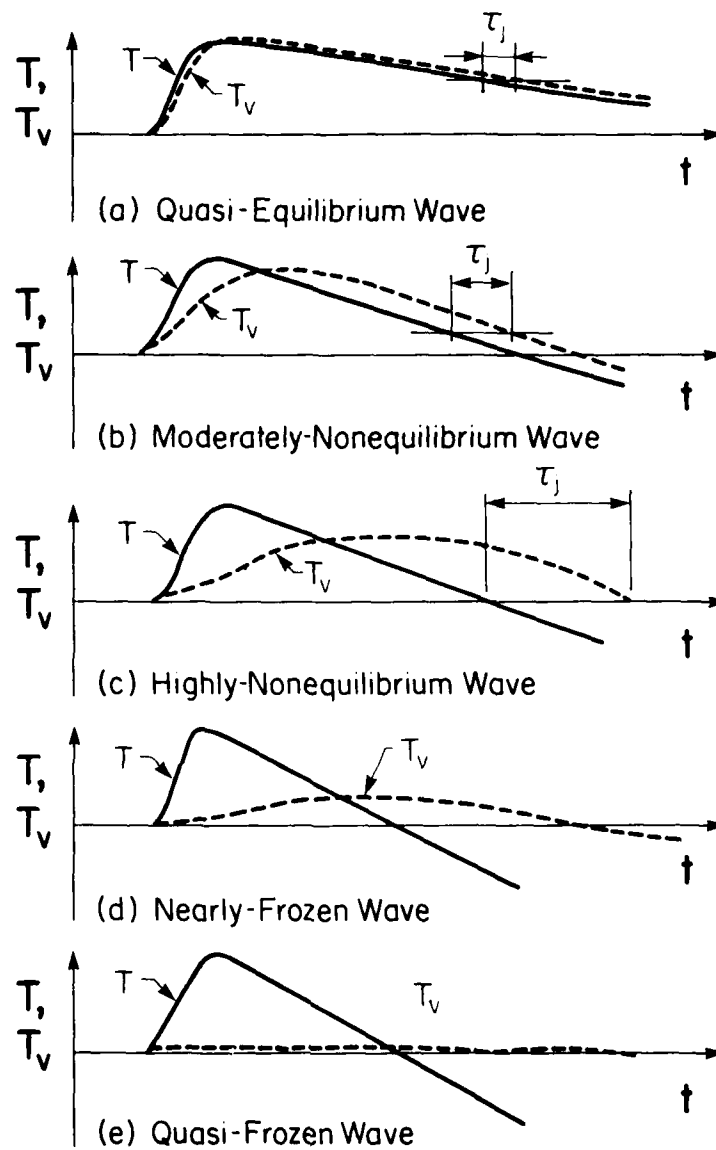


FIG. 3.20 CLASSIFICATION OF N-WAVES ACCORDING TO THE DEGREE OF NONEQUILIBRIUM.

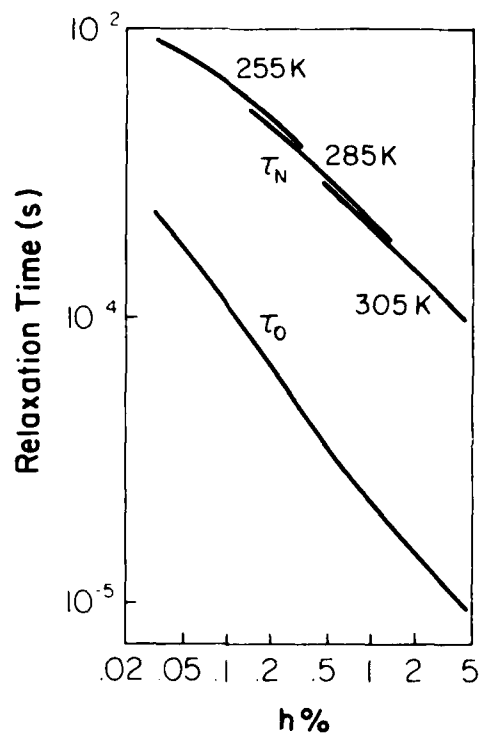


FIG. 4.1 RELAXATION TIMES OF OXYGEN AND NITROGEN IN ATMOSPHERIC AIR IN THE RELATIVE HUMIDITY RANGE 10% < RH < 100% (REF. 12).

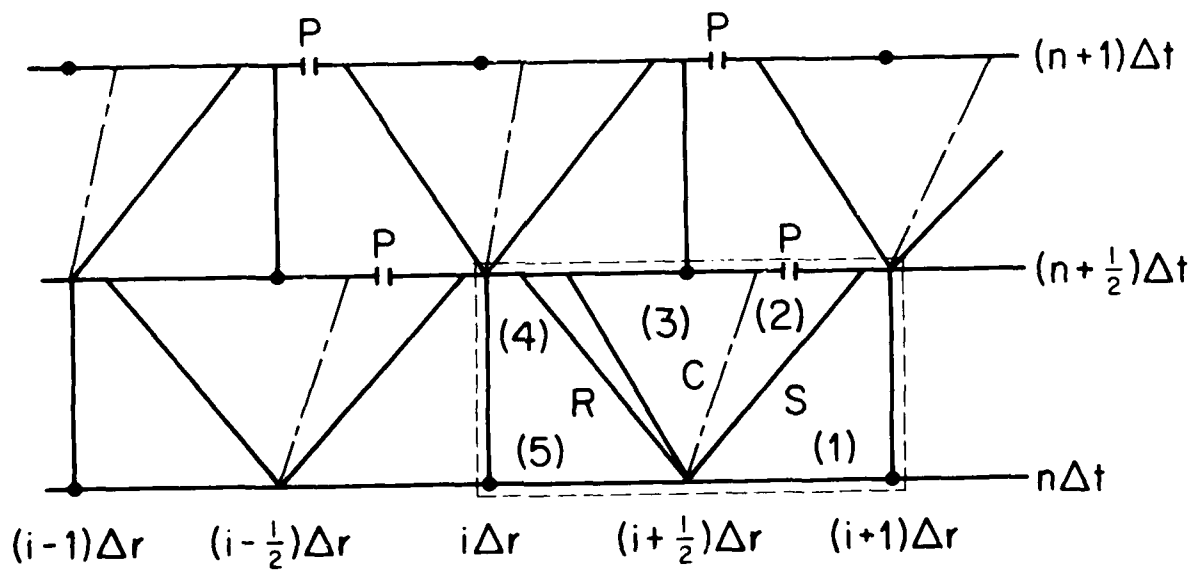


FIG. 4.2 ILLUSTRATION OF RANDOM CHOICE METHOD.
S - SHOCK WAVE; C - CONTACT SURFACE, R - RAREFACTION WAVE.

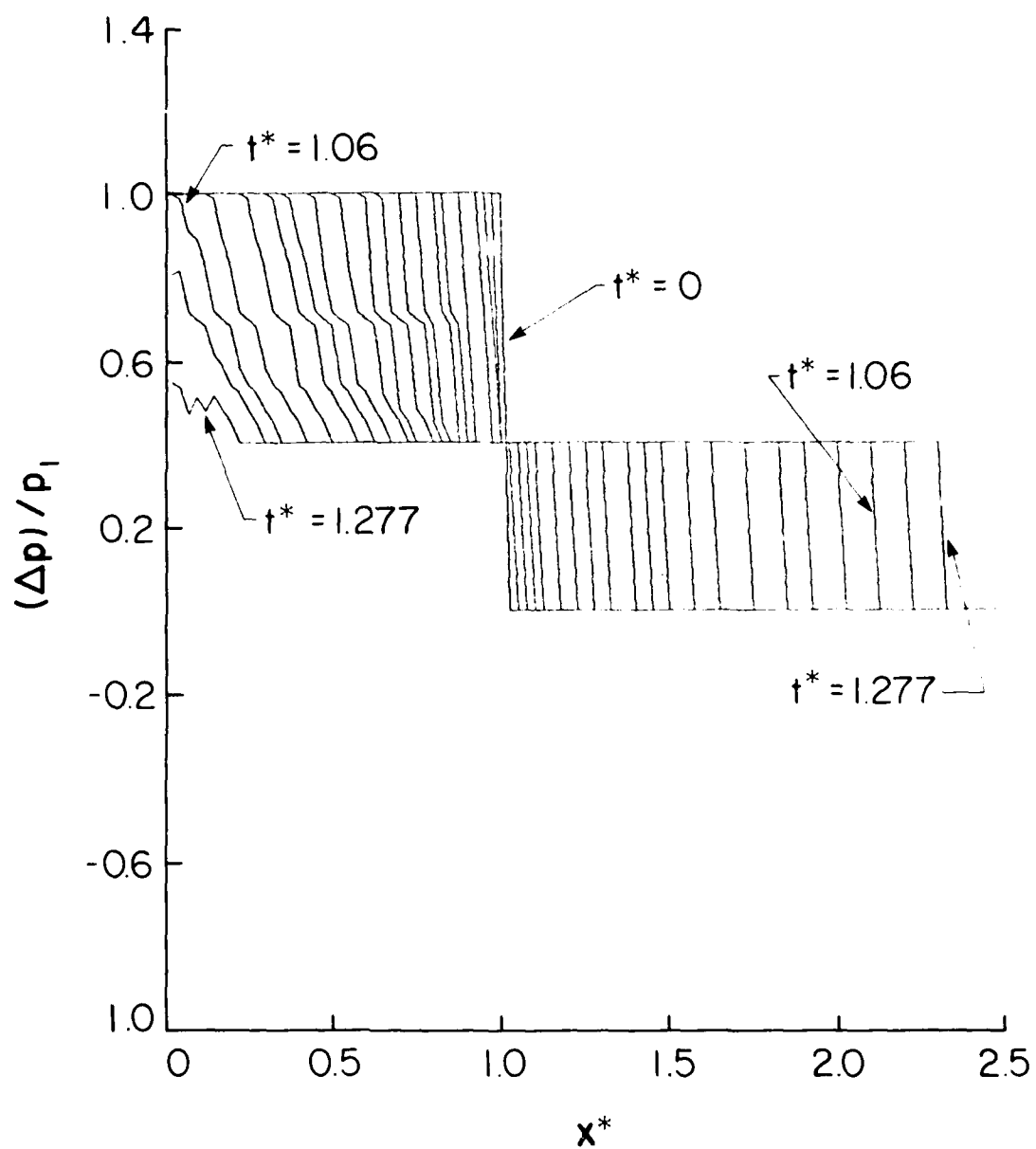


FIG. 4.3 SHOCK-TUBE PROBLEM USING RANDOM-CHOICE METHOD FOR A PERFECT-INVISCID FLOW ($P_{41} = 2.0$, $T_{41} = 1.0$, $\Delta x^* = 1/40$).

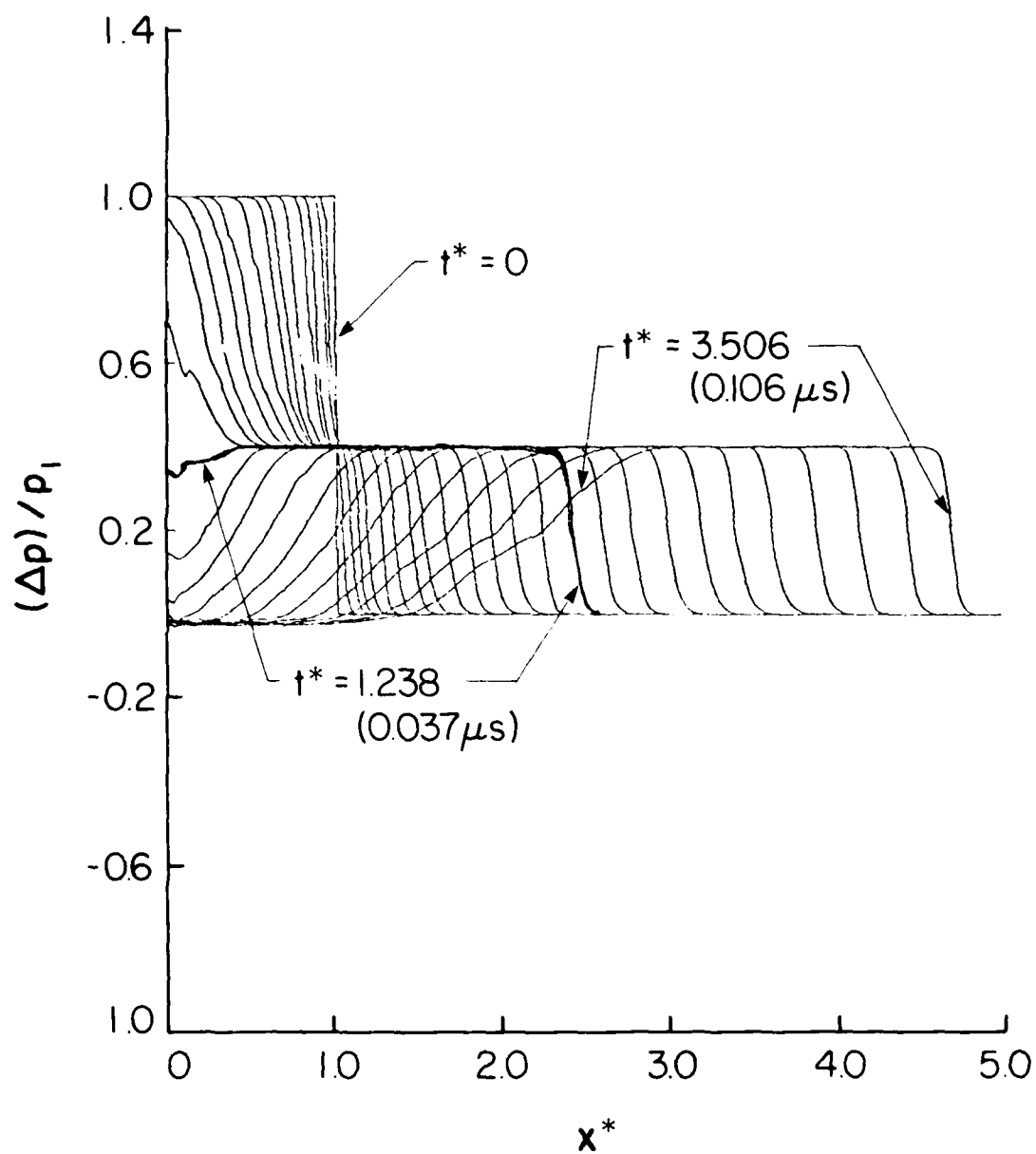


FIG. 4.4 SHOCK-TUBE PROBLEM USING RANDOM-CHOICE METHOD FOR A PERFECT-VISCOUS FLOW ($P_{41} = 2.0$, $T_{41} = 1.0$, $\Delta x^* = 1/40$, $x_0 = 0.001$ cm).

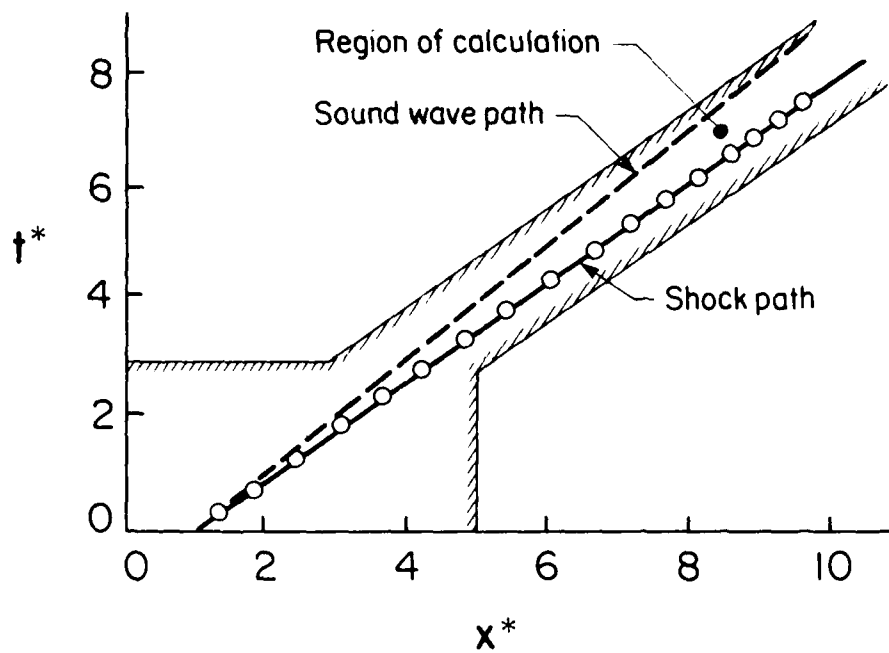
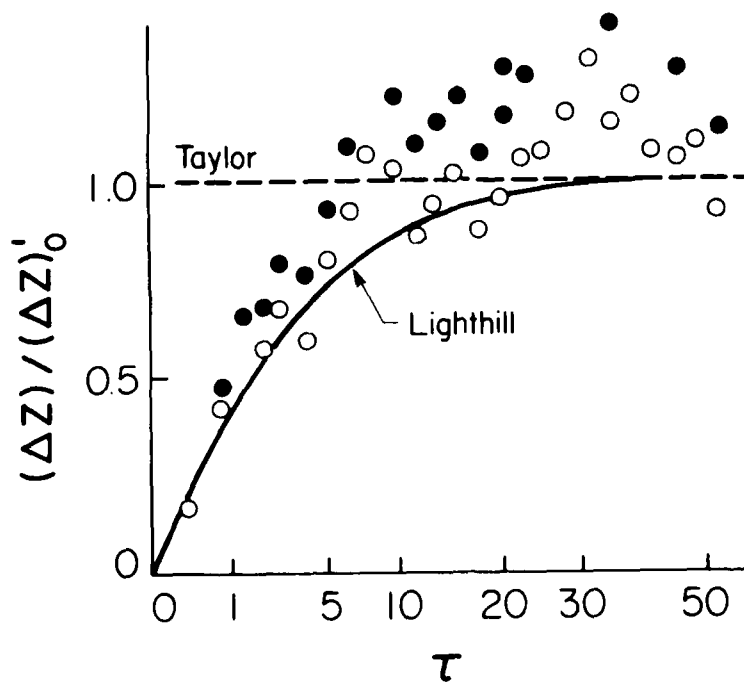
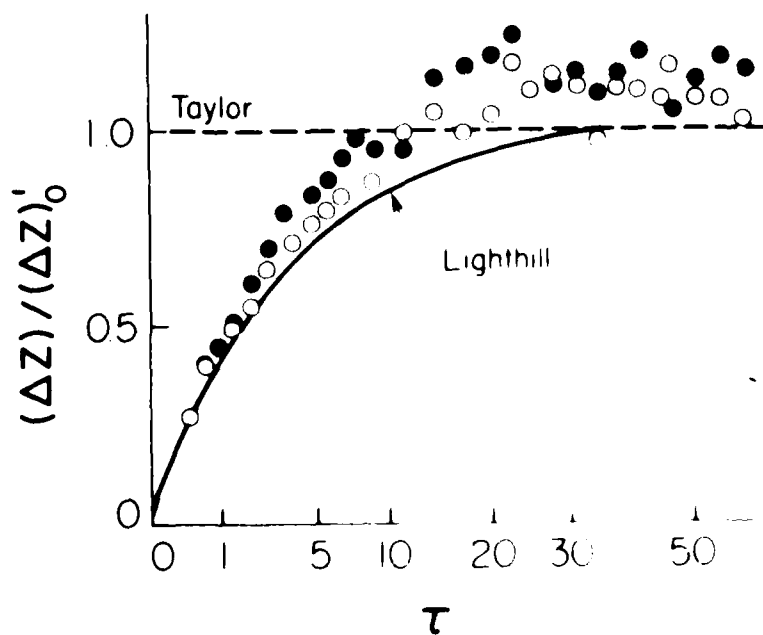


FIG. 4.5 REGION OF CALCULATION AND SHOCK-FRONT PATH.
 O - RANDOM-CHOICE METHOD ($\Delta x \approx 1.25 \times 10^{-5}$ cm),
 —, ——— ANALYTICAL.

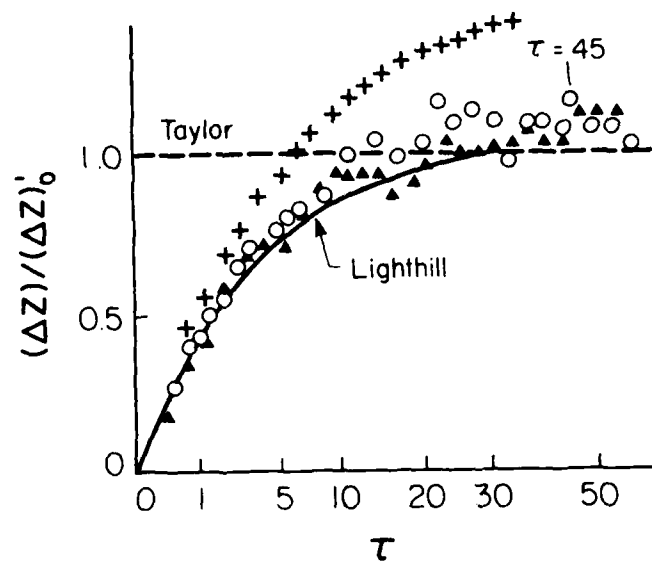


(a) EFFECT OF MULTIPLE TIME STEPS
 $(x^* = 1.40; x = 2.5 \times 10^{-5} \text{ cm})$
 \circ $k = 10$, \bullet $k = 1$



(b) EFFECT OF RANDOM NUMBER
 $(x^* = 1.80; x = 1.1 \times 10^{-5} \text{ cm})$
 \circ LCRS (LINEAR CONGRUENTIAL SEQUENCE)
 \bullet MERS (MAXIMUM LENGTH LINEARLY RECURRING SEQUENCE)

FIG. 4.6 TRANSIENT BEHAVIOUR OF SHOCK THICKNESS FOR SHOCK-TUBE PROBLEM USING RCM FOR A PERFECT VISCOUS FLOW ($P_{41} = 2.0$, $T_{41} = 1.0$, $T_1 = 275 \text{ K}$, $p_1 = 101.5 \text{ kPa}$).



(c) COMPARISON BETWEEN RCM AND MEM (MacCORMACK'S FINITE-DIFFERENCE METHOD)

+ $\Delta x = 1.25 \times 10^{-5}$ cm (MacCORMACK)

○ $\Delta x = 1.25 \times 10^{-5}$ cm, ▲ $\Delta x = 0.75 \times 10^{-5}$ cm (RANDOM-CHOICE)

FIG. 4.6 - CONTINUED - TRANSIENT BEHAVIOUR OF SHOCK THICKNESS FOR SHOCK-TUBE PROBLEM USING RCM FOR A PERFECT-VISCOUS FLOW
($P_{41} = 2.0$, $T_{41} = 1.0$, $T_1 = 273$ K, $p_1 = 101.5$ kPa).

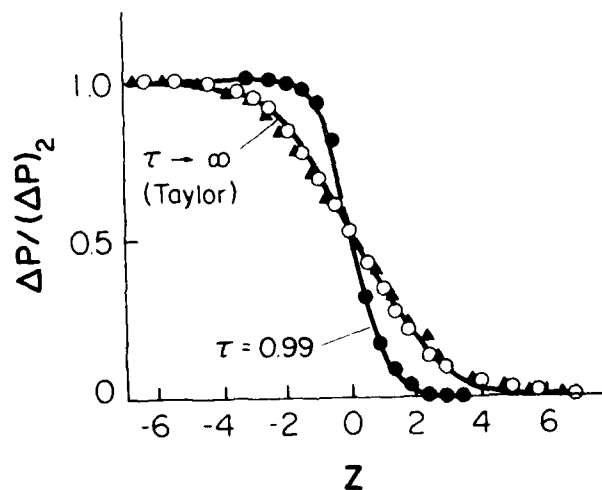


FIG. 4.7 TRANSIENT SHOCK PRESSURE PROFILES FOR SHOCK-TUBE PROBLEM USING RCM FOR A PERFECT-VISCOUS FLOW. ($P_{41} = 2.0$, $T_{41} = 1.0$, $T_1 = 273$ K, $p_1 = 101.5$ kPa, $\Delta x = 1.25 \times 10^{-5}$ cm).

—— LIGHTHILL, ● $\tau = 0.99$, ▲ $\tau = 45.0$, ○ $\tau = 58.3$.

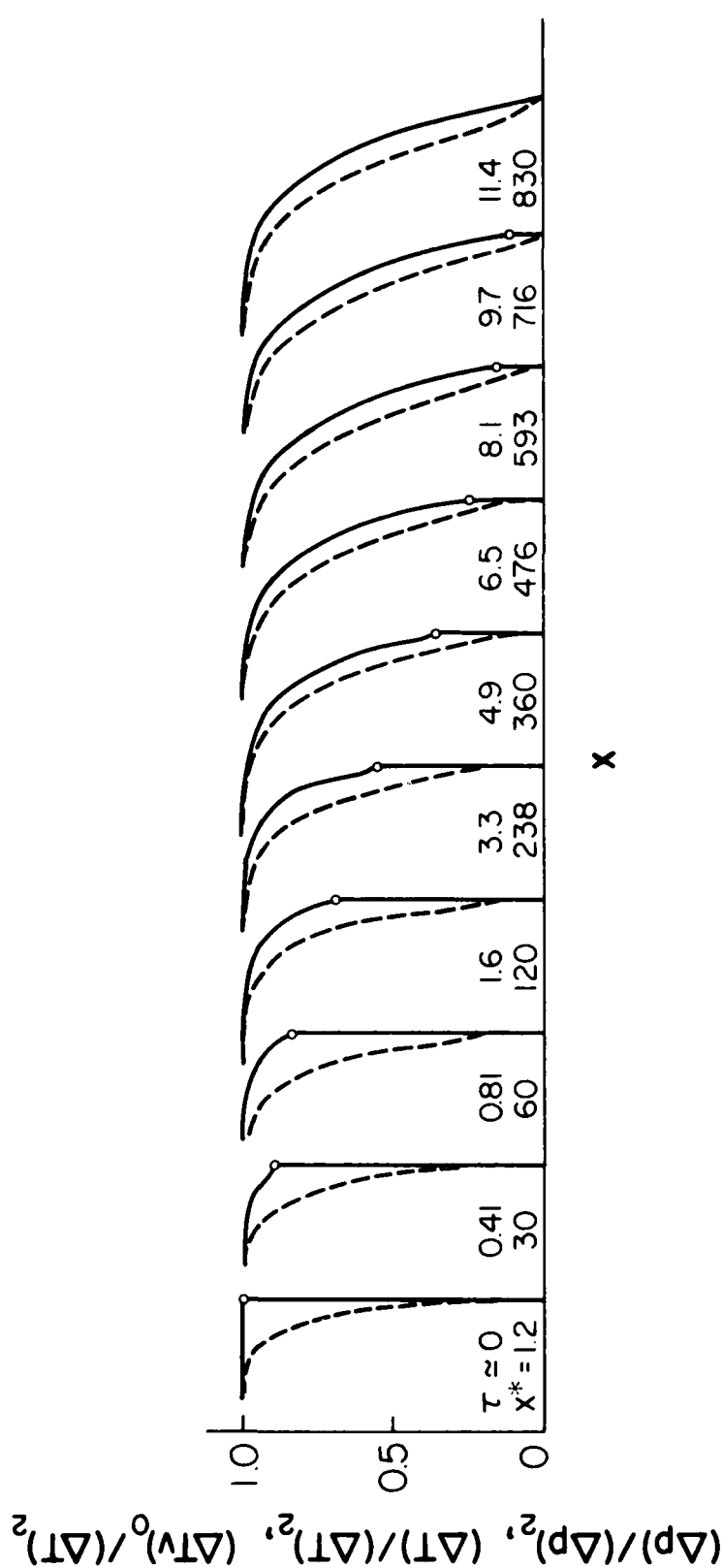


FIG. 4.8 TRANSIENT SHOCK PRESSURE AND TEMPERATURE PROFILES FOR SHOCK-TUBE PROBLEM USING RCM FOR A REAL-INVISCID FLGW [p₄₁ = 1.0018, T₄₁ = 1.0, p₁ = 101.5 kPa, T₁ = 303.15 K, RH = 90%, M₀ = 1.0004, (Δp)₂ = 91.1 Pa, (ΔT)₂ = 0.0777 K, τ₀ = 1.04 μsec, x₀ = 0.5 cm, x = 0.0125 cm].

— (p)/(p)₂ or (T)/(T)₂, ---- (T_v)₀/(T)₂,
o FROZEN SHOCK FRONT.

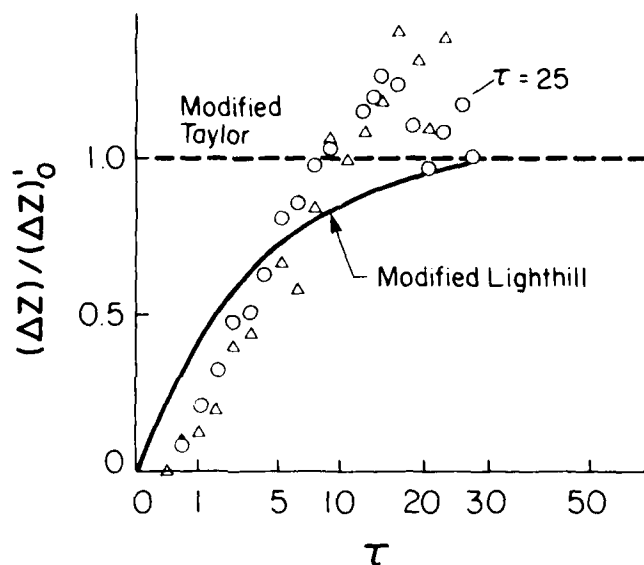


FIG. 4.9 TRANSIENT BEHAVIOUR OF SHOCK THICKNESS FOR SHOCK-TUBE PROBLEM USING RCM FOR A REAL-INVISCID FLOW [$P_{41} = 1.0018$, $T_{41} = 1.0$, $p_1 = 101.3$ kPa, $T_1 = 503.15$ K, RH = 90%, $M_e = 1.0004$, $(\Delta p)_2 = 91.1$ Pa].

$\Delta x = 0.025$ cm, $\circ x = 0.0125$ cm.

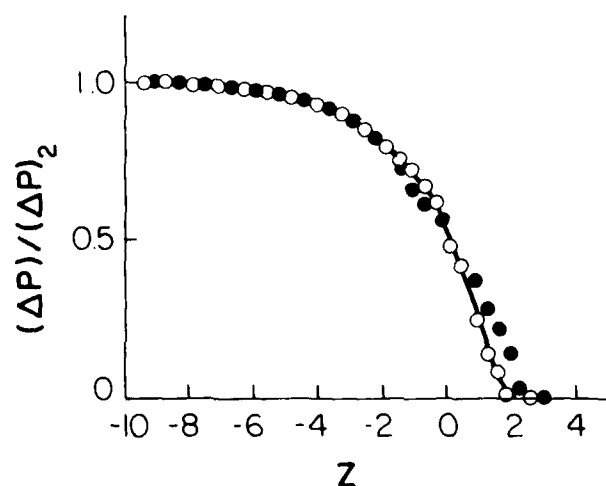


FIG. 4.10 STEADY SHOCK-PRESSURE PROFILE FOR SHOCK-TUBE PROBLEM USING RCM FOR A REAL-INVISCID FLOW [$P_{41} = 1.0018$, $T_{41} = 1.0$, $p_1 = 101.3$ kPa, $T_1 = 503.15$ K, RH = 90%, $M_e = 1.0004$, $(\Delta p)_2 = 91.1$ Pa, $(\Delta T)_2 = 0.0777$ K, $t_0 = 1.04$ sec, $x_0 = 0.5$ cm, $\Delta x = 0.0125$ cm].

— ANALYTICAL, $\bullet t = 25.0$, $\circ t = 27.6$

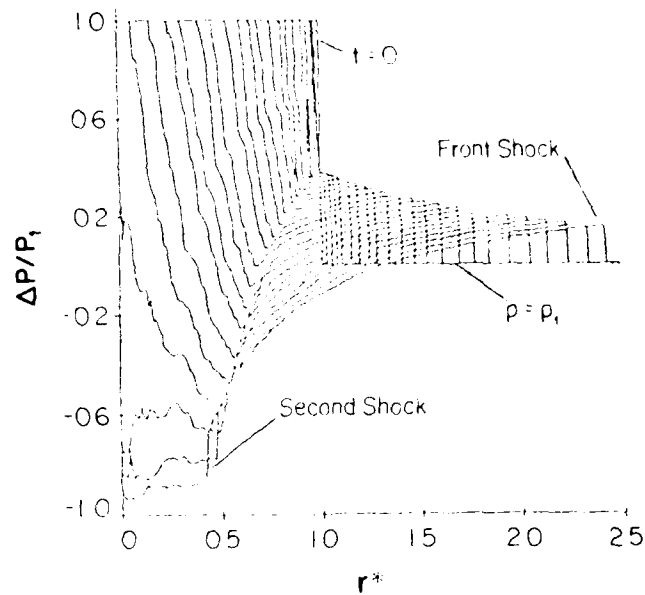


FIG. 4.11 NEAR-FIELD SOLUTION OF EXPLOSION OF A PRESSURIZED AIR SPHERE USING RANDOM-CHOICE METHOD FOR A PERFECT INVISCID FLOW (CASE A), $P_{11} = 2.0$, $P_{11} = 1.0$, $r^* = 1.80$.

(a) INITIAL PROCESS OF EXPLOSION

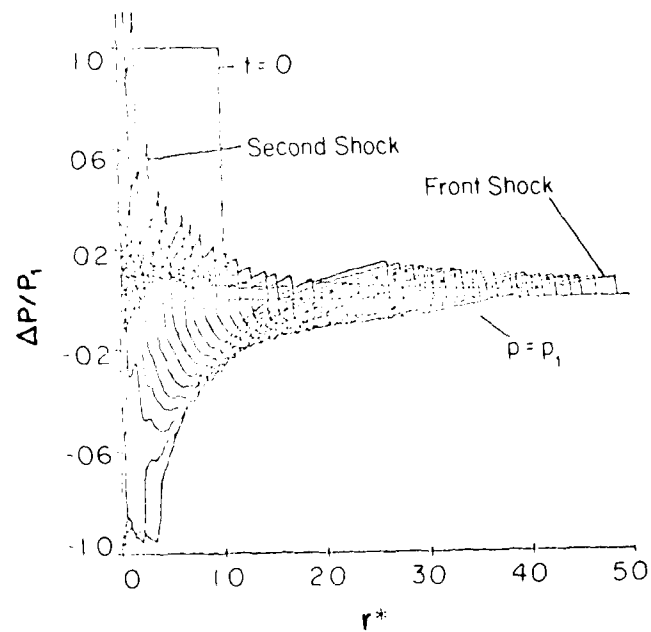


FIG. 4.11 CONTINUED
NEAR-FIELD SOLUTION OF EXPLOSION OF A PRESSURIZED AIR SPHERE USING RANDOM-CHOICE METHOD FOR A PERFECT INVISCID FLOW (CASE A), $P_{11} = 2.0$, $P_{11} = 1.0$, $r^* = 1.40$.

(b) FORMATION OF N-WAVE

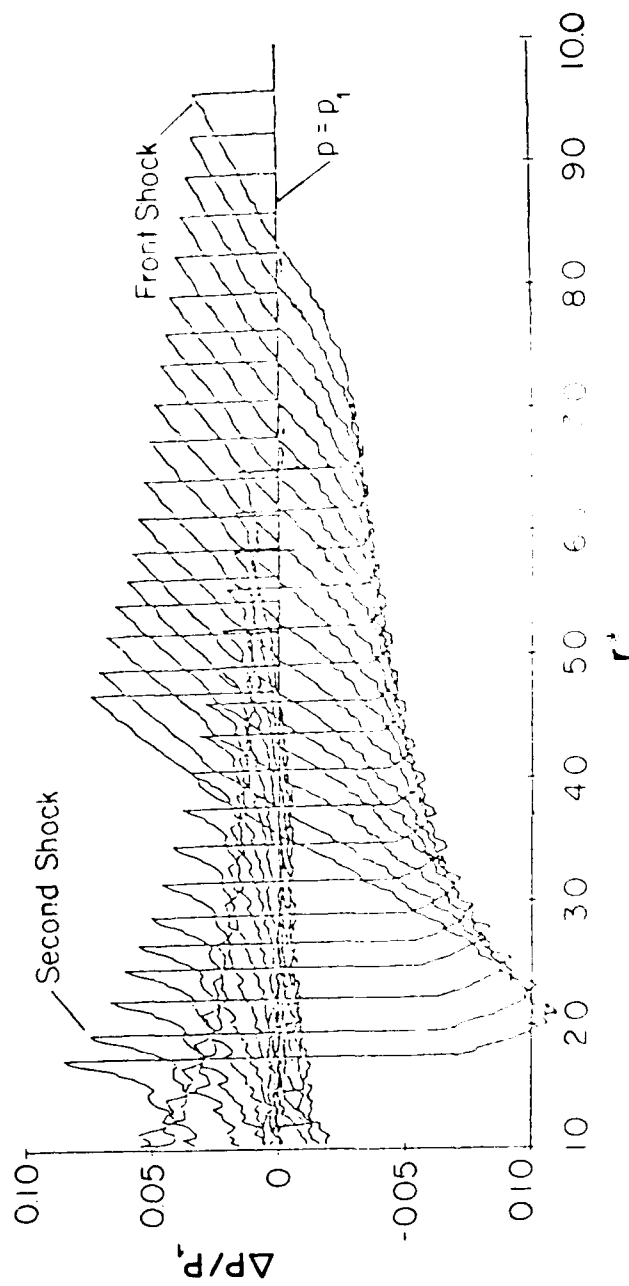
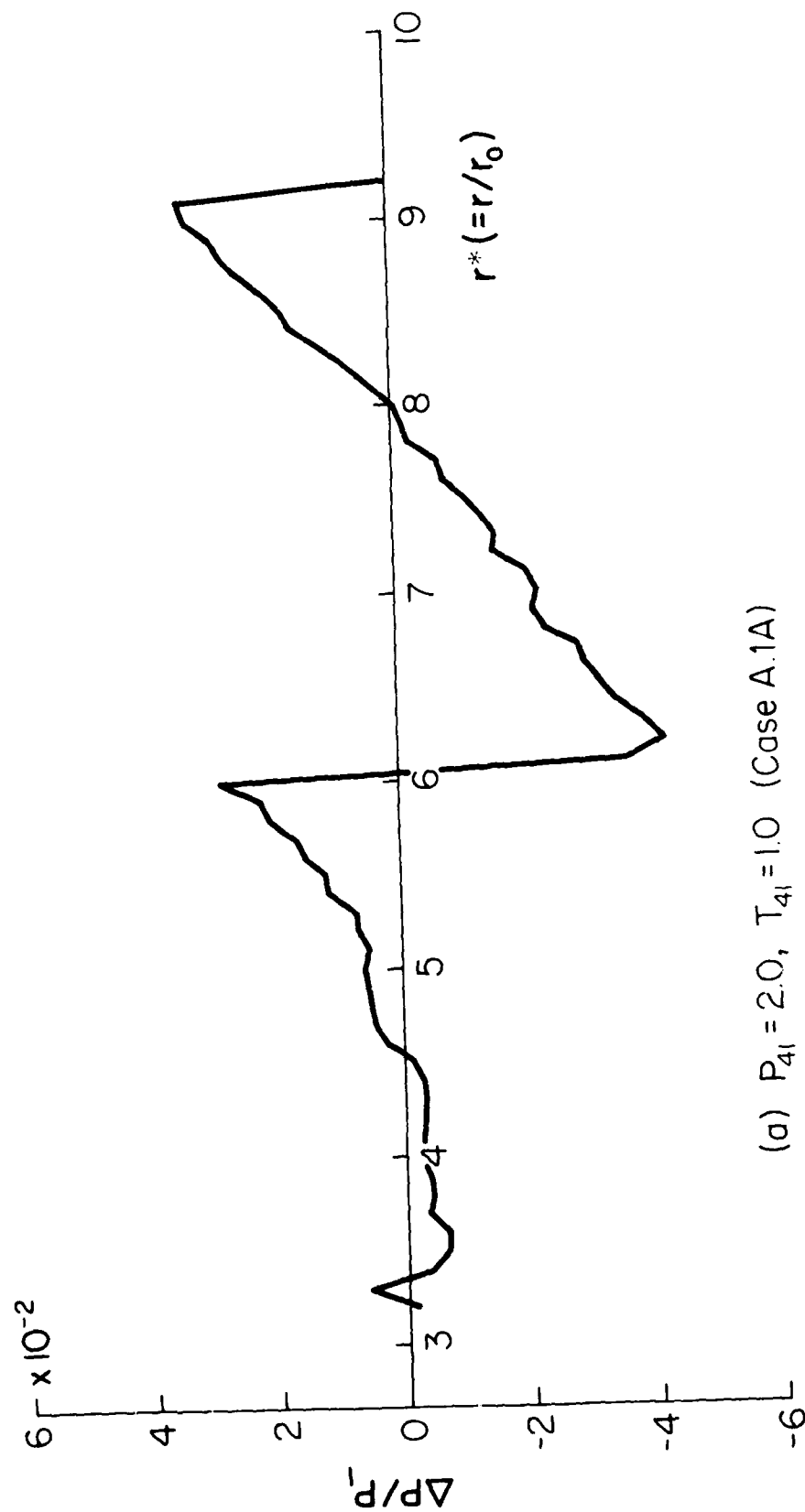


FIG. 4.11 - CONTINUED - NEAR-FIELD SOLUTION OF EXPLOSION OF A PRESSURIZED AIR SPHERE USING RANDOM CHOICE METHOD FOR A PERFECT-INVISCID FLOW (CASE VI, $P_{11} = 2.0$, $T_{11} = 1.0$, $r^* = 1.40$).

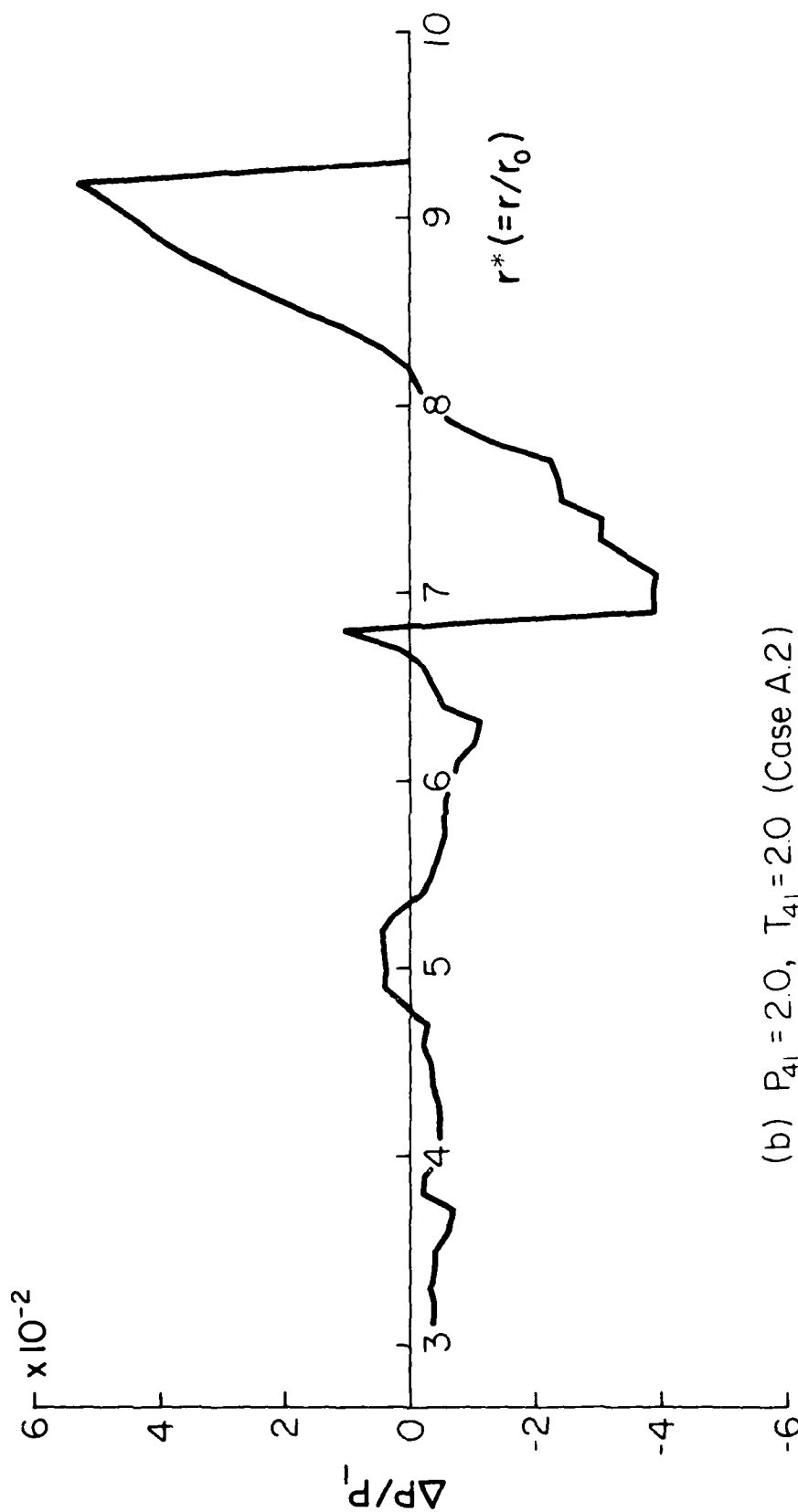
(c) PROPAGATION OF SPHERICAL N-WAVE



(a) $P_{4i} = 2.0$, $T_{4i} = 1.0$ (Case A.1A)

FIG. 4.12 EFFECTS OF INITIAL PRESSURE AND TEMPERATURE RATIOS P_{4i} AND T_{4i} ON N-WAVE PROFILE ($r^* = 1/10$).

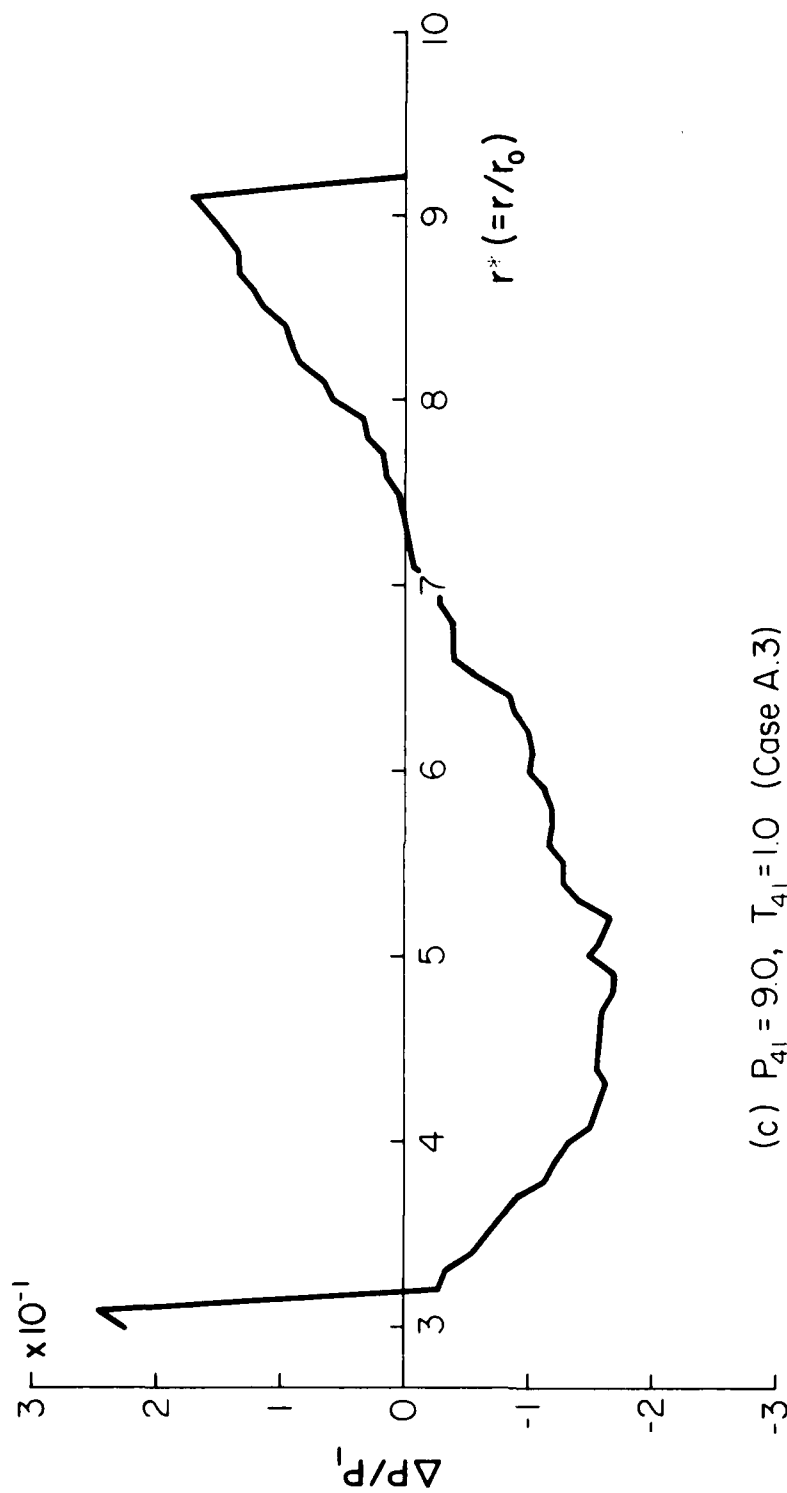
(a) $P_{4i} = 2.0$, $T_{4i} = 1.0$ (CASE) A.1A



(b) $P_{41} = 2.0$, $T_{41} = 2.0$ (Case A.2)

FIG. 4.12 - (CONTINUED) - EFFECTS OF INITIAL PRESSURE AND TEMPERATURE RATIOS P_{41} AND T_{41} ON N-WAVE PROFILE. ($r^* = 1/10$).

(b) $P_{41} = 2.0$, $T_{41} = 2.0$ (CASE A.2)



(c) $P_{41} = 9.0$, $T_{41} = 1.0$ (Case A.3)

FIG. 4.12 - CONTINUED EFFECTS OF INITIAL PRESSURE AND TEMPERATURE RATIOS P_{41} AND T_{41} ON X-WAVE PROFILE ($r^* = 1/10$).

(c) $P_{41} = 9.0$, $T_{41} = 1.0$ (Case A.3)

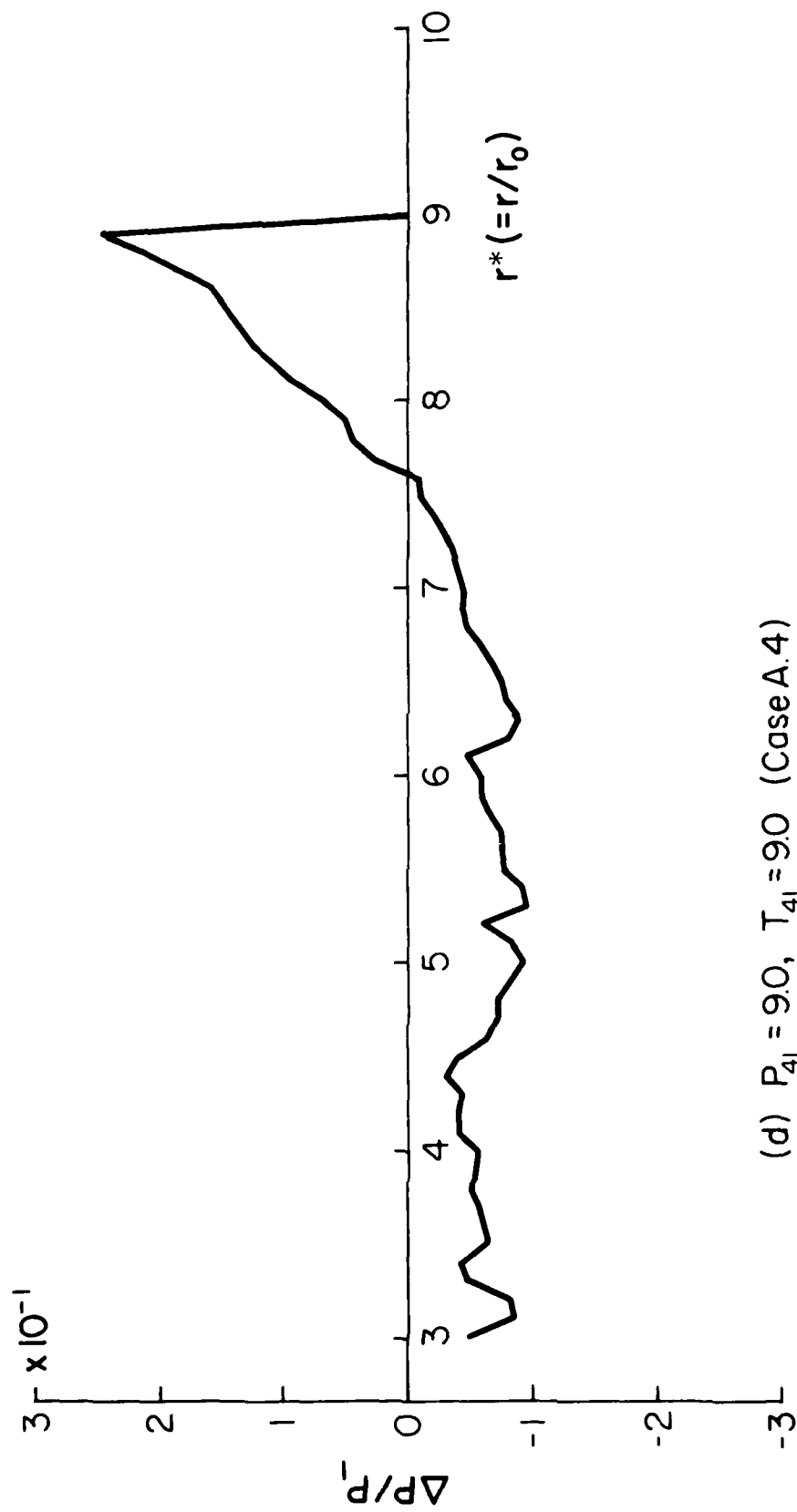


FIG. 4.12 - CONTINUED - EFFECTS OF INITIAL PRESSURE AND TEMPERATURE RATIOS P_{41} AND T_{41} ON N-WAVE PROFILE ($C.F.* = 1/10$).

(d) $P_{41} = 9.0, T_{41} = 9.0$ (CASE A4)

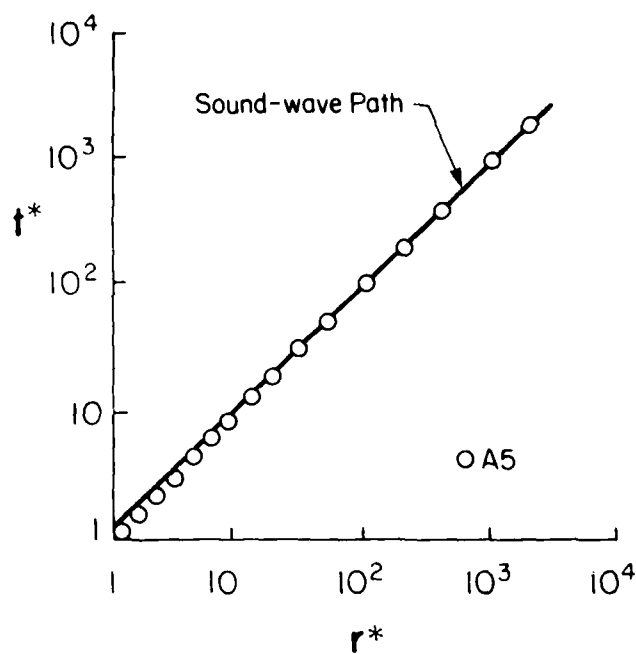


FIG. 4.13 PATH OF SHOCK FRONT FOR A PERFECT-INVISCID FLOW (CASE A5).

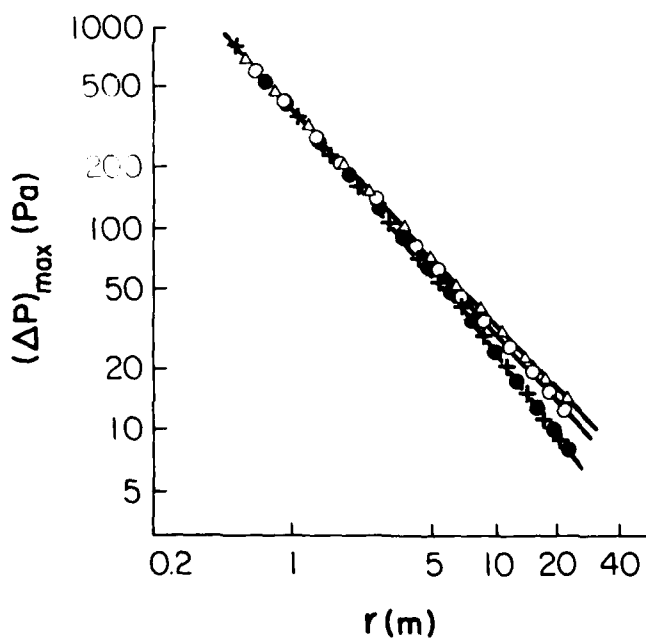


FIG. 4.14 COMPARISON FOR PERFECT-INVISCID (A5 - Δ), PERFECT-VISCOUS (B1 - \circ), REAL-INVISCID (C1 - $+$), AND REAL-VISCOUS (D1 - \bullet), FAR-FIELD RCM SOLUTIONS OF ATTENUATION OF MAXIMUM OVERPRESSURE.

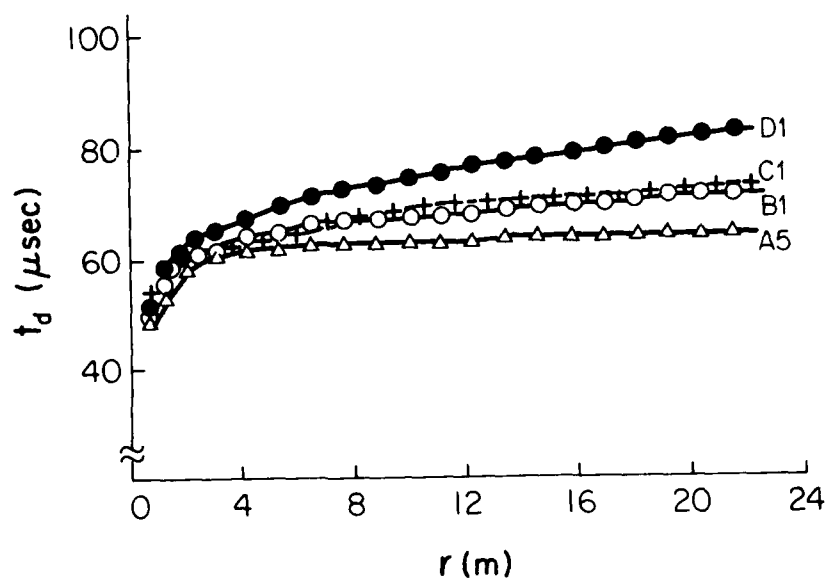


FIG. 4.15 COMPARISON BETWEEN PERFECT-INVISCID (A5 - Δ), PERFECT-VISCOUS (B1 - \circ), REAL-INVISCID (C1 - $+$), AND REAL-VISCOUS (D1 - \bullet), FAR-FIELD RCM SOLUTIONS: HALF-DURATION t_d VS DISTANCE r .

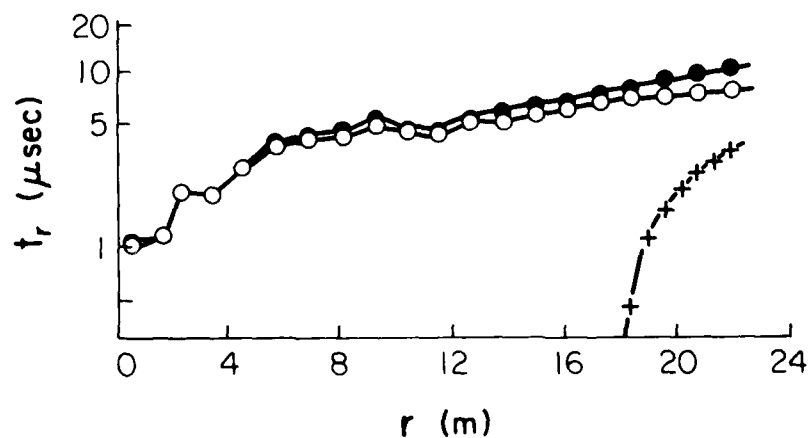
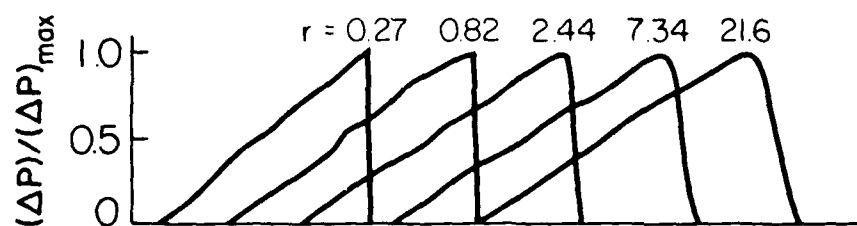


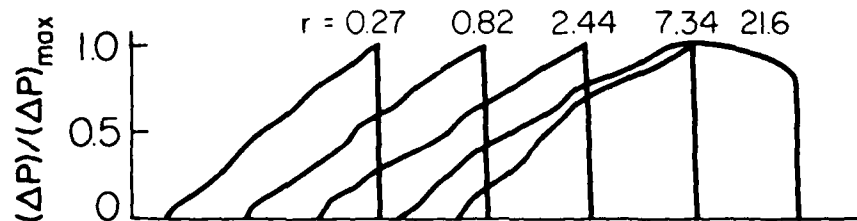
FIG. 4.16 COMPARISON BETWEEN RISE TIMES t_r VS DISTANCE r FOR PERFECT-INVISCID ($t_r = 0$), PERFECT-VISCOUS (B1 - \circ), REAL-INVISCID (C1 - $+$), AND REAL-VISCOUS (D1 - \bullet), FAR-FIELD RCM SOLUTIONS: RISE TIME t_r VS DISTANCE r .



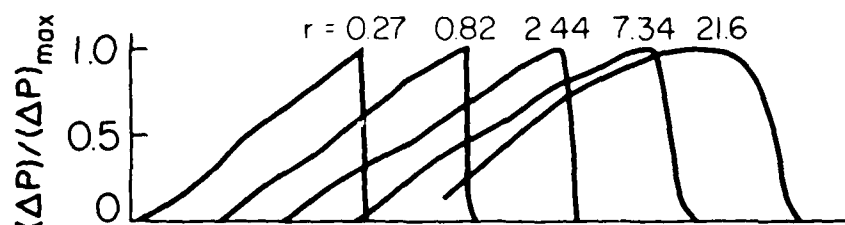
(a) Perfect-inviscid (Case A5)



(b) Perfect-viscous (Case B1)



(c) Real-inviscid (Case C1)



(d) Real-viscous (Case D1) 5mm

FIG. 4.17 COMPARISON OF PERFECT-INVISCID, PERFECT-VISCOUS, REAL-INVISCID AND REAL-VISCOUS PRESSURE PROFILES AT SEVERAL LOCATIONS FOR REAL-VISCOUS, FAR-FIELD RCM SOLUTIONS.

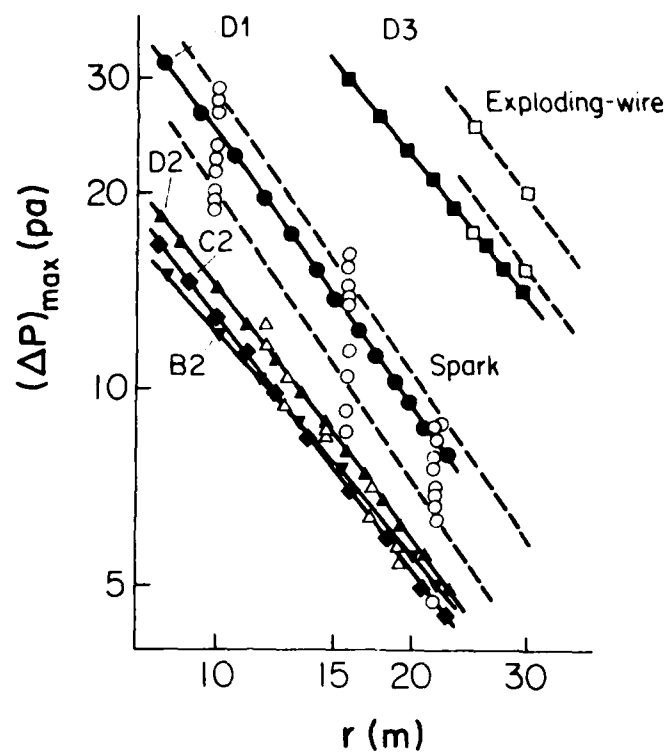


FIG. 4.18 COMPUTER SIMULATION OF MAXIMUM OVERPRESSURE ATTENUATION FOR SPARK AND EXPLODING-WIRE DATA.

NUMERICAL: ∇ B2, \blacklozenge C2, \bullet D1, \blacktriangle D2, \blacksquare D3
 EXPERIMENTAL: \circ SERIES I, \triangle SERIES II, \square SERIES IV

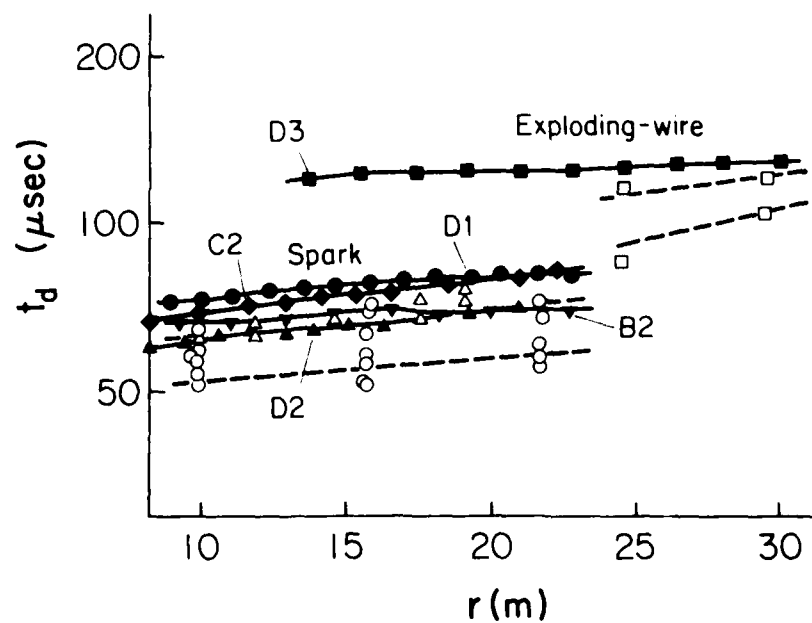


FIG. 4.19 COMPUTER SIMULATION OF HALF-DURATION AS A FUNCTION OF DISTANCE FOR SPARK AND EXPLODING-WIRE DATA.

NUMERICAL: ∇ B2, \blacklozenge C2, \bullet D1, \blacktriangle D2, \blacksquare D3
 EXPERIMENTAL: \circ SERIES I, \triangle SERIES II, \square SERIES IV

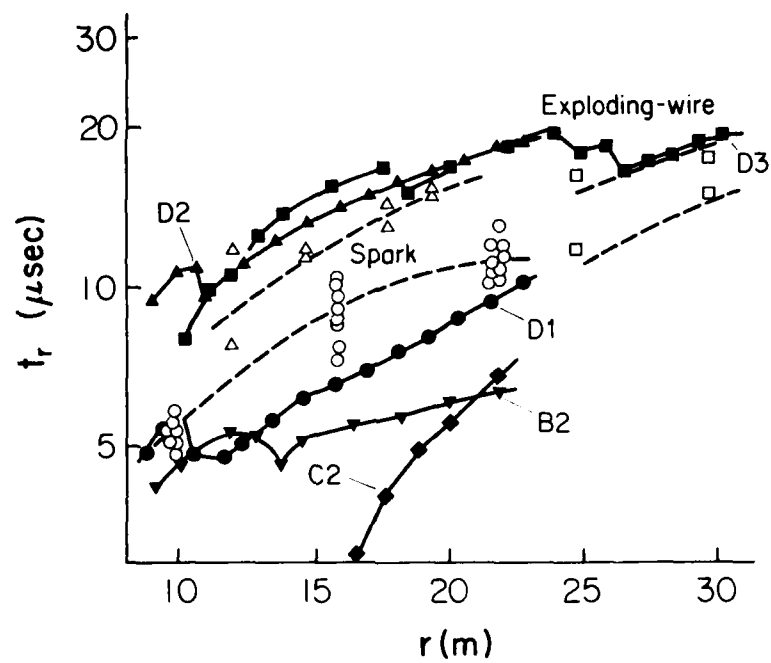


FIG. 4.20 COMPUTER SIMULATION OF RISE TIME AS A FUNCTION OF DISTANCE FOR SPARK AND EXPLODING-WIRE DATA.

NUMERICAL: ∇ B2, \blacklozenge C2, \bullet D1, \blacktriangle D2, \blacksquare D3
 EXPERIMENTAL: \circ SERIES I, \triangle SERIES II, \square SERIES IV

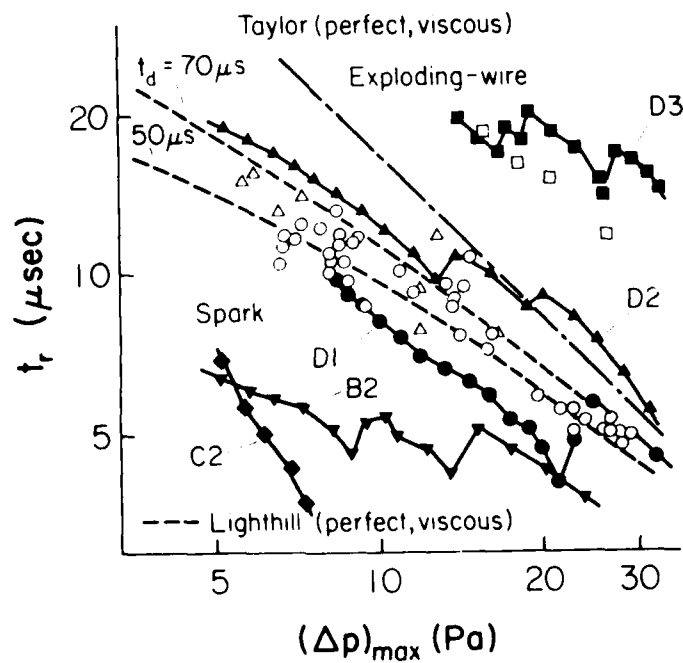


FIG. 4.21 COMPUTER SIMULATION OF RISE TIME AS A FUNCTION OF MAXIMUM OVERPRESSURE FOR SPARK AND EXPLODING-WIRE DATA.

NUMERICAL: ∇ B2, \blacklozenge C2, \bullet D1, \blacktriangle D2, \blacksquare D3
 EXPERIMENTAL: \circ SERIES I, \triangle SERIES II, \square SERIES IV

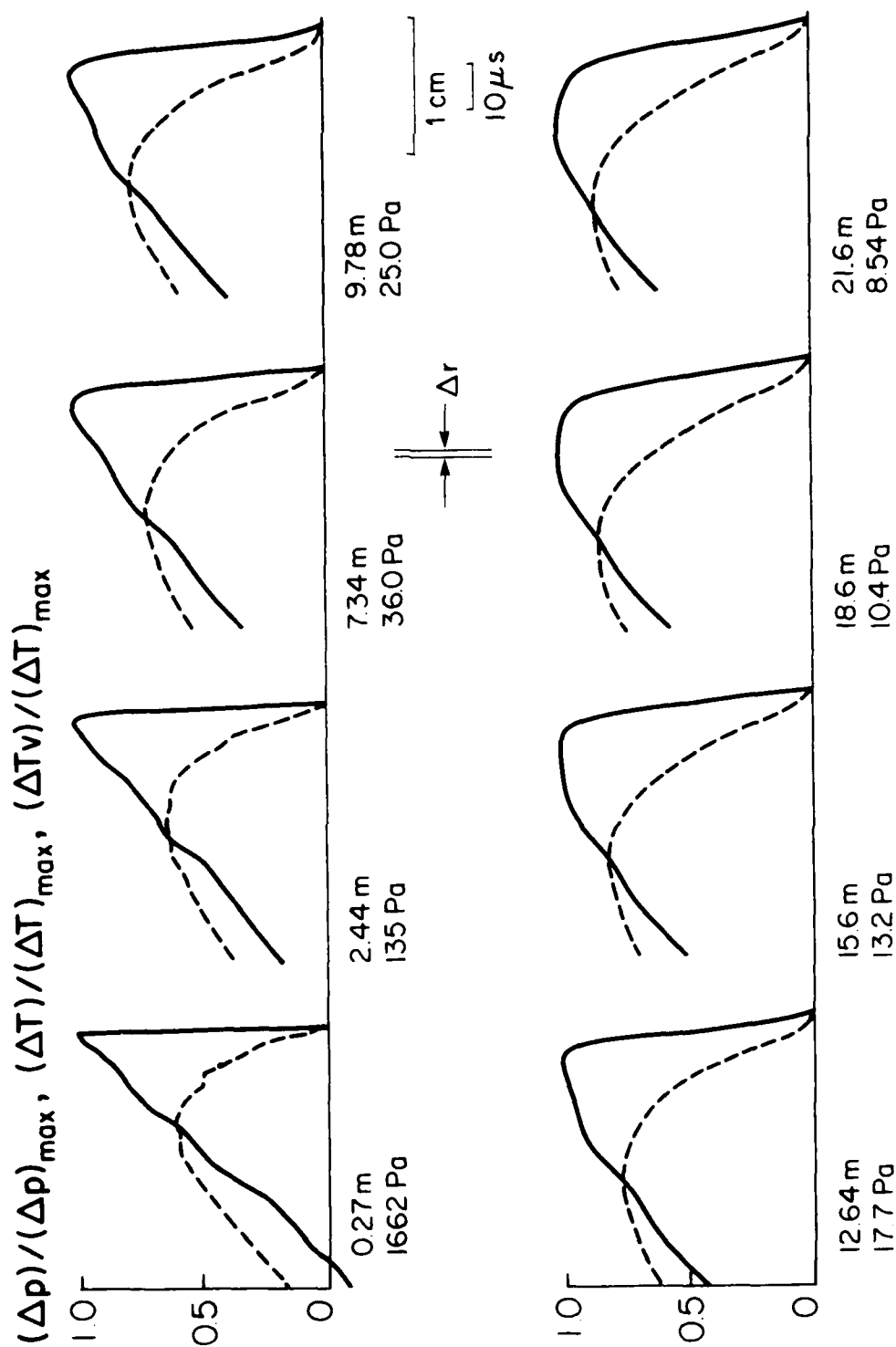


FIG. 1.22(a)

TRANSIENT SHOCK PRESSURE AND TEMPERATURE PROFILES FOR SPHERICAL N-WAVES IN AIR SOLVED BY RCM FOR A REAL-VISCOUS FLOW: SIMULATION FOR SERIES 1 EXPERIMENT (SPARK).
 $[p_{41} = 2.44, T_{41} = 1.0, p_1 = 101.3 \text{ kPa}, T_1 = 275 \text{ K}, R_1 = 6.7\%, r_0 = 1.15 \text{ cm}, \tau_0 = 0.0585 \text{ cm}, \tau_0 = 15.6 \text{ } \mu\text{sec}, (p)_{cr,0} = 52.2 \text{ Pa}]$.

— $(p)/(p)_{\max}$ or $T/(T)_{\max}$, --- $(T_v)/(T)_{\max}$

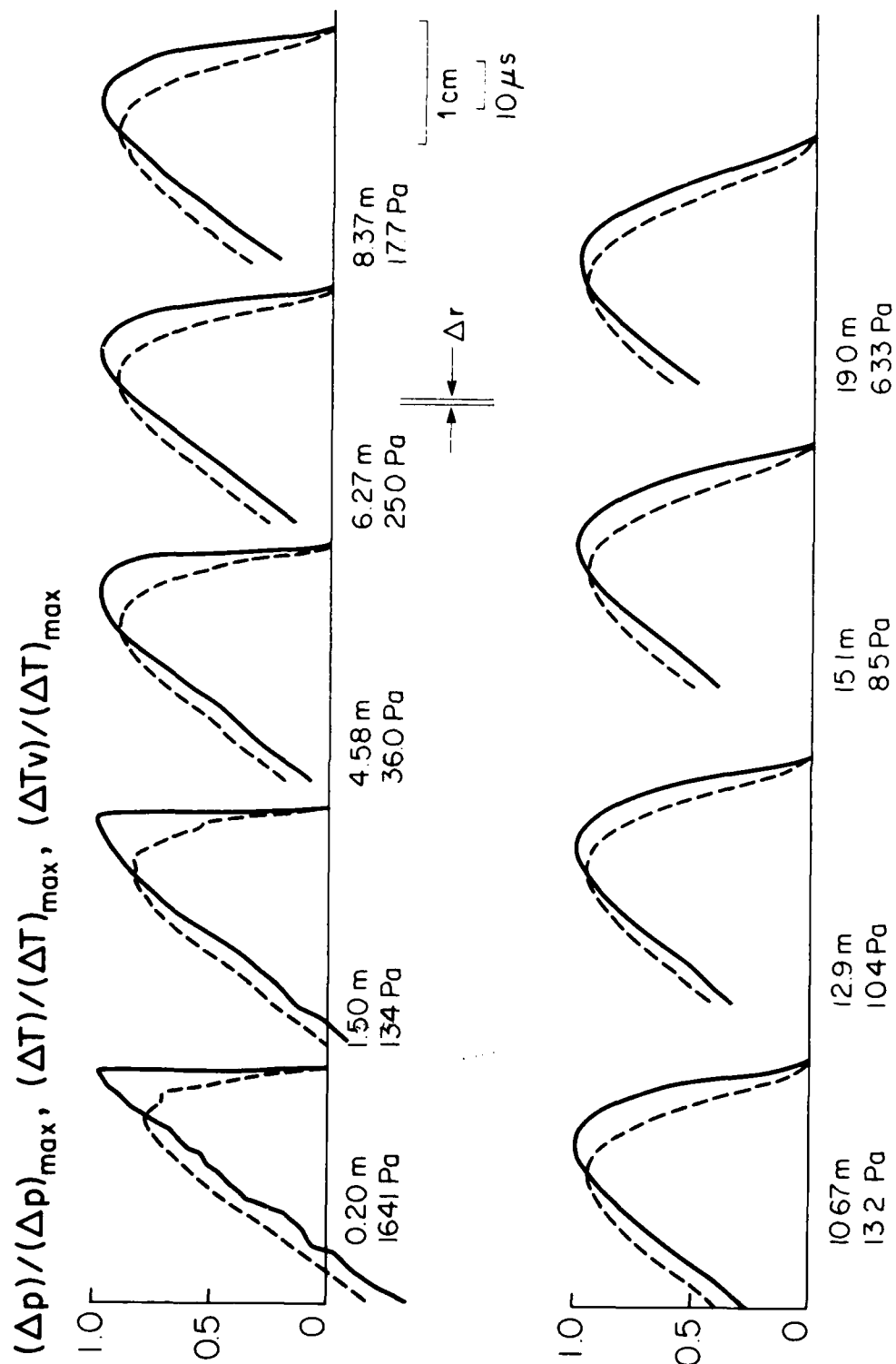


FIG. 1.22(b) TRANSIENT SHOCK PRESSURE AND TEMPERATURE PROFILES FOR SPHERICAL WAVES IN AIR
 SOLVED BY RCM FOR A REAL-VISCIOUS FLOW: SIMULATION FOR SERIES 11 EXPERIMENT (STAMP 11)
 $P_{11} = 1.8$, $T_{11} = 1.0$, $p_1 = 101.5$ kPa, $T_1 = 289$ K, $RH = 50$, $r_0 = 1.15$ cm, $t_0 = 0.0055$ s,
 $c_{p,cr,0} = 75.15$ Pa]

----- $(\Delta p)/(\Delta p)_{\max}$ or $(\Delta T)/(\Delta T)_{\max}$, ----- $(\Delta p)/(\Delta p)_{\max}$

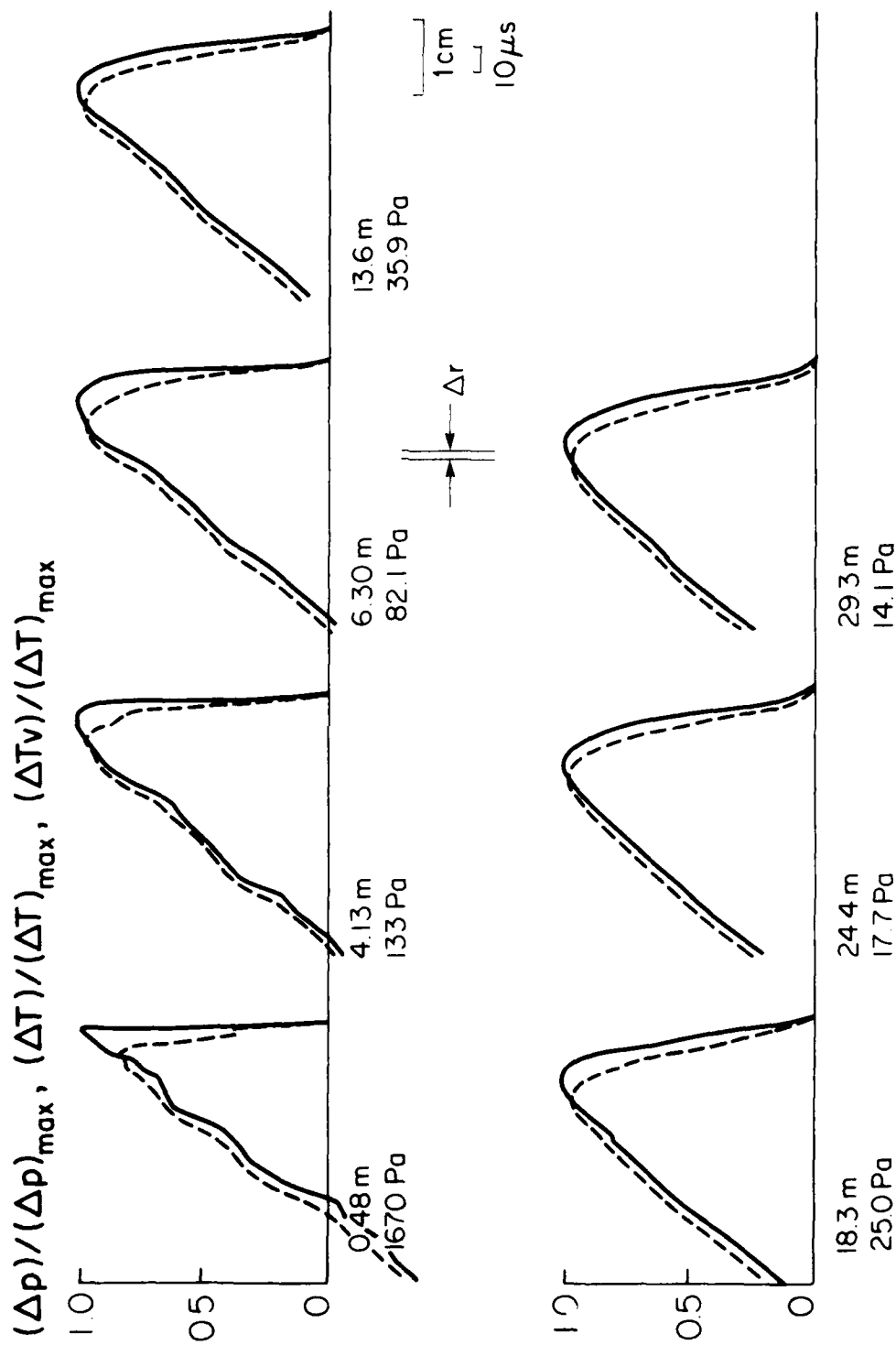
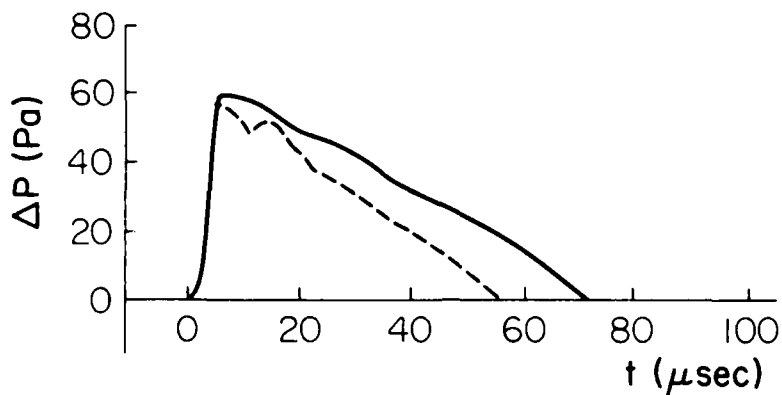


FIG. 4.22(c) TRANSIENT SHOCK PRESSURE AND TEMPERATURE PROFILES FOR SPHERICAL N-WAVES IN AIR SOLVED BY PCN FOR A REAL VISCOUS FLOW; SIMULATION FOR SERIES IV EXPERIMENT (EXPLODING-WIRE); $p_{11} = 3.5$, $T_{11} = 1.0$, $p_1 = 101.5$ kPa, $T_1 = 280$ K, RH = 87.5%, $r_0 = 1.8$ cm, $r = 9.09$ cm, $\sigma = 5.75$ μ sec, $(p)_{cr,0} = 60.95$ Pa]

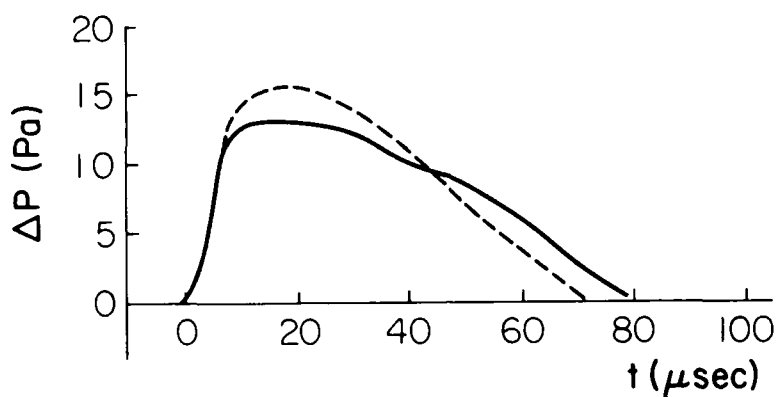
----- $(p)/(p)_{\max}$ or $(T)/(T)_{\max}$, ---- $(T)/(T)_{\max}$



Altitude = 4.85m

NUMERICAL: $(\Delta p)_{\max} = 59.99 \text{ Pa}$, $t_r = 5 \text{ μs}$, $t_d = 68.52 \text{ μs}$

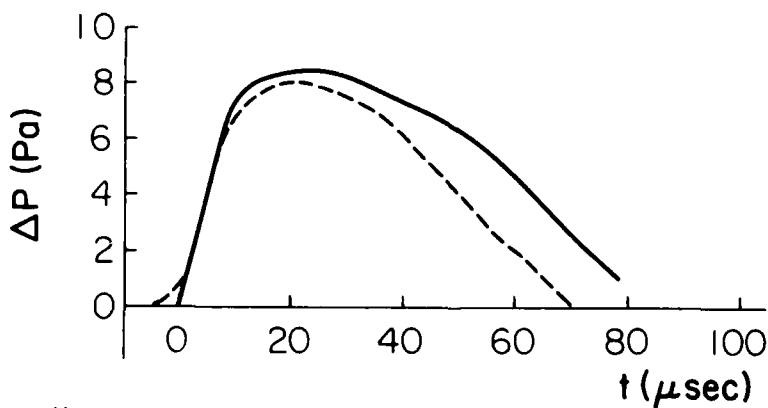
EXPERIMENTAL: $(\Delta p)_{\max} = 56.7 \text{ Pa}$, $t_r = 2 \text{ μs}$, $t_d = 53.8 \text{ μs}$



Altitude = 15.0m

NUMERICAL: $(\Delta p)_{\max} = 13.2 \text{ Pa}$, $t_r = 6.65 \text{ μs}$, $t_d = 78.9 \text{ μs}$

EXPERIMENTAL: $(\Delta p)_{\max} = 15.9 \text{ Pa}$, $t_r = 7.15 \text{ μs}$, $t_d = 75 \text{ μs}$

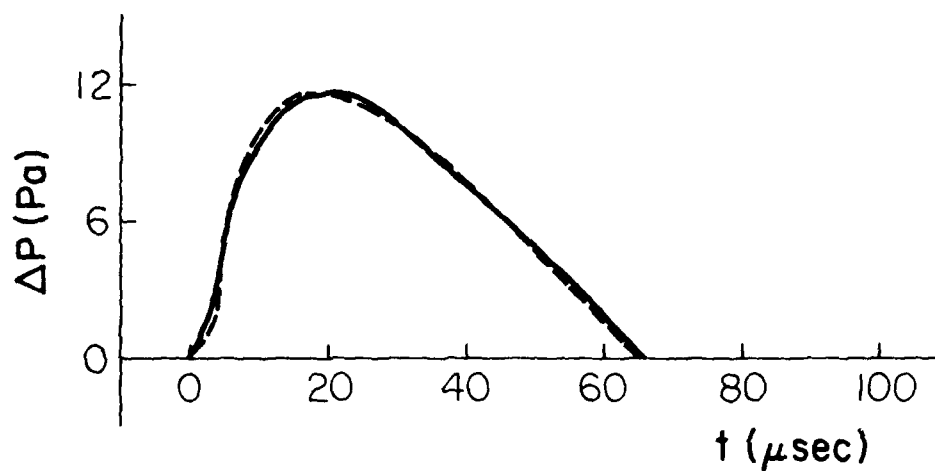


Altitude = 21.0m

NUMERICAL: $(\Delta p)_{\max} = 8.52 \text{ Pa}$, $t_r = 9.79 \text{ μs}$, $t_d = 82.74 \text{ μs}$

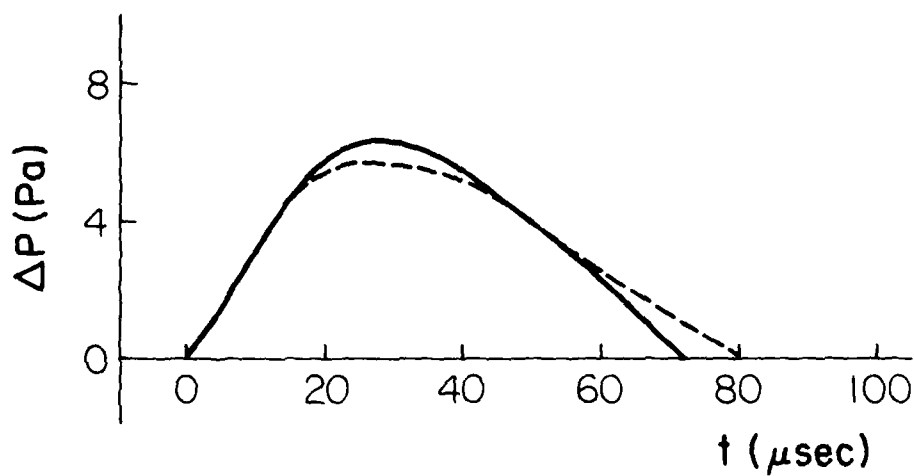
EXPERIMENTAL: $(\Delta p)_{\max} = 8.16 \text{ Pa}$, $t_r = 11.7 \text{ μs}$, $t_d = 72 \text{ μs}$

FIG. 4.23 COMPARISON OF SPARK PRESSURE PROFILES OF COMPUTED N-WAVE WITH EXPERIMENTAL DATA: SERIES I VS CASE DE.



At $r = 11.7\text{m}$

----- NUMERICAL: $(\Delta p)_{\text{max}} = 11.8 \text{ Pa}$, $t_p = 10.56 \text{ } \mu\text{s}$, $t_d = 65.6 \text{ } \mu\text{s}$
 ----- EXPERIMENTAL: $(\Delta p)_{\text{max}} = 11.77 \text{ Pa}$, $t_p = 7.8 \text{ } \mu\text{s}$, $t_d = 61.5 \text{ } \mu\text{s}$



At $r = 19\text{m}$

----- NUMERICAL: $(\Delta p)_{\text{max}} = 6.55 \text{ Pa}$, $t_p = 16.78 \text{ } \mu\text{s}$, $t_d = 69.57 \text{ } \mu\text{s}$
 ----- EXPERIMENTAL: $(\Delta p)_{\text{max}} = 5.85 \text{ Pa}$, $t_p = 15.5 \text{ } \mu\text{s}$, $t_d = 76.8 \text{ } \mu\text{s}$

FIG. 4.24 COMPARISON OF SHARK PRESSURE PROFILES OF COMPUTED X-WAVE WITH EXPERIMENTAL DATA: SERIES 11 VS CASE D2.

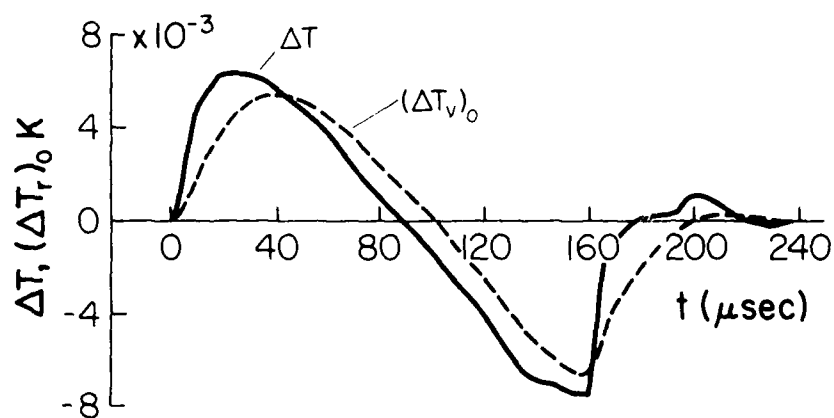
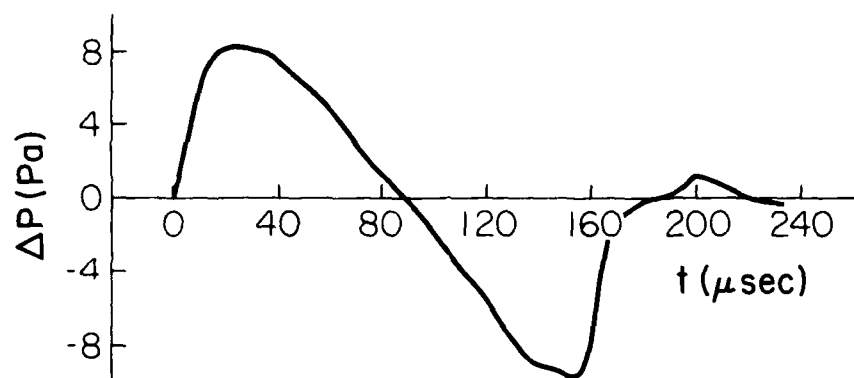


FIG. 4.25 FULL N-WAVE PROFILES OF PRESSURE, TEMPERATURE AND VIBRATIONAL TEMPERATURE AT $r = 21.6\text{m}$ FOR CASE D1A.
 $[P_{\text{max}} = 8.29 \text{ Pa}, t_p = 12.59 \mu\text{s}, t_d = 88.8 \mu\text{s}]$

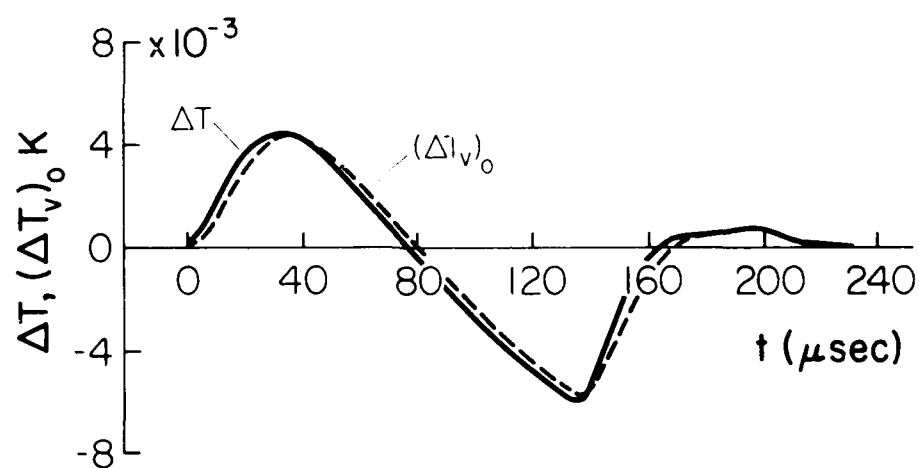
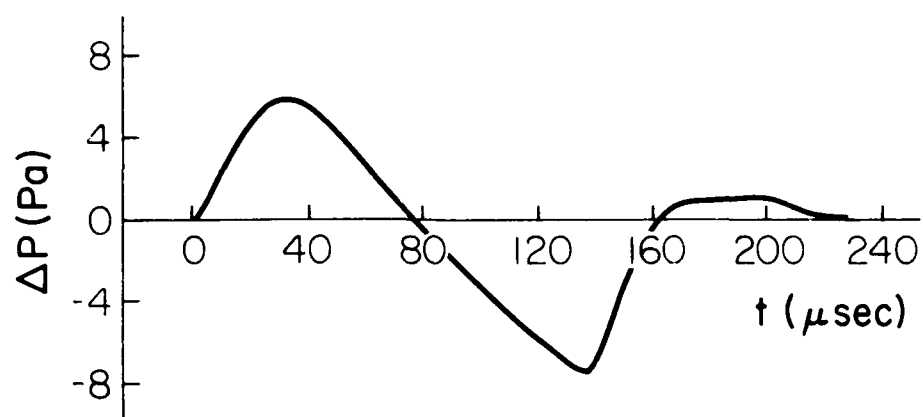


FIG. 4.26 FULL N-WAVE PROFILES OF PRESSURE, TEMPERATURE AND VIBRATIONAL TEMPERATURE AT $r = 19\text{m}$ FOR CASE D2A.
 $[(p)_{\text{max}} = 5.87 \text{ Pa}, t_r = 20 \text{ } \mu\text{s}, t_d = 73.5 \text{ } \mu\text{s}]$

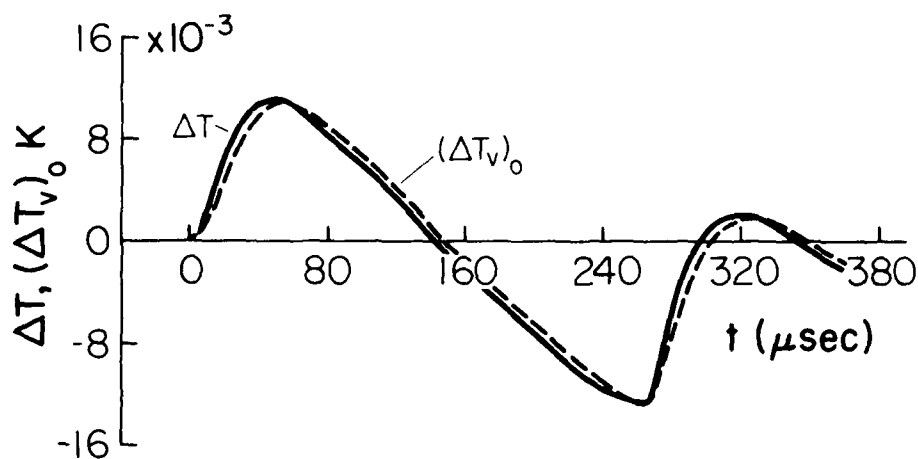
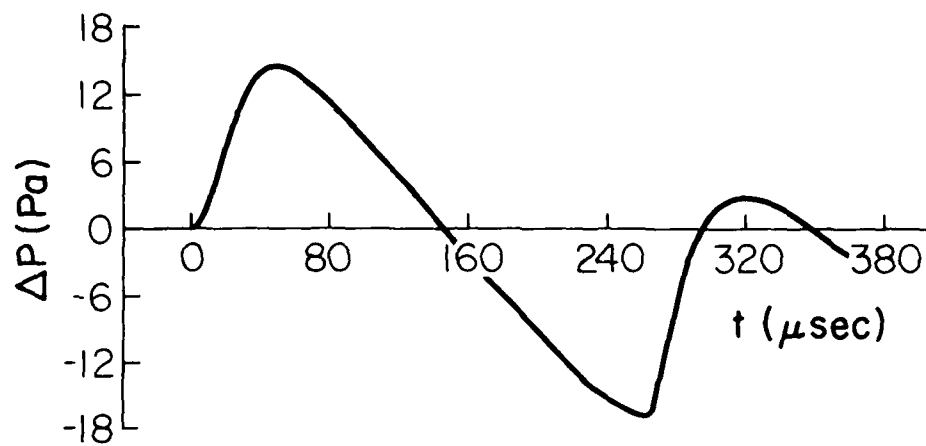


FIG. 4.27 FULL N-WAVE PROFILES OF PRESSURE, TEMPERATURE AND VIBRATIONAL TEMPERATURE AT $r = 29.3\text{m}$ FOR CASE D3A.
 $[(\Delta p)_{\text{max}} = 14.5 \text{ Pa}, t_r = 27.5 \mu\text{s}, t_d = 156.3 \mu\text{s}]$

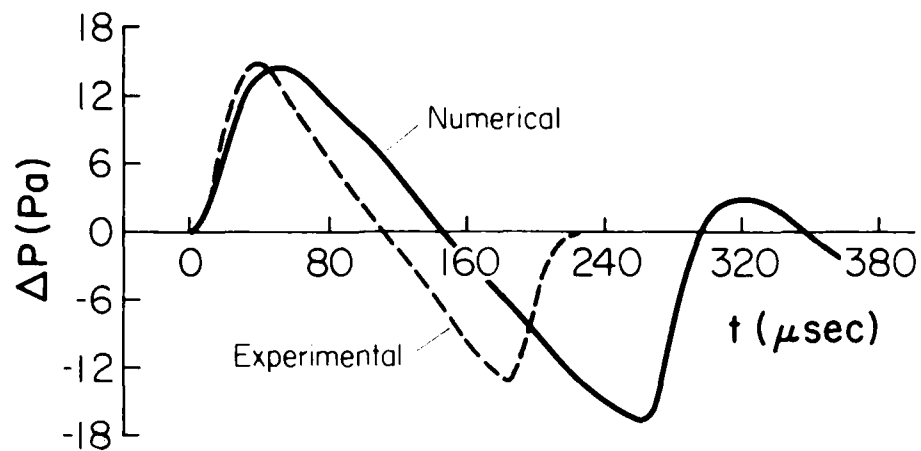


FIG. 4.28 COMPARISON OF PRESSURE PROFILES AT $r = 29.5\text{m}$ OF COMPUTED N-WAVE WITH EXPERIMENTAL DATA: SERIES IV VS CASE D5.

———— NUMERICAL: $(\Delta p)_{\text{max}} = 14.5 \text{ Pa}$, $t_p = 27.5 \text{ } \mu\text{s}$, $t_d = 105.5 \text{ } \mu\text{s}$
 - - - - - EXPERIMENTAL: $(\Delta p)_{\text{max}} = 15.5 \text{ Pa}$, $t_p = 18.7 \text{ } \mu\text{s}$, $t_d = 105.5 \text{ } \mu\text{s}$

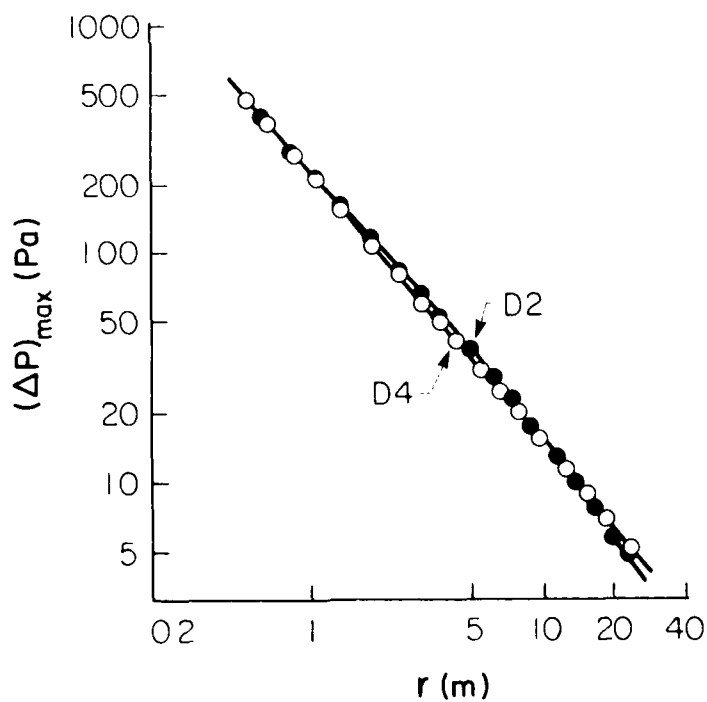


FIG. 4.29 COMPARISON OF $(\Delta p)_{\text{max}}$ VS r FOR CASES D2 AND D4 FOR DIFFERENT VIBRATIONAL RELAXATION TIMES (D2: $3.51 \text{ } \mu\text{sec}$, D4: $15.6 \text{ } \mu\text{sec}$ FOR γ_0).

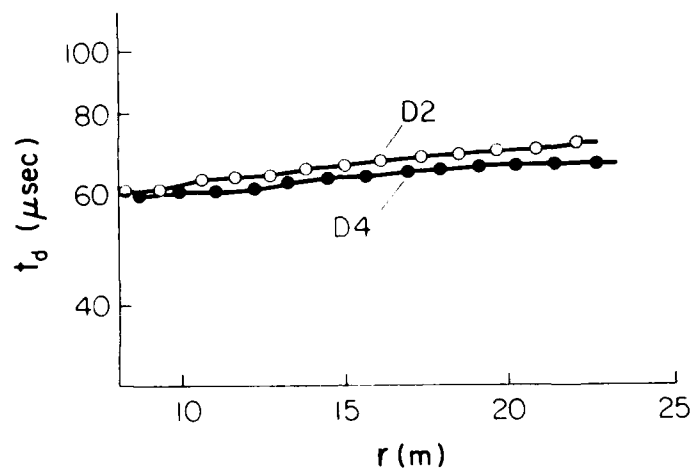


FIG. 4.50 COMPARISON OF t_d VS r FOR CASES D2 AND D4 FOR DIFFERENT VIBRATIONAL RELAXATION TIMES (D2: 5.54 μsec , D4: 15.6 μsec for γ_0).

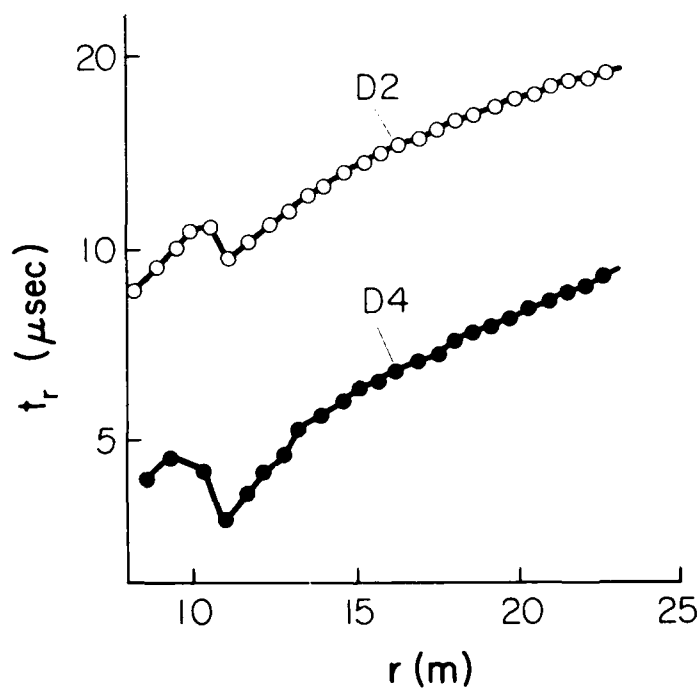


FIG. 4.51 COMPARISON OF t_r VS r FOR CASES D2 AND D4 FOR DIFFERENT VIBRATIONAL RELAXATION TIMES (D2: 5.54 μsec , D4: 15.6 μsec for γ_0).

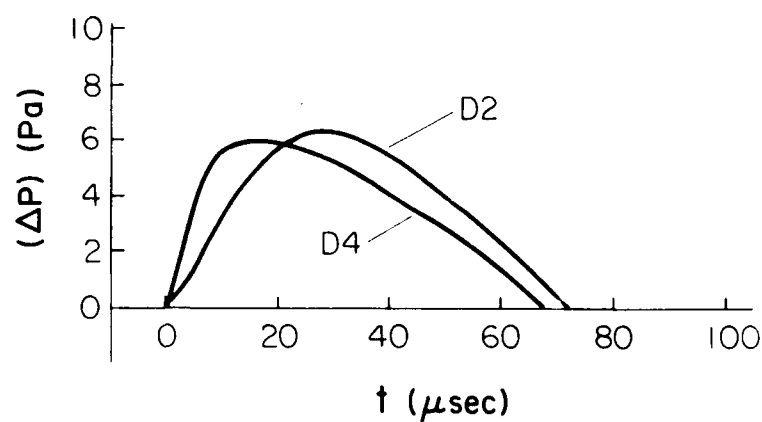


FIG. 4.32 COMPARISON OF Δp VS t FOR CASES D2 AND D4 FOR DIFFERENT VIBRATIONAL RELAXATION TIMES (D2: 5.54 μ sec, D4: 15.6 μ sec FOR τ_0).

D2: $r = 19m$, $(\Delta p)_{\max} = 6.55$ Pa, $t_p = 16.78$ μ sec, $t_d = 69.57$ μ sec
D4: $r = 19m$, $(\Delta p)_{\max} = 6.0$ Pa, $t_p = 7.7$ μ sec, $t_d = 66.5$ μ sec

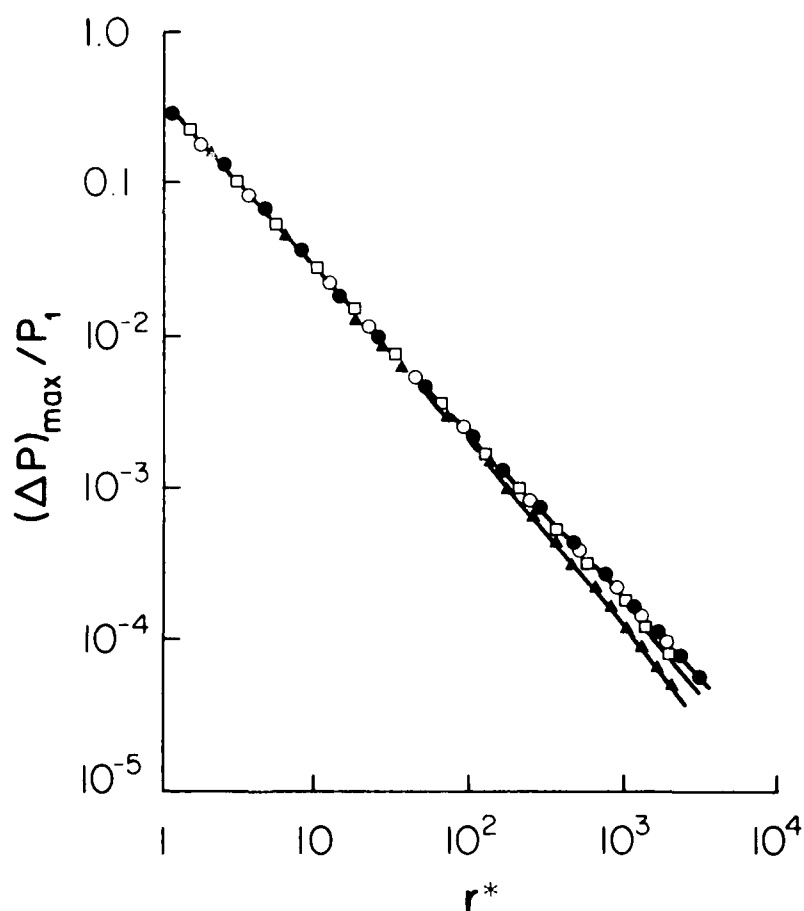


FIG. 4.33 COMPARISON OF $(\Delta p)_{\max}/P_1$ VS r^* FOR PERFECT-INVISCID CASE A6 \circ AND REAL-VISCOUS CASES D2 \blacktriangle , D5 \square AND D6 \blacksquare ($P_{41} = 1.8$, $r_0 = 1.15$ cm FOR D2).

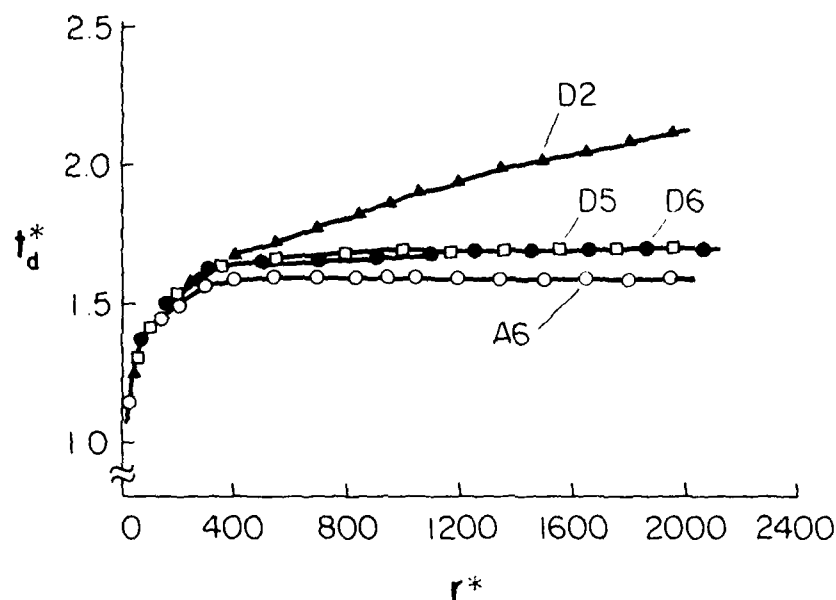


FIG. 4.34 COMPARISON OF t_d^* VS r^* FOR CASES A6 (PERFECT-INVISCID), D2, D5 AND D6 (REAL-VISCOUS) FOR DIFFERENT HALF DURATIONS ($P_{41} = 1.8$, $r_0 = 1.15$ cm FOR D2, D4: 11.5 cm, D6: 57.5 cm).

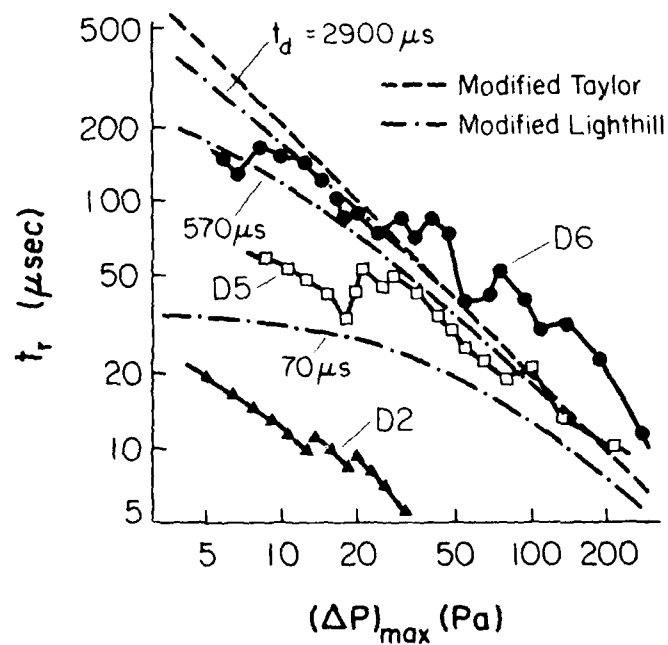


FIG. 4.35 COMPARISON OF t_r VS $(\Delta p)_{\max}$ FOR DIFFERENT HALF DURATIONS FOR REAL-VISCOUS CASES D2, D5 AND D6 ($P_{41} = 1.8$, $r_0 = 1.15$ cm FOR D2. D5: 11.5 cm, D6: 57.5 cm).

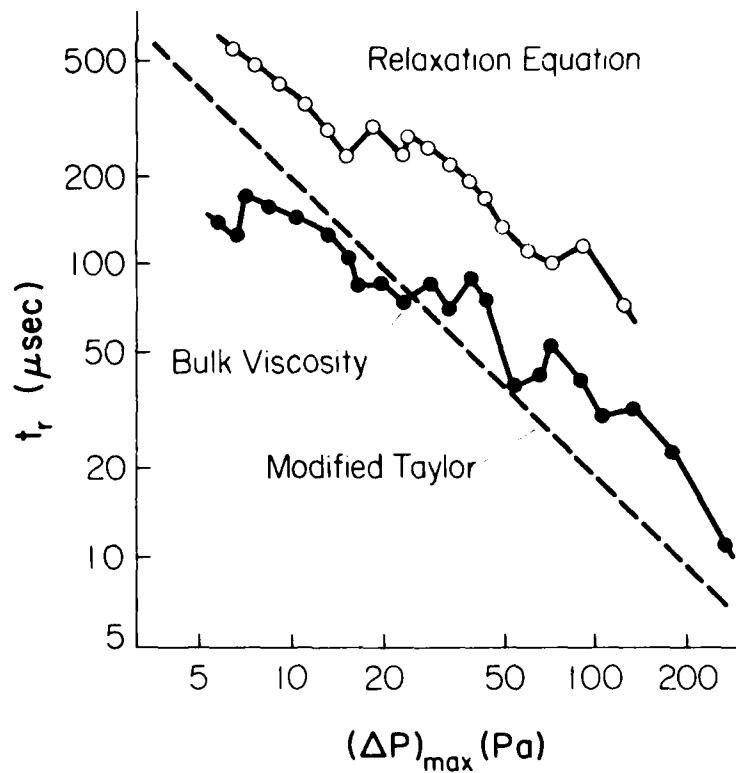


FIG. 4.56 COMPARISON OF t_r VS $(\Delta P)_{\max}$ FOR REAL VISCOUS CASES D6 AND D6a USING RELAXATION EQUATION AND BULK VISCOSITY CONCEPT SOLUTIONS FOR A WAVE OF LONG DURATION ($P_{11} = 1.8$, $r_0 = 57.5$ cm).

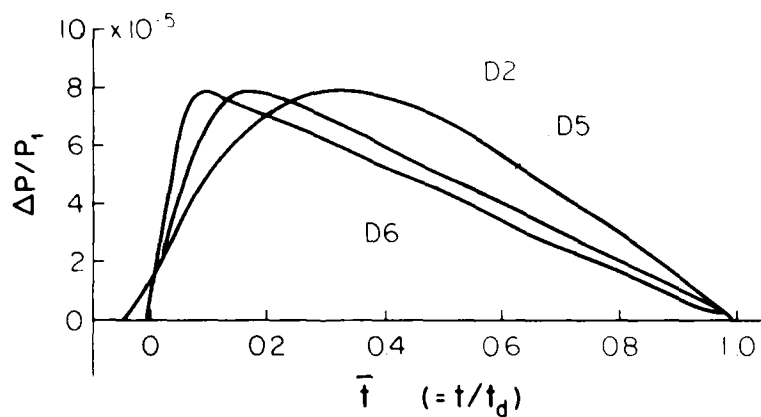


FIG. 4.57 COMPARISON OF PRESSURE PROFILES $\Delta P/P_1$ VS t FOR REAL VISCOUS CASES D2, D5 AND D6 FOR DIFFERENT HALF DURATIONS ($P_{11} = 1.8$, $r_0 = 1.15$ cm FOR D2, D5; 11.5 cm, D6; 57.5 cm).

D2: $r^* = 1380.4$, $(\Delta P)_{\max} = 7.98$ Pa, $t_r = 14.98$ μ s, $t_d = 67.14$ μ s
D5: $r^* = 1950.0$, $(\Delta P)_{\max} = 7.98$ Pa, $t_r = 59.5$ μ s, $t_d = 570.5$ μ s
D6: $r^* = 2208.3$, $(\Delta P)_{\max} = 7.98$ Pa, $t_r = 159.1$ μ s, $t_d = 2906$ μ s

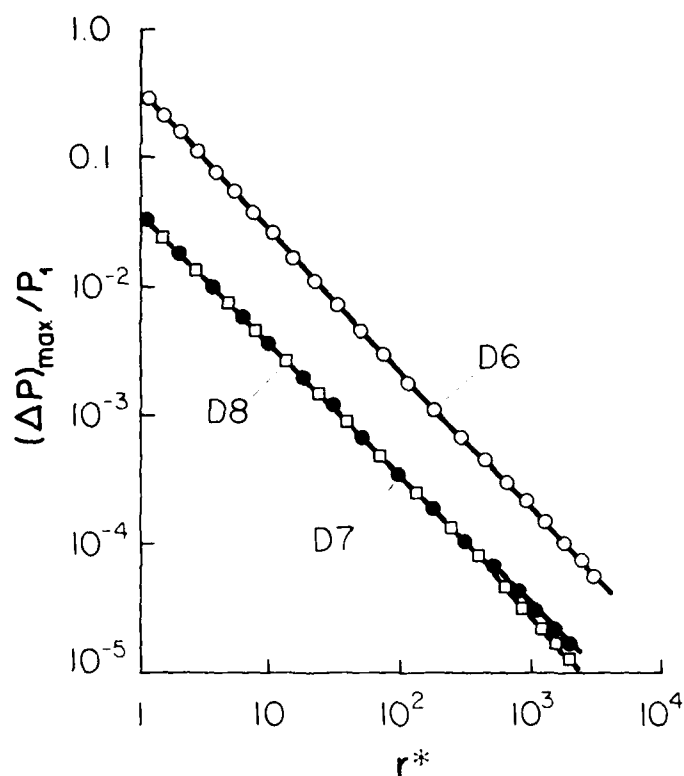


FIG. 4.38 PLOT OF $(\Delta p)_{\max}/P_1$ VS r^* FOR COMPARISON OF REAL-VISCOUS CASES D6, D7 AND D8 FOR EFFECT OF VIBRATIONAL RELAXATION OF NITROGEN ($P_{41} = 1.8$ FOR D6; D7, D8: 1.08 , $r_0 = 57.5$ cm; D6, D7: O_2 ONLY, D8: O_2+N_2).

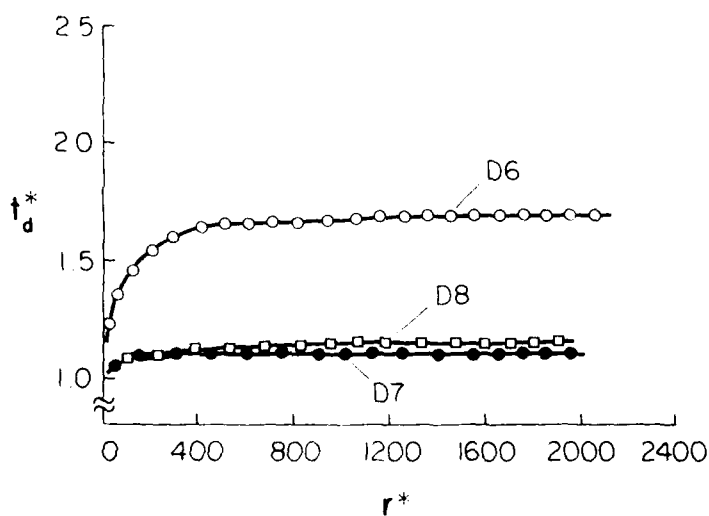


FIG. 4.59 COMPARISON OF t_d^* VS r^* FOR CASES D6, D7 AND D8 FOR EFFECT OF VIBRATIONAL RELAXATION OF NITROGEN ($P_{41} = 1.8$ FOR D6; D7, D8: 1.08 ; $r_0 = 57.5$ cm; D6, D7: O_2 ONLY, D8: O_2+N_2).

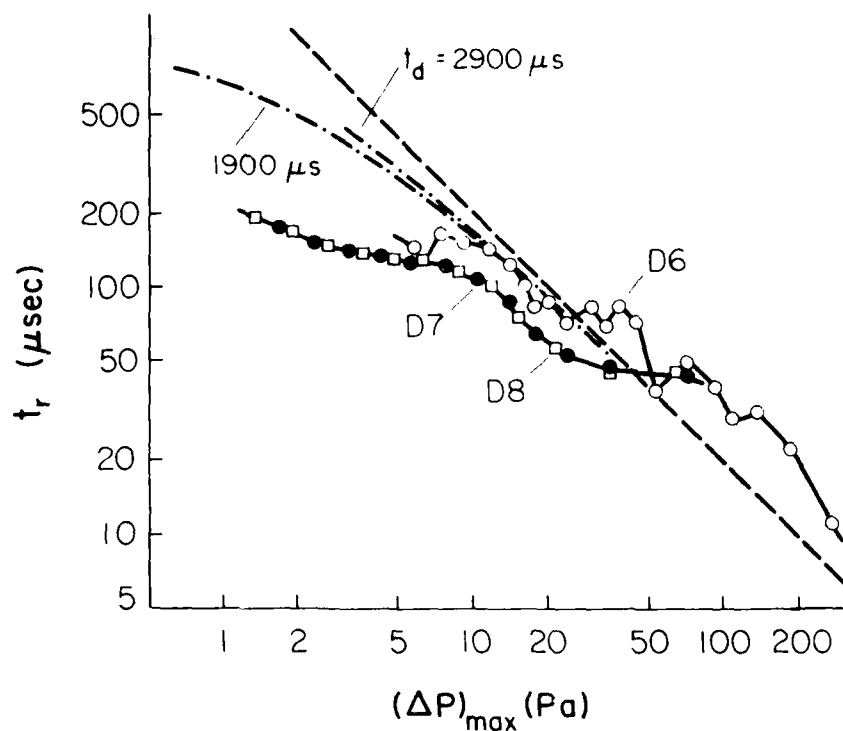


FIG. 4.40 COMPARISON OF t_r VS $(\Delta p)_{\max}$ FOR CASES D6, D7 AND D8 FOR EFFECT OF VIBRATIONAL RELAXATION OF NITROGEN ($P_{f1} = 1.8$ FOR D6; D7, D8: 1.08; $r_0 = 57.5$ cm; D6, D7: O_2 ONLY, D8: O_2+N_2).

--- MODIFIED TAYLOR, - - MODIFIED LIGHTILL

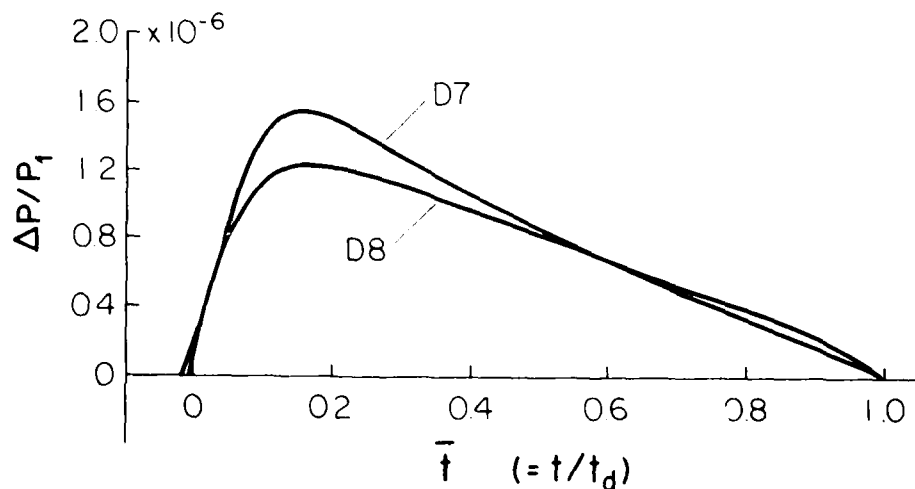


FIG. 4.41 COMPARISON OF PRESSURE PROFILES $\Delta p/p_1$ VS \bar{t} FOR CASES D7 AND D8 FOR EFFECT OF VIBRATIONAL RELAXATION OF NITROGEN ($P_{f1} = 1.08$; $r_0 = 57.5$ cm; D7: O_2 ONLY, D8: O_2+N_2).

D6: $r^* = 1950$, $(\Delta p)_{\max} = 1.55$ Pa, $t_r = 174.7$ μ s, $t_d = 1876.5$ μ s
D7: $r^* = 1950$, $(\Delta p)_{\max} = 1.25$ Pa, $t_r = 191.6$ μ s, $t_d = 1949.4$ μ s

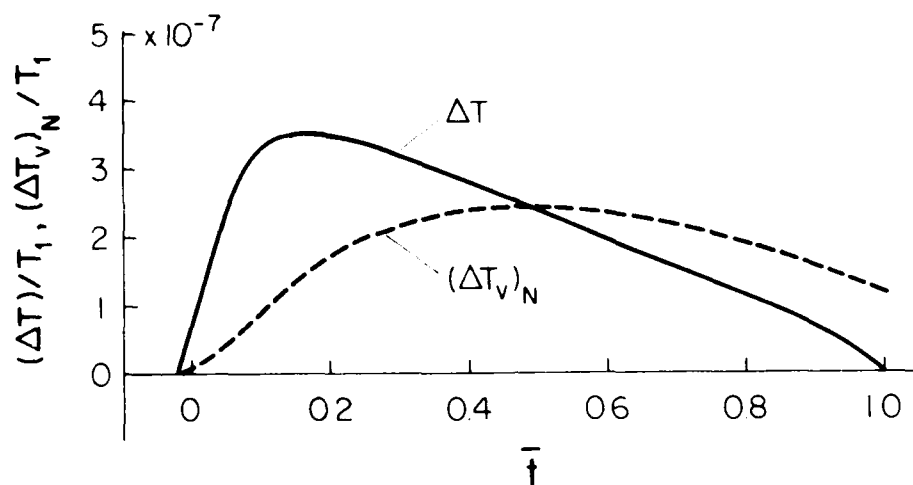


FIG. 4.42 PROFILES OF TEMPERATURE ΔT AND VIBRATIONAL TEMPERATURE $(\Delta T_v)_N$ VS $\bar{t} = t/t_d$ FOR NITROGEN AT $r^* = 1950$ FOR REAL-VISCOUS CASE D8.

GAS TEMPERATURE, ----- N_2 VIBRATIONAL TEMPERATURE

APPENDIX A

EVALUATION OF \bar{P}_{max} , $\bar{\tau}_2$ AND $\bar{\tau}_d$ IN THE LIGHTRILL N-WAVE SOLUTION

The centre of the shock front of an N-wave can be given by

$$\bar{c} = (2/n) \exp(\text{Re}) - 1 \quad (\text{A.1})$$

which is derived from Eq. (5.15), where \bar{c} is the \bar{c} at $\bar{P} = 0.5$ in the shock front.

The peak point of an N-wave can be obtained from $(d\bar{P}/d\bar{r})_{\text{Re=const}} = 0$. This gives the relation

$$\exp(\text{Re}) - 1 = (\bar{c}_m^2 - 1) \exp(\bar{c}_m^2/2) \quad (\text{A.2})$$

where \bar{c}_m is the \bar{c} at $\bar{P} = \bar{P}_{max}$. Equation (A.2) is rewritten as

$$\bar{c}_m^2 = 2/n \frac{\exp(\text{Re}) + 1}{\bar{c}_m^2 - 1} \quad (\text{A.3})$$

to evaluate \bar{c}_m . The method of successive iteration is used to solve Eq. (A.3) for \bar{c}_m^2 . The centre value \bar{c} was used for the initial value of iteration. The value of \bar{P}_{max} is obtained by substituting $\bar{c} = \bar{c}_m$ into Eq. (5.15).

The shock thickness $\bar{\tau}$ and the half-duration $\bar{\tau}_d$ are obtained from

$$\bar{\tau} = (\bar{c} - 1)^{-1/2} \quad \bar{\tau}_d = 1 \quad (\text{A.4})$$

where \bar{c}_1 and \bar{c}_g are the \bar{c} at $\bar{P} = 0.1 \bar{P}_{max}$ and $0.9 \bar{P}_{max}$, respectively. The values of \bar{c}_1 and \bar{c}_g are

calculated from the iterative equations, which are derived from Eq. (5.15), as

$$\frac{k+1}{9} \bar{c}_1 = 2/n \exp(\text{Re}) - 1 - \frac{1}{0.9 \bar{P}_{max}} \quad (\text{A.5})$$

$$\frac{k+1}{1} \bar{c}_g = 2/n \exp(\text{Re}) - 1 - \frac{1}{0.1 \bar{P}_{max}} \quad (\text{A.6})$$

where k is the number of iteration. The initial values of iteration used were $\bar{c}_1^0 = \bar{c}_m$ and $\bar{c}_g^0 = \bar{c}_m + 0.2 \bar{c}_m$.

The values of $\bar{\tau}_2$ and $\bar{\tau}_d$ are obtained by substituting \bar{P}_{max} , \bar{c}_1 and \bar{c}_g so obtained into Eqs. (5.14) and (5.15). The computer program for obtaining \bar{P}_{max} , $\bar{\tau}_2$ and $\bar{\tau}_d$ is given in Listing A.1, and a plot of $\bar{\tau}_d$ vs Re is shown in Fig. A.1.

In order to compare the experimental results with the Lightrill N-wave solutions, it is necessary to establish the procedure for obtaining the corresponding Lightrill rise time from the observed values of the maximum overpressure p_{max} and the observed half-duration τ_d . At first, $\bar{\tau}_d$ is determined from Eq. (5.15). Then the approximate value of Re is read out from the $\bar{\tau}_d$ -Re line in Fig. A.1. By repeating the process of Eqs. (A.1) - (A.6), an approximate value of $\bar{\tau}_d$ is found. The iterative process is repeated when $\bar{\tau}_d$ so obtained does not coincide with the exact $\bar{\tau}_d$. Finally, the corresponding value of Re is determined and $\bar{\tau}_2$ is obtained. The actual shock thickness is obtained from Eq. (5.14). The computer program for this procedure is given in Listing A.2.

```

*****
# USER = TA3000
# PROCEDURE = LOGON2
#
# TSLOG STARTED TIME=11:51:55 DATE=82-12-08
*****
READY
E L=1 F7(F1)
E
LIST
00010 C LIST.A:1 ANALYTICAL SOLUTION OF N-WAVE
00020 C
00030 C COMPUTE OF DURATION PARAMETER AND THICKNESS PARAMETER
00040 C OF N-WAVE FROM GIVEN REYNOLDS NUMBER R BY LIGHTHILL'S
00050 C ANALYTICAL SOLUTION
00060 C IMPLICIT REAL*8(A-H,P-Z)
00070 C DIMENSION R(1000)
00080 C GAM=1.4
00090 C GZ=0.8GAM/(GAM+1.0)
00100 C READ(5,10)
00110 C KK=1/7+1
00120 C DO 20 J=1,NY
00130 C K=(1-J)*7
00140 C READ(5,12) (R(MY+J),J=1,7)
00150 C CONTINUE
00160 C WRITE(6,22)
00170 C DO 70 I=1,N
00180 C RR=R(I)
00190 C ERR=EXP(RR)-1.0
00200 C ETAC=2.0*LOG(ERR)
00210 C GZC=5*INT(ETAC)
00220 C ETAM=ETAC
00230 C 10 IF(RR.LT.2.0) THEN
00240 C ETAM1=1.0+ERR/EXP(ETAM/2.0)
00250 C ELSE
00260 C ETAM1=2.0*LOG(ERR/(ETAM-1.0))
00270 C END IF
00280 C IF(DABS(ETAM1-ETAM).LT.1.0D-08) GO TO 19
00290 C ETAM=ETAM1
00300 C GO TO 18
00310 C 19 GZ=DSQRT(ETAM1)
00320 C PMAX=GZ/(1.0+EXP(ETAM1/2.0)/ERR)
00330 C P9=0.9*PMAX
00340 C P1=0.1*PMAX
00350 C GZ9=GZ
00360 C 21 GZ9A=DSQRT(2.0*LOG(ERR*(GZ9/P9-1.0)))
00370 C IF(DABS(GZ9A-GZ9).LT.1.0D-08) GO TO 30
00380 C GZ9=GZ9A
00390 C GO TO 31
00400 C 30 GZ1=2.0*GZC-GZ9A
00410 C 41 GZ1A=DSQRT(2.0*LOG(ERR*(GZ1/P1-1.0)))
00420 C IF(DABS(GZ1A-GZ1).LT.1.0D-08) GO TO 40
00430 C GZ1=GZ1A
00440 C GO TO 41
00450 C 40 GZ=GZ1A-GZ9A
00460 C GZ=GZ1A
00470 C LZ=G*GZ*PMAX
00480 C ZG=G*GZ*PMAX
00490 C WRITE(6,50) RR,LZ,ZG
00500 C 50 CONTINUE
00510 C 10 FORMAT(110)
00520 C 12 FORMAT(7F10.2)
00530 C 22 FORMAT(/1H ,10X,'*** LIGHTHILL ANALYTICAL SOLUTION OF DURATION PA
00540 C RAMETER AND THICKNESS PARAMETER ',/1H ,16X,
00550 C ' OF N-WAVE FROM GIVEN REYNOLDS NUMBER ***',
00560 C ' //1H ,22X,'R',13X,'DZ',13X,'ZD'//)
00570 C 50 FORMAT(1H ,10X,3015.7)
00580 C STOP
00590 C END
END OF DATA
END S
SAVED TO DATA SET ('TA3000.LH1.FORT')
READY
TSLOG END
*****
# USER = TA3000
# PROCEDURE = LOGON2
#
# TSLOG ENDED TIME=11:53:12 DATE=82-12-08
*****

```



```

*****
R  USERID   = TAD000
R  PROCEDURE = L060N2
R
R                                     TSDG STARTED TIME=11:44:58 DATE=82-12-04
*****
READY
E LH2 F7(F1)
E
LIST
00010 C      LIST=A.2 ANALYTICAL SOLUTION OF N-WAVE
00020 C
00030 C      COMPUTE RISE TIME TO DE-AWAVE FROM 0.1% HALF MAXIMUM
00040 C      TO AND OVERPRESSURE BY LINTHILL ANALYTICAL SOLUTION
00050 C      IMPLICIT REAL*8 (D=7)
00060 C      REAL (8,8) T,T0,TMAX,DT,TA,PCN
00070 C      PARAMETER (N=100)
00080 C      REAL (8) AM,DM,AM2,DT2
00090 C      AM=311.4575,DT=0.14,PCN
00100 C      T=0
00110 C      T0=0
00120 C      TMAX=0
00130 C      DT2=DT*DT
00140 C      IF (N117) GOTO 1000
00150 C      T=T+DT
00160 C      T0=T0+DT
00170 C      TMAX=TMAX+DT
00180 C      IF (T-TMAX) GOTO 1000
00190 C      IF (T-T0) GOTO 1000
00200 C      IF (T-TMAX) GOTO 1000
00210 C      IF (T-T0) GOTO 1000
00220 C      IF (T-TMAX) GOTO 1000
00230 C      IF (T-T0) GOTO 1000
00240 C      IF (T-TMAX) GOTO 1000
00250 C      IF (T-T0) GOTO 1000
00260 C      IF (T-TMAX) GOTO 1000
00270 C      IF (T-T0) GOTO 1000
00280 C      IF (T-TMAX) GOTO 1000
00290 C      IF (T-T0) GOTO 1000
00300 C      IF (T-TMAX) GOTO 1000
00310 C      IF (T-T0) GOTO 1000
00320 C      IF (T-TMAX) GOTO 1000
00330 C      IF (T-T0) GOTO 1000
00340 C      IF (T-TMAX) GOTO 1000
00350 C      IF (T-T0) GOTO 1000
00360 C      IF (T-TMAX) GOTO 1000
00370 C      IF (T-T0) GOTO 1000
00380 C      IF (T-TMAX) GOTO 1000
00390 C      IF (T-T0) GOTO 1000
00400 C      IF (T-TMAX) GOTO 1000
00410 C      IF (T-T0) GOTO 1000
00420 C      IF (T-TMAX) GOTO 1000
00430 C      IF (T-T0) GOTO 1000
00440 C      IF (T-TMAX) GOTO 1000
00450 C      IF (T-T0) GOTO 1000
00460 C      IF (T-TMAX) GOTO 1000
00470 C      IF (T-T0) GOTO 1000
00480 C      IF (T-TMAX) GOTO 1000
00490 C      IF (T-T0) GOTO 1000
00500 C      IF (T-TMAX) GOTO 1000
00510 C      IF (T-T0) GOTO 1000
00520 C      IF (T-TMAX) GOTO 1000
00530 C      IF (T-T0) GOTO 1000
00540 C      IF (T-TMAX) GOTO 1000
00550 C      IF (T-T0) GOTO 1000
00560 C      IF (T-TMAX) GOTO 1000
00570 C      IF (T-T0) GOTO 1000
00580 C      IF (T-TMAX) GOTO 1000
00590 C      IF (T-T0) GOTO 1000
00600 C      IF (T-TMAX) GOTO 1000
00610 C      IF (T-T0) GOTO 1000
00620 C      IF (T-TMAX) GOTO 1000
00630 C      IF (T-T0) GOTO 1000
00640 C      IF (T-TMAX) GOTO 1000
00650 C      IF (T-T0) GOTO 1000
00660 C      IF (T-TMAX) GOTO 1000
00670 C      IF (T-T0) GOTO 1000
00680 C      IF (T-TMAX) GOTO 1000
00690 C      IF (T-T0) GOTO 1000
00700 C      IF (T-TMAX) GOTO 1000
00710 C      IF (T-T0) GOTO 1000
00720 C      IF (T-TMAX) GOTO 1000
00730 C      IF (T-T0) GOTO 1000
00740 C      IF (T-TMAX) GOTO 1000
00750 C      IF (T-T0) GOTO 1000
00760 C      IF (T-TMAX) GOTO 1000
00770 C      IF (T-T0) GOTO 1000
00780 C      IF (T-TMAX) GOTO 1000
00790 C      IF (T-T0) GOTO 1000
00800 C      IF (T-TMAX) GOTO 1000
00810 C      IF (T-T0) GOTO 1000
00820 C      IF (T-TMAX) GOTO 1000
00830 C      IF (T-T0) GOTO 1000
00840 C      IF (T-TMAX) GOTO 1000
00850 C      IF (T-T0) GOTO 1000
00860 C      IF (T-TMAX) GOTO 1000
00870 C      IF (T-T0) GOTO 1000
00880 C      IF (T-TMAX) GOTO 1000
00890 C      IF (T-T0) GOTO 1000
00900 C      IF (T-TMAX) GOTO 1000
00910 C      IF (T-T0) GOTO 1000
00920 C      IF (T-TMAX) GOTO 1000
00930 C      IF (T-T0) GOTO 1000
00940 C      IF (T-TMAX) GOTO 1000
00950 C      IF (T-T0) GOTO 1000
00960 C      IF (T-TMAX) GOTO 1000
00970 C      IF (T-T0) GOTO 1000
00980 C      IF (T-TMAX) GOTO 1000
00990 C      IF (T-T0) GOTO 1000
01000 C      STOP
01010 C      END
01020 C
01030 C      *****
01040 C      *****
01050 C      *****
01060 C      *****
01070 C      *****
01080 C      *****
01090 C      *****
01100 C      *****
01110 C      *****
01120 C      *****
01130 C      *****
01140 C      *****
01150 C      *****
01160 C      *****
01170 C      *****
01180 C      *****
01190 C      *****
01200 C      *****
01210 C      *****
01220 C      *****
01230 C      *****
01240 C      *****
01250 C      *****
01260 C      *****
01270 C      *****
01280 C      *****
01290 C      *****
01300 C      *****
01310 C      *****
01320 C      *****
01330 C      *****
01340 C      *****
01350 C      *****
01360 C      *****
01370 C      *****
01380 C      *****
01390 C      *****
01400 C      *****
01410 C      *****
01420 C      *****
01430 C      *****
01440 C      *****
01450 C      *****
01460 C      *****
01470 C      *****
01480 C      *****
01490 C      *****
01500 C      *****
01510 C      *****
01520 C      *****
01530 C      *****
01540 C      *****
01550 C      *****
01560 C      *****
01570 C      *****
01580 C      *****
01590 C      *****
01600 C      *****
01610 C      *****
01620 C      *****
01630 C      *****
01640 C      *****
01650 C      *****
01660 C      *****
01670 C      *****
01680 C      *****
01690 C      *****
01700 C      *****
01710 C      *****
01720 C      *****
01730 C      *****
01740 C      *****
01750 C      *****
01760 C      *****
01770 C      *****
01780 C      *****
01790 C      *****
01800 C      *****
01810 C      *****
01820 C      *****
01830 C      *****
01840 C      *****
01850 C      *****
01860 C      *****
01870 C      *****
01880 C      *****
01890 C      *****
01900 C      *****
01910 C      *****
01920 C      *****
01930 C      *****
01940 C      *****
01950 C      *****
01960 C      *****
01970 C      *****
01980 C      *****
01990 C      *****
02000 C      *****

```

APPENDIX B

DERIVATION OF ANALYTICAL RELATIONS IN SECTION 3.4

B.1 Derivation of Eq. (3.29): Critical Overpressure

Consider a steady normal shock wave in a gas with vibrational excitation and assume the equilibrium states for both sides of the shock front. Then, the equations of continuity, momentum and energy are given by

$$\rho_1 u_1 = \rho_2 u_2 \quad (B.1)$$

$$p_1 + \rho_1 u_1^2 = p_2 + \rho_2 u_2^2 \quad (B.2)$$

$$c_p T_1 + \frac{1}{2} u_1^2 = c_p T_2 + \frac{1}{2} u_2^2 \quad (B.3)$$

where the subscripts 1 and 2 denote the states ahead of and behind the shock front, respectively; ρ , density; u , velocity; p , pressure; T , temperature; c_p , vibrational energy; c_p , specific heat at constant pressure for translational and rotational energy, assumed constant. The equation of state and the vibrational energy are assumed to be expressed by

$$p = \rho R T \quad (B.4)$$

$$c_p = c_v + R \quad (B.5)$$

where R is the gas constant; c_v , vibrational specific heat for the molecule, assumed constant across the shock.

From Eqs. (B.1) and (B.2)

$$p_2/p_1 = (u_1^2/u_2^2) \left(\frac{\rho_2}{\rho_1} \right) = \frac{1}{M_1^2} \left(\frac{u_1^2}{u_2^2} \right) \quad (B.6)$$

$$\frac{p_2}{p_1} = \frac{1}{M_1^2} \left(\frac{u_1^2}{u_2^2} \right) \left(\frac{\rho_2}{\rho_1} \right) = \frac{1}{M_1^2} \left(\frac{u_1^2}{u_2^2} \right) \left(\frac{\rho_2}{\rho_1} \right)$$

where M_1 is the frozen Mach number, defined by $M_1^2 = u_1^2 / (p_1 / \rho_1)$.

Using the relation (B.5) and (B.6), Eqs. (B.3) and (B.4) may be written as

$$\frac{p_2}{p_1} = \frac{1}{M_1^2} \left(\frac{u_1^2}{u_2^2} \right) \left(\frac{\rho_2}{\rho_1} \right) = \frac{1}{M_1^2} \left(\frac{u_1^2}{u_2^2} \right) \left(\frac{\rho_2}{\rho_1} \right) \quad (B.7)$$

$$\frac{p_2}{p_1} = \frac{1}{M_1^2} \left(\frac{u_1^2}{u_2^2} \right) \left(\frac{\rho_2}{\rho_1} \right) = \frac{1}{M_1^2} \left(\frac{u_1^2}{u_2^2} \right) \left(\frac{\rho_2}{\rho_1} \right) \quad (B.8)$$

Substituting Eq. (B.8) into Eq. (B.7) obtains

$$\frac{p_2}{p_1} = \frac{1}{M_1^2} \left(\frac{u_1^2}{u_2^2} \right) \left(\frac{\rho_2}{\rho_1} \right) = \frac{1}{M_1^2} \left(\frac{u_1^2}{u_2^2} \right) \left(\frac{\rho_2}{\rho_1} \right) \quad (B.9)$$

Substituting Eq. (B.9) into Eq. (B.6), then

$$\frac{p_2}{p_1} = \frac{1}{M_1^2} \left(\frac{u_1^2}{u_2^2} \right) \left(\frac{\rho_2}{\rho_1} \right) = \frac{1}{M_1^2} \left(\frac{u_1^2}{u_2^2} \right) \left(\frac{\rho_2}{\rho_1} \right) \quad (B.10)$$

Putting $M_1 = 1$, the expression for the critical overpressure (p_{cr}/p_1) is

$$\frac{p_{cr}}{p_1} = \frac{1}{M_1^2} \left(\frac{u_1^2}{u_2^2} \right) \left(\frac{\rho_2}{\rho_1} \right) = \frac{1}{M_1^2} \left(\frac{u_1^2}{u_2^2} \right) \left(\frac{\rho_2}{\rho_1} \right) \quad (B.11)$$

B.2 Derivation of Eq. (3.31): Diffusivity D

Equation (3.26) for $(\sqrt{D})_2$ can be rewritten as

$$\left(\frac{\sqrt{D}}{u_2} \right)^2 = \frac{1}{u_2^2} \left(\frac{D}{u_2^2} \right) = \frac{1}{u_2^2} \left(\frac{D}{u_2^2} \right) \quad (B.12)$$

where c_v is the ratio of specific heat in vibrational equilibrium; c_v , specific heat at constant volume for translational and rotational energy.

Using the relation (3.29), obtain from Eq. (B.12)

$$\left(\frac{\sqrt{D}}{u_2} \right)^2 = \frac{1}{u_2^2} \left(\frac{D}{u_2^2} \right) = \frac{1}{u_2^2} \left(\frac{D}{u_2^2} \right) \quad (B.13)$$

B.3 Derivation of Eq. (3.32): Parameter k

The parameter k appearing in Eq. (3.24) can be rewritten as

$$k = \frac{u_1^2}{u_2^2} \left(\frac{1}{u_2^2} \right) = \frac{u_1^2}{u_2^2} \left(\frac{1}{u_2^2} \right) \quad (B.14)$$

$$\frac{u_1^2}{u_2^2} = \frac{1}{u_2^2} \left(\frac{u_1^2}{u_2^2} \right) = \frac{1}{u_2^2} \left(\frac{u_1^2}{u_2^2} \right) \quad (B.15)$$

Using the notations for a normal shock in Ref. (10)

$$2V_0 = u_1 u_2$$

AD-A135 903

RANDOM CHOICE SOLUTIONS FOR WEAK SPHERICAL SHOCK-WAVE
TRANSITIONS OF N-WA..(U) TORONTO UNIV DOWNSVIEW
(ONTARIO) INST FOR AEROSPACE STUDIES H HONMA ET AL.
JUL 83 UTIAS-253 AFOSR-TR-83-1041

2/2

UNCLASSIFIED

F/G 20/1

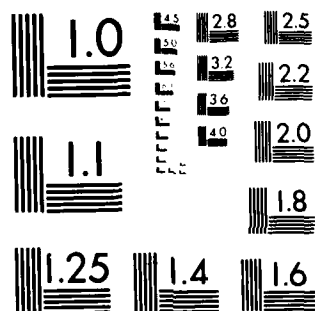
NL

END

FORMED

2-34

DTIC



MICROCOPY RESOLUTION TEST CHART
NATIONAL BUREAU OF STANDARDS 1963-A

$$\frac{\tilde{v}_0}{a_e} = \frac{\tilde{v}_0}{a_1} = \frac{1}{2} \frac{\tilde{u}_1}{a_1} \frac{\tilde{u}_1 - \tilde{u}_2}{\tilde{u}_1} = \frac{1}{2\gamma M_f} \frac{(\Delta p)_2}{p_1} = \frac{1}{2\gamma} \frac{(\Delta p)_2}{p_1} \quad (B.13)$$

Substituting Eq. (B.13) into Eq. (B.12), obtain

$$\frac{1}{k} = \frac{\gamma+1}{2\gamma} \frac{(\Delta p)_2}{p_1} \frac{\gamma}{(\gamma-1)^2 c_j} = \frac{(\Delta p)_2}{p_1} \frac{p_1}{(\Delta p)_{cr,j}} = \frac{(\Delta p)_2}{(\Delta p)_{cr,j}} \quad (3.32)$$

B.4 Derivation of Eq. (3.34) from Eq. (3.24): Polyakova et al (Ref. 21)

Equation (3.24) can be rewritten as

$$\frac{y+y_0}{k\tau_j} = \left(1 - \frac{1}{k}\right) \ln \left(1 + \frac{\tilde{v}}{\tilde{v}_0}\right) - \left(1 + \frac{1}{k}\right) \ln \left(1 - \frac{\tilde{v}}{\tilde{v}_0}\right) \quad (B.14)$$

Using the notations for a normal shock in B.1

$$\tilde{u}_1 - \tilde{u} = \tilde{v} + \tilde{v}_0 \quad (B.15)$$

$$1 + \frac{\tilde{v}}{\tilde{v}_0} = 2 \frac{\tilde{u}_1 - \tilde{u}}{\tilde{u}_1 - \tilde{u}_2} = 2 \frac{p_1}{(\Delta p)_2} \frac{(\Delta p)}{p_1} = 2 \frac{(\Delta p)}{(\Delta p)_2} \quad (3.33)$$

Using the expression (3.32) for k

$$\frac{y}{k\tau_j} = \frac{\gamma+1}{2\gamma} \frac{(\Delta p)_2}{p_1} \frac{\gamma}{(\gamma-1)^2 c_j} \frac{y}{\tau_j} = \frac{\gamma+1}{2\gamma} \frac{a_1^2 y}{(\delta v)_j} \frac{(\Delta p)_2}{p_1} = -\frac{\gamma+1}{2\gamma} Z \quad (B.16)$$

where Z is defined as

$$Z = -\frac{a_1^2 y}{(\delta v)_j} \frac{(\Delta p)_2}{p_1} \quad (3.35)$$

Substituting Eqs. (3.33), (B.16) and (3.35) into Eq. (B.14) obtains

$$\frac{\gamma+1}{2\gamma} (Z - Z_0) = \left[1 + \frac{(\Delta p)_2}{(\Delta p)_{cr,j}}\right] \ln \left[1 - \frac{(\Delta p)}{(\Delta p)_2}\right] - \left[1 - \frac{(\Delta p)_2}{(\Delta p)_{cr,j}}\right] \ln \left[\frac{(\Delta p)}{(\Delta p)_2}\right] \quad (3.34)$$

where

$$Z_0 = \frac{2\gamma}{\gamma+1} \left[\frac{y_0}{k\tau_j} + \frac{2}{k} \ln 2\right] = \text{const} \quad (B.17)$$

B.5 Derivation of Eq. (3.34) from Eq. (3.37): Johannesen and Hodgson (Ref. 12)

From Eq. (B.10)

$$M_f^2 = \frac{[\gamma+1+2(\gamma-1)c_j](\Delta p)_2/p_1 + 2[\gamma+(\gamma-1)c_j]}{2\gamma[1+(\gamma-1)c_j]} \quad (B.18)$$

Introducing the relation (3.29), then

$$1 - M_f^2 = \frac{\gamma+1}{2\gamma} \left[\frac{2(\gamma-1)^2 c_j}{\gamma+1} - \frac{(\Delta p)_2}{p_1} \right] = \frac{\gamma+1}{2\gamma} \frac{(\Delta p)_{cr,j}}{p_1} \left[1 - \frac{(\Delta p)_2}{(\Delta p)_{cr,j}} \right] \quad (B.19)$$

The terms in Eq. (3.37) can now be rewritten as

$$\left[1 + \gamma M_f^2 - (\gamma+1) M_f^2 \frac{\tilde{u}_2}{\tilde{u}_1} \right] \frac{\tilde{u}_2}{\tilde{u}_1} = \frac{\gamma+1}{2\gamma} \frac{(\Delta p)_{cr,j}}{p_1} \left[1 + \frac{(\Delta p)_2}{(\Delta p)_{cr,j}} \right], \quad (B.20)$$

$$-(\gamma+1) M_f^2 \frac{\tilde{u}}{\tilde{u}_1} \left(1 - \frac{\tilde{u}_2}{\tilde{u}_1} \right) = -\frac{\gamma+1}{\gamma} \frac{(\Delta p)_2}{p_1}, \quad (B.21)$$

and

$$\frac{M_f^2 [(\gamma+1)+2(\gamma-1)c_j]}{2\tilde{u}_1 \tau_j} x \left(1 - \frac{\tilde{u}_2}{\tilde{u}_1} \right) = \frac{(\gamma+1)x}{2\gamma a_1 \tau_j} \frac{(\Delta p)_2}{p_1} \quad (B.22)$$

Thus, Eq. (3.37) can be rewritten as

$$\begin{aligned} \frac{(\gamma+1)x}{2\gamma a_1 \tau_j} \frac{(\Delta p)_2}{p_1} = & -\frac{\gamma+1}{\gamma} \frac{(\Delta p)_2}{p_1} \\ & + \frac{\gamma+1}{2\gamma} \frac{(\Delta p)_{cr,j}}{p_1} \left[1 - \frac{(\Delta p)_2}{(\Delta p)_{cr,j}} \right] \ln \left[\frac{1}{\gamma M_f^2} \frac{(\Delta p)_2}{p_1} \frac{(\Delta p)}{(\Delta p)_2} \right] \\ & - \frac{\gamma+1}{2\gamma} \frac{(\Delta p)_{cr,j}}{p_1} \left[1 + \frac{(\Delta p)_2}{(\Delta p)_{cr,j}} \right] \ln \left[\frac{1}{\gamma M_f^2} \frac{(\Delta p)_2}{p_1} \right] \\ & \times \left\{ 1 - \frac{(\Delta p)}{(\Delta p)_2} \right\} \end{aligned} \quad (B.23)$$

Define

$$Z = -\frac{2\gamma}{\gamma+1} \frac{x}{a_1 \tau_j} \frac{(\Delta p)_2}{(\Delta p)_{cr,j}} \quad (3.39)$$

$$Z_0 = \frac{2\gamma}{\gamma+1} \frac{2(\Delta p)_2}{(\Delta p)_{cr,j}} \left[1 + \ln \left\{ \frac{1}{\gamma M_f^2} \frac{(\Delta p)_2}{p_1} \right\} \right] = \text{const} \quad (B.24)$$

then obtain

$$\begin{aligned} \frac{\gamma+1}{2\gamma} (Z - Z_0) = & \left[1 + \frac{(\Delta p)_2}{(\Delta p)_{cr,j}} \right] \ln \left[1 - \frac{(\Delta p)}{(\Delta p)_2} \right] \\ & - \left[1 - \frac{(\Delta p)_2}{(\Delta p)_{cr,j}} \right] \ln \left[\frac{(\Delta p)}{(\Delta p)_2} \right] \end{aligned} \quad (3.34)$$

B.6 Derivation of Eq. (3.41): Frozen-Shock Overpressure

Generally, the frozen overpressure can be expressed as

$$\frac{(\Delta p)_f}{p_1} = \frac{2\gamma}{\gamma+1} (M_f^2 - 1) \quad (B.25)$$

Substituting Eq. (B.19) into Eq. (B.25), obtain

$$\frac{(\Delta p)_f}{p_1} = \frac{(\Delta p)_2}{p_1} - \frac{(\Delta p)_{cr,j}}{p_1} \quad (3.41)$$

APPENDIX C

PROGRAM LISTING FOR RANDOM-CHOICE METHOD

The program for solving Eq. (4.1) using the RCM with an operator-splitting technique is given in this section. The normalized variables used for computation are:

$$E' = E/(\rho_1 RT_1), \quad v' = v/\sqrt{RT_1}, \quad p' = p/p_1,$$

$$\rho' = \rho/\rho_1, \quad T' = T/T_1, \quad \sigma_j' = \sigma_j/(RT_1),$$

$$r' = r/L_0, \quad t' = a_1 t/(\sqrt{\gamma} L_0)$$

where L_0 is a reference length, taken as $L_0 = 5r_0$, in most calculations.

The time step is determined from the maximum value for the local stability criterion (CFL condition) at each time step:

$$\Delta t' = \max[\Delta r' / \{|v'| + \sqrt{\gamma p'/\rho'}\}]$$

The program listing given below was used for the computations of real-viscous spherical waves.

```

C      RANDOM CHOICE METHOD    VARIATION  H2.
C      * SPHERICAL WAVE *
C      * REAL , VISCOUS *
      IMPLICIT REAL*8 (A-H,P-Z)
      DIMENSION KT1(10),PT1(10),TT1(10),TV1(10)
      REAL XARRAY(416),YARRAY(416)
      COMMON/IK/KR1,KL,ISTP,KR,NP1,ITT,N
      COMMON/DT,RL,UL,PL,R,U,P,E,RR,UR,PR,X1,Y,GAM,SOL,SOS,SOR
      COMMON/OUT/TIME,DX,RHO(416),PRE(416),UX(416),ENG(416),XR(416)
1,PRFAC
      COMMON/RAD/ETA,RE0,PRAN,TA(416),U2(416)
      COMMON/RELAX/SD(416),UZ(416),E1,TH1,TAU
      COMMON/TSU/ISK,ISS,ILM
      INTEGER TSTP

C      DATA READING
C      READ(5,81) NPRINS
      READ(5,81) ISTART
      READ(5,81) NQQT
      READ(5,81) IQ
      READ(5,81) NSTOP
      READ(5,81) JCT
      READ(5,81) JD
      READ(5,81) N
      READ(5,81) NHALF
      READ(5,81) NQG
      READ(5,81) IXYP
      READ(5,81) INCR
      READ(5,81) ISK
      READ(5,81) ISS
      READ(5,82) TMAX
      READ(5,82) TMIN
      READ(5,82) PMAX
      READ(5,82) PMIN
      READ(5,82) XP1
      READ(5,82) XP2
      READ(5,82) XFAC
      READ(5,82) RMAX
      READ(5,82) PRFAC
      READ(5,82) ESS
      READ(5,82) ETA
      READ(5,82) WL
      READ(5,82) PL
      READ(5,82) RL
      READ(5,82) T0
      READ(5,82) RH
      READ(5,82) COEP
      READ(5,82) COET
81  FORMAT(I10)
82  FORMAT(F15.7)
C      COEFFICIENT OF XYPLOT
      YP1=-PMIN
      YP2=(PMAX+PMIN)/12.0
      YP3=-TMIN
      YP4=(TMAX+TMIN)/12.0
      JCTM=JCT-JD
      LMT=1
      NP1=N+1
      NP2=N+15
      NPM=N-1
      NPX=N-5

```


APPENDIX D

PROGRAM OF MACCORMACK'S FINITE-DIFFERENCE METHOD

In Section 4.3.2, the RCM solutions are compared with MacCormack's solution for a perfect-viscous plane wave. In this section, the scheme and the program of the MacCormack method are given for the perfect-viscous plane wave.

The basic equation (4.1) can be written for perfect-viscous plane waves as

$$\frac{\partial U}{\partial t} + \frac{\partial F}{\partial x} - \frac{\partial^2 C}{\partial x^2} = 0$$

$$U = \begin{bmatrix} \rho \\ \rho v \\ E \end{bmatrix}, \quad F = \begin{bmatrix} \rho v \\ \rho v^2 + p \\ (E+p)v \end{bmatrix}, \quad C = \begin{bmatrix} 0 \\ 2\mu v \\ \lambda T + \mu v^2 \end{bmatrix}$$

$$E = \rho \left(e + \frac{1}{2} v^2 \right), \quad e = \frac{5}{2} RT, \quad p = \rho RT$$

The corresponding finite difference scheme of the MacCormack method are the predictor step:

$$\bar{U}_i^{n+1} = \bar{U}_i^n - \frac{\Delta t}{\Delta x} (\bar{F}_{i+1}^n - \bar{F}_i^n) + \frac{\Delta t}{(\Delta x)^2} (\bar{C}_{i+1}^n - 2\bar{C}_i^n + \bar{C}_{i-1}^n)$$

and the corrector step

$$U_i^{n+1} = \frac{1}{2} (\bar{U}_i^{n+1} + U_i^n) - \frac{\Delta t}{2\Delta x} (\bar{F}_i^{n+1} - \bar{F}_{i-1}^{n+1}) + \frac{\Delta t}{(\Delta x)^2} (\bar{C}_{i+1}^{n+1} - 2\bar{C}_i^{n+1} + \bar{C}_{i-1}^{n+1})$$

The normalized variables used for computation are

$$E' = E/(\rho_1 \gamma RT_1), \quad v' = v/\sqrt{\gamma RT_1}, \quad p' = p/p_1,$$

$$\rho = \rho/\rho_1, \quad T' = T/T_1, \quad x' = x/L_0, \quad t' = a_1 t/L_0$$

where L_0 is the reference length, and put as $L_0 = 5x_0$.

The time step is determined from 90% of the maximum value for the local stability criterion (CFL condition) at each time step:

$$t' = \max[0.9 \Delta x' / (\sqrt{T'} + |v'|)]$$

```

*****
*   USERID   = TN3D000
*   PROCEDURE = LOGON2
*
*   TSLOG STARTED TIME=10:57:08 DATE=82-12-08
*****
READY
E MAC F7(F1)
E
LIST
00010 C          PROGRAM LIST OF MACCORMACK METHOD
00020 C
00030 C          * SHOCK TUBE *
00040 C          * PERFECT, VISCOUS *
00050 C          * MACCORMACK *
00060          IMPLICIT REAL*8 (A-H,P-Z)
00070          DIMENSION U1(401,3),U2(401,3),V2(401),X(401),PA(415)
00080          1 ,KT1(10),PT1(10)
00090          2,VC(401),TC(401)
00100          REAL XARFAY(401),YARRAY(401)
00110 C          * DATA READING *
00120          KJ=399
00130          NMAX=220
00140          NN0=4
00150          ID=161
00160          INC=2
00170          NQG=0
00180          NPRINT=1
00190          ESS=0.03
00200          XFAC=2.5
00210          PFAC=1.00
00220          CFAC=0.9000
00230          P4=2.0000
00240          T4=1.0000
00250          WL=0.005
00260 C          * CONSTANTS *
00270          KJ1=KJ+1
00280          KJ2=KJ+2
00290          KJJ=KJ+13
00300          KS0=ID+19
00310          KL0=ID-20
00320          MPX=KJ1-5
00330          NC0=4.0*NN0
00340          ES1=ESS*0.01
00350          LX=1.0/DFLOAT(KJ1)
00360          GF=1.4000
00370          G2=GF*(GF-1.0)
00380          G1=1.0/G2
00390          VISC=1.5D-05
00400          RE0=(0.1013D+04)*WL/340.0/VISC
00410          GFPR=0.7000*(GF-1.0)
00420 C          * PRINTING OF CONSTANTS *
00430          WRITE(6,111)
00440          111 FORMAT(/1H0,10X,'*****',/1H ,10X,
00450          *   ' * SHOCK TUBE          *'/1H ,10X,' * PERFECT , VISCOUS *'
00460          *   ,/1H ,10X,' * MACCORMACK          *',
00470          *   /1H ,10X,'*****')
00480          WRITE(6,112) KJ1,NMAX,NN0,ID,INC,NQG,NPRINT,ESS,XFAC,
00490          *   PFAC,CFAC,P4,T4,WL,VISC
00500          112 FORMAT(/1H , 'KJ1=',I3,' , NMAX=',I3,' , NN0=',
00510          *   I2,' , ID=',I3,' , INC=',I2,' , NQG=',
00520          *   I3,' , NPRINT=',I2,/1H , 'ESS=',F7.5,' , XFAC=',
00530          *   F5.2,' , PFAC=',F5.3,' , CFAC=',F7.5,
00540          *   ' , P4=',F10.5,' , T4=',F10.5,' , WL=',F7.5,
00550          *   /1H , 'VISCOSITY=',D15.7)

```

```

00560 C      * MESH *
00570      X(1)=-0.5#DX
00580      DO 190 J=1,KJ1
00590      190 X(J+1)=X(J)+DX
00600 C      * INITIAL CONDITIONS *
00610      DO 206 J=1,ID
00620      U1(J,1)=P4/T4
00630      U1(J,2)=0.0
00640      V2(J)=0.0
00650      VC(J)=0.0
00660      TC(J)=T4
00670      U1(J,3)=G1#P4
00680      206 PA(J)=P4
00690      ID1=ID+1
00700      DO 207 J=ID1,KJ2
00710      U1(J,1)=1.0
00720      U1(J,2)=0.0
00730      V2(J)=0.0
00740      VC(J)=0.0
00750      TC(J)=1.0
00760      U1(J,3)=G1
00770      207 PA(J)=1.0
00780      DO 2070 J=KJ2,KJJ
00790      2070 PA(J)=1.0
00800      DO 208 I=1,3
00810      208 U1(ID,I)=0.5*(U1(ID+1,I)+U1(ID-1,I))
00820      PA(ID)=0.5*(PA(ID+1)+PA(ID-1))
00830      TC(ID)=0.5*(TC(ID+1)+TC(ID-1))
00840      Y=0.0
00850      NNF=NN0
00860      NCA=NC0
00870 C      * PLOT 1# ---FOR SLOW PLOTTER
00880      CALL DEVICE('XYPLOT ',0,0,0,0)
00890      CALL P4IND(0,0,200#80,260#80)
00900      CALL VSINI(0.0,0.0,20.0,26.0)
00910      DO 250 I=1,KJ
00920      XARRAY(I)=XFAC*(FLOAT(I-1)/FLOAT(KJ1)+0.5#DX)
00930      250 YARRAY(I)=PA(I+1)-1.0
00940      YARRAY(I)=-0.7
00950      CALL PLOT(4.0,4.0,-3)
00960      CALL SCALE(XARRAY,12.5,KJ,1)
00970      CALL SCALE(YARRAY,15.5,KJ,1)
00980      CALL AXIS(0.0,0.0,6HX-AXIS,-6,12.5,0.0,
00990      * XARRAY(KJ1),XARRAY(KJ2))
01000      CALL AXIS(0.0,0.0,12H0VERPRESSURE,12,15.5,90.0,
01010      * YARRAY(KJ1),YARRAY(KJ2))
01020      YARRAY(1)=1.0
01030      CALL LINE(XARRAY,YARRAY,KJ,1,0,0)
01040      CALL SYMBOL(1.2,17.0,0.3,37H*ACCORDMACK METHOD (NR=160,TX=0.9#CFL),
01050      * 0.0,37)
01060      CALL SYMBOL(1.2,16.0,0.3,33H*PERFECT,VISCOUS(P41=2.00,T41=1.0),
01070      * 0.0,33)
01080 C      * MACCORMACK *
01090      DO 209 J=1,KJ2
01100      DO 209 I=1,3
01110      209 U2(J,I)=U1(J,I)
01120      KS1=KS0
01130      KL1=KL0
01140      DO 360 N=1,NMAX
01150      CFL1=1.0
01160      DO 300 J=KL1,KS1
01170      CFL2=1.0/(DSQRT(V2(J))+DSQRT(DABS(PA(J)/U1(J,1))))
01180      IF(CFL1.LT.CFL2) GO TO 300
01190      CFL1=CFL2
01200      JCFL=J
01210      300 CONTINUE

```

```

01220      DTX=CFL1*CFAC
01230      DT=DTX*DX
01240      DW=2.0*DT
01250      D3=0.5*DTX
01260      D4=DTX/DX/RE0
01270      D5=D4/GFPR
01280      D6=0.5*D4
01290      D7=0.5*D5
01300      Y=Y+DT
01310      DO 302 J=KL1,KS1
01320      DDD=DTX
01330      U2(J,1)=U1(J,1)-DTX*U1(J+1,2)+DDD*U1(J,2)
01340      U2(J,2)=U1(J,2)-DTX*U1(J+1,1)*V2(J+1)+DDD*U1(J,1)*V2(J)-DTX*
01350      1 (PA(J+1)-PA(J))/GF
01360      * +D4*(VC(J+1)-2.0*VC(J)+VC(J-1))
01370      U2(J,3)=U1(J,3)-DTX*U1(J+1,2)*(U1(J+1,3)+PA(J+1)/GF)/U1(J+1,1)
01380      1 +DDD*U1(J,2)*(U1(J,3)+PA(J)/GF)/U1(J,1)
01390      * +D5*(TC(J+1)-2.0*TC(J)+TC(J-1))+D4*(V2(J+1)-2.0*V2(J)+V2(J-1))
01400 302 CONTINUE
01410      DO 303 J=KL1,KS1
01420      VB=U2(J,2)/U2(J,1)
01430      IF(DABS(VB).LT.(0.1D-08)) GO TO 3010
01440      V2(J)=VB**2
01450      GO TO 3011
01460 3010 V2(J)=0.0
01470 3011 PA(J)=G2*(U2(J,3)-0.5*V2(J)*U2(J,1))
01480      VC(J)=2.0*VB
01490      TC(J)=PA(J)/U2(J,1)
01500 303 CONTINUE
01510      DO 304 I=1,3
01520 304 U2(1,I)=U2(2,I)
01530      U2(1,2)=-U2(1,2)
01540      V2(1)=V2(2)
01550      PA(1)=PA(2)
01560      VC(1)=VC(2)
01570      TC(1)=TC(2)
01580      DO 306 J=KL1,KS1
01590      DDD=D3
01600      U1(J,1)=0.5*(U1(J,1)+U2(J,1))-DDD*U2(J,2)+D3*U2(J-1,2)
01610      U1(J,2)=0.5*(U1(J,2)+U2(J,2))-DDD*U2(J,1)*V2(J)+D3*U2(J-1,1)
01620      1 *V2(J-1)-D3*(PA(J)-PA(J-1))/GF
01630      * +D6*(VC(J+1)-2.0*VC(J)+VC(J-1))
01640      U1(J,3)=0.5*(U1(J,3)+U2(J,3))-DDD*U2(J,2)*(U2(J,3)+PA(J)/GF)/U2(J
01650      1 ,1)+D3*U2(J-1,2)*(U2(J-1,3)+PA(J-1)/GF)/U2(J-1,1)
01660      * +D7*(TC(J+1)-2.0*TC(J)+TC(J-1))+D6*(V2(J+1)-2.0*V2(J)+V2(J-1))
01670 306 CONTINUE
01680      DO 307 J=KL1,KS1
01690      VB=U1(J,2)/U1(J,1)
01700      IF(DABS(VB).LT.(0.1D-08)) GO TO 347
01710      V2(J)=VB**2
01720      GO TO 348
01730 347 V2(J)=0.0
01740 348 PA(J)=G2*(U1(J,3)-0.5*V2(J)*U1(J,1))
01750      VC(J)=2.0*VB
01760      TC(J)=PA(J)/U1(J,1)
01770 307 CONTINUE
01780      DO 314 I=1,3
01790 314 U1(1,I)=U1(2,I)
01800      U1(1,2)=-U1(1,2)
01810      V2(1)=V2(2)
01820      PA(1)=PA(2)
01830      VC(1)=VC(2)
01840      TC(1)=TC(2)
01850      DO 3145 I=KL1,KS1
01860      J=KS1-I+KL1
01870      PAA=PA(J)-1.0000

```

```

01880      IF(PAA.GT.E51) GO TO 3150
01890      U1(J,1)=1.0000
01900      U1(J,2)=0.000000
01910      U1(J,3)=G1
01920      PA(J)=1.000000
01930      VC(J)=0.00000
01940      TC(J)=1.00000
01950      3145 V2(J)=0.000000
01960 C      * STEP CONTROL *
01970      3150 IF(KL1.EQ.2) GO TO 315
01980      KL1=KL1-1
01990      315 IF(KS1.GE.KJ1) GO TO 316
02000      KS1=KS1+1
02010      316 IF(MOD(N,NNN).NE.0) GO TO 360
02020      IF(N.LT.NN0) GO TO 888
02030      WRITE(6,2001) N,Y,DTX,JCFL
02040      2001 FORMAT(1H0,5X,2H1=,17,5X,2HY=,F13.5,5X,4HDTX=,E13.5,5X,5HJCFL=,16)
02050      KM=(KS1-KL1)/10
02060      KM1=KM+1
02070      KM2=KL1+KM
02080      DO 2500 I=KL1,KM2,NPRINT
02090      DO 2400 J=1,10
02100      KT1(J)=I+KM1*(J-1)
02110      2400 PT1(J)=PFAC*(PA(KT1(J))-1.0)
02120      WRITE(6,2501) (KT1(J),PT1(J),J=1,10)
02130      2500 CONTINUE
02140      2501 FORMAT(14,F8.4,14,F8.4,14,F8.4,14,F8.4,14,F8.4,14,F8.4,14,F8.4,14,F8.4,14,
02150      1 F8.4,14,F8.4,14,F8.4)
02160 C      * PLOT 2 *
02170      PSA=PA(NPX)-1.0
02180      IF(PSA.GT.E55) GO TO 999
02190      DO 260 I=1,KJ
02200      YARRAY(I)=PA(I+1)-1.0
02210      260 CONTINUE
02220      CALL LINE(XARRAY,YARRAY,KJ,1,0,0)
02240      888 IF(MOD(N,NCA).NE.0) GO TO 360
02240      NNN=NNN+NN0
02250      NCA=NCA+INCNCO
02260      INC=INC+1
02270      360 CONTINUE
02280      999 CALL VSTERM(0,0)
02290      CALL GPSLTM
02300 C      * END *
02310      WRITE(6,611)
02320      611 FORMAT(///40X,15H***** END *****///)
02330      STOP
02340      END
END OF DATA

```

INPUT

E

END S

SAVED TO DATA SET ('TN3D000.MAC.FORT')

READY

TSLOG END

```

*****
*   USERID   = TN3D000
*   PROCEDURE = LOGON2
*
*   TSLOG ENDED   TIME=10:58:30 DATE=82-12-08
*
*****

```

APPENDIX E

COMPARISON BETWEEN NEAR-FIELD SOLUTIONS OF THE EXPLOSION OF A PRESSURIZED AIR SPHERE USING LAX, MacCORMACK AND RANDOM-CHOICE METHODS (RCM) FOR A PERFECT-INVISCID FLOW

In the initial stage of the present study, several numerical methods were tried to solve the problem of the explosion of a pressurized air sphere. Some of the results are presented here to show the superiority of the RCM over other methods for analysing shock-transitions of spherical N-waves.

The near-field solutions using Lax, MacCormack and RCM for the same case as A1 ($P_{41} = 2.0$, $T_{41} = 1.0$) are shown in Figs. E.1, E.2 and E.3, respectively. In Figs. E.1 and E.2 (Lax and MacCormack methods), the time steps were selected to be 80% of the CFL condition to avoid undesirable oscillations of numerical values. As seen in Figs. E.1(a) and

E.2(a), the Lax and MacCormack solutions give smoothed shock-transitions due to the effect of artificial viscosity in a rough mesh size of $\Delta r^* = 1/80$. By using the finer mesh sizes [$\Delta r^* = 1/320$, Figs. E.1(b) and E.2(b)], this smoothing is improved, and the Lax method gives a better result. However, the smoothing at the front shock still remains. The RCM solutions [Figs. E.2(a) and (b)] show discontinuous shock fronts irrespective of mesh sizes ($\Delta r^* = 1/40$, $1/80$), though some randomnesses appear in the expansion part of a pressure profile. In our analysis of shock transition, it is necessary to clarify the effects of viscosity and vibrational nonequilibrium on shock thickness without the effect of artificial viscosity. Consequently, we adopted the RCM.

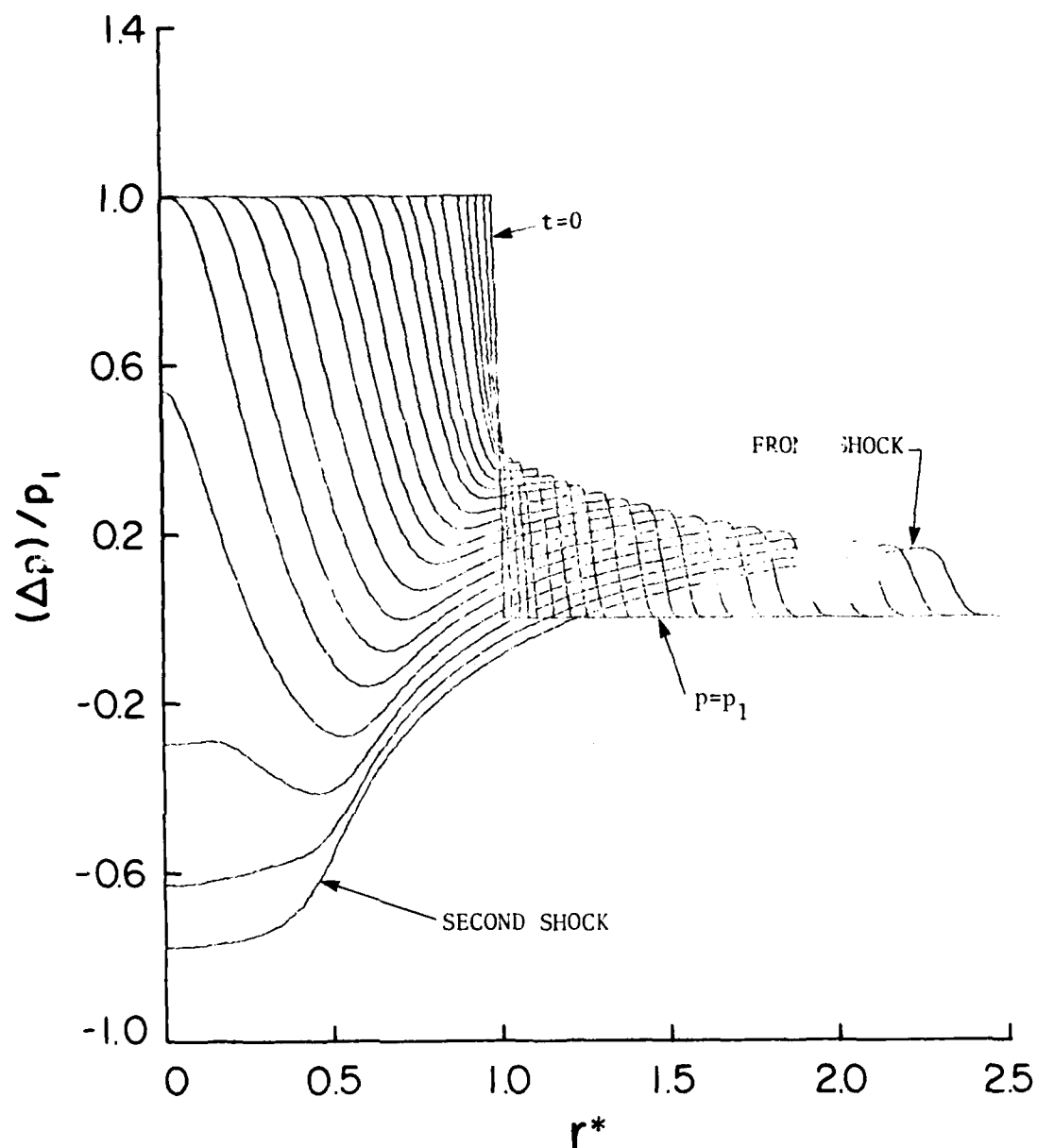


FIG. E.1(a) NEAR-FIELD SOLUTION OF EXPLOSION OF A PRESSURIZED AIR SPHERE USING LAX METHOD FOR PERFECT-INVISCID FLOW (CASE A1). MESH SIZE $\Delta r^* = 1/80$.

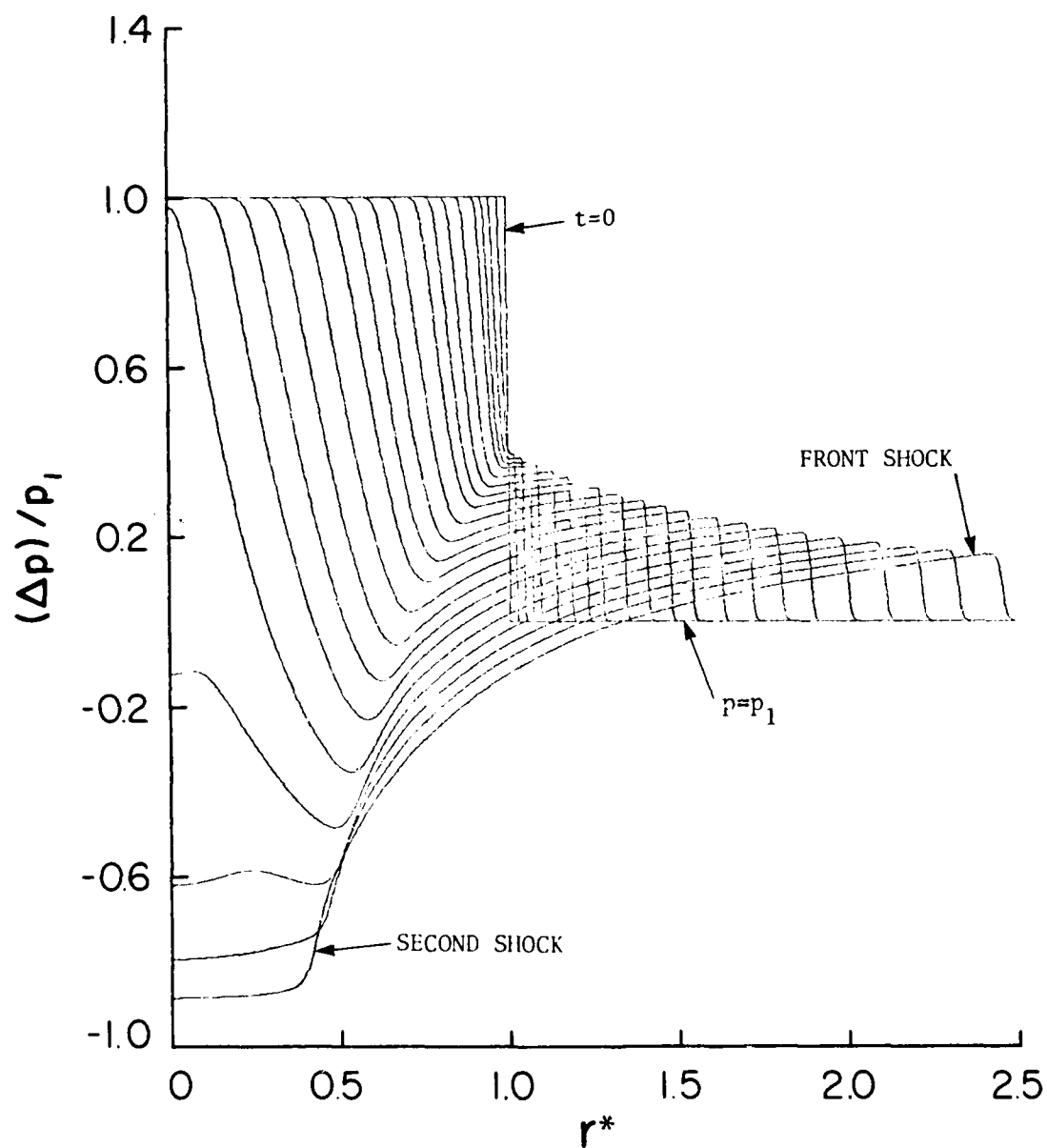


FIG. E.1(b) NEAR-FIELD SOLUTION OF EXPLOSION OF A PRESSURIZED AIR SPHERE USING LAX METHOD FOR A PERFECT-INVISCID FLOW (CASE A1). MESH SIZE $\Delta r = 1/320$.

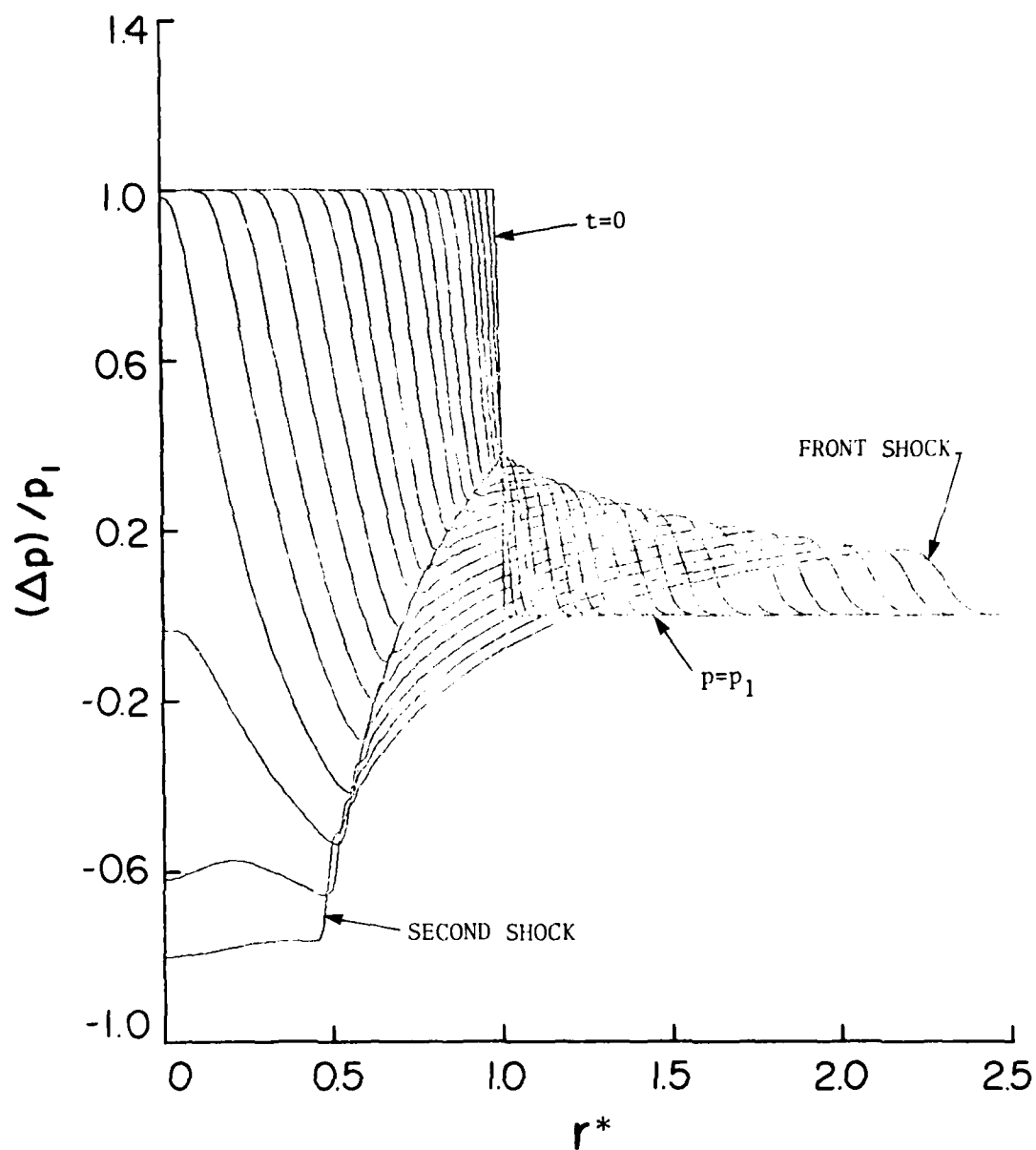


FIG. E.2(a) NEAR-FIELD SOLUTION OF EXPLOSION OF A PRESSURIZED AIR SPHERE USING MacCORMACK METHOD FOR A PERFECT-INVISCID FLOW (CASE A1). MESH SIZE $\Delta r^* = 1/80$.

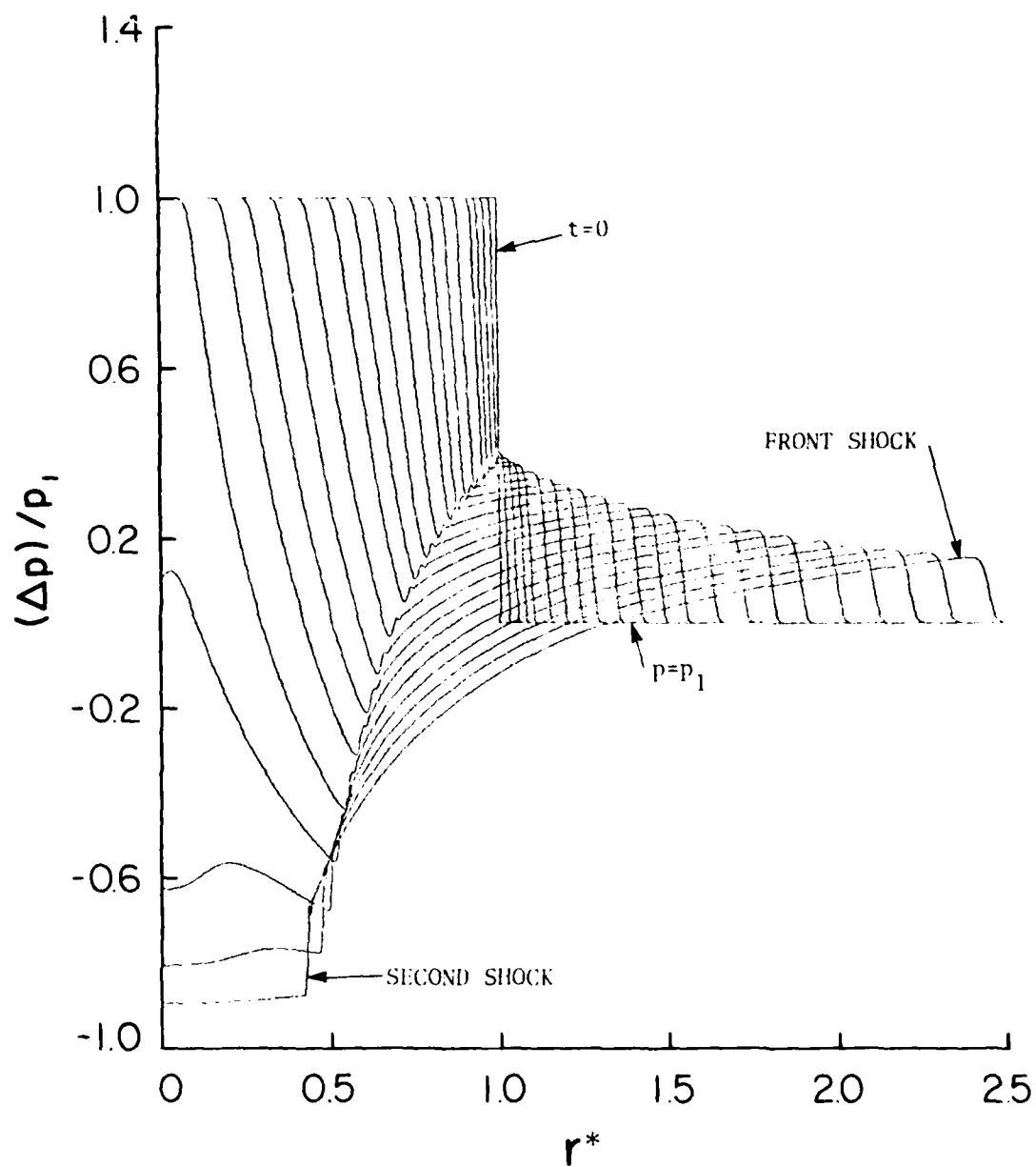


FIG. 1.2(b) NEAR-FIELD SOLUTION OF EXPLOSION OF A PRESSURIZED AIR SPHERE USING MACCORMACK METHOD FOR A PERFECT-INVISCID FLOW (CASE A1), MESH SIZE $\Delta r^* = 1/520$.

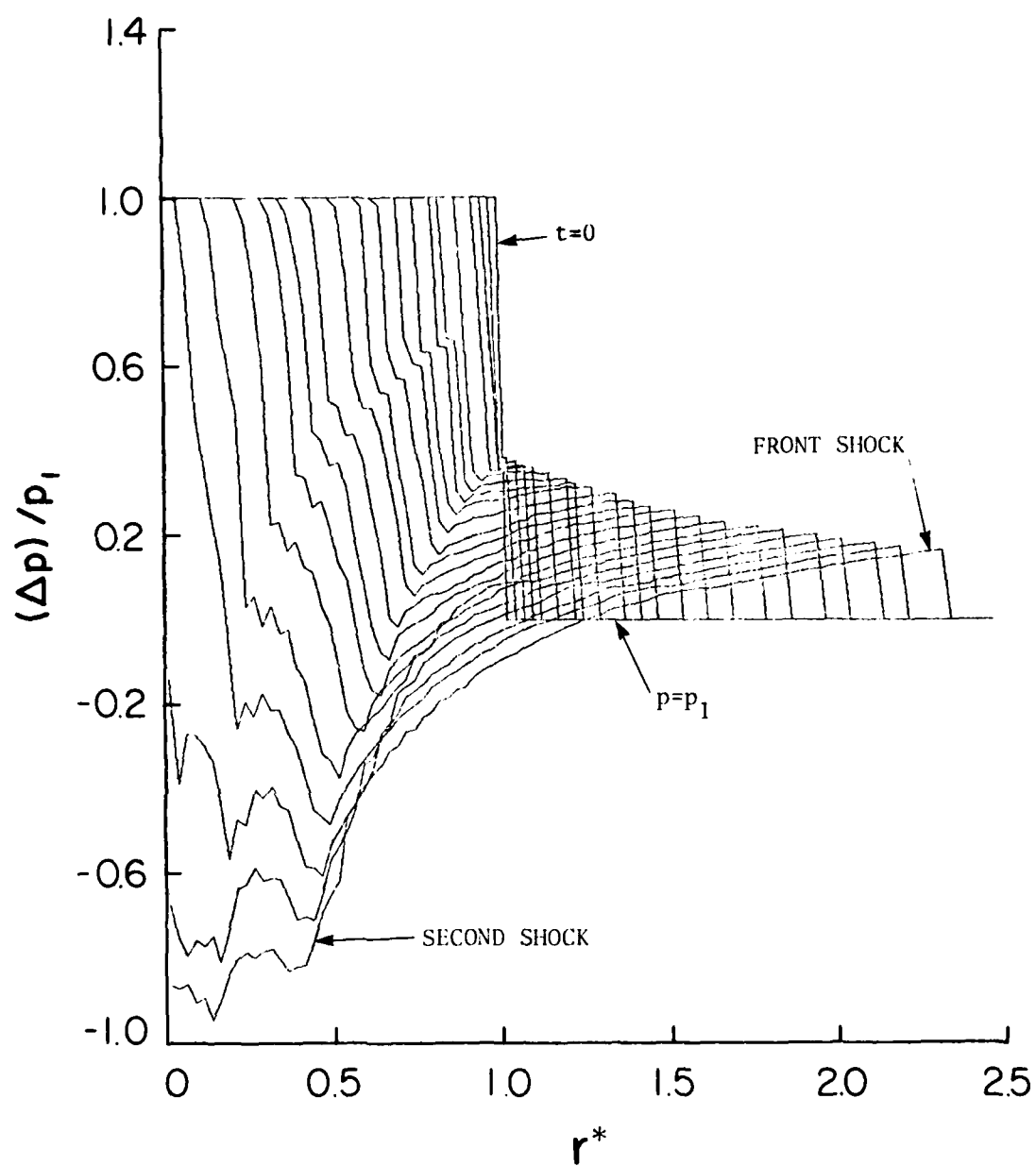


FIG. E.5(a) NEAR-FIELD SOLUTION OF EXPLOSION OF A PRESSURIZED AIR SPHERE USING RANDOM-CHOICE METHOD FOR A PERFECT-INVISCID FLOW (CASE A1). MESH SIZE $\Delta r^* = 1/40$.

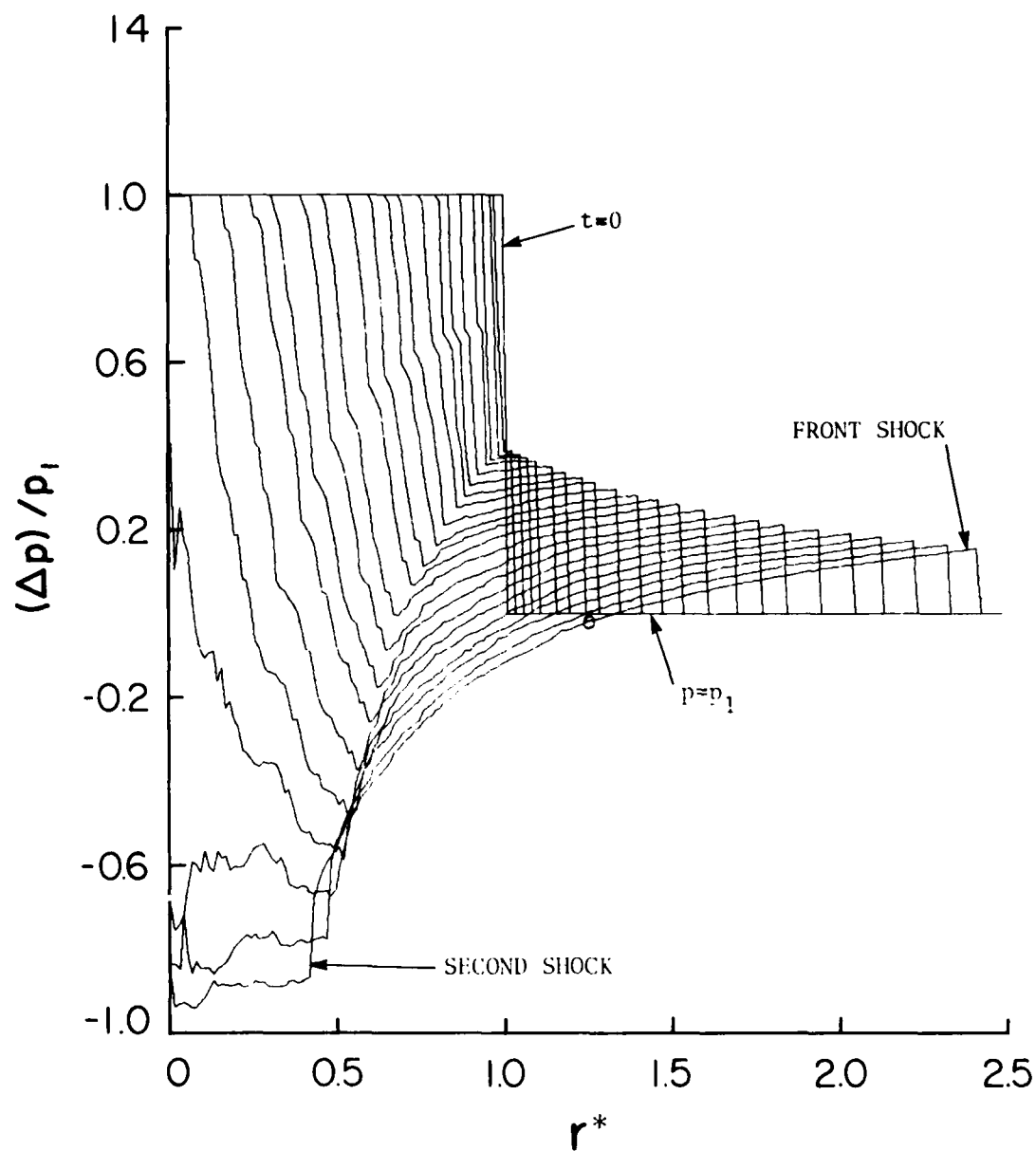


FIG. 1.5(b) NEAR-FIELD SOLUTION OF EXPLOSION OF A PRESSURIZED AIR SPHERE USING RANDOM-CHOICE METHOD FOR A PERFECT-INVISCID FLOW (CASE 1.1, MESH SIZE $\Delta r^* = 1/80$).

APPENDIX F

BULK VISCOSITY ANALYSIS FOR VIBRATIONAL RELAXATION FOR OXYGEN

In Sections 4.4.5 and 4.4.6, the bulk viscosity concept is introduced to evaluate the vibrational relaxation for oxygen instead of solving the relaxation equation for oxygen. The basic equations are shown in some detail as follows:

$$\frac{\partial U}{\partial t} + \frac{\partial F}{\partial r} \left(\frac{v^2}{2} + \frac{1}{r} \frac{\partial}{\partial r} \right) C + j(H_I + H_V) - H_R = 0 \quad (F.1)$$

$$U = \begin{bmatrix} \rho \\ \rho v \\ E \\ \rho v N \end{bmatrix}, \quad F = \begin{bmatrix} \rho v \\ \rho v^2 + p \\ (E+p)v \\ \rho v N \end{bmatrix}$$

$$C = \begin{bmatrix} 0 \\ 2\rho_e v \\ \rho T + \rho_e v^2 \end{bmatrix}, \quad H_I = \frac{1}{r} \begin{bmatrix} \rho v \\ \rho v^2 \\ (E+p)v \\ \rho v N \end{bmatrix}$$

$$H_V = \frac{1}{r^2} \begin{bmatrix} 0 \\ 2\rho_e v \\ 0 \\ 0 \end{bmatrix}, \quad H_R = \begin{bmatrix} 0 \\ 0 \\ 0 \\ \rho[(\sigma_N)_e - \sigma_N]/\tau_N \end{bmatrix}$$

$$p = \rho RT, \quad E = \rho \left[e + \frac{1}{2} v^2 \right] \quad (F.2)$$

$$e = \frac{5}{2} RT + (\sigma_O)_e + \sigma_N$$

instead of Eqs. (4.1) and (4.2), where ρ_e is an effective viscosity including the bulk viscosity $(\mu_v)_O$ for oxygen, defined by

$$\rho_e = \mu + (\mu_v)_O/2 \quad (F.3)$$

The bulk viscosity $(\mu_v)_O$ is evaluated from Eq. (3.25):

$$(\mu_v)_O = (a_f^2 - a_e^2) \rho_O$$

$$= \frac{1}{4} a_f^2 (1 - \epsilon_e) \rho_O \quad (F.4)$$

where

$$\epsilon_e = \frac{\frac{7}{2} + C_0}{\frac{5}{2} + C_0}, \quad C_0 = 0.209 \left[\frac{C_0}{T_1} \right]^2 \exp \left[-\frac{C_0}{T_1} \right] \quad (F.5)$$

The operator-splitting technique was applied to Eq. (F.1) as well as Eq. (4.1). The effect of vibrational relaxation for oxygen was taken into account in the step of viscous correction [Step 3; Eq. (4.11)] of the operator splitting through Eqs. (F.3)-(F.5). More precisely, in the first step, the RCM solution should be obtained by solving the Riemann problem for oxygen in vibrational equilibrium, since the whole flow field may be considered for oxygen as in quasi-equilibrium. However, in the present report, the effects of oxygen vibrational excitation is taken into account only through the bulk viscosity, since its contribution to the internal energy specific heats of the air molecules may be considered as very small as long as it is nearly in equilibrium at room temperature. Thus, the RCM solutions were obtained by using the inviscid-frozen program, excluding the term $(\sigma_O)_e$ in Eq. (F.2).



Institute for Aerospace Studies, University of Toronto (U.T.A.S.),
4925 Dufferin Street, Downsview, Ontario, Canada, M3H 5T6

RANDOM-CHOICE SOLUTIONS FOR NEAR SPHERICAL SHOCK-WAVE TRANSITIONS OF N-WAVES IN AIR WITH VIBRATIONAL EXCITATION

11 SEP 1964

- 1 Shock-wave transitions 2 Effects of viscosity, heat-conduction and vibrational excitation
3 Spherical shock waves 4 Exploding wires 5 Numerical methods
6 Index, H. class 1 11 IRIIS Report No. 255

In order to clarify the effects of vibrational excitation on shock-wave transitions of weak, spherical N-waves, which were generated by using sparks and exploding wires as sources, the compressible Navier-Stokes equations were solved numerically, including a vibrational-relaxation equation for oxygen and nitrogen. A small, pressurized air-sphere explosion was used to simulate the N-waves generated from the actual sources. By employing the random-choice method (RCM) with an operator-splitting technique, the effects of artificial viscosity appearing in finite-difference schemes were eliminated and accurate profiles of the shock transitions were obtained. However, a slight randomness in the variation of the shock thickness remains. It is shown that a computer simulation is possible by using a proper choice of initial parameters to obtain the variations of the N-wave overpressure and half-duration with distance from the source. The calculated rise times are also shown to simulate both spark and exploding-wire data. It was found that, in addition to the vibrational-relaxation time of oxygen, both the duration and attenuation rate of a spherical N-wave are important factors controlling its rise time. The effects of the duration and attenuation rate of a spherical N-wave on its rise time, which are designated as the *Wu-Yeh effect* and the *Wu-Yeh effect*, respectively, are discussed in more detail pertaining to Lighthill's analytical solutions and the RCM solutions for nonstationary plane waves and spherical N-waves. It is also shown that the duration and attenuation rate of a spherical N-wave are affected by viscosity and vibrational nonequilibrium, so that it can deviate from the results of classical linear acoustic theory for very weak spherical waves.

Available copies of this report are limited. Return this card to UTIAS, if you require a copy.



Institute for Aerospace Studies, University of Toronto, 1414
4925 Baffin Street, Downsview, Ontario, Canada M3H 5T6

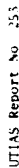
RANDOM CRACK SOLUTIONS FOR BEAM SPHERICAL SHOCK-WAVE TRANSITIONS OF WAVES IN AIR WITH VIBRATIONAL EXCITATION

Hon. Mr. Justice Gauthier:

1. Shock wave transitions 2. Effects of viscosity, heat conduction, and vibrational excitation
3. Spherical shock waves 4. Exploding wires 5. Numerical methods
Honma, H. Class. 1 1 II. IITAS Report No. 353

In order to clarify the effects of vibrational excitation on shock-wave transitions of weak, spherical N-waves, which were generated by using sparks and exploding wires as sources, the compressible Navier-Stokes equations were solved numerically, including a vibrational-relaxation equation for oxygen in the initial sources. A small, pressurized air-sphere explosion was used to simulate the N-wave generator in the actual sources. By employing the random-choice method (PCM) with a operator-splitting technique, the effects of artificial viscosity appearing in finite-difference schemes were eliminated and realistic profiles of the shock transitions were obtained. However, a slight randomness in the variation of the shock thickness remains. It is shown that a computer simulation is possible by using a proper choice of initial parameters to obtain the variations of the N-wave overpressure and half-duration with distance from the source. The calculated rise times are also shown to simulate both spark and exploding-wire data. It was found that, in addition to the vibrational-relaxation time of oxygen, both the duration and attenuation rate of a spherical N-wave are important factors controlling the rise time. The effects of the duration and attenuation rate of a spherical N-wave on its rise time, which are designated as the *N-wave error* and the *nonzero-error effect*, respectively, are discussed in more detail pertaining to Lighthill's analytical solutions and the PCM solutions for nonstationary plane waves and spherical N-waves. It is also shown that the duration and attenuation rate of a spherical N-wave are affected by viscosity and vibrational nonequilibrium, so that it can deviate from the results of classical, linear acoustic theory for very weak spherical waves.

Available copies of this report are limited. Return this card to UTIAS, if you require a copy.



Institute for Aerospace Studies, University of Toronto, 437
4925 Buzzerin Street, Downsview, Ontario, Canada M3H 5T6

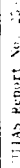
RANDOM-CHOICE SOLUTIONS FOR NEAR SPHERICAL SHOCK-WAVE TRANSLATIONS OF A WAVE IN AIR WITH VIBRATIONAL EXCITATION

Honora H. Glass, Ph.D.

1. Shock-wave transitions - Effects of viscosity, heat conduction and vibration on
2. Explosive waves - 3 Numerical methods
3. Spherical shock waves - 4 Explosive waves - 5 Numerical methods

In order to clarify the effects of vibrational excitation on shock-wave transitions of weak, spherical N_2 waves, which were generated by using spark and exploding wires as sources, the compressible Navier-Stokes equations were solved numerically, including a vibrational-relaxation equation for oxygen or nitrogen. A small, pressurized air-sphere explosion was used to simulate the N_2 waves generated from the actual sources. By employing the random-phase method (RPM) with a generator-splitting technique, the effects of artificial viscosity appearing in the numerical calculations were eliminated and accurate profiles of the shock transitions were obtained. However, owing to randomness in the variation of the shock thickness results, it is shown that a complete simulation is possible by using a proper choice of initial parameters to obtain the variations of the wave pressure and half-duration with distance from the source. The calculated rise times are also shown to simulate both spark and exploding-wire data. It was found that, in addition to the vibrational-relaxation time of oxygen, both the duration and attenuation rate of a spherical wave are important factors controlling its rise time. The effects of the duration and attenuation rate of a spherical wave on its rise time, which are designated as the "wave center" and the "wave edge," respectively, are discussed in more detail pertaining to lightning analytical solutions and the PWC equations for ionospheric plane waves and spherical waves. It is also shown that the duration and attenuation rate of a spherical wave are affected by viscosity and vibrational excitation, so that it can deviate from the results of classical linear acoustic theory for very weak spherical waves.

Available copies of this report are limited. Return this card to UTIAS, if you require a copy.



Institute for Aerospace Studies, University of Toronto
1-25 Baffert Street, Downsview, Ontario, Canada, M3H 5T6

RANDOM-WALK SOLUTIONS FOR WEAK SPHERICAL SHOCK-WAVE TRANSMISSION IN A MEDIUM WITH VIBRATIONAL FLUCTUATION

1. *Introduction*

2. shock wave transitions
3. Effects of viscosity, heat conduction and vibrational excitation
4. Exploding wires
5. Numerical methods
6. Homoclinic orbits
7. Homoclinic bifurcation
8. Homoclinic bifurcation
9. Homoclinic bifurcation
10. Homoclinic bifurcation
11. Homoclinic bifurcation
12. Homoclinic bifurcation
13. Homoclinic bifurcation
14. Homoclinic bifurcation
15. Homoclinic bifurcation
16. Homoclinic bifurcation
17. Homoclinic bifurcation
18. Homoclinic bifurcation
19. Homoclinic bifurcation
20. Homoclinic bifurcation
21. Homoclinic bifurcation
22. Homoclinic bifurcation
23. Homoclinic bifurcation
24. Homoclinic bifurcation
25. Homoclinic bifurcation
26. Homoclinic bifurcation
27. Homoclinic bifurcation
28. Homoclinic bifurcation
29. Homoclinic bifurcation
30. Homoclinic bifurcation
31. Homoclinic bifurcation
32. Homoclinic bifurcation
33. Homoclinic bifurcation
34. Homoclinic bifurcation
35. Homoclinic bifurcation
36. Homoclinic bifurcation
37. Homoclinic bifurcation
38. Homoclinic bifurcation
39. Homoclinic bifurcation
40. Homoclinic bifurcation
41. Homoclinic bifurcation
42. Homoclinic bifurcation
43. Homoclinic bifurcation
44. Homoclinic bifurcation
45. Homoclinic bifurcation
46. Homoclinic bifurcation
47. Homoclinic bifurcation
48. Homoclinic bifurcation
49. Homoclinic bifurcation
50. Homoclinic bifurcation
51. Homoclinic bifurcation
52. Homoclinic bifurcation
53. Homoclinic bifurcation
54. Homoclinic bifurcation
55. Homoclinic bifurcation
56. Homoclinic bifurcation
57. Homoclinic bifurcation
58. Homoclinic bifurcation
59. Homoclinic bifurcation
60. Homoclinic bifurcation
61. Homoclinic bifurcation
62. Homoclinic bifurcation
63. Homoclinic bifurcation
64. Homoclinic bifurcation
65. Homoclinic bifurcation
66. Homoclinic bifurcation
67. Homoclinic bifurcation
68. Homoclinic bifurcation
69. Homoclinic bifurcation
70. Homoclinic bifurcation
71. Homoclinic bifurcation
72. Homoclinic bifurcation
73. Homoclinic bifurcation
74. Homoclinic bifurcation
75. Homoclinic bifurcation
76. Homoclinic bifurcation
77. Homoclinic bifurcation
78. Homoclinic bifurcation
79. Homoclinic bifurcation
80. Homoclinic bifurcation
81. Homoclinic bifurcation
82. Homoclinic bifurcation
83. Homoclinic bifurcation
84. Homoclinic bifurcation
85. Homoclinic bifurcation
86. Homoclinic bifurcation
87. Homoclinic bifurcation
88. Homoclinic bifurcation
89. Homoclinic bifurcation
90. Homoclinic bifurcation
91. Homoclinic bifurcation
92. Homoclinic bifurcation
93. Homoclinic bifurcation
94. Homoclinic bifurcation
95. Homoclinic bifurcation
96. Homoclinic bifurcation
97. Homoclinic bifurcation
98. Homoclinic bifurcation
99. Homoclinic bifurcation
100. Homoclinic bifurcation

[illegible]

Available copies of this report are limited. Return this card to UTIAS, if you require a copy.

